The Dissertation Committee for Stefano Larentis Certifies that this is the approved version of the following Dissertation:

Electronic Properties and Electron-Electron Interaction Effects in Transition Metal Dichalcogenides

Committee:

Emanuel Tutuc, Supervisor

Sanjay K. Banerjee

Allan H. MacDonald

Leonard F. Register

Li Shi

Electronic Properties and Electron-Electron Interaction Effects in Transition Metal Dichalcogenides

by

Stefano Larentis

Dissertation

Presented to the Faculty of the Graduate School of

The University of Texas at Austin

in Partial Fulfillment

of the Requirements

for the Degree of

Doctor of Philosophy

The University of Texas at Austin

August, 2018

Dedication

To my grandparents Roberto, Viola, Silvio, and Ines,

to my parents Maurizio and Lorenza, and to Giulia

Acknowledgements

First and foremost, I would like to thank my advisor Prof. Emanuel Tutuc, for his patience and his guidance during my entire PhD. His ability to navigate the research world, from experimental techniques to the publication stage, has been invaluable. I also thank him for many suggestions, and in particular the early intuition to investigate electron transport in transition metal dichalcogenides. A special thank you goes also to the other members of my dissertation committee Prof. Sanjay K. Banerjee, Prof. Allan H. MacDonald, Prof. Leonard F. Register and Prof. Li Shi. I also had the pleasure to directly collaborate with Prof. Sanjay K. Banerjee, and Prof. Allan H. MacDonald in different projects and in the preparation of manuscripts.

Many of the results that I present in this dissertation would not have been obtained without the collaboration among the students & postdocs in Dr. Tutuc group. The friendships that I forged with many of the group members will be an enduring memory of my PhD. I would like to thank Babak Fallahazad, for his patience and support over the years, Hema C. P. Movva for the late nights at Magnet Lab and his constant help, Kyoung Kim for his infinite fabrication wisdom, John. R. Tolsma for his help with many-body physics, Dave C. Dillen for his help with the magnet and vacuum, and the many get together organized, Kayoung Lee for the many discussions and late-night help, Jiamin Xue for cleanroom and physics wisdom, En-Shao Liu for being a patient teacher, Micah Points for his CVD, Chris Corbet for cheering us up at every holiday, Will Burg and Feng Wen for the many scientific and sports discussions, Johnny Rojas and Armand Berhoozi for the great exfoliation efforts.

I would like to thank other friends that I interacted with both inside and outside the MRC cleanroom: Oleksiy Slobodyan, Jian Zhang, Jeff Schmulen, Francesco Monticone, Alessandro Garufo, Nicola Ciocchini, Tanuj Trivedi, Anne Lampman, Yimeng Wang, Mike Rodder, Amritesh Rai, Atresh Sanne, Harry Chou, Jaehyun Ahn, Sangwoo Kang, Tanmoy Pramanik, Jason Mantey, William Hsu, Sk Fahad Chowdhury, Nitin Prasad, Saungeun Park, Milo Holt, Nasibeh Rahimi, Avinash Nayak, Rudresh Ghosh, Anupam Roy, Dan Fine, Praveen Pasupathy, Seungyong Jung, Nishant Nookala, Karun Vijayraghavan, Daniele Palaferri, Feng Lu, Christopher Brennan, Rodolfo Salas, Donghwan Kim, Mir Mohammad Sadeghi, and Gabriella Coloyan.

I would like to also thank the MRC staff, in particular Christine Wood, Jean Toll, Jesse James, Bill Ostler, Ricardo Garcia, David Farnsworth, Gerlinde Sehne, Joyce Kokes, Jackie Srnensky. Darren Robbins, and James Hiltzfelder.

The PhD per-se is a long and trying endeavor, and I think navigating it alone would be nearly impossible. Over the years I have been very lucky, my family and friends in Italy and in the US have been extremely supportive. A special thanks goes to Ing. Giancarlo Pagni, without the inspiration he gave me I would have probably never pursued all this. At last, I need to thank my parents Maurizio and Lorenza, and Giulia the person I hope to spend the rest of my life with, you have been a never-ending source of support, care and love. Without you I would never have arrived at this point, from the deep of my heart thank you.

Abstract

Electronic Properties and Electron-Electron Interaction Effects in Transition Metal Dichalcogenides

Stefano Larentis, Ph.D.

The University of Texas at Austin, 2018

Supervisor: Emanuel Tutuc

Transition metal dichalcogenides (TMDs) are a new class of two-dimensional layered materials characterized by a MX_2 chemical formula, where M (X) stands for a transition metal (chalcogen). MoS_2, $MoSe_2$ and $MoTe_2$ are semiconducting TMDs, which at the monolayer limit possess bandgaps >1 eV, rendering them attractive as possible channel material for scaled transistors. The bandstructures of monolayers feature coupled spin and valley degrees of freedom, thanks to large spin-orbit interaction, and large effective masses (m^*), suggesting that electron-electron interaction effects are expected to be important in these semiconductors. In this dissertation we discuss the fabrication and electrical characterization of TMD-based electronic devices, with a focus on their electronic properties, including scattering mechanisms contributing to the mobility, carriers' effective mass, band offset in heterostructures, electronic compressibility, and spin susceptibility. We begin studying the four-point field-effect mobilities of few-layers MoS_2, $MoSe_2$ and $MoTe_2$ field effect transistors (FETs), in top-contact, bottom-gate architectures. Using hexagonal boron-nitride dielectrics, we fabricate FETs with an improved bottom-contact, dual-gate architecture to probe transport at low temperatures in monolayer MoS_2, and mono- and bilayer $MoSe_2$. From conductivity and carrier density measurements we determine the Hall mobility, which shows strong temperature

dependence, consistent with phonon scattering, and saturates at low temperatures because of impurity scattering. High mobility MoSe$_2$ samples probed in perpendicular magnetic field, at low temperatures show Shubnikov-de Haas oscillations. Using magnetotransport we probe carriers in spin split bands at the K point in the conduction band and extract their $m^* = 0.8m_e$; m_e is the bare electron mass. Quantum Hall states emerging at either odd or even filling factors are explained by a density dependent, interaction enhanced Zeeman splitting. Gated graphene-MoS$_2$ heterostructures reveal a saturating electron branch conductivity at the onset of MoS$_2$ population. Magnetotransport measurements probe the graphene electron density, which saturates and decreases as MoS$_2$ populates, a finding associated with the negative compressibility of MoS$_2$ electrons, modeled by a decreasing chemical potential, where many-body contributions dominate. Using a multi-gate architecture in monolayer MoTe$_2$ FETs, that allows for independent contact resistance and threshold voltage tuning, we integrate reconfigurable n- and p-FETs, and demonstrate a complementary inverter.

Table of Contents

x

List of Tables

List of Figures

xvi

Chapter 1: Introduction

The inflection point for research interest in transition metal dichalcogenides (TMDs) dates back to 2010, when the seminal paper from Mak *et al*. [1] presented for the first time the optical properties of mono- and few-layers MoS_2. Significant research efforts on bulk TMDs predate the aforementioned work, dating back to the sixties, seventies, and eighties where considerable efforts were devoted to the theoretical understanding, the optical and the electrical characterization of this class of materials [2]–[4]. The rise of graphene in the early 2000's has also played a decisive role in laying the groundwork for investigation of mono- and few-layer TMDs.

In this dissertation we will study of the electronic properties and the electron-electron interaction effects in molybdenum based TMDs. In this first chapter we will introduce the physical and electronic properties of this class of materials, to help the reader to familiarize with these material systems. We will begin discussing TMDs crystal and band structure, to understand their distinctive properties. Techniques used to isolate and grow mono- and few-layer flakes will be presented. An overview of the vibrational and optical properties and their dependence on the number of layers will also be provided. At last we review the basic theory of quantum Hall effect, in both gapped 2D electron systems and in mono- and bilayer graphene. In this dissertation magnetotransport will used as tool to probe the bandstructure and the electron-electron interaction effects in molybdenum based TMDs.

1.1 TRANSITION METAL DICHALCOGENIDES

Transition metal dichalcogenides are a new family of layered two-dimensional (2D) materials, characterized by a MX_2 formula where M stands for a transition metal (e.g. Ti, V, Mo, W, Pt…), and X stands for a chalcogen (S, Se or Te) [6]. About 40 different TMDs crystallize in a layered form. Sixteen different transition metals and three chalcogens, highlighted in the periodic table of Figure 1.1, can be used to synthetize layered materials characterized by MX_2 chemical formula [7].

Figure 1.1: Periodic table where elements used to synthetize TMDs are highlighted: 16 transition metals between groups 4 to 10 and three chalcogens (S, Se, Te). Co, Rh, Ir, Ni are partially highlighted to indicate that only when combined with some of the chalcogenides, they present a layered structure. Reprinted by permission from Springer Customer Service Centre GmbH: Nature, Nature Chemistry, 5, 263, "The chemistry of two-dimensional layered transition metal dichalcogenide nanosheets" M. Chhowalla, Hyeon S. Shin, G. Eda, L.-J. Li, K. P. Loh and H. Zhang, Ref. [7] © Springer Nature 2013.

1.1.1 Crystal structure

Transition metal dichalcogenides are layered materials that present a graphite-like structure, where the three-dimensional solid is formed by a series of 2D layers that consist of a X-M-X structure. Within each layer the M-X bonds are covalent, while separate layers are bonded via weak van der Waals interactions (vdW), as shown in Figure 1.2(a). Within each layer metal and chalcogen (X-M-X) atoms are characterized by two possible

coordinations: trigonal prismatic, point group D_{3h} (1H), and octahedral, point group D_{3d} (1T), as shown in Figures 1.2(b) and 1.2(c), respectively. Figure 1.2(d) shows three different stacking polytypes that are encountered in TMDs: 2H, 3R and 1T. The number in the polytype labeling stands for the number of layers in the stacking sequence and the number of X-M-X units in the unit cell, while the letter stands for: hexagonal, rhombohedral and trigonal. When the thickness of a 2H or 3R polytype is reduced to a single X-M-X monolayer, the polytype is defined as 1H [Figures 1.2(b) and 1.2(d)]. Lattice constants a and c are used to describe TMDs' crystal structure [Figures 1.2(d)].

This dissertation will focus on 2H (1H) polytypes, presenting trigonal prismatic coordination [Figures 1.2(b) and 1.2(d)], and only molybdenum based TMDs will be considered, namely: MoS_2, $MoSe_2$ and $MoTe_2$. The symmetry properties of bulk 2H crystals and 1H monolayers are different and determined by D_{6h} and D_{3h} point groups respectively. Most notably 1H monolayers lack inversion symmetry, restored in 2H-bilayers. The lattice parameters a and c for 2H Mo-based TMDs indicated in Figure 1.2(d) are summarized in Table 1.1. In 2H (1H) polytypes $c/2$ is defined as the single layer thickness, typically between 6-7 Å [Table 1.1]. When viewed from the top a TMD monolayer (polytype 1H) presents a hexagonal lattice, reminiscent of single layer graphene [Figure 1.2(b)]. For comparison a in graphene is $= 2.46$ Å. The shaded area in Figure 1.2(b) corresponds to one primitive cell for 1H monolayer MX_2.

	a(Å)	c(Å)
MoS_2	3.160	12.294
$MoSe_2$	3.299	12.938
$MoTe_2$	3.522	13.968

Table 1.1: Table of lattice constants a and c for 2H MoS_2, $MoSe_2$ and $MoTe_2$ quoted from Ref. [8].
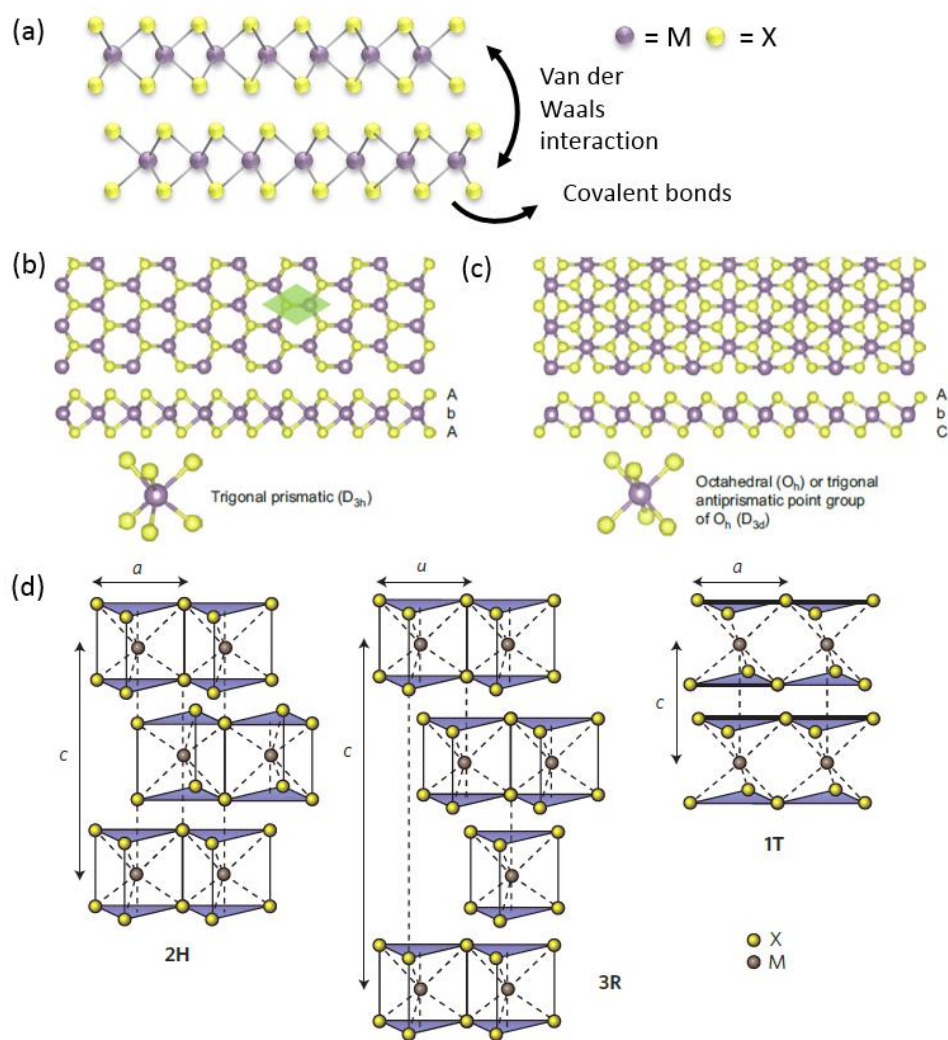
Figure 1.2: (a) Schematic representation, lateral view, of a 2H-MX$_2$ structure, highlighting the nature of the bonding. (b) Single TMD layer in trigonal prismatic coordination, polytype 1H. (c) Single TMD layer in octahedral coordination , polytype 1T. Panel (b) and (c) adapted by permission from Springer Customer Service Centre GmbH: Nature, Nature Chemistry, 5, 263, "The chemistry of two-dimensional layered transition metal dichalcogenide nanosheets" M. Chhowalla, Hyeon S. Shin, G. Eda, L.-J. Li, K. P. Loh and H. Zhang, Ref. [7] © Springer Nature 2013. (d) Structural schematics for 1H, 2H, 3R, 1T polytypes; the lattice constants a and c are marked for each polytype. Panel (d) adapted by permission from Springer Customer Service Centre GmbH: Nature, Nature Chemistry, 7, 699, "Electronics and optoelectronics of two-dimensional transition metal dichalcogenides" Q. H. Wang, K. Kalantar-Zadeh2, A. Kis, J. N. Coleman, and M. S. Strano, Ref. [6] © Springer Nature 2012.

1.1.2 Bandstructure

Molybdenum based 2H-TMDs combine a layered 2D nature with semiconducting properties that strongly differentiate them from graphene. Monolayer graphene is characterized by a linear energy-momentum dispersion close to the Dirac point, with massless carriers. MoS_2, $MoSe_2$, and $MoTe_2$ are instead characterized by a parabolic dispersion close to the band edges with comparatively large effective masses. The nature and size of the bandgap varies as we scale the material thickness from bulk to monolayer.

All three materials (MoS_2, $MoSe_2$, $MoTe_2$) in the bulk limit are indirect bandgap semiconductors and present a similar bandstructure, where the band extrema location is material invariant, but the bandgap sizes and the effective masses are different for each material. Figure 1.3(a) shows a representative calculated bandstructure for bulk 2H-MoS_2, including the highest and lowest conduction and valence bands respectively, labeled ($c1$, $v1$, $v2$) [1]. This calculated bandstructure includes interlayer coupling, but without losing generality excludes spin-orbit interaction (SOI). The SOI contribution will be discussed later in the context of the bandstructure of monolayers.
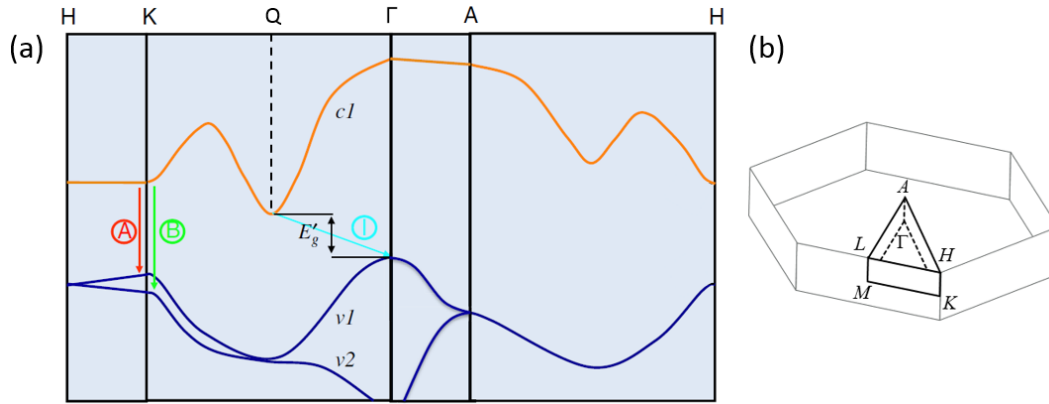
Figure 1.3: (a) Bandstructure of bulk 2H-MoS_2 including interlayer coupling and excluding SOI; $c1$ labels to the lowest conduction band and $v1,2$ label the highest split valence bands. Direct (indirect) bandgap transition are marked: *A* and *B* (*I*). Reprinted with permission from <u>K. F. Mak, C. Lee, J. Hone, J. Shan, and T. F. Heinz Phys. Rev. Lett 105, 136805 (2010)</u>, Ref. [1], © 2010 by the American Physical Society. (b) Brillouin zone of bulk 2H-MX_2. High symmetry points marked.

The bandstructure of bulk MoS_2 features minima at the K and Q point in the conduction band (CB), and maxima at the Γ and K point in the valence band (VB). The Q point is situated half-way between Γ and K point. The indirect bandgap transition (I) between the Q point in the CB to the Γ point in the VB, is marked in Figure 1.3(a). The larger direct bandgap ($\underline{E}_g$) is localized at the K point, where two transitions labeled A and B, after Ref. [9], are marked. Table 1.2 summarizes bandgap values of molybdenum based TMDs, obtained from photocurrent measurements in bulk MoS_2 and $MoSe_2$ [10] and photoluminescence measurements in bulk $MoTe_2$ [11].

When the thickness of the material is reduced to a monolayer, the bandgap transitions from an indirect to direct, where CB and VB extrema are located at the K (K') point, as shown for monolayer MoS_2 in Figure 1.4(a). A comparison between the bandgap of bulk and monolayer molybdenum-based TMDs is provided in Table 1.2. Experimental bandgap values of monolayer MoS_2, $MoSe_2$ and $MoTe_2$ are obtained from scanning tunneling spectroscopy (STS) measurements, while theoretical values are obtained from density functional theory (DFT) and GW calculations.

	Bandgap (eV) Experimental		Direct Bandgap Monolayer (eV) Calculations [12]	
	Bulk Indirect	Monolayer Direct	DFT	GW
MoS_2	1.23 [10]	2.17 [13]	1.7	2.8
$MoSe_2$	1.09 [10]	2.18 [14]	1.4	2.3
$MoTe_2$	0.9 [11]		1	1.8

Table 1.2: Indirect bandgap measured in bulk MoS_2, $MoSe_2$ and $MoTe_2$, using optical techniques. Bandgap calculations (DFT, GW) and measurements (STS) obtained for monolayer MoS_2, $MoSe_2$ and $MoTe_2$.
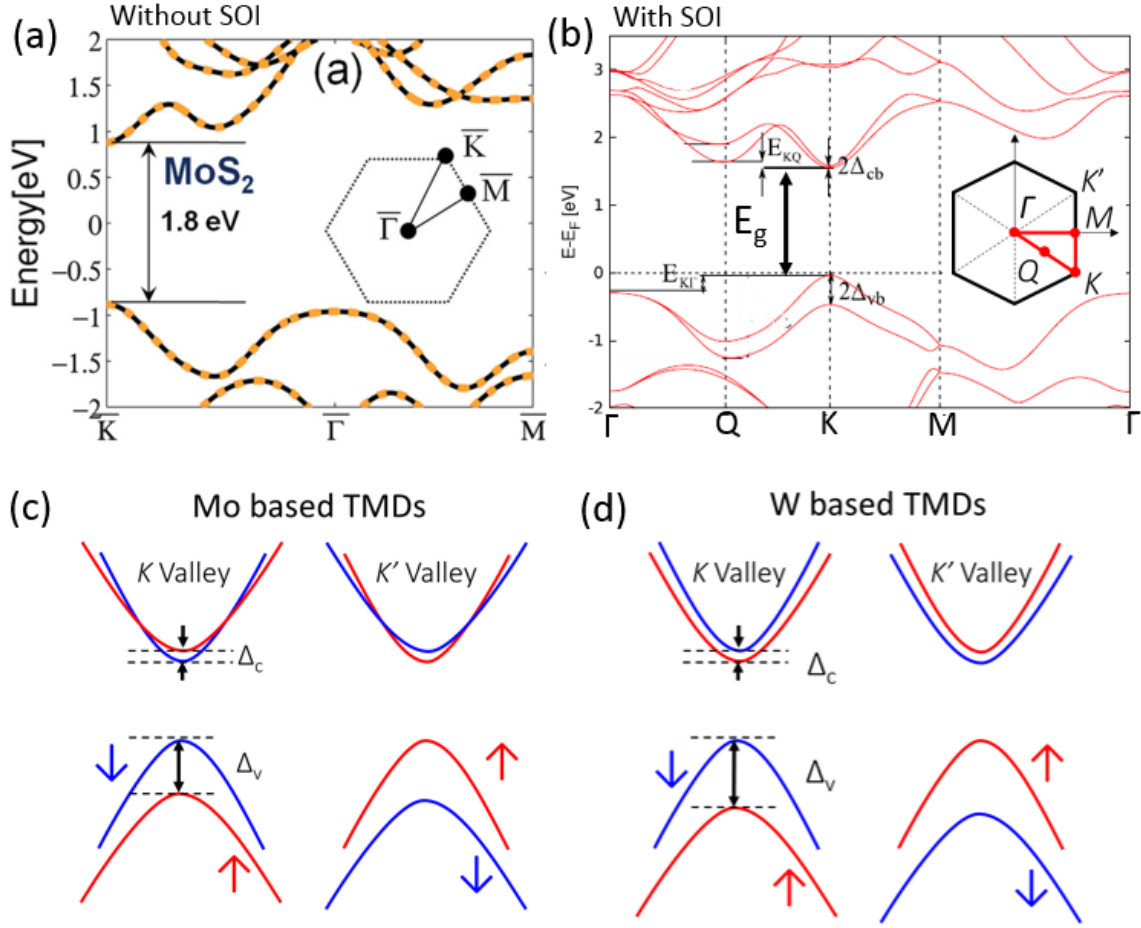
Figure 1.4: (a) Monolayer MoS$_2$ bandstructure excluding SOI, presenting spin-valley degenerate CB and VB minima. Inset: Brillouin zone of monolayer 1H-MX$_2$, with high symmetry points marked. Reprinted from J. Chang, L. F. Register and S. K. Banerjee, Appl. Phys. Lett 115, 084506 (2014), Ref. [15], with the permission of AIP Publishing. (b) Monolayer TMD representative bandstructure including SOI. Broken inversion symmetry and SOI in monolayer 1H-MX$_2$ determines spin-split CB and VB bands away from Γ and M points. Inset: Brillouin zone of monolayer 1H-MX$_2$, with high symmetry points marked. Adapted from A. Kormányos *et al.* 2D Mater. 2 (2015) 049501, Refs. [12], doi:10.1088/2053-1583/2/4/049501, CC License 3.0. Direct bandgap transitions are marked at the K point in panels (a) and (b). (c) CB and VB spin-splitting schematic for Mo and W based TMDs, at K ($\tau = 1$) and K' ($\tau = -1$) points, and red (blue) bands label spin up $s = 1$, $\uparrow$ (down, -1, $\downarrow$)) bands. Panel (a),(b), and caption adapted from Refs. [12]

Once 2H-molybdenum based TMDs thickness is reduced to one monolayer (1H), the crystal symmetry is reduced, and the inversion symmetry is broken, i.e. taking the metal

atom as the inversion center maps the chalcogen atoms to empty locations [Figure 1.2(b)] [16]. Inversion symmetry leads to the following band structure symmetry in reciprocal space: $E^{\uparrow}(\mathbf{k}) = E^{\uparrow}(-\mathbf{k})$, where $\uparrow$ ($\downarrow$) denote the particle spin up (down). In addition to the reduced crystal symmetry, the presence of a strong SOI, stemming from the nature of the d orbitals that characterize the transition metal atoms [16], [17], alters the bandstructure of Figure 1.4(a), obtained in absence of SOI, causing the CB and VB to spin-split, away from the time-reversal invariant point M and Γ, as shown in Figure 1.4(b). Time reversal leads to the following band structure symmetry in reciprocal space: $E^{\uparrow}(\mathbf{k}) = E^{\downarrow}(-\mathbf{k})$. The strong SOI and the absence of inversion symmetry effectively undo Kramer's degeneracy found in bulk: $E^{\uparrow}(\mathbf{k}) = E^{\downarrow}(\mathbf{k})$, where bands are spin degenerate.

DFT Band parameters [12]			
	MoS₂	**MoSe₂**	**MoTe₂**
Conduction Band			
m_{cb}^*/m_e **K-point lower**	0.46	0.56	0.62
m_{cb}^*/m_e **K-point upper**	0.43	0.49	0.53
2Δ$_{cb}$ (meV)	3	22	36
E_{KQ} **(meV)**	207	163	173
Valence Band			
m_{vb}^*/m_e **K-point upper**	0.54	0.59	0.66
m_{vb}^*/m_e **K-point lower**	0.61	0.7	0.82
2Δ$_{vb}$ (meV)	148	184	219
$E_{K\Gamma}$ **(meV)**	70	342	540

Table 1.3:   Bandstructure parameters obtained from DFT calculations in Ref. [12]. Upper and lower m^*/m_e, refer to the relative energetic position of the bands [Figures 1.4(c) and 1.4(d)], where the mass is calculated; m_e is the bare electron mass.

The spin-splitting lifts the four-fold spin-valley degeneracy at the K point [Figure 1.4(a)], present for example in monolayer graphene. Time reversal symmetry still requires opposite spin direction for each spin split band at K, K' point, as shown in Figure 1.4(c) scheme, where s and τ label spin and valley degrees of freedom, respectively. The lower (higher) spin-split CB (VB) is labeled by indices $\tau s = -1$ [Figure 1.4(c)]. In summary, a combination of strong SOI and broken inversion symmetry in molybdenum based TMDs

8

yields coupled spin and valley degrees of freedom at the K (K') point [16]. While spin-splitting is present in both CB and VB, its magnitude is significantly different in each band [Figure 1.4(b)], for example at the K point in MoSe$_2$ $2\Delta_{vb}/2\Delta_{cb} \sim 10$, where $2\Delta_{cb}$ ($2\Delta_{vb}$) is CB (VB) spin splitting at the K point [Table 1.3]. It should be noted that the spin-polarization of the split CB valleys at the K point in Mo and W based TMDs is opposite, as shown in Figure 1.4(d).

In addition to the K point minima, the CB features six spin-split minima at the Q point. The energy separation between lowest spin-split band at the K and Q point is E_{KQ} [Figure 1.4(b)]. A second maximum at the Γ point is also present in the VB, and its energy separation with respect to the higher spin-split VB at the K point is $E_{K\Gamma}$ [Figure 1.4(b)]. A set of calculated bandstructure parameters, including K-valley effective masses, for monolayer MoS$_2$, MoSe$_2$ and MoTe$_2$ are summarized in Table 1.3 [12]. It should be noted that the effective mass of upper and lower spin-split band extrema in CB (VB) is different. For molybdenum based TMDs the lower spin-split CB minima has a lighter mass compared with the higher spin-split minima, as shown in Figure 1.4 (c), we should therefore expect band crossings.

Once we examined the bandstructure for both bulk and monolayer limit, it of interest to understand the how the direct to indirect band transition develops as the number of layers increase. Figure 1.5 panels (a) to (f) show a series of angle-resolved photoemission spectroscopy (ARPES) measurements [panels (a) to (d)], and their second derivative [panels (e) to (h)], of the VB of mono-, bi-, tri- and 8-layer MoSe$_2$. Figure 1.5 panels (i) to (l) show the corresponding DFT bandstructure calculations [18]. Bandstructure calculations and ARPES measurements elucidate the direct to indirect bandgap transition presented by molybdenum based TMDs once the number of layers is increased from monolayer up [8], [18]. A number of noteworthy findings emerge from a combination of experimental and theoretical observations shown in Figure 1.5 [18]. First, as the thickness is increased from a mono- to a few-layers $E_{K\Gamma}$ changes sign and becomes negative, corresponding to a change in energy and momentum of the VB maxima, namely from K to Γ point. Other bandstructure calculations report an analogous trend in the CB, where as

thickness is increased E_{KQ} becomes negative and the CB minima changes position from the from K to Q point [8]. Second, calculations and ARPES data, highlight the valence band splitting at the K point. Because of inversion symmetry breaking in monolayer we obtain two spin split bands [marked in blue and red in Figure 1.5(i)], but in bilayer as inversion symmetry is restored we observe spin degenerate bands [Figure 1.5(j)].
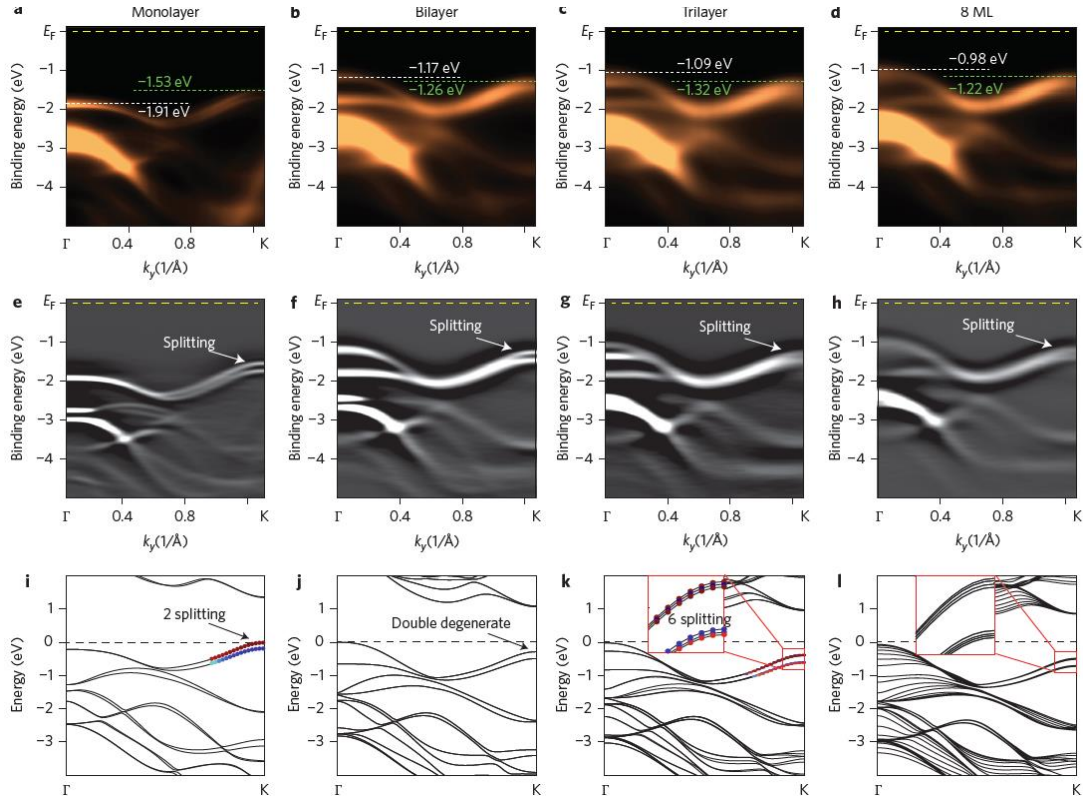
Figure 1.5: (a-d) ARPES spectra, (e-f) second derivative of the ARPES spectra in (a-d) and (e-h) bandstructure DFT calculations for mono-, bi-, tri- and 8-layer $MoSe_2$. The bandstructure feature a thickness invariant direct gap at the K point and an indirect gap my VB extrema at the Γ point and CB extrema at the Q point (midway between K and Γ points) . Insets of (k) and (l) detail the nature of the VB at the K point, in particular the presence or absence of spin splitting. In panels (i) to (k), different colors of the VB at the K point label the spin flavor. Reprinted by permission from Springer Customer Service Centre GmbH: Nature, Nature Nanotechnology, 9, 111, "Direct observation of the transition from indirect to direct bandgap in atomically thin epitaxial $MoSe_2$" Y. Zhang, T.-R. Chang, Bo Zhou, Y.-T. Cui, H. Yan, Z. Liu, F. Schmitt, J. Lee, R. Moore, Y. Chen, H. Lin, H.-T. Jeng, S.-K. Mo, Z. Hussain, A. Bansil and Z.-X. Shen, Ref. [18] © Springer Nature 2014.

Another feature presented by DFT calculations of the bandstructure [19] is the thickness invariance of the direct bandgap at the *K* point. A finding can be understood as follows, the CB and VB minima at the *K* point stem predominantly from the localized *d*-orbitals associated to the metal atom [12], [20]. In TMD crystals metal atoms are sandwiched between chalcogen atoms and are therefore relatively unaffected by interlayer interaction as the thickness of the material changes [21]. This picture is consistent with photoluminescence measurements of mono-, bi- and few-layer MoS_2 and $MoSe_2$ of Section 1.1.5. PL data present direct bandgap *A* transitions [Figure 1.3] largely independent of the layer number.

It should be noted that GW calculations predict a significantly larger bandgap than DFT for monolayers [Table 1.3], and show a decreasing direct bandgap size as the number of layer is increased [22]. The difference between GW and DFT gaps hints to the relevance of excitonic effects, discussed in Section 1.1.5, which are themselves thickness dependent.

1.1.3 Few layer Isolation

In the previous sections we discussed the physical and electronic structure of molybdenum based TMDs, where the capability to scale at will the thickness of TMD layers is assumed. Only after the discovery of single layer graphene both top-down and bottom-up methods have been devised to obtain mono- and few-layers TMD films (or flakes) sufficiently large to fabricate electronic devices on a single crystallographic grain. In the following we will describe two established methods used to obtain mono- and few-layers TMDs, as well as other vdW materials, suitable for the fabrication of electronic devices: micromechanical exfoliation method [23] (top-down) and direct growth using chemical vapor deposition (CVD) [6] (bottom-up). Other methods, notably liquid phase exfoliation using lithium intercalation and/or sonication are effective in exfoliating layered materials but produce an uneven solution of sub-micrometer flakes, unsuitable for electrical measurements.

1.1.3.1 Micromechanical exfoliation method

The micromechanical exfoliation process is carried out using low-tack adhesion polyethylene tape (commercially available at Ultratape), which is effectively used to delaminate a vdW material down to a mono- or a few-layer flake. Van der Waals materials such as TMDs, graphene or hexagonal boron-nitride (hBN), are obtained either in crystal of power form. $MoSe_2$ power and a typical MoS_2 crystal are shown in Figure 1.6(a) and 1.6(b), respectively.
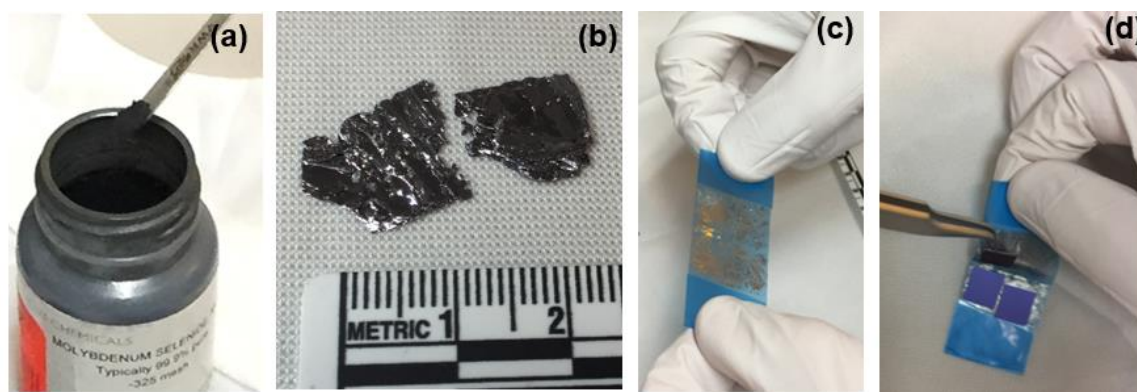
Figure 1.6: (a) $MoSe_2$ powder purchased from Materion Inc. (b) Natural MoS_2 crystal purchased from SPI Inc., typical size ~1 cm^2. (c) MoS_2 crystal cleaved on tape (tape width 1 in.). (d) SiO_2/Si substrates are placed on the tape and gently removed to transfer few layer flakes on the SiO_2/Si substrates.

Once a vdW powder or crystal is placed on the tape the adhesion between the tape and the bulk material is sufficient to delaminate part of the material. The tape is then folded several times to further reduce the crystal thickness, as shown in Figure 1.6(c). Once desired thickness is reached, SiO_2/Si substrates (~1 cm^2) are placed on the tape. Gently removing the SiO_2/Si substrates, as shown in Figure 1.6(d), will result in randomly cleaving mono- and few-layer TMD flakes from the tape and transferring them on the SiO_2/Si substrate. Once the substrates are prepared and the material has been exfoliated the next task requires to manually inspect the substrate under the microscope and find flakes of interest.
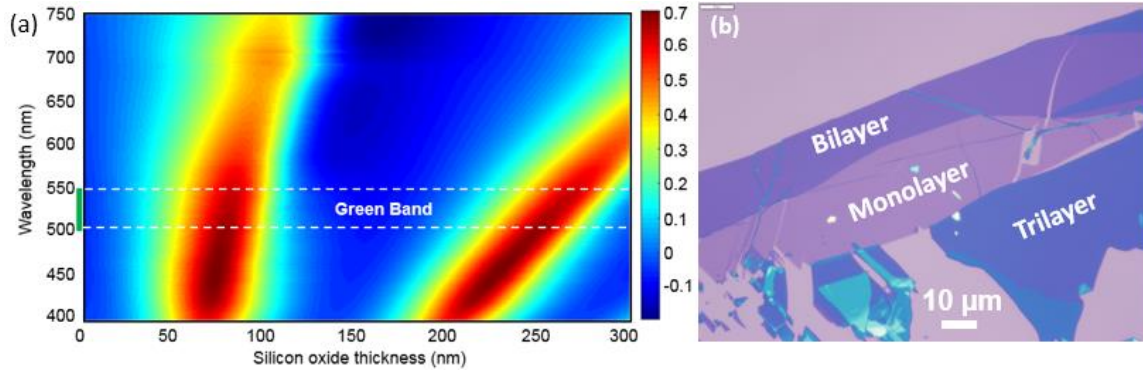
Figure 1.7: (a) Contrast contour plot of Monolayer MoS$_2$ as function of the SiO$_2$ thickness and the visible light wavelength, two prominent positive contrast peaks are identified. A green light wavelength band is marked. (b) Optical micrograph of a MoSe$_2$ flake on a SiO$_2$/Si substrate, characterized by different terraces. Each terrace shows different contrast, related to its thickness.

The SiO$_2$ thickness is intentionally optimized to allow identification, under optical microscope, of TMD flakes down to a monolayer. Figure 1.7(a) shows the calculated contrast for monolayer MoS$_2$ as function of the SiO$_2$ thickness and visible light wavelength, determined using the dielectric functions of MoS$_2$ and SiO$_2$ [24], [25]. The contrast map indicates that we expect two positive contrast peaks for green light (~530 nm), dominant in human vision, for oxide thicknesses of 90 and 270 nm [24], [25]. For positive contrast peaks flakes are expected to be darker than the substrate, as shown in Figure 1.7(b) for a SiO$_2$ thickness of ~285 nm. Contrast peaks for other 2D materials such as graphene, hBN and other molybdenum based TMDs are comparable [24], [25]. Figure 1.7(b) shows a large MoSe$_2$ flake exfoliated from a crystal, characterized by multiple terraces. Lighter colors identify thinner regions. The color gradient can be used to quickly and effectively determine the thickness for mono, bi-, and tri-layers. It should be noted that it is typically easier to obtain large and thin flakes, down to a monolayer, using large exfoliation crystals.

1.1.3.2 Chemical vapor deposition growth

The exfoliation process described in Section 1.1.3.2 can be only employed for prototyping purposes where exploratory devices are fabricated to characterize the electrical

and optical properties of TMDs. Such process clearly cannot be employed in high-volume manufacturing. Following the effort in growing large area monolayer graphene [26], recently, significant interest has been devoted to the growth of large area TMDs using different types of CVD techniques. The most popular approaches are the following [6]: (i) a thin layer of Mo is annealed in a chalcogen rich environment [27]; (ii) solid state MoO_3 and chalcogen powders are vaporized in a tube furnace and co-deposited on a neighboring SiO_2/Si or sapphire substrate, as shown Figure 1.8(a).
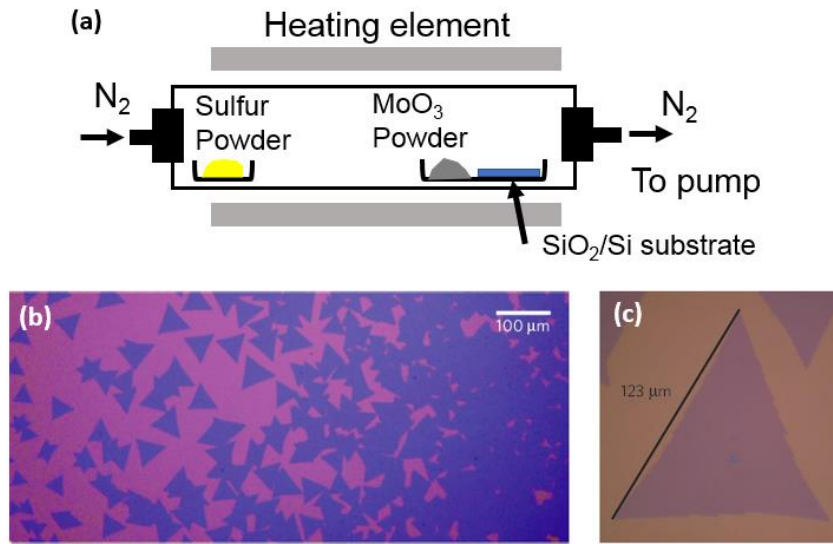
Figure 1.8: (a) Hot-wall, quartz-tube furnace schematic. Precursors are loaded in quartz boats, neighboring a bare SiO_2/Si wafer. Optical micrograph of monolayer MoS_2 growth on 285 nm SiO_2/Si substrate forming (b) single triangular domain with lateral size >100 µm[28], and (c) pseudocontinuous film. Panel (b) and (c) reprinted by permission from Springer Customer Service Centre GmbH: Nature, Nature Materials, 12, 554, "Grains and grain boundaries in highly crystalline monolayer molybdenum disulphide" A. M. van der Zande, P. Y. Huang, D. A. Chenet, T. C. Berkelbach, Y. You, G.-H. Lee, T. F. Heinz, D. R. Reichman, D. A. Muller and J. C. Hone, Ref. [28] © Springer Nature 2013.

The latter CVD growth process is carried in a hot wall, quartz tube furnace at a temperature between 500 and 700 °C in an atmospheric pressure, high flow (>200 sccm) nitrogen ambient, which serves as the carrier gas. Before the growth process the quartz-tube is pump and purged to reduce contaminants [Figure 1.8(a)]. Recent studies have

employed powder precursors CVD to grow large area monolayer MoS_2 triangular domains of lateral size > 100 μm on SiO_2/Si substrates, as shown in Figure 1.8(b) [28], [29]. MoS_2 triangular domains can merge and form pseudo-continues films [Figure 1.8(c)], covering areas up to tens of mm^2 [28], [29]. Similar results have been obtained for CVD growth of monolayer $MoSe_2$ and monolayer $MoTe_2$, using metal-oxychloride precursors [30]. While the growth process is not performed in high vacuum, rendering the technique relatively inexpensive, wafer size control of the TMDs thickness remains a problem [6]. The introduction of liquid/gas phase precursors may allow more precise control of the growth process and to elucidate its dynamics.

1.1.4 Lattice dynamics

Lattice vibrations of molybdenum based TMDs can be classified using group theory. As introduced earlier 2H-TMDs are characterized by a 6 atoms unit cell with D_{6h} symmetry, resulting in 18 allowed phonons modes, of which 3 are acoustic, and 15 are optical [31]. Monolayer TMDs (1H) have 3 atoms unit cell with reduced D_{3h} symmetry, and present 9 allowed phonons modes, of which 3 are acoustic, and 6 are optical [31]. Figures 1.8(a) and 1.8(b) shows the calculated phonon dispersions for monolayer and bulk MoS_2 [32]. The phonon dispersion of monolayer MoS_2 is characterized by linearly dispersive acoustic branches modes at frequency $\omega < 250$ cm^{-1}. Acoustic branches are labeled as follows: in-plane longitudinal acoustic (LA), transverse acoustic (TA), and out-plane acoustic (ZA) modes [Figure 1.8(a)]. A gap of ~50 cm^{-1}, between the acoustic and the less dispersive optical branches, emerges in the dispersions of both monolayer and bulk MoS_2 [Figures 1.8(a) and 1.8(b)]. As the thickness of MoS_2 is increased from monolayer to bulk, each optical branch in the dispersion of monolayer MoS_2 correspond to two almost degenerate branches in the dispersion of bulk MoS_2, because of the weak interlayer interaction [32]. The main difference between the phonon dispersion of bulk and monolayer MoS_2 is the emergence of three low frequency optical modes, aside from the LA, TA, and ZA modes which are shared between the dispersions of monolayer and bulk.

15

These low frequency optical modes in bulk, labeled LB and C [31], disperse with a quadratic wavevector (q) dependence, below the frequency gap as shown in Figure 1.9(b) [32]. At $q = 0$ (Γ point) they present finite frequency ~ 50 cm^{-1}. The calculated bulk MoS$_2$ phonon dispersion is compared with neutron scattering measurements [symbols of Figure 1.9(b)], which allow to probe the dispersion as function of the phonon wavevector.

The symmetry classification of the vibrational modes at Γ point is presented in Figure 1.9(c). As the symmetry is reduced in monolayer a new classification is listed. In the bulk 2H-MX$_2$ (point grop D$_{6h}$) we identify twelve modes, including three E double-degenerate modes:

$$\Gamma \rightarrow A_{1g} + 2A_{2u} + 2B_{2g} + B_{1u} + E_{1g} + 2E_{1u} + 2E_{2g} + E_{2u}$$

where A$_{2u}$, E$_{1u}$ are acoustic, A$_{1g}$, E$_{1g}$, E$^1_{2g}$, E$^2_{2g}$ are Raman active, A$_{2u}$, E$_{1u}$ are infra-red (IR) active and the other are optically inactive [31]–[33]. As detailed in Figure 1.9(c) schematic, A and B modes are out-of-plane modes and E are in-plane modes. Raman and IR active modes refer to modes that can be probed using Raman spectroscopy or IR reflectance [31]–[33].

Raman spectroscopy is a powerful non-destructive technique that has been traditionally employed to probe the vibrational properties of 2D materials; see for example the investigation of carbon allotropes by M. S. Dresselhaus and collaborators at MIT [34], [35]. In a Raman scattering process, the incident photon can absorb (emit) a phonon when it scattered by the crystal. As a result, the photon may gain (lose) energy and we observe a Stokes shift (anti-Stokes shift) [31]. The process described involves only one phonon, and can be effectively considered momentum conserving, if we compare the photon wavelength and the crystal lattice constant. A vibrational mode classification at the Γ point is therefore appropriate, given in a first order Raman scattering process only phonons with momentum $q \sim 0$ (Γ point) contribute.

In the following Sections 1.1.3.1 to 1.1.3.3, we will discuss the Raman spectra for MoS$_2$, MoSe$_2$ and MoTe$_2$ flakes on SiO$_2$/Si substrates. Each distinct Raman signature can be used to unequivocally confirm the nature of the TMD considered and allows to determine the flake thickness, in the limit of a few-layers. The Raman spectra discussed in

Sections 1.1.3.1 to 1.1.3.3 are obtained using a Renishaw InVia Raman microscope fitted with a 100x microscope lens and 2400 or 3000 l/mm gratings. Two different excitation wavelengths are available: 442 nm with a nominal laser power of 30 mW and a 532 nm with a nominal laser power of 5 mW.

Figure 1.9: Calculated phonon dispersion for (a) bulk and (b) monolayer MoS_2, different branches are labeled accordingly. Experimental data (dots) obtained from neutron scattering in Ref. [36] are also presented in panel (b). Panel (a) and (b) are reprinted with permission from A. Molina-Sánchez and L. Wirtz, Phys. Rev. B 84, 155413 (2011), Ref. [32], © 2011 by the American Physical Society. (c) Schematic illustration and labeling of in-plane (E) and out-of-plane (A, B) vibrational modes in bulk (2H) and monolayer (1H) group VI TMDs, each mode is labeled Raman active, IR inactive, optically inactive, and acoustic (LA/TA/ZA). Bulk Raman active modes are highlighted in yellow. Adapted from Ref. [21], [31]–[33].

Even though group theory predicts that four vibrational modes should be Raman active (A_{1g}, E_{2g}, E^1_{2g}, E^2_{2g}), only the A_{1g} and E^1_{2g} modes (A'$_1$ and E' in monolayer's

17

notation) are accessible by our experiments. E^2_{2g} is typically a very low frequency mode (~30 cm^{-1} for MoS$_2$), as shown in the dispersion of Figure 1.9(b) where the mode is labeled as C, and typically falls outside of range of Raman shifts probed in our studies [21], [31]. In addition, our backscattering measurement geometry forbids access to the E_{1g} mode [21], [37]. While a vibrational mode labeling for monolayer MX$_2$ is presented in Figure 1.9(c), in the following section we will use the bulk labels also for the Raman spectra of monolayers, as is conventional in literature.

1.1.4.1 MoS$_2$ Raman spectroscopy

Figure 1.10(a) shows the Raman spectra acquired from neighboring MoS$_2$ flakes, showing large plateaus at different thicknesses [Figure 1.10(c)]. Raman spectra are acquired using a 532 nm excitation wavelength with ~20 µW excitation power measured at the sample. Each spectrum acquired, independent on MoS$_2$ thickness sampled, presents two prominent peaks respectively associated with the E^1_{2g} and A_{1g} vibrational modes [Figure 1.10(c)] [37], consistent with the calculated phonon dispersions of Figures 1.9(a) and 1.9(b). The Monolayer MoS$_2$ spectrum features E^1_{2g} and A_{1g} modes at 385 cm^{-1} and 405 cm^{-1}, respectively. The A_{1g}, E^1_{2g} frequency difference is typically < 20 cm^{-1} in monolayer MoS$_2$.

The Raman peak intensity and the peak separation increases when we compare the spectra of monolayer and thicker flakes, in the limit of a few layers. The intensity drops again for very thick, bulk like flakes. The E^1_{2g} mode is found to red-shift while the A_{1g} is found to blue-shift as we probe thicker flakes. Figure 1.10(b) shows the thickness dependence of the frequency difference between A_{1g} and E^1_{2g} modes. If we compare mono- and bilayer flakes the frequency difference of A_{1g} and E^1_{2g} modes varies significantly, > 2 cm^{-1} allowing a quick and effective thickness identification based on the peak separation. Raman measurements can also be correlated to the flake contrast under the optical microscope providing a valuable tool to quickly assess the flake thickness during the inspection of SiO$_2$/Si substrates.
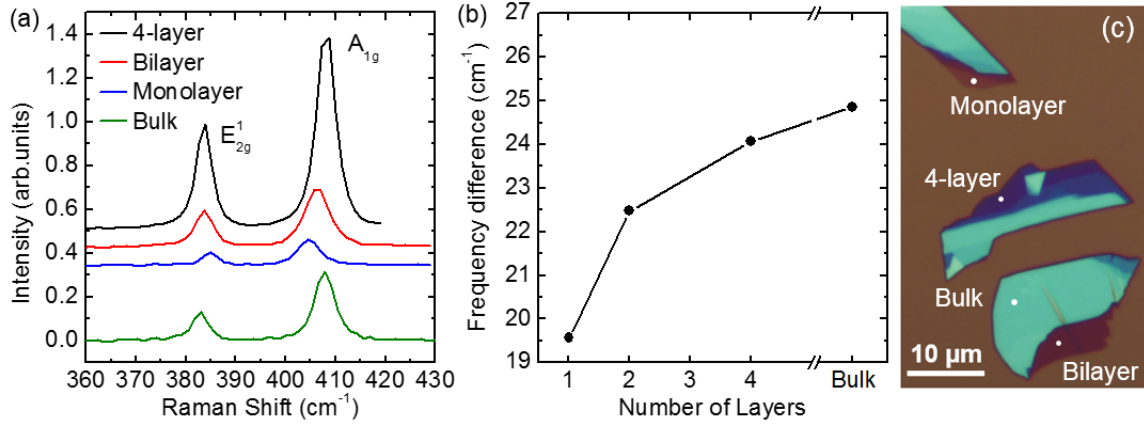
Figure 1.10 (a) Raman spectra of mono-, bi-, 4-layer and bulk MoS_2 shown in panel (c), measured using a 532 nm excitation wavelength. Prominent peaks emerge at ~383 cm^{-1} and ~406 cm^{-1} associated with E^1_{2g} and A_{1g} modes. Traces are offset for clarity. (b) A_{1g}, E^1_{2g} modes frequency difference as function of the number of layers. (c) Optical micrograph of the measured flakes, labeled according to their thickness.

1.1.4.2 MoSe$_2$ Raman spectroscopy

Figure 1.11(a) shows the Raman spectra of mono- and few-layer MoSe$_2$ acquired from neighboring flakes [Figure 1.7(b)], using a 532 nm excitation wavelength with ~100 µW excitation power measured at the sample. The Raman spectra features a prominent peak at ~244 cm^{-1} associated with the A_{1g} vibrational mode, shifted ~150 cm^{-1} compared to the MoS$_2$ spectra [Figure 1.10(a)] [21], [38]. A lower intensity peak at ~288 cm^{-1} is associated with the E^1_{2g} mode [21], [38]. In addition to the A_{1g} and E^1_{2g} modes, an unexpected peak at ~354 cm^{-1} emerges in spectra obtained probing bilayer and thicker flakes [Figure 1.11(b)]. This additional peak allows to distinguish monolayers from other flakes, using a 532 nm excitation wavelength [21], [38]. Unlike in MoS$_2$ where both E^1_{2g} and A_{1g} modes shift significantly as the thickness is increased in MoSe$_2$ the A_{1g} red-shift is significant only between mono- and bilayer. However the emergence of a shoulder in the peak at ~245 cm^{-1}, i.e. the emergence of a second, almost-degenerate, peak eases the identification of trilayer flakes. The emergence of a degenerate peak in the trilayer spectrum is evidenced by a double gaussian fit in Figure 1.11(a), and is established in

19

literature as associated to the so-called Davydov splitting [21], [38]. The A_{1g} vibrational mode consists in an in-phase out-of-plane movement of the chalcogen atoms, while the transition metal is stationary [Figure 1.9(c)]. Unlike in mono- and bilayer, in trilayer we identify two sets of chalcogen atoms vibrations, where the relative vibration phases between the layers differ by 180° [Figure 1.11(b)]. The interlayer interaction labeled in red (for bilayer) and in red/green depending on the phase, for trilayer [Figure 1.11(b)], results in a softening or hardening of the A_{1g} mode, effectively obtaining a two separate, albeit almost degenerate peaks (3.5 cm^{-1} peak separation), in the spectrum for trilayer flakes [Figure 1.11(a)]. This vibrational picture explains why the higher frequency peak aligns with the A_{1g} mode of bilayer, given the interlayer interaction is the same [labeled in red in Figure 1.11(b)], and the A_{1g} mode of monolayer, where there is no interlayer coupling, lies in between the two trilayer peaks. Davydov splitting survives only in crystals between 3-5 layers, where for thicker crystals the interlayer effect is averaged and only one peak is distinguished [Figure 1.12]. An analogue discussion of the Davydov splitting is obtained introducing the otherwise Raman inactive B_{1u} mode, which would emerge in 3-5 layers crystals as a result of resonance [38].

Figure 1.12 shows the Raman spectra of a ~10-layer MoSe$_2$ flake, obtained using 442 nm and 532 nm excitation wavelength. The spectrum of Figure 1.12(a) is measured using 532 nm excitation wavelength and is consistent with spectra of Figure 1.11(a), where we distinguish a dominant peak at 242 cm^{-1}, consistent to with the A_{1g} mode. Interestingly aside from the 285 cm^{-1} peak associated to the E^1_{2g} mode as in Figure 1.12(a), two other low-intensity peaks at 169, 352 cm^{-1} emerge. The Raman spectrum of Figure 1.12(b), obtained using an excitation wavelength of 442 nm, shows a similar peaks as in Figure 1.12(a) data, but the E^1_{2g} mode and the additional peaks at 169 and 352 cm^{-1} emerge with significantly stronger intensity. Tuning the excitation wavelength allows to for different Raman peaks associated with vibrational modes to emerge with different intensity.

20
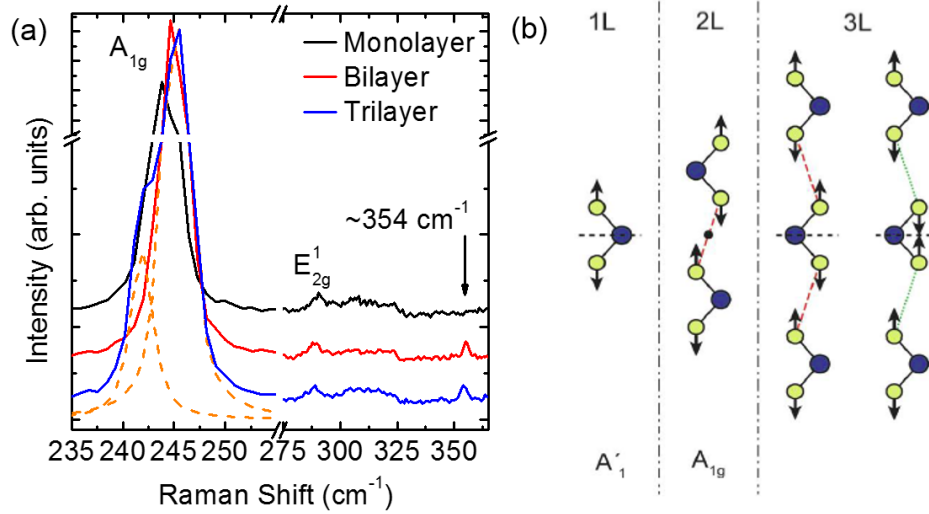
Figure 1.11 (a) Raman spectra of mono-, bi-, and trilayer MoSe$_2$ flakes, obtained using a 532 nm excitation wavelength. A prominent peak emerges at ~244 cm^{-1}, associated with the A$_{1g}$ mode. Dashed lines correspond to the double gaussian fit of the trilayer 245 cm^{-1} peak. Traces are offset for clarity. (b) Schematic illustration of the out-of-plane A$_{1g}$ mode in monolayer (1L), bilayer (2L), trilayer (3L), to explain the emerge of Davydov splitting in trilayer MoSe$_2$. Green (red) dashed lines mark different interlayer interactions, associated with decrease (increase) of the A$_{1g}$ mode frequency. Adapted with permission from Ref. [21], OSA.

The excitation-wavelength peak-intensity dependence is an observation consistent with previous studies, which indicate that the A$_{1g}$ mode is better resolved at longer excitation wavelengths [38], [39]. We assign the peak at 169 cm^{-1} to the E$_{1g}$ mode, which should be forbidden for back-scattering measurements, but it emerges in our measurements of few layer flakes, possibly because of resonant effects, i.e. excitation energy matches the C-exciton energy [38], [40]. Similar measurement has also been reported in WSe$_2$ few-layers flakes [41]. Lastly, we discuss the assignment of the ~353 cm^{-1} peak [Figure 1.11(a) and 1.12(a) and 1.12 (b)], which is to date more controversial. This peak may correspond to either the B$^1_{2g}$ Raman inactive mode [21] or the A$_{2u}$ IR active mode [33], [38]–[40]. The emergence of an inactive or IR mode in the Raman spectrum can be associated to either: (i) breakdown of translational symmetry in few-layer flakes [21], (ii) C-exciton resonant effects [38], [40], (iii) breakdown of inversion symmetry in small flakes, possibly because of the substrate, as seen in Raman spectroscopy studies of Bi$_2$Te$_3$ nanoplates [42].
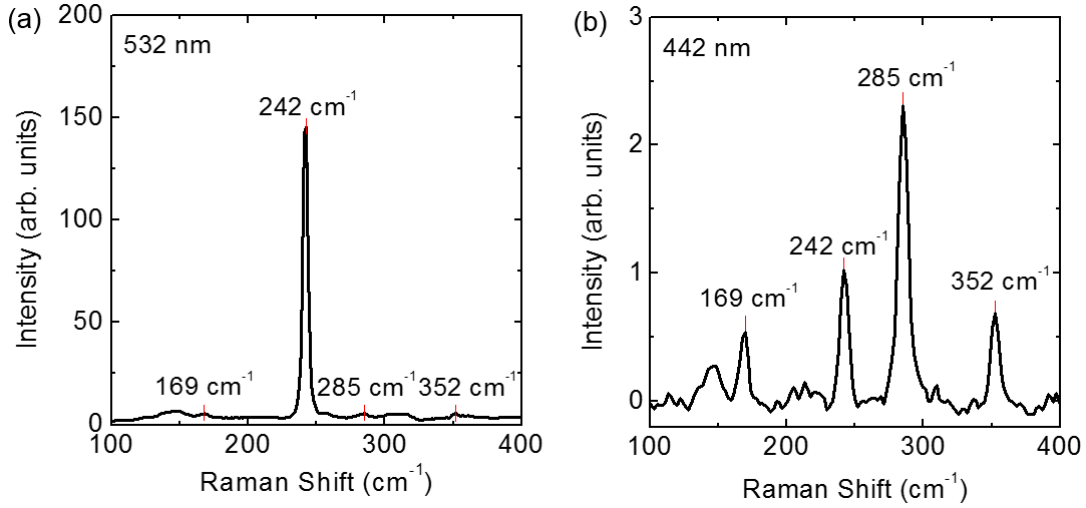
Figure 1.12 Raman spectra of a ~10-layer MoSe$_2$ flake, measured using excitation wavelengths of 532 nm (a), and 442 nm (b). Measurements obtained with different excitation wavelengths show different relative peak intensity. Reprinted from S. Larentis *et al.* Appl. Phys. Lett 101, 223104 (2012), Ref. [5], with the permission of AIP Publishing.

1.1.4.3 MoTe$_2$ Raman spectroscopy

Figure 1.13(a) shows the MoTe$_2$ Raman spectra measured on a flake with terraces of different thicknesses, as shown by the optical micrograph and the atomic force microscopy (AFM) topography of Figure 1.13(b) and 1.13(c), respectively. Raman spectra are acquired using a 532 nm excitation wavelength with ~100 µW excitation power measured at the sample. The Raman spectrum of monolayer MoTe$_2$, shown in Figure 1.13(a), bears similarities to both the MoS$_2$ and the MoSe$_2$ spectra. It presents two peaks at 175 cm^{-1} and 235 cm^{-1} associated to A_{1g} and E^1_{2g} modes [33], but as opposed to the Raman spectrum of MoSe$_2$ the E^1_{2g} peak is predominant. The thickness dependence of the spectrum is characterized by the emergence of a peak at ~291 cm^{-1} for thicknesses greater than a monolayer, associated with the B^1_{2g} mode, which intensity peaks for measurements in bilayer [11], [33]. As observed in Raman spectra obtained from MoSe$_2$ flakes of different thickness, the presence or absence of the B^1_{2g} peak provides an effective way to identify monolayers. Using a 532 nm excitation wavelength, the intensity thickness dependence of

22

the predominant E^1_{2g} mode is non-monotonic. The intensity increases from mono- to bilayer, and begins decreasing as the number of layers is increased, vanishing in the bulk. The position of the E^1_{2g} peak is also thickness dependent, namely we observe a 2 cm^{-1} peak downshift from monolayer to bulk [33]. The observed peak shift is small, rendering the thickness identification beyond mono- and bilayer more challenging as compared to MoS_2. Recent studies question the assignment of the peak at 170 cm^{-1} to the A_{1g} mode, suggesting it may instead the result of different Raman response, e.g. a two-phonon process [11]. In fact, when Raman spectra are acquired as a function of thickness and excitation wavelength (532 and 633 nm), they show an excitation-independent, thickness-dependent intensity scaling for E^1_{2g} and B^1_{2g} modes but not for the A_{1g} mode [11].
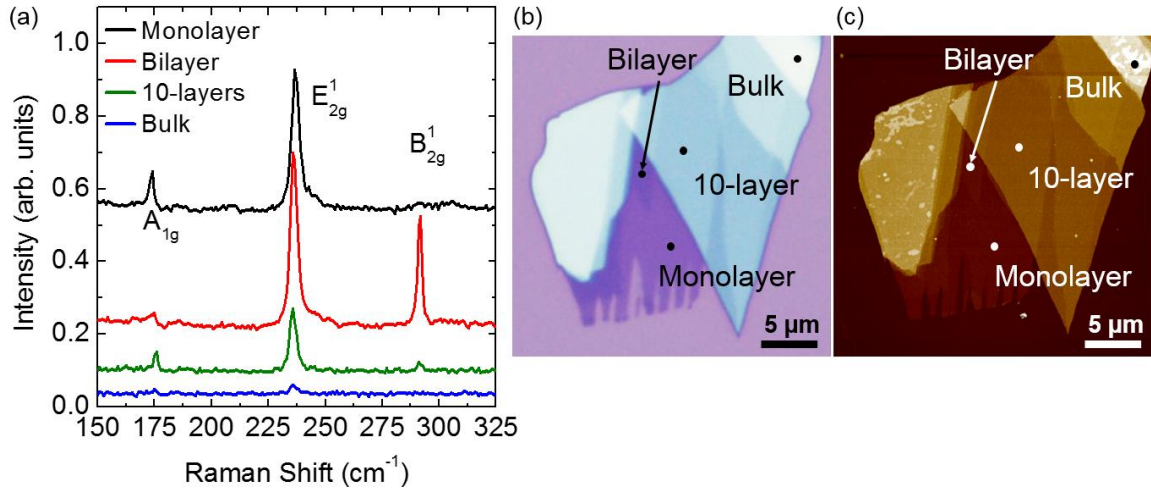
Figure 1.13 Raman spectra of mono-, bi, 10-layer and bulk $MoTe_2$, measured using a 532 nm excitation wavelength, showing prominent peaks at ~175 cm^{-1} and ~235 cm^{-1} associated to the A_{1g} and E^1_{2g} modes, respectively. The peak at 291 cm^{-1} is associated with the B^1_{2g} mode and allows to identify monolayers. Traces are offset for clarity. $MoTe_2$ terraces at different thickness are marked in the (b) optical micrograph and (c) AFM topography.

1.1.5 Optical properties

As introduced in Section 1.1.2 the band structure of molybdenum based 1H-monolayers MX_2 presents a direct bandgap > 1 eV and a sizable spin-splitting the in the

valence band [Figure 1.4(b)]. As the number of layers is increased the bandgap turns indirect as $E_{K\Gamma}$ and E_{KQ} change sign and become negative. However, the direct bandgap size, as predicted by DFT calculations and probed optically, does not change significantly [Section 1.1.2]. Figure 1.14(a) show the photoluminescence (PL) measured in monolayer MoS_2, $MoSe_2$ and $MoTe_2$ flakes at room temperature [11]. The availability of different direct bandgaps in the visible and near-infrared spectra hints to possible optoelectronic applications, e.g. spectrum splitting [6] and security applications [43].

The strong and sharp (FWHM < 100 meV) PL spectra observed for all three materials is consistent with bandstructure calculations which assign a direct bandgap at the K point to this class of materials and is associated to the A exciton/transition between the almost spin degenerate CB and the upper spin split subband in the VB [Figure 1.4(b)]. A comparison of bandgap values probed using STS measurements [Table 1.2] and the optical gaps (E_{opt}) measured in Figure 1.14(a), reveal a large discrepancy, an observation that often render a definition of the bandgaps in TMDs contradictory. The difference between the STS gap and E_{opt} is effectively the exciton binding energy (E_b), equal to ~0.3 and 0.5 eV for MoS_2 and $MoSe_2$, respectively. Large values of E_b, more than an order of magnitude larger than in conventional semiconductors (Si,Ge), are associated with strong electron-electron interaction in these material systems [13], [14], [44], for this reason GW-calculated bandgaps tent to agree better with STS measured gaps.

In the following Sections 1.1.5.1 and 1.1.5.2, we will discuss the PL of mono- and few-layer MoS_2 and $MoSe_2$ on Si/SiO_2 substrates. Measurements are obtained using a Renishaw InVia spectrometer using an excitation wavelength of 2.33 eV (532 nm), a 100x objective lens, a 1200 l/mm grating and a silicon detector. Measurements of $MoTe_2$ mono- and few layer flakes are impossible in our system because the PL peak is smaller than the bandgap of silicon.
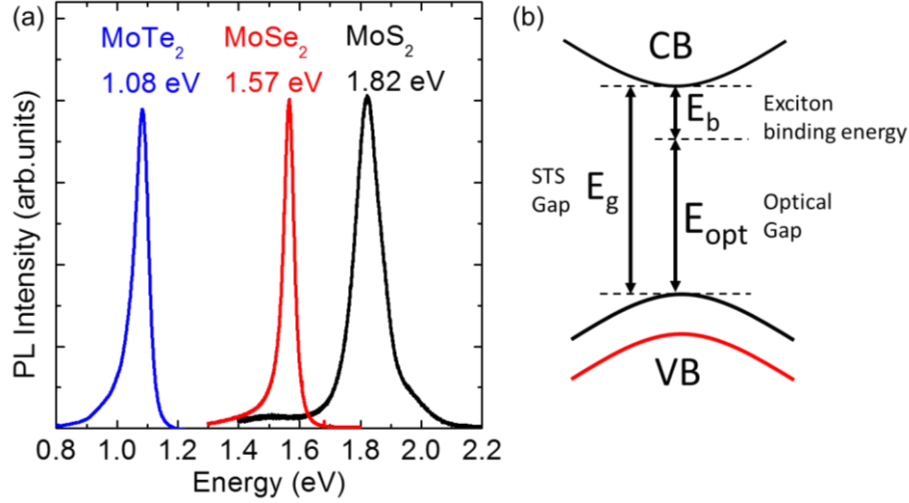
Figure 1.14: (a) Normalized PL spectra of monolayer MoS_2, $MoSe_2$ and $MoTe_2$ measured at room temperature. (b) Bandstructure schematic at the K point highlighting the difference between the E_g probed with STS measurements and the optical gap E_{opt}, which corresponds to the exciton binding energy. PL data for $MoTe_2$ are obtained from Ref. [11].

1.1.5.1 MoS₂ Photoluminescence

Figure 1.15 shows the room temperature PL spectra for mono-, bi-, tri- and 4-layer MoS_2. The PL spectrum of monolayer MoS_2 shows a predominant feature at 1.82 eV and a small secondary feature at ~1.95 eV, which are assigned to the *A* and *B* exciton, respectively [1], [45]. The *A* and *B* transitions/excitons results from the (spin-split) split bandstructure at the *K*-point in (monolayer) bulk, as shown by the inset schematic of Figure 1.15. In monolayer, the energy difference between A and B transitions provides an experimental estimation of $2\Delta_{vb}$, assuming that the binding energy for the two excitons is the same and $\Delta_{cb} << \Delta_{vb}$, conditions that in the first approximation are satisfied for MoS_2 [12]. The measured $2\Delta_{vb} \sim 150$ meV obtained from Figure 1.15 data is comparable with calculated values of Table 1.3, and other experimental reports in literature [13].

The PL spectrum of bilayer shows similar *A* and *B* features at high energy, with a third peak at ~1.5 eV emerging in the spectrum, which is associated with indirect bandgap transition (*I*), consistent with MoS_2 turning into an indirect semiconductor at thicknesses

greater than a monolayer. As the thickness is increased the *I* peak shifts toward lower energies, approaching the bulk values at five layers [Table 1.2], [45]. The intensity of the peak associated to the *A* exciton drops significantly from mono- to bilayer, but its energy remains nearly constant for thicker flakes, consistent with a thickness independent optical direct gap at the *K* point [1], [4], [19]. The position of both peaks, associated with *A* and *B* excitons, is consistent with reflectance measurement in literature [1], [46]. It should be noted that often times the optical gap of monolayer MoS_2 is quoted as 1.9 eV, a value obtained from on suspended samples [1][45]. In addition to Raman spectroscopy, discussed in Section 1.1.4, PL measurements can also be used to quickly asses the material nature and the flake thickness.
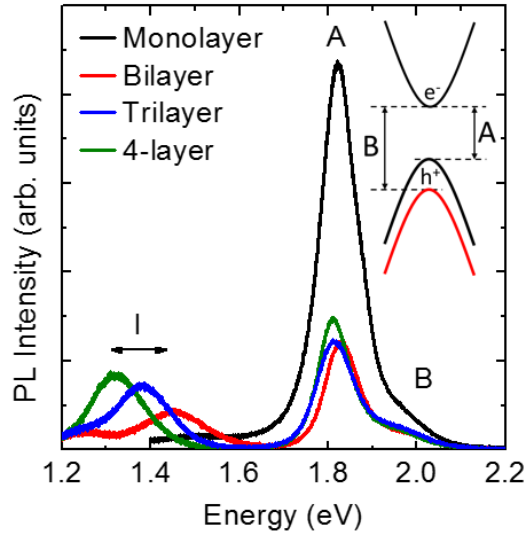
Figure 1.15: Room temperature PL spectra mono-, bi-, tri- and 4-layer of MoS_2. Inset: bandstructure schematic at the *K* point labeling direct bandgap highlighting *A* and *B* transitions.

1.1.5.2 MoSe₂ Photoluminescence

Figure 1.16 shows the PL spectra for mono-, bi- and trilayer $MoSe_2$ measured at room temperature. The PL spectra of monolayer (bilayer) $MoSe_2$ presents a principal peak at 1.57 (1.54) eV, which is assigned to the *A* exciton [21], [47]. The trilayer spectra presents instead two different broad peaks, one that coincides with the *A* exciton as in mono- and

bilayer spectra, and a lower energy peak attributed to the indirect gap. The lack of a second peak in the PL spectrum of bilayer, associated to an indirect transition, may indicate that the bandgap in bilayer remains direct, as predicted by some, but not all bandstructure calculations [38], [48]. Unlike PL spectra of MoS_2 flakes, PL spectra of $MoSe_2$ flakes show a marked intensity decrease as the thickness is increased. Bilayer and trilayer data of Figure 1.16 are multiplied by a factor of 20 and 50, respectively. Similar to what observed in PL data of MoS_2 [Figure 1.15], the peak associated with *A* exciton appears largely thickness independent, and consistent with reflectance measurements [3], [11], [49]. The layer dependent PL spectra discussed in this section can be also be used to quickly identify the flake thickness.
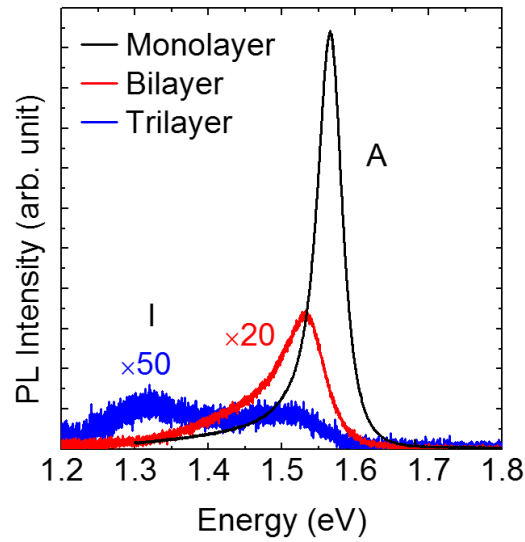
Figure 1.16: Photoluminescence spectra of mono-, bi- and trilayer $MoSe_2$.

1.2 TWO-DIMENSIONAL ELECTRON SYSTEM IN PERPENDICULAR MAGNETIC FIELD

In this section we will introduce the fundamentals of electron transport in a perpendicular magnetic field (*B*) for a two-dimensional electron system (2DES). First, we will discuss the classical Hall effect, where a Hall voltage proportional to the perpendicular *B*-field develops perpendicular to the current direction. Second, the discussion is expanded

to the quantum Hall effect (QHE), where the Hall voltage takes quantized values. Finally, QHE in graphene is discussed highlighting differences with gapped 2DES.

1.2.1 Classical Hall Effect

Free electrons immersed in a perpendicular B-field, move in circular orbits, where the angular frequency, known as the cyclotron frequency is fixed $\omega_c = eB/m^*$; m^* is the carriers effective mass and e is the electron charge. A (quantum) Hall effect experiment is conducted applying an in-plane electric field (E), in addition to perpendicular B-field. In absence of a magnetic field, in homogeneous and isotropic material Ohm's law writes: $J = \sigma E$, where J is the current density vector, and σ is the scalar conductivity, therefore we expect J and E to be parallel. In presence of a perpendicular B-field J and E are no longer parallel, and the scalar σ needs to be replaced by a conductivity tensor:

$$J = \sigma E \rightarrow \begin{pmatrix} J_x \\ J_y \end{pmatrix} = \begin{pmatrix} \sigma_{xx} & \sigma_{xy} \\ -\sigma_{xy} & \sigma_{xx} \end{pmatrix} \begin{pmatrix} E_x \\ E_y \end{pmatrix} \qquad 1.1$$

where, J_x, J_y and E_x, E_y are the current density and electric field components. Electrons that move within a crystal structure are scattered, by either phonons or impurities. A scattering time (τ) is introduced to model the scattering process, as time between scattering events. The electron motion can be described using the Drude model:

$$m^* \frac{d\boldsymbol{v}}{dt} = -e\boldsymbol{E} - e\boldsymbol{v} \times \boldsymbol{B} - \frac{m^*\boldsymbol{v}}{\tau} \qquad 1.2$$

where, $\boldsymbol{v}$ is the carrier velocity. In steady state this equation reads:

$$v_x = -\frac{e\tau}{m^*} E_x - \omega_c \tau v_y \qquad 1.3$$

$$v_y = -\frac{e\tau}{m^*} E_y + \omega_c \tau v_x \qquad 1.4$$

28
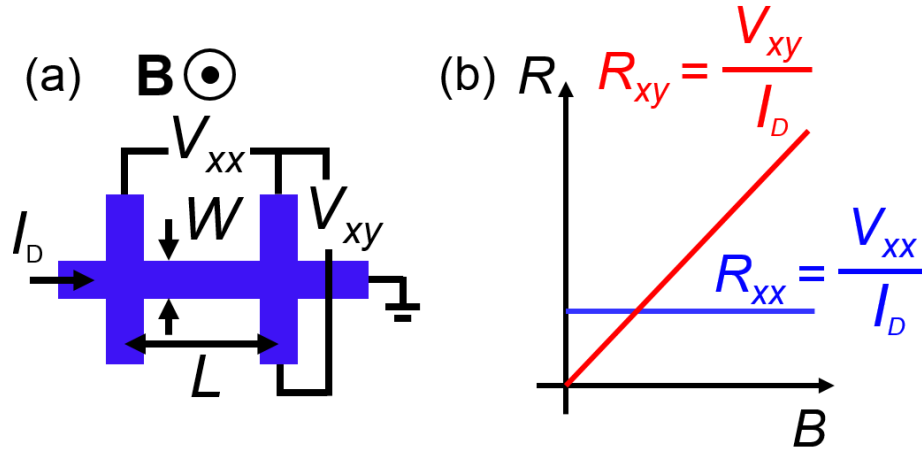
Figure 1.17: (a) Measurement setup for a Hall-bar in perpendicular magnetic field, measuring V_{xx} and V_{xy}; (b) R_{xx}, R_{xy} classical hall effect B-field dependence.

At this point it is useful to introduce the experimental setup for a Hall effect experiment. QHE experiments use the same setup. Figure 1.17(a) shows a Hall bar structure with longitudinal and perpendicular contacts, which can be obtained etching the excess semiconductor material. The Hall-bar geometry enables to independently measure the longitudinal (V_{xx}) and Hall (V_{xy}) voltage, while flowing a constant current (I_D) along the longitudinal direction. Both voltages are measured using high-impedance meters, thus no current flow is allowed in the y direction ($J_y = 0$, $v_y = 0$). Comparing Equation 1.1, 1.3 and 1.4 we obtain:

$$\frac{E_y}{E_x} = \frac{\sigma_{xy}}{\sigma_{xx}} = -\omega_c \tau \qquad\qquad 1.5$$

Writing $J_x = -nev_x$, and inverting the conductivity matrix, we can define the following resistivities:

$$\rho_{xx} \equiv \frac{E_x}{J_x} = \frac{\sigma_{xx}}{\sigma_{xx}^2 + \sigma_{xy}^2} = \frac{1}{en}\frac{m^*}{e\tau} = \frac{1}{en\mu} \qquad\qquad 1.6$$

$$\rho_{xy} \equiv \frac{E_y}{J_x} = \frac{\sigma_{xy}}{\sigma_{xx}^2 + \sigma_{xy}^2} = \frac{B}{en} \qquad\qquad 1.7$$

29

Comparing Equations 1.6 and 1.7 to measurable voltages V_{xx}, V_{xy}, and I_D applied we obtain:

$$\rho_{xx} \equiv \frac{E_x}{J_x} = \frac{\frac{V_{xx}}{L}}{\frac{I_D}{W}} = \frac{V_{xx}}{I_D}\frac{W}{L} \rightarrow R_{xx} \equiv \frac{V_{xx}}{I_D} \tag{1.8}$$

$$\rho_{xy} \equiv \frac{E_y}{J_x} = \frac{\frac{V_{xy}}{W}}{\frac{I_D}{W}} = \frac{V_{xy}}{I_D} \equiv R_{xy} \tag{1.9}$$

where W and L are the length and width of the Hall bar, marked in Figure 1.17(a). The expected B-field dependence of the longitudinal (R_{xx}) and Hall (R_{xy}) resistances is sketched in Figure 1.17(b). The slope of the Hall resistance can used to extract the 2DES carrier density (n):

$$n = \frac{1}{e\frac{dR_{xy}}{dB}} \tag{1.10}$$

1.2.2 Quantum Hall Effect

Quantum Hall effect experimental results can be understood by first considering the effect of a perpendicular B-field in the Schrödinger equation considering a parabolic 2DES, described by the effective mass. The most convenient algebra that captures the effect of a perpendicular B-field is the Landau quantization. The B-field is introduced in the Hamiltonian using a magnetic vector potential $\mathbf{A} = (0, Bx, 0)$, known as the Landau gauge, where $B\mathbf{z} = \nabla \times \mathbf{A}$. For an electron gas in a perpendicular B-field the Hamiltonian writes:

$$H = \frac{1}{2m^*}(\mathbf{p} + e\mathbf{A})^2 = \frac{1}{2m^*}\left(p_x^2 + \left(p_y + eBx\right)^2\right) \tag{1.11}$$

because cartesian vectors are mutually perpendicular, and $\mathbf{p}$ is the momentum operator. Given vector potential is not a function of y, the wavefunction should be of the form: $\psi_k(x,y) = u(x)e^{iky}$, where k is the wavevector, substituting the wavefunction in Equation 1.11 we obtain:

$$\left[-\frac{\hbar^2}{2m^*}\frac{d^2}{dx^2} + \frac{1}{2}m\omega_c^2\left(x + \frac{\hbar k}{eB}\right)^2 \right]u(x) = Eu(x) \qquad 1.12$$

where $\hbar$ is the reduced Plank constant. Equation 1.12 confirms the wavefunction choice is appropriate, with the plane wave canceling out on both sides. What we are then left with is the well know Schrödinger equation for a one-dimensional oscillator. The frequency of the oscillator is the same as in the classical case, ω_c and the energy eigenvalues are as follows:

$$E_l = \hbar\omega_c\left(l + \frac{1}{2}\right), \qquad where \;\; l = 0, 1, 2, 3 \ldots \qquad 1.13$$

We can highlight two noteworthy features of this result: first, the energy levels E_l are k independent and only function of l, secondly the density of states associated with this dispersion is formed by a series of delta functions with energy separation $\hbar\omega_c$, as shown in Figure 1.18(a). In a real sample Landau levels (LLs) are broadened because of scattering, by a $\delta E = \hbar/\tau$. The effect of a B-field on a 2DES dispersion become relevant only when LLs are well-spaced, namely $\hbar\omega_c \gg \hbar/\tau$, or in other words $\omega_c\tau \gg 1$. This condition is satisfied in the limit of high B-fields and high mobility samples, and separates classical and quantum-mechanical regimes, i.e. the emergence of "discrete" LL. The carrier density associated to a spin (two-fold) degenerate LL corresponds to the density of states of a 2D band in a range of energy $\hbar\omega_c$:

$$2n_B = \frac{m^*}{\pi\hbar^2}\hbar\omega_c = \frac{2eB}{h} \qquad 1.14$$

where h is Plank's constant. The n/n_B ratio corresponds to the number of occupied LLs, known as the filling factor (FF).
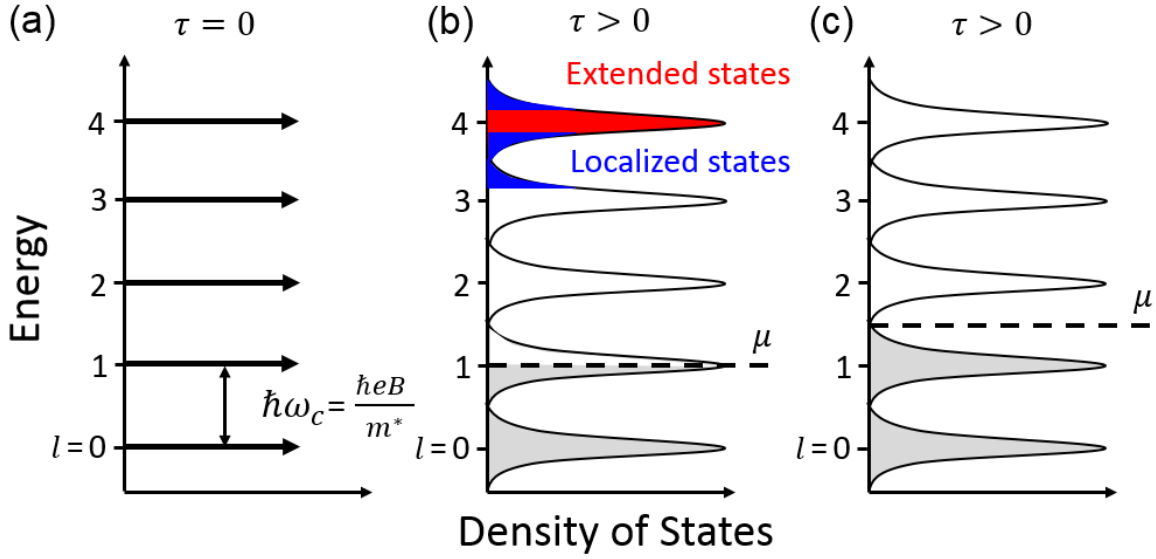
Figure 1.18: (a) LL density of states at $\tau = 0$, (b, c) LL density of states at $\tau > 0$, for two positions of μ, the grey shaded regions correspond to states filled with electrons. Each broadened state is characterized by extended (highlighted in red) and localized states extended (highlighted in blue).

Looking at the LL occupancy picture of Figure 1.18(b) and 1.18(c), in the limit of absolute zero temperature, we can deduce that the conductivity of the 2DES will assume an opposite behavior when the chemical potential (μ), will lie within a LL, assuming a finite broadening δE, or within a gap. Considering spin (two-fold) degenerate LLs, if the highest occupied LL is half-full the FF is odd [μ lies within a LL, Figure 1.18(b)], and the system behaves like a metal with a high conductivity. If the LL is completely filled with no empty states available at the Fermi energy, the FF is even [μ lies in the gap, Figure 1.18(b)], and the system behaves like an insulator. While a description based on the 2DES conductivity is intuitive, it is impractical, given actual measurements probe R_{xx} and R_{xy}. Recalling Equations 1.5, 1.6, and 1.8, in the limit of high fields ($\omega_c \tau \gg 1$), we obtain $\rho_{xx} \approx \sigma_{xx}/\sigma_{xy}^2$, a result that indicate the longitudinal conductance and resistivity are directly proportional, therefore to low (high) σ_{xx} for a (half) filled LL, correspond to low (high) ρ_{xx} or R_{xx}.

In an experiment where the carrier density is kept fixed, and the perpendicular B-field is swept, R_{xx} is expected to oscillate between high and low resistance. These

oscillations are known as Shubnikov-de Haas (SdH) oscillations. The period (Λ) of R_{xx} oscillations as function of $1/B$ is given by:

$$\Lambda(1/B) = \frac{2e}{hn} \qquad\qquad 1.15$$

where the factor of 2 accounts for spin degenerate LL. Extracting the R_{xx} vs $1/B$ data oscillation frequency is a viable method to extract n, assuming the LL degeneracy is known. A comparison of n extracted from the low B-field Hall data (classical Hall effect) and the SdH oscillation frequency allows to determine the LL degeneracy.

Figure 1.19 shows an example of a R_{xx}, R_{xy} vs B measured in a GaAs 2DES. R_{xx} vs B data present an oscillatory behavior at first, and as the B-field is further increased R_{xx} vanishes for integer values of v, the filling factor. The concurrent measurement of the Hall resistance shows two noteworthy figures: first, as expected from the classical Hall effect the R_{xy} is a linear function of B; second, at high B-fields the R_{xy} plateaus and becomes field independent where R_{xx} vanishes. However, the most interesting feature are the quantized values that R_{xy} assumes:

$$R_{xy} \equiv \frac{V_{xy}}{I} = \frac{1}{v}\frac{h}{e^2} \approx \frac{25182\ \Omega}{v} \qquad\qquad 1.16$$

The experimental discovery of a quantized Hall resistance by German physicist Von Klitzing in 1980, earned him the Nobel prize in 1985. This quantized resistance values are determined only by fundamental constants, can be measured very accurately, and as a result did become the standard for resistance measurement.

Figure 1.19 shows R_{xy} plateaus at even $v = 10, 8, 6\ldots$ at low B-field, with R_{xy} plateaus at integer FF emerging at higher B-fields. This is a consequence of the spin splitting of LLs, also known as Zeeman splitting. So far, we have described the LLs as spin degenerate labeled by an index l. More accurately the LL energy writes as sum of cyclotron and Zeeman energy:

$$E_l = \hbar\omega_c\left(l+\frac{1}{2}\right) \pm \frac{1}{2}g^*\mu_b B, \qquad where\ \ l = 0,1,2,3\ldots \qquad 1.17$$

where μ_B is Bohr's magnetron and g^* is the effective g-factor. The Zeeman splitting ($g^*\mu_B B$) is typically smaller than $\hbar\omega_c$, e.g. $g^* = -0.44$ in GaAs, therefore odd FFs are

33

resolved only at higher B-field, as shown in Figure 1.19, where spin degeneracy is lifted. In this spin-split picture the filling factor v is an integer and represents the number of filled spin-split LLs:

$$v = \frac{nh}{eB_v} \qquad\qquad 1.18$$

where B_v is the magnetic field corresponding to the filling factor v.
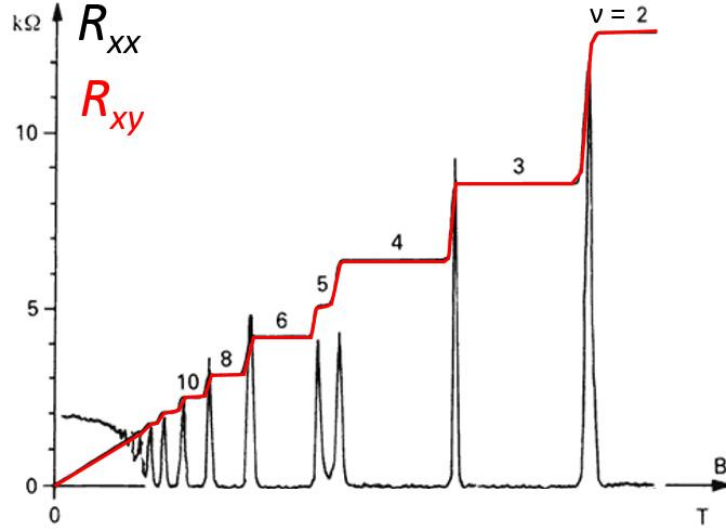
Figure 1.19: R_{xx}, R_{xy} vs B measured in a GaAs 2DES [50], showing quantized plateaus of R_{xy} and vanishing R_{xx}. Plateaus emerging at odd filling factors are associated to spin-split LLs. Figure adapted from Ref. [51] (Kosmos 1986).

The emergence of wide R_{xy} plateaus is at odds with the QHE picture discussed so far. We would in fact expect a quantized R_{xy} only at one particular B-field when an integer number of LL is completely filled, not over a finite range of magnetic fields, as experimental data show in Figure 1.19. The presence of disorder in actual samples not only broadens the levels, as introduced earlier, but also generates an uneven potential distribution across the sample. This uneven potential distribution gives rise to two set of states: extended states near the center of the LL, labeled in red in Figure 1.18(b), and localized states in the tail of the LL labeled in blue in Figure 1.18(b). At a given B-field μ may coincide with a filled LL ($R_{xx} \sim 0$, R_{xy} = quantized) [Figure 1.18(c)]. As we begin

varying the B-field we would expect the R_{xx} and the R_{xy} to increase, a behavior consistent with a partially filled LL. However, before μ comes close to the center of the next LL, localized states [blue band in Figure 1.18(b)], that that do not contribute the conduction, are first populated rendering R_{xy} and R_{xx} effectively B-independent for this B-field range. In essence, the emergence of large plateaus is explained by disorder.

Thus far we have discussed the QHE theory in the limit of absolute zero temperature (T). Experiments are conducted at low temperatures, and if $\hbar\omega_c > k_B T$ oscillations of R_{xx} can be observed at sufficiently high B-fields; k_B is the Boltzmann constant. Two-dimensional electron systems are obtained using semiconductor structures such as Si metal-oxide-semiconductor field-effect transistors (FETs) and GaAs-(Al,Ga)As heterostructures and quantum wells, for either electron or holes systems. Two-dimensional systems realized in III-V semiconductor have been extensively used to investigate QHE, owing to their high mobility (low τ) at low temperatures.

1.2.3 Quantum Hall Effect in Graphene

1.2.3.1 Monolayer Graphene

Monolayer graphene QHE presents distinctive half integer quantization of R_{xy}, which stems from graphene's linear energy momentum dispersion at equivalent K and K' points of the hexagonal Brillouin zone, where carriers behave as Dirac massless fermions. Figure 1.20(a) shows an example of R_{xx}, R_{xy} vs B measured at $T = 30$ mK, and an electron density $n = 7.0 \times 10^{11}$ cm^{-2}, in an etched monolayer graphene Hall bar sample. The inset of Figure 1.20(a) presents a similar measurement performed at a hole density $p = 3.2 \times 10^{11}$ cm^{-2}. Using gated Hall bars, graphene samples can be electrostatically doped with electron or holes. Both measurements show clear quantum hall states (QHSs) developing a $\nu = \pm2, \pm6, \pm10, \pm12\ldots$ The electron-hole symmetry typical of the Dirac cone bandstructure, manifest

itself in equivalent quantized plateaus for electron and hole doped samples. The QHS sequence for monolayer graphene writes as follows:

$$\nu = \pm 4(m + 1/2) \qquad\qquad 1.19$$

where m = 0, 1, 2, 3…, +/- refer to the electron and hole LLs, respectively, and ½ refers to the half integer quantization observe in monolayer graphene. Each LL labeled by m is four-fold degenerate, accounting for spin and valley (sublattice) degeneracy. This picture holds at moderate B-fields, while at high B-fields the spin degeneracy is lifted and QHS at $\nu = \pm 1, \pm 4$… begin to emerge.
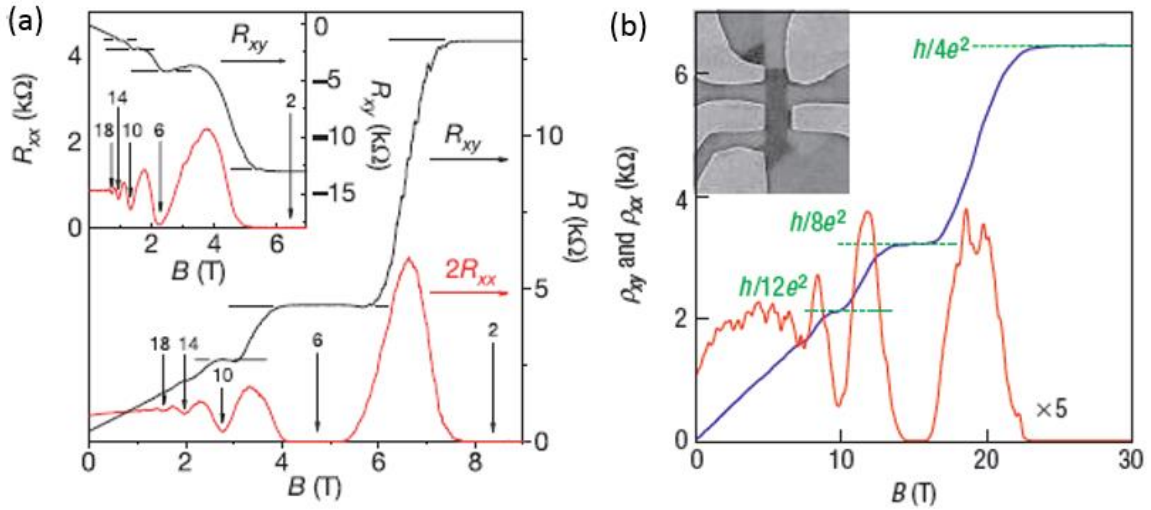
Figure 1.20: (a) R_{xx}, R_{xy} vs B measured in monolayer graphene at $T = 30$ mK and $n = 7.0 \times 10^{11}$ cm^{-2}. A a similar measurement is shown in the inset at $p = 3.2 \times 10^{11}$ cm^{-2}. Reprinted by permission from Springer Customer Service Centre GmbH: Nature, Nature, 438, 201, "Experimental observation of the quantum Hall effect and Berry's phase in graphene" Y. Zhang, Y-W. Tan, H. L. Stormer, P. Kim, Ref. [52] © Springer Nature 2005. (b) R_{xx}, R_{xy} vs B measured in bilayer graphene at $T = 4$ K and $n = 2.5 \times 10^{12}$ cm^{-2}. Reprinted by permission from Springer Customer Service Centre GmbH: Nature, Nature Physics, 2, 177, "Unconventional quantum Hall effect and Berry's phase of 2π in bilayer graphene" K. S. Novoselov, E. Mccann, S. V. Morozov, V. I. Fal'ko, M. I. Katsnelson, U. Zeitler, D. Jiang, F. Schedin And A. K. Geim, Ref. [53] © Springer Nature 2005.

As introduced earlier, a 2DES in a perpendicular B-field forms a LL energy spectrum. In monolayer graphene, the LL energies are no longer linear as a function of the B-field:

$$E_m = \pm\sqrt{2e\hbar v_F^2 |m| B} \qquad\qquad 1.20$$

where $v_F \sim 10^6$ m/s is the Fermi velocity in monolayer graphene. The LL spectrum of monolayer graphene presents two noteworthy features, first the LL spacing is uneven and $\propto \sqrt{|m|}$, second the $m = 0$ LL is pinned at zero energy, where electron and holes are degenerate, consistent with R_{xy} plateaus at $\pm h/2e^2$.

1.2.3.2 Bilayer Graphene

Quantum Hall effect in bilayer graphene presents features that differ both from monolayer graphene and conventional 2DES. Figure 1.20(b) shows an example of a R_{xx}, R_{xy} vs B measured in an etched bilayer graphene Hall bar sample at $T = 4$ K and $n = 2.5 \times 10^{12}$ cm^{-2}. The experimental data show developed QHS at $v = 4, 8, 12$. The QHS sequence in bilayer graphene writes:

$$v = \pm 4(m + 1) \qquad\qquad 1.21$$

where m = 0, 1, 2, 3…, and +/- refers to the electron and hole LLs, respectively. Bilayer graphene four-fold QHS could be associated to a fermion system with spin and valley (four-fold) degeneracy, however the LL energy spectrum:

$$E_m = \pm\hbar\omega_c\sqrt{m(m-1)} \qquad\qquad 1.22$$

present features that differ from a fermion system, most notably the lowest energy LLs levels E_0 and E_1 ($m = 0, 1$) are degenerate at zero energy, forming and effectively eight-fold degenerate LL, consistent with R_{xy} plateaus at $\pm h/4e^2$. A LLs spectrum with a zero energy LL is reminiscent of QHE in monolayer graphene, i.e. Dirac massless fermions, and contrasts with QHE in a 2D fermion system. Bilayer graphene carriers behave as massive chiral fermions and present distinct behavior compared to both carriers in graphene and in other conventional 2DESs.

1.3 CHAPTER ORGANIZATION

In Chapter 2, we discuss the fabrication and electrical characterization of top-contact, bottom-gate and bottom-contact, dual-gate molybdenum-based TMD field-effect transistors and focus on the characterization of the electron mobility. In Chapter 3, we study the magnetotransport of dual-gated mono- and bilayer $MoSe_2$ samples, measuring the effective mass and spin-splitting of K-valley electrons and probing the interaction enhanced, density dependent g-factor. In Chapter 4, we introduce a graphene-MoS_2 heterostructure, which we use to study the charge partitioning between the two layers and probe the negative compressibility of MoS_2 electrons, a manifestation of electron-electron interaction in the MoS_2 system. At last in Chapter 5, we discuss the development of reconfigurable monolayer $MoTe_2$ field-effect transistors using a multi-gate device architecture used to integrate complementary devices and an inverter gate.

Chapter 2: Transition Metal Dichalcogenides Field-Effect Transistors

In this chapter, we discuss the fabrication of TMD FETs using on MoS_2, $MoSe_2$ and $MoTe_2$ flakes, with thickness ranging between ten and one layer (7 - 0.7 nm). Specifically, two types of structures are going to be introduced. First, a simpler top-contact and bottom-gate architecture, where few-layers flakes are directly exfoliated onto the bottom dielectric (SiO_2), and the highly doped Si substrate serves as the bottom-gate. Contacts are then patterned on top of the flake, as shown in Figure 2.1(a). A more complex, bottom-contact, dual-gate architecture is introduced in the latter part of the chapter and is based on the complementary approach. We first pattern bottom-contacts on the bottom-dielectric, then we transfer the TMD layer along with the top-gate dielectric onto the existing contacts. Once the transfer is completed, a top-gate is patterned in alignment with the underlying contacts, as shown in Figure 2.1(b). The inherent challenge that characterizes this second architecture is the ability to transfer 2D materials, rather than rely on direct exfoliation.
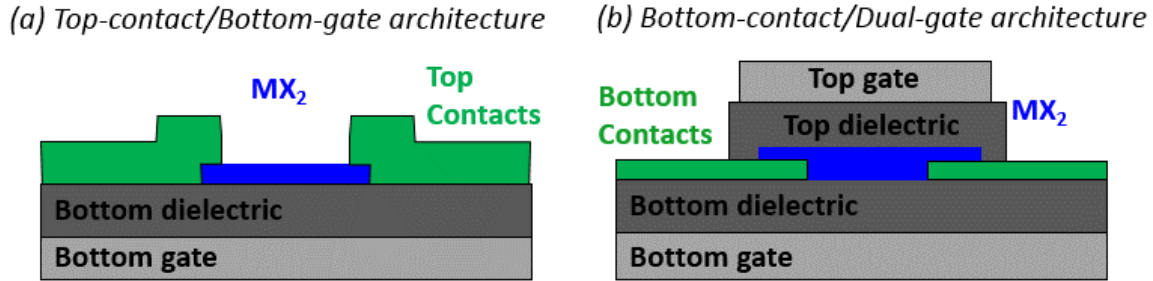
Figure 2.1: TMDs FET schematic illustrating a (a) top-contact, bottom-gate architecture, and a (b) a bottom-contact, dual-gate architecture.

One key challenge that characterizes the development of molybdenum based TMD FETs is the quest for low-resistance, ohmic contacts. The semiconducting nature of TMDs,

as opposed for example to the semi-metal graphene, requires us to develop specific fabrication techniques to obtain low-resistance contacts. High-resistance Schottky barrier contacts significantly impact the FET performance, and may obscure the intrinsic electrical properties of these materials in two-point measurements, requiring four-point measurement to decouple contact effects.

Devices fabricated using few-layer molybdenum-based TMDs are integrated using a top-contact, bottom gate architecture and are characterized using two- and four-point gated measurements schemes, to extract the field-effect electron mobility and its temperature dependence. Monolayer MoS_2, mono- and bilayer $MoSe_2$ Hall-bars are fabricated using a bottom-contact, dual-gate architecture which enables low temperature gated four-point characterization and Hall measurements. Independent measurements of the conductivity and carrier density allow us to compare field-effect and Hall mobility. Hall mobility temperature and carrier density dependence data are used to investigate and decouple different scattering mechanisms limiting electron mobility.

2.1 INTRODUCTION

A renewed research interest in the electrical characterization of molybdenum-based TMD resumed in 2010 [54], following the "rise of graphene" of the early 2000's [55], [56]. Recent electrical characterization studies focus on molybdenum based TMDs in the few-layer limit (< 20 layers), while older studies dating back to the 1960's focused on the bulk material [9]. The most investigated TMD to date is MoS_2, which was also the first TMD studied at the monolayer limit [1], [54]. Its popularity depends on its geological availability and its environmental stability over long periods of time. $MoSe_2$ and $MoTe_2$ are not naturally available crystals and need to be artificially synthetized.

Mono- and few-layers MoS_2 flakes were first isolated on 285 nm-thick SiO_2/Si substrates, to optically distinguish monolayers, as discussed in Chapter 1, and for these reasons most of the early devices, including ours, were first integrated on SiO_2/Si substrates. More complicated structures using a dual-gate, top-contact architecture have

been integrated using high-k and SiO_2 as the top- and bottom-dielectric, respectively [54], [57]. Early MoS_2 FETs fabricated using Au contacts show n-type transfer characteristics, characterized by high ON-OFF ratios (I_{ON}/I_{OFF}) > 10^6, and moderate ON-currents (~10 μA/μm). The large negative threshold voltages typical in these type of devices suggests significant unintentional n-type doping, that may result from the dipole generated by non-stoichiometric high-k oxides [54], [58], [59]. The emergence of n-type conduction using Au contacts is also surprising. Typically, Au contacts are typically used for hole injection, because of Au high work-function (~5.4 eV), for example in organic semiconductor FETs [60]. This behavior hints to a significant Fermi level pinning near the conduction band at the Au-MoS_2 interface, which results in Schottky barriers forming at the metal-semiconductor interface [61]. Schottky contacts impact both subthreshold and ON-current performances in FETs. Obtaining low-resistance, ohmic contacts is one of key research challenges in the 2D materials community [62].
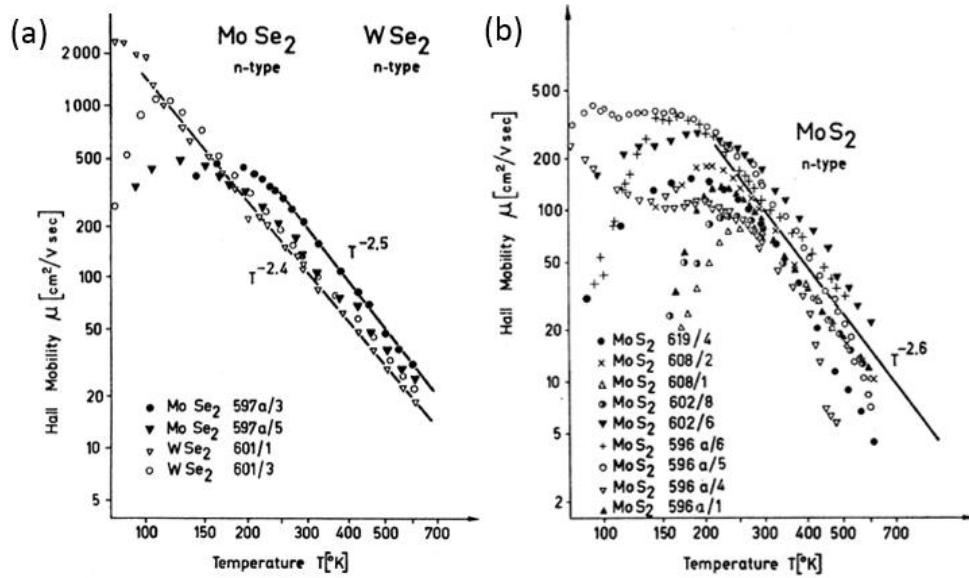
Figure 2.2: Electron Hall mobility as a function of temperature, measured in bulk $MoSe_2$ (a), WSe_2 (a) and $MoSe_2$ (b). The temperature dependence reveals a mobility dominated by phonon scattering. Reprinted with permission from R. Fivaz, and E. Mooser, Phys. Rev. 163, 743 (1967), Ref. [2], © 1967 by the American Physical Society.

The characterization of molybdenum based TMDs' electron mobility is a key metric to assess material quality, characterize the transport properties, and compare this family of materials to other know semiconductors. From a technological standpoint the carrier mobility is a key benchmark metric for next generation channel materials that may be used to integrate aggressively scaled FETs. Early assessment of monolayer MoS_2's room temperature (RT) electron mobility of ~200 cm^2/Vs [54], were disputed [63], [64], because they were determined from two-point measurements [57] without decoupling the contact resistance from the channel resistance, and calculated using an underestimated capacitance value [54], thereby underestimating the actual electron density in the channel.
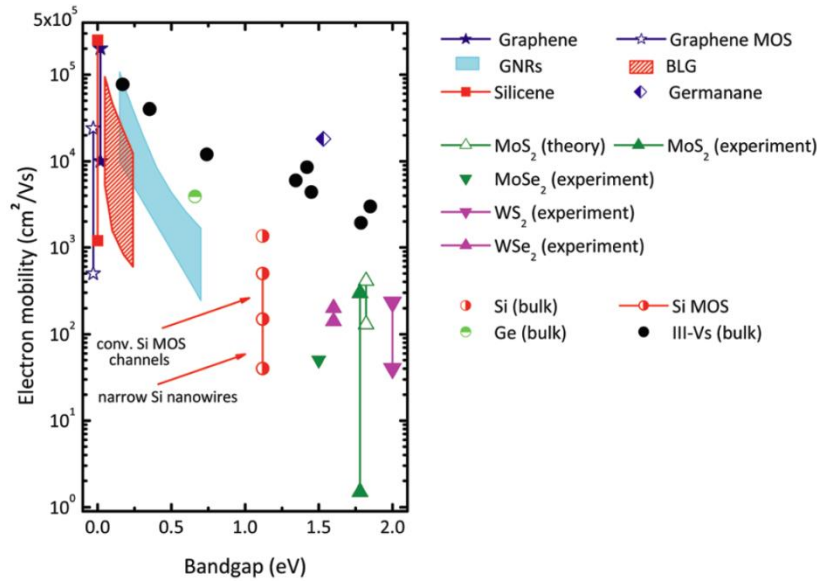
Figure 2.3:   Room temperature electron mobility as function of the material bandgap for an array of semiconductors with E_g up to 2 eV. Reprinted from F. Schwierz, J. Pezoldt and R. Granzner, Nanoscale, 2015, 7, 8261, Ref. [65]- Published by The Royal Society of Chemistry

The accurate measurement of MoS_2, $MoSe_2$ and $MoTe_2$ electron mobility can guide research and development efforts toward the higher mobility material, and determine whether this family of materials may be competitive with present day technology and eventually be suitable for future nodes integration. The investigation of bulk MoS_2 and $MoSe_2$ mobilities dates back to 1960's, where monocrystalline bulk TMD samples with

thickness between 5 and 10 mm, grown using transport reaction methods, were investigated [2]. Figure 2.2 shows the electron Hall mobility temperature dependence measured in MoS_2, $MoSe_2$ and WSe_2 bulk samples. For all TMDs probed the Hall mobility increases as T is reduced, suggesting that phonon scattering dominates in these samples, for T between 150 and 600 K [2].

In order to compare the electron mobility among different materials, such as Si, MoS_2 and graphene, it is important to remember a general trend in semiconductors, exemplified in Figure 2.3, the RT mobility is expected to decrease as the gap size increases [65]. Given TMDs are characterized by a bandgap the ranges between 1 and 2 eV [Table 1.2, Figure 1.14], we should therefore expect a lower mobility as compared to graphene, a 2D semi-metal with no gap. Figure 2.3 summarizes a set of electron mobility data as function of the bandgap of material measured at RT, including Si, III-Vs and 2D materials, providing a summary on where the state-of-the-art technology stands.

2.2 TOP-CONTACT, BOTTOM-GATE ARCHITECTURE

2.2.1 Device fabrication

In this section, we discuss the device fabrication of few-layer $MoSe_2$, MoS_2 and $MoTe_2$ FETs using a top-contact, bottom-gate device architecture. Largely all fabrication process steps are shared between devices based on these TMDs.

The device fabrication begins with the micromechanical exfoliation of commercially available powder (Materion Inc.) with grain size < 44 μm (mesh -325) for $MoSe_2$ [Figure 1.6(a)], natural/synthetic crystals for MoS_2 (SPI Inc [Figure 1.6(b)], 2DSemiconductors.com) and $MoTe_2$ (2DSemiconductors.com, Princeton University, Graphene HQ), as described in Section 1.1.3.1. TMD powders or crystals are exfoliated onto a 285 nm-thick SiO_2 dielectric, thermally grown on highly doped n-type Si (100) wafers ($N_D > 10^{20}$ cm^{-3}), which serves as a bottom-gate in this architecture. The SiO_2/Si substrates are inspected under the optical microscope. The SiO_2 thickness is intentionally optimized to allow identification, under optical microscope, of TMD flakes down to a

monolayer [Section 1.1.3.1]. When good candidates are identified their thickness and topography is then measured using AFM.
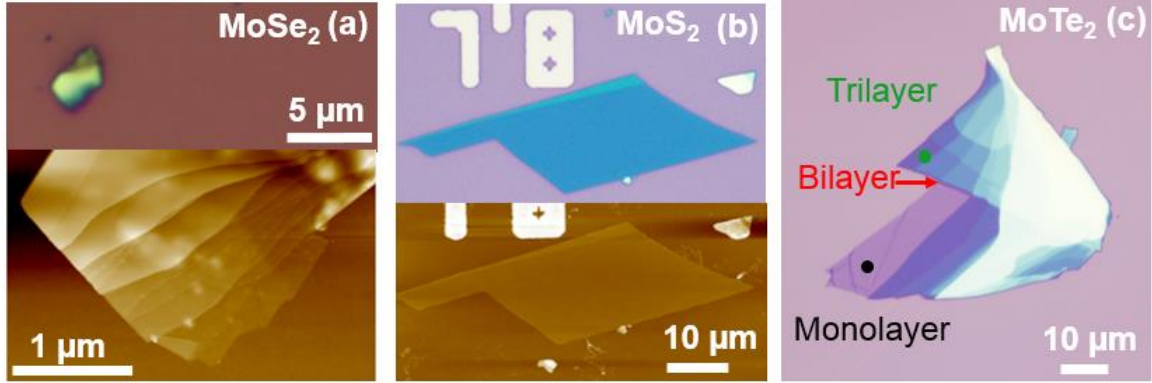
Figure 2.4: (a) Optical micrograph of a MoSe$_2$ flake on a SiO$_2$/Si substrate, exfoliated from powder. AFM topography of the thinner section, showing clear layering, corresponding to the darker section in the optical image. (b) AFM topography and optical micrograph of a few-layer MoSe$_2$ flake exfoliated on SiO$_2$/Si, showing a large uniform terrace, without tape residues. (c) Optical micrograph of a MoTe$_2$ flake with terraces of different thickness. Mono-, bi-, and tri-layer terraces are marked.

Figure 2.4(a) shows an optical micrograph of a MoSe$_2$ flake on a SiO$_2$/Si substrate exfoliated from MoSe$_2$ powder, and its topography, probed by AFM, illustrating clear layered staking. Flakes exfoliated from powder are typically rather small, 1-5 μm in size, and their thickness ranges between ~3 to 50 nm. Figure 2.4(b) shows a MoS$_2$ flake exfoliated from a large crystal (~1×1 cm^2) [Figure 1.6(b)]. Flakes exfoliated from crystals are generally characterized by larger areas and bigger uniform terraces. The typical surface roughness of a terrace probed with AFM ranges between 0.2 and 0.5 nm. Figure 2.4(c) shows a large MoTe$_2$ flake exfoliated from a crystal, characterized by multiple terraces. Lighter colors identify thinner regions. The optical contrast gradient, among layer of different thickness can be used to quickly and effectively determine if a flake is a mono, a bi-, or a tri-layer, particularly when contrast observations are correlated with AFM, Raman spectroscopy [Section 1.1.4], and PL [Section 1.1.5] data. Even though MoSe$_2$ exfoliated from powder show clear evidence of layered stacking in the AFM topography [Figure 2.4(a)], we confirm the MoSe$_2$ powder crystallinity performing X-ray diffraction (XRD).

The powder XRD, shown in Figure 2.5, matches with the 2H-Drysadallite patterns [66], ensuring our powder is characterized by a trigonal-prismatic 2H-$MoSe_2$ structure with space group D_{6h} (P^6_3/mmc) [4], in agreement with previous $MoSe_2$ powder XRDs studies [67], [68]. The full width at half maximum (FWHM) of the <002> peak is 0.223°.
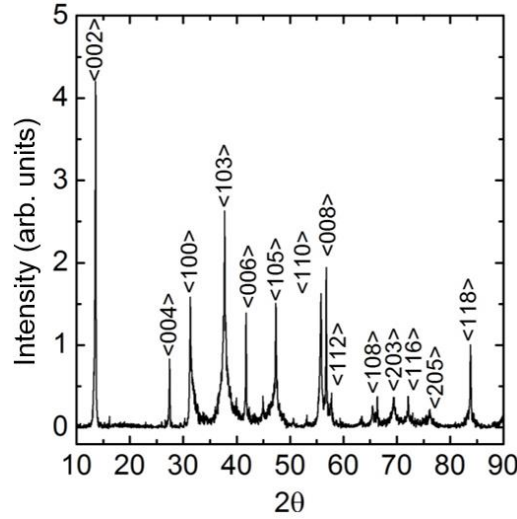
Figure 2.5: $MoSe_2$ powder XRD data, confirming 2H-Drysallite crystal structure, with respective peaks labeled. Reprinted from S. Larentis *et al*. Appl. Phys. Lett 101, 223104 (2012), Ref. [5], with the permission of AIP Publishing.

To electrically probe an exfoliated molybdenum based TMD flake, we select a single terrace with uniform thickness, and define the active region of our FET in that area. As an example, Figure 2.6(a) shows a few-layer MoS_2 flake (4.5 nm-thick), characterized by a large terrace. Before beginning the device fabrication, the flake topography is measured to verify that the flake is flat and clean free of tape residue [Figure 2.6(a) inset]. Electron-beam lithography (EBL) is used to pattern a polymethyl methacrylate (PMMA) mask to define either a two-point, a four-point or a Hall bar [Figure 2.6(b)] device structure. The excess material outside the uniform terrace is etched using Cl_2 reactive ion etching (RIE), as shown in Figure 2.6(c). Typical Cl_2 RIE parameters are the following: plasma power: 100W, Cl_2 pressure: 40 mTorr, etching time: up to 2 min using 500 nm-thick PMMA mask. Typical etching rates for molybdenum based TMDs are ~1 nm/sec. Similar etching rates are obtained for MoS_2, $MoSe_2$ and $MoTe_2$ showing how the metal atom

forming the TMD is the limiting factor for RIE. Once the material is first etched and then exposed to air, a second etching is characterized by a significantly slower etching rate, suggesting the etched material may be more reactive to air, unlike the pristine material exfoliated. The metal contacts are defined performing a second EBL step followed by an e-beam metal evaporation and acetone lift-off overnight. The completed device is shown in Figure 2.6(d). We tested several different metals contacts, including: Au, Cr, In, Ir, Mo, Ni, Nb, Pt, Pd, Ti and V. The best results in terms of contact resistance and maximum drain current are obtained using, Ni for MoSe$_2$, Ti-Au for MoS$_2$ and In or Ni for MoTe$_2$ based devices.
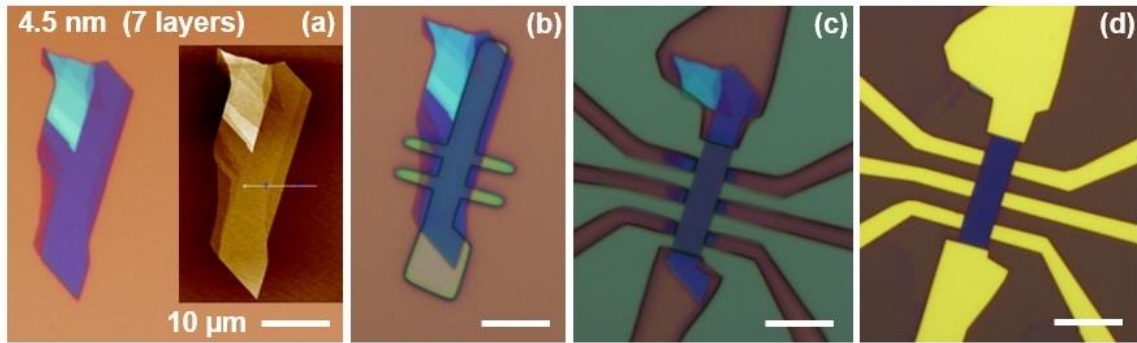
Figure 2.6:   (a) Optical micrograph of a MoS$_2$ flake, with a large 4.5 nm-thick terrace, on SiO$_2$/Si substrate. Inset: AFM topography of flake, confirms the terrace is flat and does not show any tape residue. (b) PMMA etching mask to define a Hall bar structure. (c) After the Cl$_2$ etching, electron-beam lithography is used to define metal contacts mask. (d) Completed device after e-beam metal evaporation of Ti-Au and overnight lift-off.

2.2.2 Few-layer TMD FETs electrical characterization

In this section, we report the electrical characterization of top-contact, bottom-gate FETs based on few-layer MoSe$_2$, MoS$_2$ and MoTe$_2$. We begin studying the output and transfer characteristics at RT, then we focus on the gated four-point conductance characterization to extract the field-effect mobility temperature dependence. Samples in both two- and four-point configurations are measured using a parameter analyzer. For each material considered, several two- and four-point devices have been investigated showing

similar results. MoSe$_2$ and MoTe$_2$ based samples are measured in a vacuum probe station (10^{-6} torr) at temperatures between 300 K and 77 K. MoS$_2$ devices are wirebonded and probed at temperatures down to $T = 4$ K, using a He cryostat, fitted with a variable temperature insert that allows temperature control between 300 and 1.5 K.

2.2.2.1 MoSe$_2$

The MoSe$_2$ based devices presented in this section are obtained from powder exfoliation and are fabricated using small ($< 5 \times 5$ µm^2) few-layer-thick flakes. The output and transfer characteristics of a FET fabricated on a 5.8 nm-thick MoSe$_2$ flake (~ 8 layers), with channel length of 1.8 µm and width of 0.8 µm are shown in Figure 2.7. In each measurement, the source contact is grounded, while the drain contact is biased. Figure 2.7(a) shows the output characteristics defined as drain current (I_D) vs drain voltage (V_D), measured at various bottom-gate voltages (V_{BG}) at RT. The I_D vs V_D dependence is mostly linear, and does not show saturation at high drain bias, in contrast to a conventional FETs. Moreover, the I_D vs V_D data exhibit a super-linear behavior at low V_D, which suggests that the electrons are injected through a Schottky barrier at metal-semiconductor interface. All the data presented in this section are obtained from devices with Ni (80 nm-thick) contacts. Other metal contacts tested, e.g. Ti-Au (2-50 nm-thick) showed worse output characteristic, with lower peak I_Ds and extended super-linear behavior.

Figure 2.7(b) shows the transfer characteristic (I_D vs V_{BG}) measured at two different drain biases $V_D = 50$ mV and $V_D = 1$ V. The device exhibits a clear n-type behavior, and is depleted from free carriers for $V_{BG} < 0$ V. From an extrapolation of the transfer characteristic's linear region to $I_D = 0$, at $V_D = 1$ V, we determine a threshold voltage, $V_T = 8$ V. The I_{ON}/I_{OFF} ratio for I_D vs V_{BG}, measured at $V_D = 1$ V, is larger than 10^6, similar to reported I_{ON}/I_{OFF} values for MoS$_2$, WS$_2$, and WSe$_2$ devices [57], [69], [70], and explained by the large energy gaps (> 1eV) that characterize this family of materials [Table 1.2].
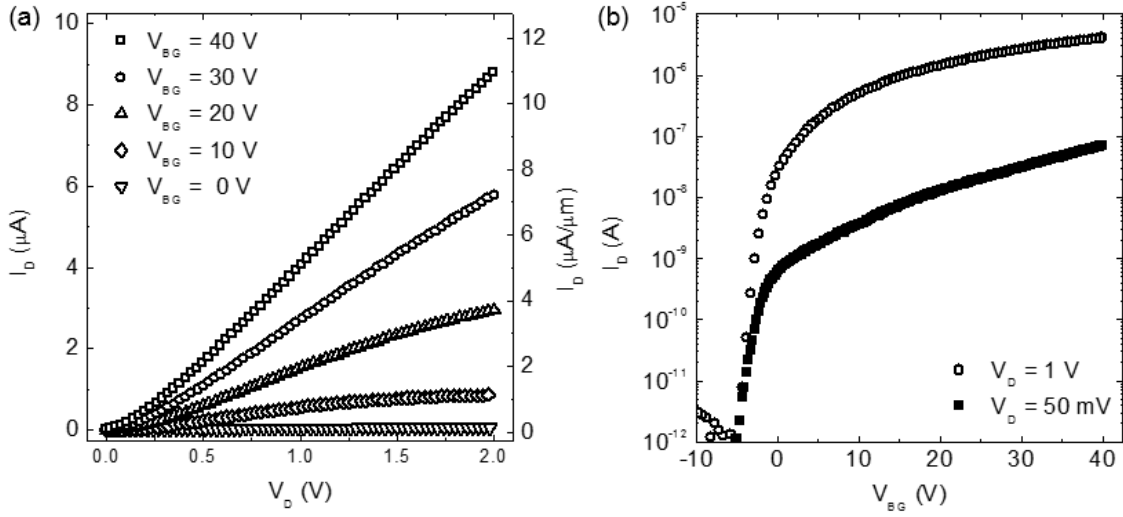
Figure 2.7   (a) I_D vs V_D measured at different V_{BG} values. The super-linear behavior observed at low V_D suggests the presence of a Schottky barrier at the metal-MoSe$_2$ contact. (b) I_D vs V_{BG} traces measured at $V_D = 50$ mV (solid squares), and $V_D = 1$ V (open circles) with $I_{ON}/I_{OFF} > 10^6$ at $V_D = 1$ V. Reprinted from S. Larentis *et al.* Appl. Phys. Lett 101, 223104 (2012), Ref. [5], with the permission of AIP Publishing.

To further probe the electron injection in MoSe$_2$, Figure 2.8 shows two sets of output characteristics measured on the same two-point bottom gated MoSe$_2$ FET, swapping the drain and source contacts in each data set. For the same V_{BG} value, different I_D values are obtained depending on which physical contact is used as source. This asymmetry in I_D–V_D data further confirms the presence of a Schottky barrier at the metal-semiconductor contact. As a result, the electron injection depends not only to the device geometry, e.g. contact area, but also on the electric field across the metal/MoSe$_2$ interface, and therefore will be sensitive to MoSe$_2$ flake thickness, SiO$_2$ dielectric thickness, as well as gate and drain bias. Schottky barrier contacts are common place for other nanoelectronic devices, such as carbon nanotube (CNT) [71] and nanowire devices [72].
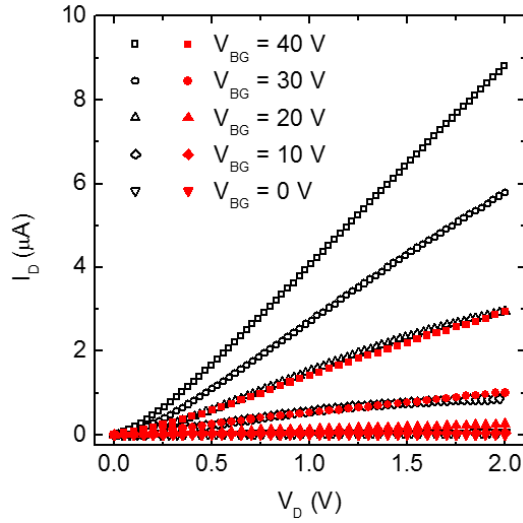
Figure 2.8 I_D vs V_D data obtained swapping drain and source contacts on the same device. The I_D values asymmetry when swapping the source and drain contacts is characteristic of FETs with Schottky contacts. Reprinted from S. Larentis *et al*. Appl. Phys. Lett 101, 223104 (2012), Ref. [5], with the permission of AIP Publishing.

The presence of non-ohmic contacts affects adversely the device performance by reducing the ON-state current and prevents a quantitative analysis of the device characteristics Most importantly renders the extraction of the intrinsic MoSe$_2$ mobility from the transfer characteristic difficult and unreliable. To probe the intrinsic mobility of MoSe$_2$ flakes, we fabricate four-point bottom-gated devices, which allow conductivity measurements without contributions from the contact resistance of the metal-semiconductor Schottky barriers. The inset of Figure 2.9(a) shows the AFM topography of a four-point MoSe$_2$ device. The outer contacts labeled S and D serve as source and drain, respectively. The inner contacts (V_1, V_2) used as voltage probes, and have a limited overlap with the MoSe$_2$ flake to minimize screening of the gate-induced charge density in the channel. The device's physical dimension defined as follows: drain-to-source channel length (L'), channel width (W), and center-to-center voltage probe separation (L), are marked in Figure 2.9(a) inset.
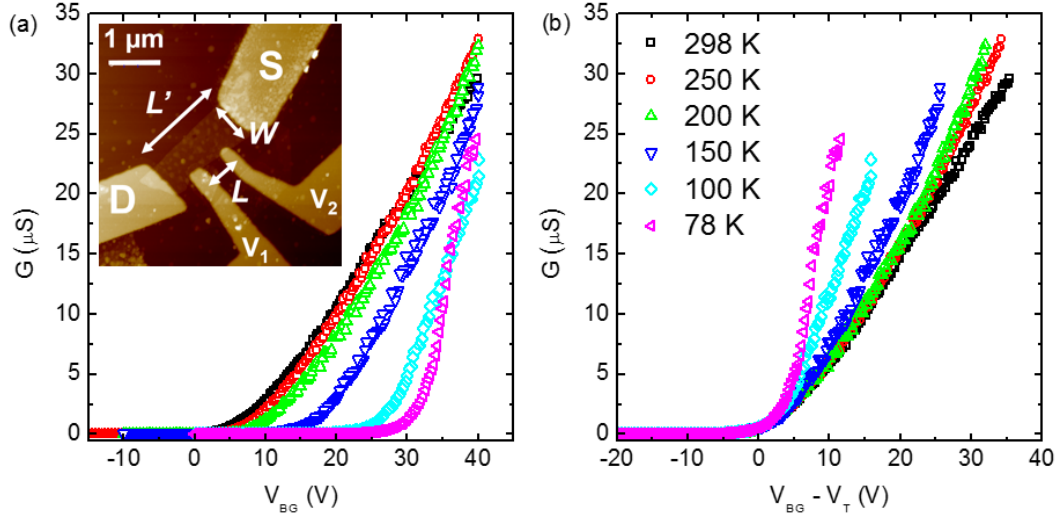
Figure 2.9 (a) G vs V_{BG} at different temperatures, ranging from 298 to 78 K in few-layer MoSe$_2$ sample 1. The data shows a linear dependence above threshold, combined with a V_T shift towards higher voltages when reducing T. Inset: AFM topography of a four-point device. The source (S), drain (D), voltage probes (V_1, V_2) and the device's physical dimensions (W, L, L') are marked accordingly. (b) G vs V_{BG}-V_T data for the same set of temperatures. Both panels share the same T legend, G data from Ref. [5].

The measured channel conductance (G) is defined as $G = I_D/(V_1–V_2)$. Figure 2.9(a) shows the G vs V_{BG} data measured at different temperatures values from 298 to 78 K, in few-layer MoSe$_2$ (5 nm-thick) sample 1, with device dimensions: $W = 0.80$ μm, $L = 0.46$ μm, $L' = 1.15$ μm. For V_{BG} values lower than a V_T, G remains vanishing. Above threshold, the G increases with V_{BG}, with an approximately linear dependence. As the temperature is reduced, V_T shifts progressively towards higher voltages. To offset the temperature dependent V_T shift, Figure 2.9(b) shows G vs V_{BG}-V_T, measured at different T values. Figure 2.9 data show a noticeable increase of the $dG/d(V_{BG}$-$V_T)$ slope with decreasing T. The field-effect mobility can be thus extracted as:

$$\mu_{FE} = \frac{dG}{d(V_{BG} - V_T)} \frac{1}{C_{ox} \, W/L} \qquad 2.1$$

where $C_{ox} = 12$ nF/cm^2 is the capacitance of the 285 nm-thick bottom SiO$_2$ dielectric. From a linear fit of G vs V_{BG}-V_T data, in the linear region at $V_{BG} > 0$ V, we obtain the $dG/d(V_{BG}$-$V_T)$. Figure 2.10(a) shows the mobility temperature dependence for three different samples,

50

fabricated with few-layer MoSe₂ flakes of comparable thickness 5-6 nm-thick. The room temperature μ_{FE} is as high as ~50 cm²/Vs, and increases almost four-fold when reducing the temperature to 78 K.
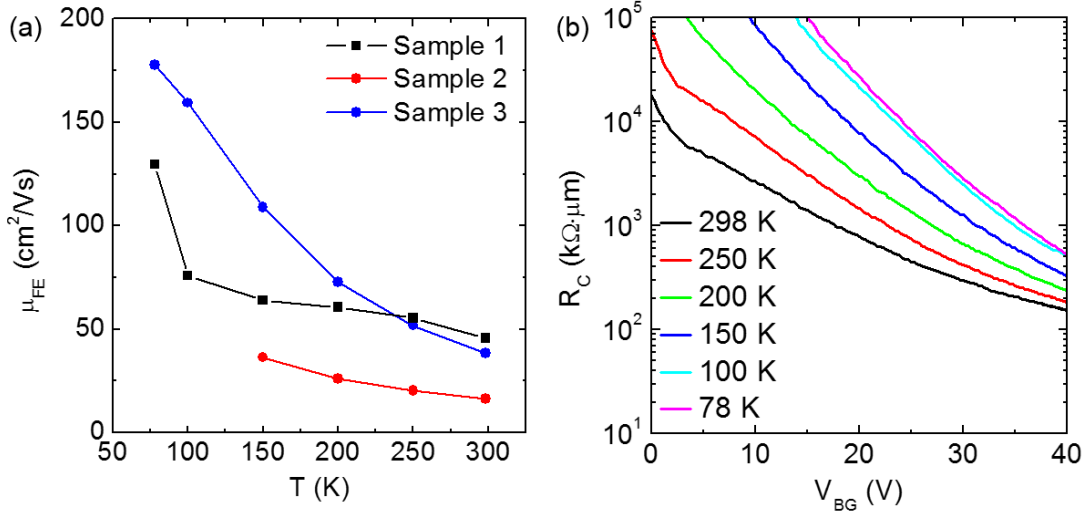
Figure 2.10 (a) μ_{FE} vs T for three different few-layer MoSe₂ devices. The RT μ_{FE} ~ 50 cm²/Vs, increasing up to 175 cm²/Vs at 78 K. Mobility data from Ref. [5]. (b) R_C vs V_{TG}, measured at different temperatures in few-layer MoSe₂ sample 1, revealing a strong V_{BG} dependence coupled with increasing R_C as T lowers.

Lastly, we address the contact resistance in our devices. Having measured the conductance using four-point devices, the specific contact resistance (R_C) can be extracted as follows:

$$R_C = \frac{W'}{2}\left(R_{2pt} - \frac{1}{G}\frac{L'}{L}\right) \qquad\qquad 2.2$$

where $R_{2pt} = V_D/I_D$ is the two-point resistance, and W' is the contact width, which in this case is flake width limited, and equal to W. Figure 2.10(b) shows the temperature dependence of R_C vs V_{BG}. At RT R_C = 150 kΩ·μm at V_{BG} = 40 V increasing to > 10 MΩ·μm as V_{BG} ~ 0 V. Reducing T leads to an increase in contact resistance, particularly at lower V_{BG}, consistent with reduced thermionic emission at the contacts. The strong V_{BG} dependence of the contact resistance provides further evidence for the presence of a

51

Schottky barrier at the metal/MoSe$_2$ interface, an obstacle which we will have to be overcome to improve FET performance, e.g. increase the ON-current.

2.2.2.2 MoS$_2$

The electrical characterization of top-contact, bottom-gate, few-layer MoS$_2$ FETs is conducted using etched Hall bar devices, as shown in Figure 2.11(a). The measurement technique for both the two- and four-point characterization is detailed in the previous section. The Hall bar of Figure 2.11(a) is fabricated using a 4.5 nm-thick (~ 7 layers) MoS$_2$ flake, exfoliated from natural MoS$_2$ crystals (SPI Inc.), with $W = 4$ μm, $L' = 10$ μm and $L = 4.5$ μm. Figure 2.11(b) shows I_D vs V_{BG} data measured between S, D contacts marked in Figure 2.11(a). The output characteristics data show similar features to MoSe$_2$ based devices, namely linear characteristic with super-linear behavior at low V_{DS} [Figure 2.11(a)]. These findings suggest that even MoS$_2$-based devices are characterized by Schottky barriers at the metal-TMD interface. In our investigation, we examined the following metal contacts stacks: Ti-Au (5-100 nm) and Mo-Ti-Au (20-5-50 nm), both showing similar results. Results in literature show that incrementally better results in terms of peak I_D can be obtained scaling the Ti layer thickness, until this layer completely removed, leaving a sole Au contact [54]. Transfer characteristics, shown in Figure 2.11(b), for $V_D = 50$ mV and $V_D = 1$ V, exhibit at clear n-type behavior, with $V_T \cong$ -10 V (obtained extrapolating the I_D vs V_{BG} linear region to $I_D = 0$ at $V_D = 50$ mV). Considering all devices tested, V_T values typically range between -10 and -30 V, suggesting flakes are generally unintentionally n-type doped. Values of the I_{ON}/I_{OFF} ratio, measured for transfer characteristics at $V_D = 1$ V, ranges between 10^5-10^6, a result consistent with what observed in MoSe$_2$ based devices.

52
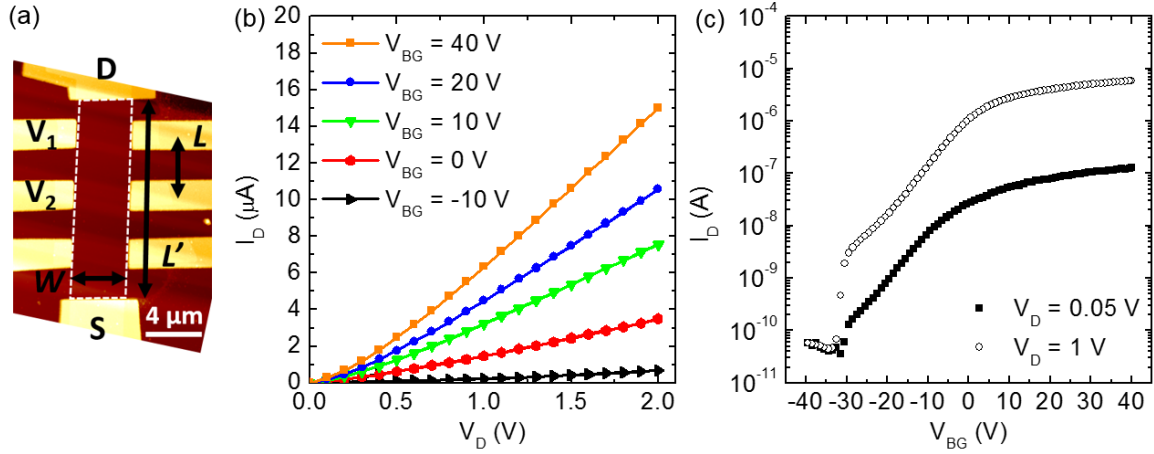
Figure 2.11 (a) AFM topography of a few-layer MoS$_2$ Hall bar. The drain (D), source (S), voltage probes (V_1, V_2), and the device's physical dimensions (W, L, L') are marked accordingly. (b) I_D vs V_D measured at different V_{BG} values. The super-linear behavior at low V_D is consistent with Schottky barrier contacts. (c) I_D vs V_{BG} traces measured at $V_D = 50$ mV (solid squares), and $V_D = 1$ V (open circles), with $I_{ON}/I_{OFF} > 10^5$ at $V_D = 1$ V.

As described in the previous section four-point conductance measurements allow to decouple contact resistance contributions and extract the intrinsic field-effect mobility. Figure 2.12(a) shows the AFM topography of the device structure, S and D contacts are marked along with the lateral contacts V_1, V_2 used as voltage probes. This Hall bar structure allows us to measure G using different sets of voltage probes. Different G vs V_{BG} datasets measured using different sets of voltage probes are consistent with each other, suggesting the device is homogenous. This allows to focus the analysis only on one set of voltage probes. Figure 2.12(a) shows a set G vs V_{BG}-V_T data measured at different T, revealing a significant increase of dG/d$(V_{BG}$-$V_T)$ with decreasing T, down to the lowest temperature (T = 4 K). The conductance is plotted as function of V_{BG}-V_T to account for the temperature dependent V_T shift, as also observed in MoSe$_2$ samples [Section 2.2.2.1] Figure 2.12(b) shows the μ_{FE} data extracted from Figure 2.12(a) data using Equation 2.1, assuming C_{ox} = 12 nF·cm^{-2}, for a 285 nm SiO$_2$ bottom gate dielectric. The RT μ_{FE} = 55 cm^2/Vs and shows a tenfold increase when the temperature is lowered to T = 4 K.
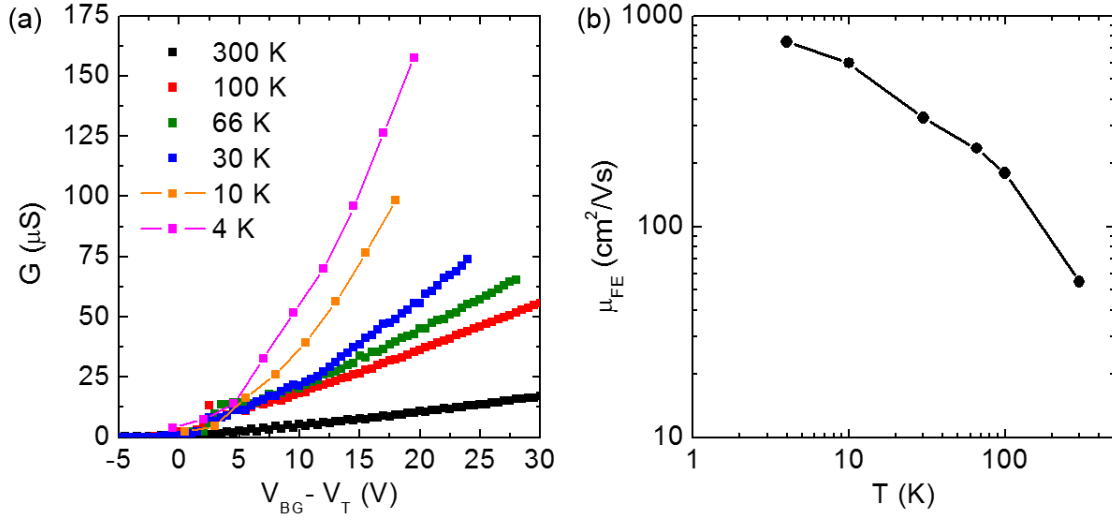
Figure 2.12 (a) G vs V_{BG}-V_T measured at different temperatures, ranging from 300 to 4 K. Conductance data shows a largely linear dependence above threshold. (b) μ_{FE} vs T extracted from panel (a) data.

2.2.2.3 MoTe₂

Top-contact, bottom-gate, few-layer MoTe₂ FETs discussed in this section are fabricated using MoTe₂ flakes exfoliated from bulk material grown at Princeton University by Prof. Cava group. Another set of devices fabricated using exfoliated MoTe₂ flakes obtained from commercially available crystals (2Dsemiconductors.com) showed similar results. Figure 2.13 shows the output and transfer characteristics measured at RT in a 6 nm-thick (~ 9 layer) MoTe₂ two-point device, with W = 3.9 μm and L' = 3.1 μm, using the same measurement technique presented in Section 2.2.2.1. Figure 2.12(a) shows linear I_D vs V_D measured at V_{BG} > 0 V. The absence of non-linearity hints to a lower Schottky barrier height at the metal-MoTe₂ contact, consistent with the narrower gap of MoTe₂ [Table 1.2]. Figure 2.12(b) shows I_D vs V_{BG} measured at V_D = 0.1, 1 V, for two samples fabricated with Ni and In contacts, using MoTe₂ flakes with same thickness and W/L; ON-currents in both devices are comparable. Both transfer characteristics present an ambipolar behavior, with contacts injecting electrons V_{BG} > -20 V (n-branch), and holes for V_{BG} < -20 V (p-branch). This result is in contrast with the unipolar behavior observed in MoSe₂ and MoS₂ FETs.

54

The ambipolar transfer characteristic may result from the MoTe$_2$'s narrower gap compared to MoS$_2$ and MoSe$_2$ [Table 1.2], coupled with the metal Fermi level pinning close to mid-gap [61]. Several other contact metal stacks have been tested: V, Ti-Au, Pd, Ir, all showing lower ON-currents as compared to In or Ni contacted devices.
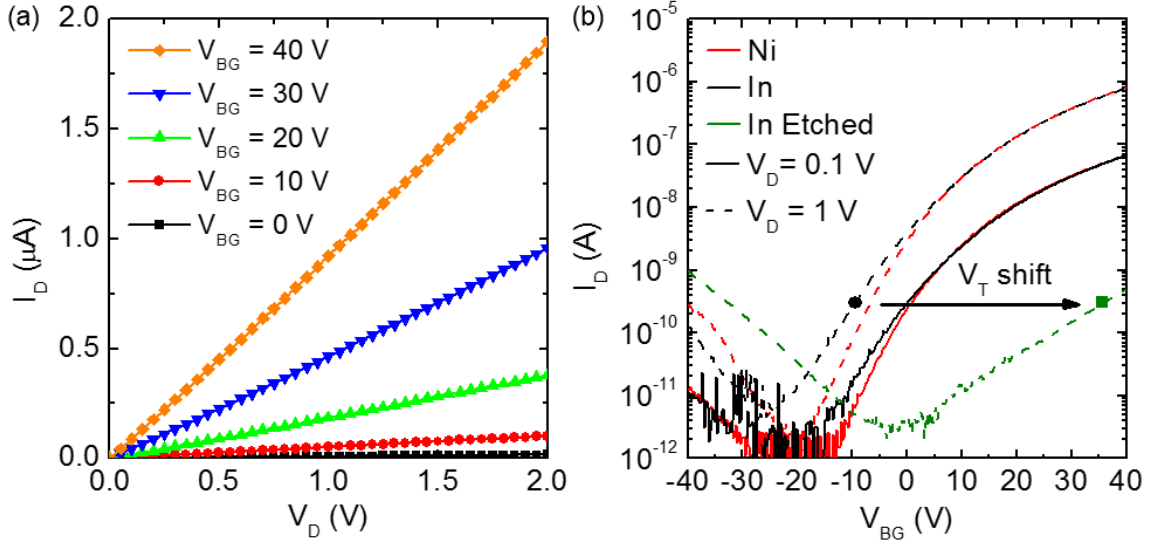
Figure 2.13 (a) I_D vs V_D measured at different $V_{BG} > 0$ V. (b) I_D vs V_{BG} measured at $V_D = 0.1$ V (solid) and $V_D = 1$ V (dashed), using a Ni (red traces), or In (black traces) contacted devices. I_D vs V_{BG} measured in the same In contacted device after partial etching at $V_D = 1$ V (green trace), note the significant I_D reduction.

A third set of I_D vs V_{BG} data, presented in Figure 2.12(b) (green trace), correspond to the same In contacted device [Figure 2.12(b) (black trace)] after half of the channel width has been etched away, using Cl$_2$ RIE. After etching the transfer characteristic presents an evident n-branch peak I_D reduction, while it shows a modest increase in the p-branch peak I_D. Comparing the I_D vs V_{BG} n-branches taken at $V_D = 1$ V before and after etching and defining a V_T at a fixed $I_D = 0.3$ nA, we observe a ~50 V V_T shift after etching. Such significant impact of etching on MoTe$_2$ hints to the environmental instability of the etched material. We speculate that either the etching species or the exposure to atmosphere after the etching process degrades the material, significantly deteriorating the electrical response.
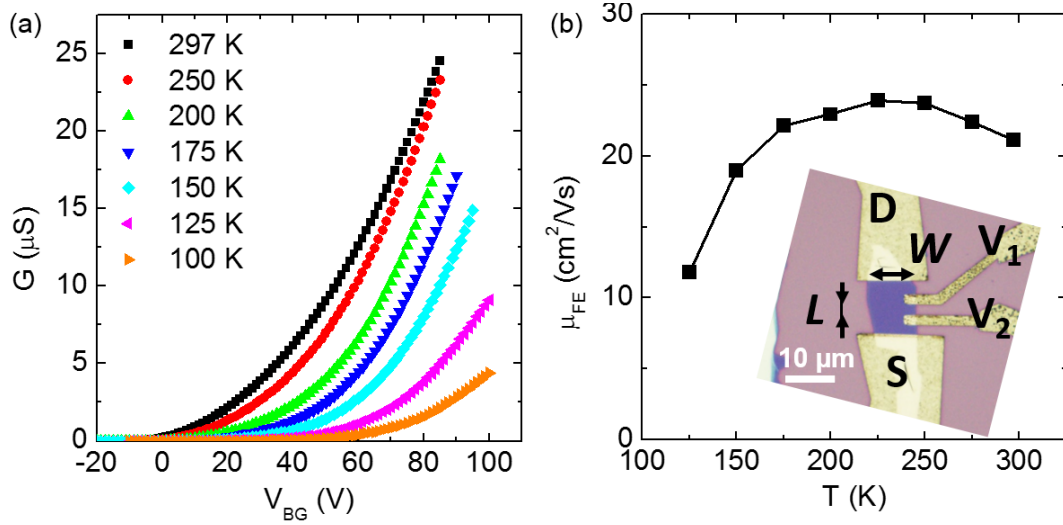
Figure 2.14   (a) G vs V_{BG} measured at different temperatures, ranging from 300 to 100 K. The data shows a decreasing dG/dV_{BG} for $T > 200$ K. (b) μ_{FE} vs T extracted from the data in (a). Inset: optical micrograph, where drain (D), source (S), voltage probes (V_1, V_2), and the device's physical dimensions (W, L) are marked accordingly.

To avoid the ON-current degradation described in Figure 2.13(a), four-point MoTe$_2$ FETs are fabricated using flakes that present a single, uniform terrace not requiring etching. An optical micrograph of a four-point, In contacted, few-layer MoTe$_2$ sample is shown in Figure 2.14(b), where $W = 10$ μm, $L = 4.4$ μm. Figure 2.14(a) shows G vs V_{BG} measured as function of temperature between 300 and 100 K, for the n-branch ($V_{BG} > 0$ V). Surprisingly, in this instance the temperature dependence of $dG/d(V_{BG}-V_T)$, does not follow a monotonic trend, while G vs V_{TG} data show a T-dependent V_T shift, comparable with what observed in MoSe$_2$ and MoS$_2$ devices [Sections 2.2.2.1, 2.2.2.2]. Figure 2.14(b) shows the field-effect mobility temperature dependence measured between RT and 125 K, extracted using Equation 2.1 assuming $C_{ox} = 12$ nF·cm^{-2} for a 285 nm SiO$_2$ bottom gate dielectric. The RT electron $\mu_{FE} = 22$ cm^2/Vs is comparable to the lower end μ_{FE} measured in MoSe$_2$ samples [Figure 2.10]. Figure 2.14(b) data show a μ_{FE} that increases as the temperature is lowered, but at $T < 225$ K the μ_{FE} vs T trend reverses, and the μ_{FE} shows a rapid decrease as the T is lowered. This μ_{FE} vs T trend is in contrast with results obtained from similar top-contact, bottom-gate MoSe$_2$ and MoS$_2$ samples.

2.2.3 Field-effect mobility temperature dependence

Characterizing the intrinsic electron field-effect mobility of all few-layer molybdenum based TMDs allows to: (i) assess the material electrical quality, (ii) determine the highest mobility molybdenum based TMD, and (iii) compare measured mobilities with bulk TMDs and other known semiconductors (e.g. Si). Aside from the technological relevance, extracting the μ_{FE} temperature dependence allows to investigate scattering mechanisms that limit mobility at different temperatures.

Figure 2.15 summarizes all the μ_{FE} data measured in few-layer molybdenum based TMDs samples, fabricated using a top-contact, bottom-gate architecture. Few-layer MoSe$_2$ and MoS$_2$ samples show the highest RT μ_{FE} ~50 cm^2/Vs, which is about 50% lower if compared to bulk samples [Figure 2.2]. Few layer TMDs show moderate mobilities at RT, and at this stage are no match for bulk Si or graphene [Figure 2.3]. However μ_{FE} values are significantly larger than what has been measured in organic semiconductors [60].
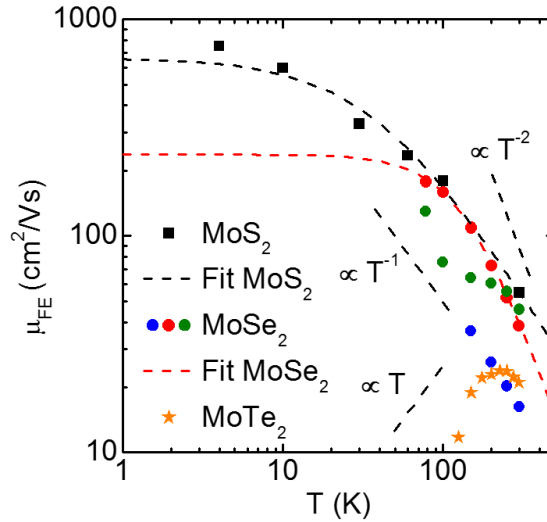
Figure 2.15 μ_{FE} vs T extracted from bottom-gate, top-contact devices based on few-layer MoS$_2$, MoSe$_2$ [5], and MoTe$_2$ (solid symbols) samples. A fit of the experimental data to Equation 2.3 is shown for MoS$_2$ and MoSe$_2$ (highest mobility dataset only) μ_{FE} data. A guide for the eye shows T, T^{-1} and T^{-2} power laws.

In a 2DES, charged impurity scattering leads to a temperature independent mobility in the degenerate limit, as in the case of graphene [73]–[75]. In a non-degenerate 2DES impurity scattering leads to a mobility $\propto T$ [74], [75]. At a given n the 2DES is degenerate (non-degenerate), i.e. the chemical potential is above (below) the band edge, when $T \ll$ ($\gg$) $T_F = \epsilon_F/k_B$; where $\epsilon_F = n/g_{2D}$ and g_{2D} is the 2D density of states; for a spin degenerate system $g_{2D} = m^*/\pi\hbar^2$. At T close to RT the mobility temperature dependence is dominated by phonon scattering, and follows a $T^{-\lambda}$ power law, where the power law exponent (λ) captures the dominating scattering mechanism. Acoustic phonon scattering is associated with $\lambda = 1$, while optical phonon scattering, including polar optical phonons, determine a stronger T-dependence ($\lambda > 1$) [76]. Considering contributions from charged impurity scattering (μ_{imp}) for a degenerate 2DES, and phonon scattering (μ_{ph}) expressed by a power law ($\propto T^{-\lambda}$), summed according to Matthiessen's rule, we obtain a functional fit of the form:

$$\mu(T) = \frac{1}{\dfrac{1}{\mu_{imp}} + \dfrac{1}{\mu_{ph}(T)}} = \frac{1}{\dfrac{1}{\mu_{imp}} + aT^{\lambda}} \qquad 2.3$$

The dashed lines in Figure 2.15 are fits using Equation 2.3 to MoS$_2$ and MoSe$_2$ (highest mobility sample only) μ_{FE} data. At high temperatures ($T > 77$ K for MoSe$_2$ data, $T > 30$ K for MoS$_2$ data) phonon scattering dominates and field-effect mobility data follow a power law dependence ($T^{-\lambda}$). Equation 2.3 fit yields $\lambda = 1.2$ for MoS$_2$ data, suggesting that acoustic phonon scattering dominates in this sample, and $\lambda = 2.2$ for MoSe$_2$ data revealing a stronger temperature dependence compared to MoS$_2$ data, indicative of optical phonon scattering. A higher λ is consistent with: (a) observations in bulk MoS$_2$ and MoSe$_2$ samples where $\lambda = 2.5$ is obtained from the Hall mobility temperature dependence data [Figure 1.3] and (b) recent literature reports of μ_{FE} measured in hBN encapsulated, few-layer MoS$_2$ ($\lambda = 2.4$) and MoSe$_2$ ($\lambda = 1.9$) samples [77]. Consistent with the model we introduced at temperatures lower than 30 K the MoS$_2$ mobility temperature dependence weakens, revealing a near temperature independent mobility limited by charged impurity scattering.

The MoTe$_2$ field-effect mobility temperature dependence data cannot be interpreted in the same framework used for MoS$_2$ and MoSe$_2$. The μ_{FE} temperature dependence is non-monotonic and presents two different T dependent regimes. At first μ_{FE} increases as T is decreased (225 K < T < 300 K), suggesting a phonon scattering limited regime in this T range. At T < 225 K the trend reverses and μ_{FE} begins to decrease as T is decreased, which may indicate a temperature activated regime associated with disorder, or a behavior consistent with a high impurity density sample in the non-degenerate limit ($\mu_{FE} \propto T$). In either case, this behavior underscores a lower electrical quality of the MoTe$_2$ flakes compared to MoS$_2$ and MoSe$_2$ flakes, which compounded with MoTe$_2$ environmental sensitivity, as revealed by etching test [Section 2.2.2.3], indicates that particular care may be required in the fabrication of MoTe$_2$ based devices to probe the intrinsic properties of the material. Chapter 5 discusses in more detail the MoTe$_2$ environmental sensitivity.

2.3 BOTTOM-CONTACT, DUAL-GATE ARCHITECTURE

In this section, we describe the fabrication and the electrical characterization of monolayer MoS$_2$, mono- and bilayer MoSe$_2$ FETs fabricated using a dual-gate, bottom-contact architecture. To fabricate a bottom-contact, dual-gate devices two key ingredients are needed: a dielectric compatible with molybdenum based TMDs and a reliable technique to transfer 2D layers on top of the contacts, rather than depositing the metal contacts on the TMDs, as described in Section 2.2.1.

Two-dimensional layers transfer techniques have evolved over time, and are generally classified as: (i) wet, where etchants are used to remove the SiO$_2$ layer on top of which flakes are exfoliated, freeing the flake and a previously spun polymer membrane, the membrane supporting the flake is subsequently aligned to the target using a water droplet; (ii) dry, when no etchants are used and flakes are either directly exfoliated on a polymer [Section 4.2], [78] or directly picked up from the SiO$_2$/Si substrates [Section 2.3.1] [79], and aligned to the target without water.

To integrate Mo-based TMD FETs using a dual-gate, bottom-contact architecture we chose hexagonal boron nitride as our dielectric. Hexagonal boron nitride is 2D layered insulator, characterized by an atomically smooth and flat surface up to three times less rough than SiO_2, and presents an energy band-gap of 5.8 eV [80]. Its dielectric properties are comparable to SiO_2, with a dielectric constant (ε_{hBN}) ~ 3. Compared with our grown SiO_2 dielectrics, hBN shows greater dielectric strength ~ 0.8 V/nm [81]. The typical dielectric strength of our thermally grown SiO_2 ~ 0.4 V/nm. This set of remarkable properties has rendered hBN the dielectric of choice for the fabrication of graphene based heterostructures, where hBN is employed as a gate dielectric or a tunneling barrier [78], [82]. Graphene devices encapsulated in hBN have shown enhanced carrier mobilities, both at room and cryogenic temperatures, compared to bottom-gated devices using SiO_2 dielectric, and dual-gated devices using high-κ metal oxides [78], [83].

The devices discussed in this section are fabricated using 10-20 nm-thick hBN dielectrics. Using hBN as top-gate dielectric allow us to probe a wider range of carrier densities and achieve better device performances in terms of ON-current, and contact resistance, particularly at low temperatures, thanks to the increased capacitance as compared to 285 nm-thick SiO_2 dielectrics [Section 2.2].

2.3.1 Device fabrication

The development of a bottom-contact, dual-gate architecture progressed through different device structures. From the least to most complicated, three different bottom-contact structures can be introduced: (#1) a dual-gate structure using a hBN top-dielectric and SiO_2 bottom-dielectric [Figure 2.16(a)]; (#2) a dual-gate, hBN encapsulated structure [Figure 2.16(b)], where the bottom-hBN is in series with the SiO_2 dielectric; both structures use a metal top-gate and a highly-doped Si bottom-gate, and (#3) a dual-gate, hBN encapsulated structure, with metal top- and bottom-gates [Figure 2.16(c)]. All three structures share a similar fabrication process, with increasing degree of complexity, where the main difference is the preparation of the bottom-gate stack. Device fabrication using a

bottom-contact, dual-gate architecture is a two-step process: first the bottom-gate stack and the bottom-contacts are patterned, then the top hBN/MX$_2$ stack is transferred onto the bottom-contacts.
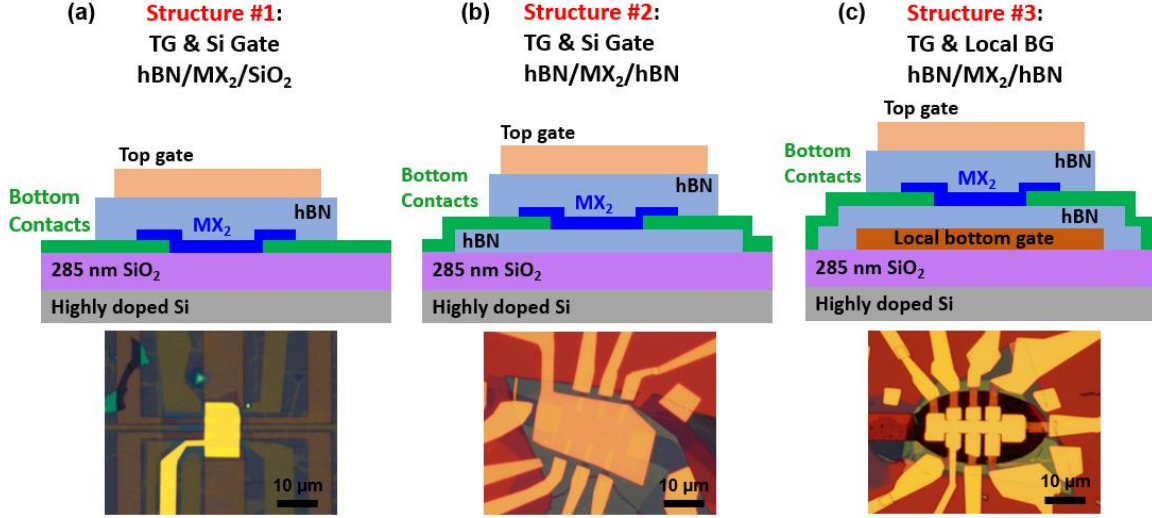
Figure 2.16: Cross-sectional schematic for different dual-gate, bottom-contact structures using: (a) hBN top-dielectric and SiO$_2$ bottom-dielectric, (b) hBN encapsulated structure, both with metal top-gate and Si bottom-gate. (c) hBN encapsulated structure, with metal top- and bottom-gate. Each panel shows an example optical micrograph of a sample fabricated using each structure.

The fabrication process for structure #3, the most complex, is summarized in Figure 2.17 using a series of schematics and optical micrographs detailing the different stages of the fabrication process. We begin from the bottom-gate stack, where a local metal bottom-gate is patterned on a 285 nm-thick SiO$_2$/Si substrate using EBL and e-beam metal evaporation (EBME), as shown Figure 2.17(f). Typical e-beam evaporated bottom-gate metal stacks are Cr-Pd and Cr-Pt (2-9 nm-thick), where Cr acts as the adhesion layer. Particular attention is paid to the cleanliness of the metal gate which is annealed in ultra-high vacuum (UHV) ($< 1 \times 10^{-8}$ Torr) at 350°C to remove organic residues. Figure 2.17(i) shows a hBN flake exfoliated from powder grown by T. Takahashi and K. Watababe's at NIMS [80], on a separate SiO$_2$/Si substrate. The TMDs exfoliation process detailed in Section 1.1.3.1 applies also to hBN. Exfoliated hBN flakes are generally large (up to 100

$\times$ 100 μm^2), and present clean and flat terraces. The individual flake topography is measured using AFM. Flakes selected to be used as top- and bottom-gate dielectrics are between 10 and 20 nm-thick. After exfoliation the hBN flakes are selectively detached from the substrate using a small contact area ($< 200 \times 200$ μm^2) hemispherical handle [Figure 2.17(a)], then aligned and released on the bottom-gate [Figures 2.17(b) and 2.17(c)]. The hemispherical handle is fabricated by drop casting of polydimethylsiloxane (PDMS) onto planar PDMS stamps bonded on glass. The resulting hemispherical structure is spin-coated with a polypropylene carbonate (PPC) adhesive layer [84], as shown in Figure 2.17(a). Different substrate temperatures (45-85°C) allow for pick-up and release of the desired flake or stack thereof, with or without detaching the PPC layer from its PDMS support [Figure 2.17(b) to (e)]. Once the hBN is released on the metal gate, PCC residues are first removed in acetone (> 30 min), then the stack undergoes a UHV anneal to remove organic residues [Figure 2.17(g)].

After the bottom dielectric is in place, a set of bottom-contacts is patterned using EBL and EBME, as shown in Figure 2.17(h). We note that in a bottom contact architecture, where the metal contacts are exposed for extended time to the atmosphere, only high work function (WF) metal contacts are suitable. In our investigation, we considered the following metals with WF > 5 eV [85]: Pd, Au, and Pt, which we assume to be largely immune from substantial surface oxidation. All deposited metals use a 3 nm Cr adhesion layer. The patterned metal contacts are 15-20 nm-thick. After metallization, the stack undergoes 350°C UHV anneal to remove organic residues, thus improve the metal-TMD interface quality. Pd and Pt contacts are typically preferred because of their ability to withstand vacuum anneal at temperatures up 400 °C. On the other hand, Au contacts when annealed in vacuum tend to form island and bubbles, detrimental for device fabrication. Anneals in forming gas ambient mitigate this issue. For structure #1 the bottom contacts are directly patterned on the SiO_2/Si substrate. For structure #2, hBN flakes are exfoliated onto SiO_2/Si substrates, then bottom contacts are patterned onto the exfoliated hBN.

Once the bottom-gate stack and contacts are fabricated, MoS_2 crystals from SPI Inc. or $MoSe_2$ crystals from HQ graphene and TENN XC are exfoliated on 285 nm-thick

SiO$_2$/Si substrates. As described in Section 1.1.4 and 1.1.5, mono- and bilayer MX$_2$ flakes are identified using optical contrast, Raman spectroscopy and PL [Figure 2.17(j)]. Using a PCC/PDMS stamp [Figure 2.17(a)], we first pick-up a hBN flake (10-15 nm), which will act as a top-dielectric [Figures 2.17(b) and 2.17(i)]. We then proceed to align the top dielectric to the exfoliated MX$_2$ and bring them into contact [Figure 2.17(c)]. Thanks to vdW bonding that develops between the two 2D surfaces we are able to pick-up the mono- or bilayer MX$_2$ from the SiO$_2$ surface, using a 45°C substrate temperature [Figures 2.17(d) and 2.17(k)]. The hBN/MX$_2$ stack is then aligned and transferred onto pre-patterned high WF metal contacts, releasing the PPC layer on the substrate at temperatures > 85°C [Figure 2.17(e)]. The released PPC layer is then dissolved in acetone (> 30 min). A variation of this process consists in first releasing the hBN layer on the MX$_2$ layer, with or without PPC. The PPC, if released, is dissolved in acetone. The newly formed hBN/MX$_2$ stack on SiO$_2$/Si is UHV annealed at 350°C to promote vdW bonding, picked-up again using a new PPC/PDMS handle, and then released on the bottom-contacts as described above.

In general, flakes can be released on an arbitrary substrate or a different flake, with or without PPC at a substrate temperature of 85 °C. Tuning contact time, i.e. for how long PPC and substrate are in contact for, contact force and the hemispherical handle curvature radius allows to achieve either result. Longer contact time, higher contact force and larger curvature radius tent to ease the release of the flake along with PPC.

The completed stack undergoes a 350°C UHV anneal to remove organic residues and reduce the bubble density [Figure 2.17(l)]. It should be noted that this transfer technique allows to completely encapsulate MX$_2$ flakes, avoiding environmental degradation and organic molecules contamination. The whole transfer process avoids for any organic material to come in to contact with the MX$_2$, a key advantage to limit contamination over wet transfer techniques [78]. Finally, a Cr-Au (5-50 nm) top-gate, defined in alignment with the bottom contact electrodes, and contact extensions are patterned using EBL and EBME, completing the device structure [Figure 2.17(m)].
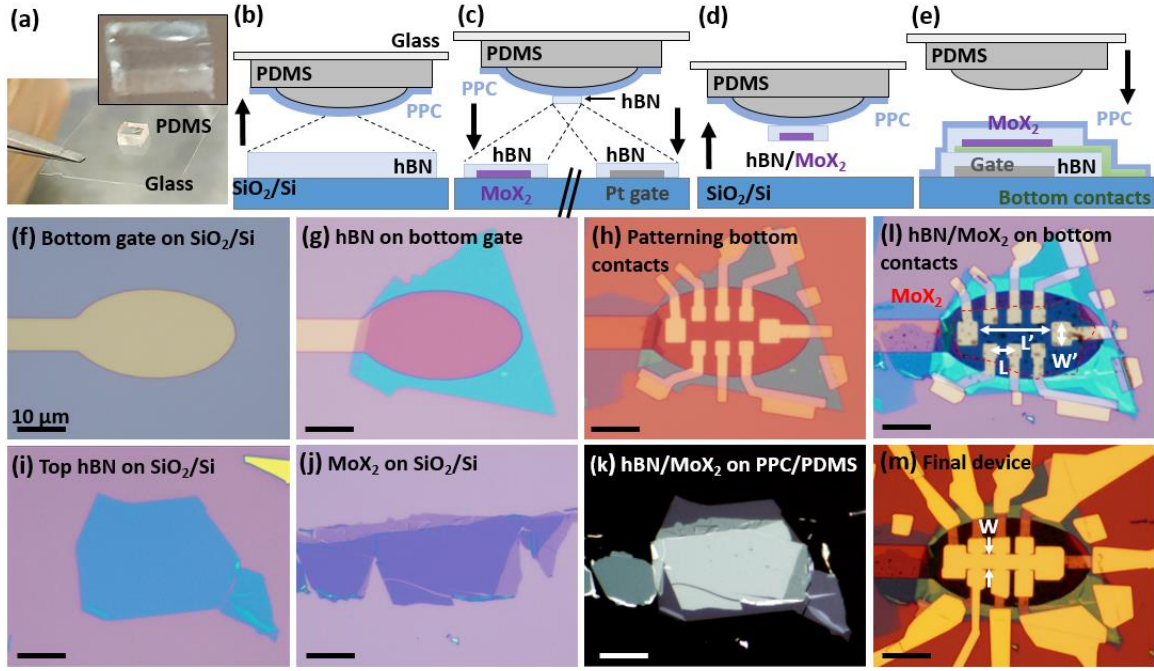
Figure 2.17: (a) PDMS micromechanical handle bonded on glass, with inset showing the handle's hemispherical shape. Cross-sectional schematic showing: (b) hBN pick-up using a PPC/PMDS coated handle; (c) top hBN contacting MX_2 at 45°C prior to pick-up, bottom hBN released on the bottom-gate; (d) hBN/MX_2 pick-up from the exfoliation substrate; (e) hBN/MX_2 stack released on the bottom contacts, along with the PPC layer. Optical micrographs showing: (f) Cr-Pd (2-9 nm) bottom-gate patterned on a SiO_2/Si substrate; (g) hBN bottom dielectric (~20 nm) transferred onto the local bottom-gate; (h) Cr-Pd (3-12 nm) bottom-contacts patterned onto the bottom dielectric; (i) top hBN dielectric and (j) bilayer $MoSe_2$ exfoliated on SiO_2/Si before pick-up with PPC/PDMS stamps; (k) hBN/$MoSe_2$ stack imaged on PPC/PDMS after sequential pick-up; (l) hBN/$MoSe_2$ stack released on bottom-contacts, after PCC removal and anneal; (m) final device after patterning of top-gate and metal contacts extension, Cr-Au (5-50 nm). In panels (l) and (m), the device's physical dimension (W, W', L, L') are marked accordingly.

2.3.2 Device fabrication using CVD grown TMDs

Section 2.3.1 described the fabrication process used to prepare bottom-contact, dual-gate samples, employing exfoliated flakes. While exfoliated flakes are useful to fabricate exploratory devices they clearly cannot be employed in high-volume

64

manufacturing. Large area growth of molybdenum-based TMDs, as described in Section 1.1.3.2, may eventually allow to obtain wafer scale MX_2 layers.
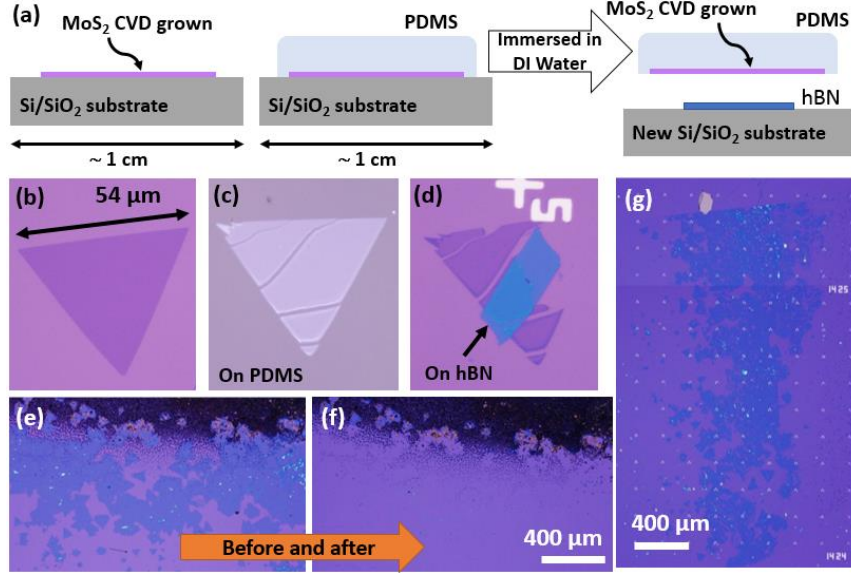
Figure 2.18: (a) Schematic showing the process used to transfer CVD grown MoS_2 to another arbitrary surface. Optical micrographs showing: (b) single CVD grown monolayer MoS_2 triangular domain; (c) the same domain transferred on PMDS after immersion in DI water; (d) MoS_2 triangular domain transferred on a hBN flake previously exfoliated on different SiO_2/Si substrate; (e) pseudo-continuous monolayer MoS_2 layer on SiO_2/Si after growth; (f) same area in shown (e) after the MoS_2 is removed peeling off the PDMS; (g) mm size monolayer MoS_2 film transferred on another SiO_2/Si substrate.

While in this dissertation we will not describe fabrication techniques aimed to directly take advantage of the large area growth, it is of interest to integrate CVD grown films in the existing fabrication process [Section 2.3.1]. Using the same fabrication process for exfoliated and grown flakes allows for an electrical quality comparison of each type of flakes. In the following, we will describe a water-based method to transfer grown MX_2 layers from the growth substrate onto a different SiO_2/Si substrate. Once the MX_2 film is transferred on different substrate specific domains may be picked up using a hemispherical handle, similarly to exfoliated flakes. In a different scenario the whole MX_2 film could be

transferred on SiO_2/Si substrate prepatterned with bottom contacts. The grown film could also be transferred only to avoid the thicker domains that typically accompany powder growth [Figure 2.18(e)].

A simple process relying on water soaking allows to separate the MoS_2 from the original growth substrate. Figure 2.18(a) schematic describe the transfer process. A PDMS film (~5 x 5 mm^2) is set on the grown MoS_2, the whole PDMS/MoS_2/SiO_2/Si stack is soaked in water between 30 min to 1 hr. The hydrophilic nature of SiO_2, allows water to diffuse between SiO_2 and MoS_2, aiding the layer separation. Once the stack is removed from the water, and dried, the PMDS is peeled off easily removing the MoS_2 film, as shown in Figure 2.18(f). The MoS_2/PDMS can now be brought in contact with the target substrate using a micromanipulator, to release the large area MoS_2 [Figure 2.18(g)]. Figures 2.18(b) to 2.18(d) show a specific triangular domain during the transfer process, from the original growth SiO_2/Si substrate, to the target hBN/SiO_2/Si substrate.

2.3.3 TMD FETs electrical characterization

In this section, we report the electrical characterization of bottom-contact, dual-gate FETs based on monolayer MoS_2, mono-, and bilayer MoS_2. Hall-bar samples are characterized using a parameter analyzer in two-point configuration to probe output and transfer characteristics, and in four-point configurations to probe the gated four-point conductance (resistance) temperature dependence, using the same measurement technique discussed in Section 2.2.2. Low-current, low-frequency lock-in techniques are used to probe the Hall resistance as function of the perpendicular B-field. Wirebonded samples are probed in Oxford He cryostat using variable temperature insert, where the temperature can be controlled between 300 K and 1.5 K. The cryostat is fitted with a superconducting magnet, allowing to probe samples up to $B = 14$ T. For each material system, several devices have been investigated showing analogous results. Table 2.1 and 2.2 provide a list of key MoS_2 and $MoSe_2$ samples discussed in Section 2.3.3.1 and 2.3.3.2, respectively.
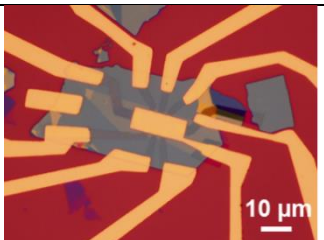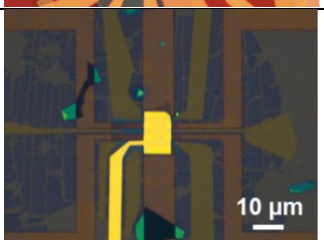
Sample name	Other name	Flake	W/L	L'/L	W' (μm)	C_{TG} (nF/cm^2)	Optical Micrograph
S-1	jhBN A_16	Exfoliated	2	3.8	3	331	
S-2	jhBN A_24	Exfoliated	2	3.3	7	494	
S-3	Pt_1	Grown	1.8	2.4	8	277	

Table 2.1: List of monolayer MoS$_2$ based devices presented in Section 2.3.3.1, detailing the nature of monolayer flake (exfoliated/grown), device physical dimensions [Figure 2.21(a)] and C_{TG}. An optical micrograph of each sample is included.
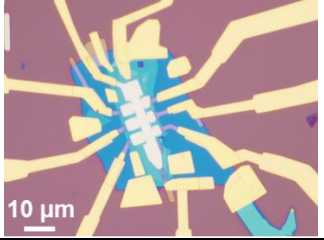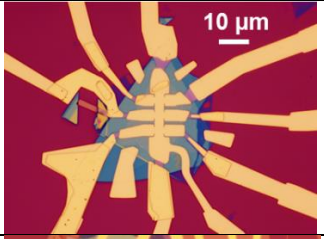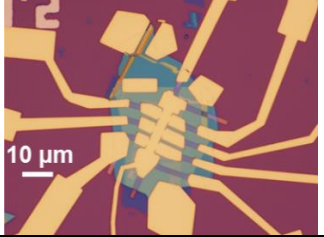
Sample name	Other name	Type	C_{TG} (nF/cm^2)	Optical Micrograph
Se-1	jhBN_A_45_A	Bilayer	197	
Se-2	jhBN_121	Monolayer	335	
Se-3	jhBN_A_45_B	Bilayer	246	
Se-4	jhBN_66	Bilayer	185	

Table 2.2: List of mono- and bilayer MoSe$_2$ samples presented in Section 2.3.3.2, detailing the flake thickness and C_{TG}. All devices presented in this table, are characterized by the same physical dimensions: $W = 3$ μm, $L = 5$ μm, $L' = 15.5$ μm, $W/L = 0.6$, $L'/L = 3.1$, and $W' = 5$ μm [Figure 2.17(l) and 2.17(m)]. An optical micrograph of each sample is included.

2.3.3.1 Monolayer MoS₂

The monolayer MoS_2 samples presented in this section are fabricated using flakes exfoliated from SPI Inc. crystals [Figure 1.6(b)] or triangular domains grown by CVD [Figure 2.18], employing structure #1 and #2 presented in Figure 2.16. The metal contact of choice for MoS_2 based devices is Au, while also Pt contacts present low contact resistance, and are used in this study. Figure 2.19 shows the output and top-gate transfer characteristic measured at $V_{BG} = 0$ V in monolayer MoS_2 sample S-3, fabricated using CVD grown films utilizing device structure #1 with Pt contacts, with $W = 7.5$ μm and $L' = 9.5$ μm.
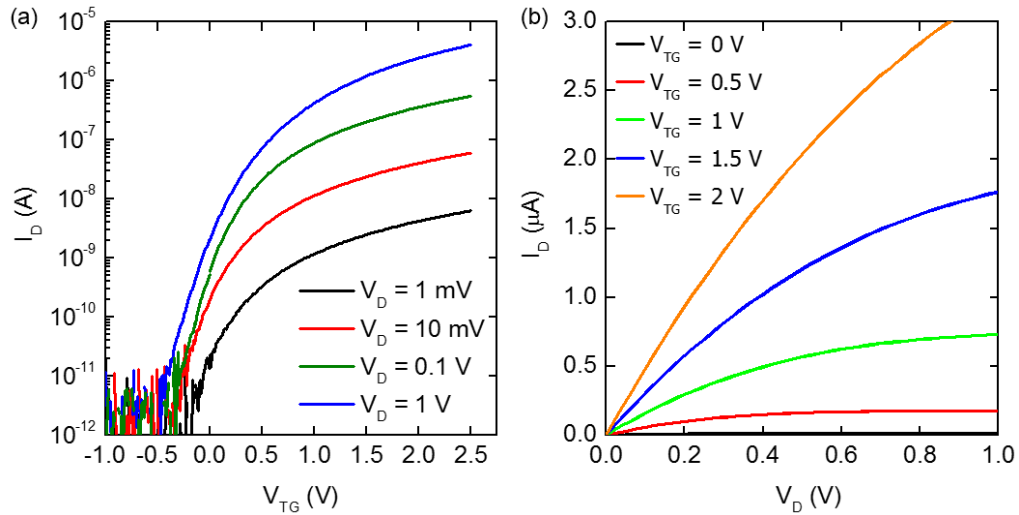
Figure 2.19   (a) I_D vs V_{TG} measured at different V_D values, showing proportional current scaling. (b) I_D vs V_D traces measured at different V_{TG}, showing absence of super-linear behavior at low V_D. All data are measured in monolayer MoS_2 sample S-3 at $V_{BG} = 0$ V.

The I_D vs V_{TG} data show clear *n*-type behavior, with $V_T \cong 0.5$ V (extracted from the I_D vs V_{TG} linear region at low V_D) and $I_{ON}/I_{OFF} > 10^6$ for $V_D = 1$ V [Figure 2.19(a)]. The insulating regime is achieved for negative V_{TG}, indicating flakes are likely unintentionally *n*-type doped, a finding consistent with previous measurements in top-contact, bottom-gate monolayer MoS_2 devices [58]. The absence of significant hysteresis and the repeatable characteristics, consistent with literature results [86], [87], confirm that the water-based

transfer method used to remove grown films from the growth substrate [Section 2.3.2], and the transfer process used to assemble the device [Section 2.3.1] do not affect the electrical properties of monolayer MoS₂. The output characteristics of Figure 2.19(a) show a linear I_D dependence at low V_D, which saturates at higher V_D. Figure 2.19 data suggest that Pt or Au bottom-contacts to MoS₂ may be ohmic or may present a small Schottky barrier at the metal-MoS₂ interface. The improved nature of the contacts, compared to top-contact, bottom-gate devices of Section 2.2.2.2, may stem from interplay of different factors: (i) the monolayer n-type unintentional doping, able to modulate the Schottky barrier width, (ii) the high-quality metal deposition, without employing any oxidizing adhesion layers (Ti, Cr), (iii) the improved mechanical contact, coupled with roughness control of the metal contact, (iv) reduction of organic residues, e.g. resist, thanks to dry transfer techniques, (v) and most importantly the increased capacitance of the top-gate, able to induce high carrier density in proximity of the metal-TMD junction, thus modulating Schottky barrier width.
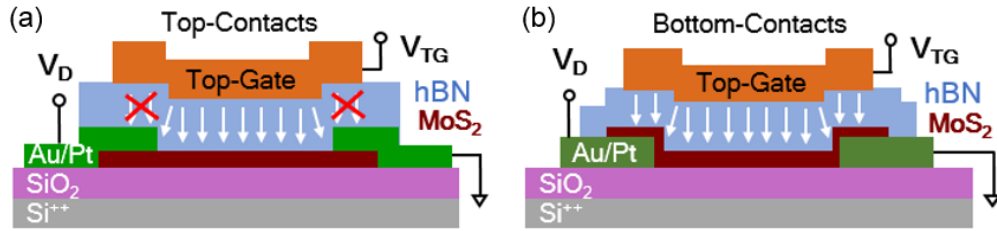
Figure 2.20 (a) Cross-sectional schematic for a top-contact, dual-gate device, where the top-gate cannot modulate the contact regions, because they are screened by the metal contacts. (b) Cross-sectional schematic for a bottom-contact, dual-gate device, where the top-gate modulates the contact regions.

The integration of a top-gate scheme is not exclusive to bottom-contact architecture. Examples in literature show the integration of top-gate stacks using high-κ dielectrics [57], [69] in top-contact devices, where the top-gate modulates only the channel region, while the contact regions are screened by the metal contacts [Figure 2.20(a)]. This approach typically yields large series resistance, degrading the device performance, unless access regions [70], contacts or channel are otherwise doped [88]. Oxygen deficient atomic layer deposited (ALD) high-κ dielectrics are known to significantly n-type dope the

channel material [69], [89]. Conversely our architecture allows the top-gate to modulate the electron concentration in both the channel and the contact regions [Figure 2.20(b)], effectively tuning the Schottky barrier width at the contacts to a degree in which the contact appears ohmic. While beneficial to the device's performance in reducing the contact resistance, gated Schottky barriers still influence the device operation in both ON and OFF state, i.e. contact are still not transparent.

Figure 2.21 shows summarizes the temperature dependent study conducted in monolayer MoS_2 sample S-2, fabricated using an exfoliated flake, utilizing device structure #2 and Au bottom contacts. Figure 2.21(a) shows on optical micrograph of the completed sample S-2, where the outline of the flake and the Au contacts are marked. An outline of the four-point measurement scheme is also provided defining D, S, V_1, and V_2 contacts. In all monolayer MoS_2 devices probed, the top-gate is patterned around the flake size, therefore W, the channel width is set by the flake size; W' on the other hand is determined by the flake or contact width whichever is the largest. Figure 2.21(a) clarifies the definition of device's physical dimensions, and values for the imaged sample S-2 are: $W = 11.6$ μm, $L = 5.8$ μm, $L' = 19.1$ μm and $W' = 7$ μm. Figure 2.21(b) I_D vs V_{TG} data measured at $V_D = 0.1$ V and $V_{BG} = 0$ V, display an apparent V_T shift (~ 1.5 V) as the temperature is reduced from 300 K down to 1.5 K while the peak I_D is largely unaffected; V_T is determined extrapolating the I_D vs V_{TG} linear region to $I_D = 0$. Gated conductance data of Figure 2.21(c) measured at $V_{BG} = 0$ V show a linear behavior and a significant increase of dG/dV_{TG} as the T is lowered, for V_{TG} above a conductance threshold (obtained from a linear extrapolation at $G = 0$), revealing a significant field-effect mobility increase as the temperature is lowered, consistent with what we observed in few-layer samples [Section 2.2.2].
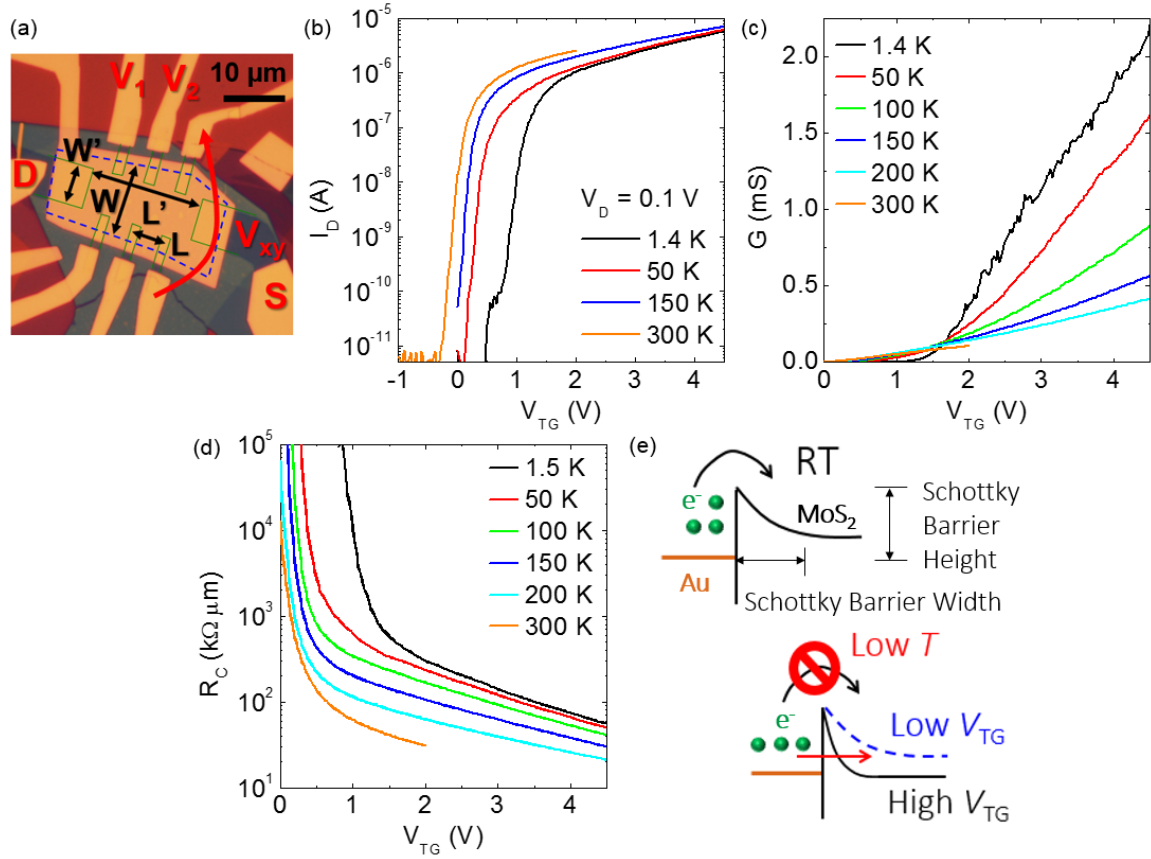
Figure 2.21 (a) Optical micrograph of bottom-contact, dual-gated monolayer MoS$_2$ sample S-2, highlighting the measurement scheme and the device dimensions. Outlines of different colors mark the Au contacts (green) and the monolayer MoS$_2$ flake (dashed blue). The device's physical dimensions (W, W', L, L') and the measurement scheme (D, S, V_1, V_2, V_{xy}) are marked accordingly. (b) I_D vs V_{TG} measured at $V_D = 0.1$ V, for different T down 1.5 K; V_T shifts as the temperature is reduced. (c) G vs V_{TG} traces measured at different T, showing a marked increase of $dG/d(V_{BG}-V_T)$ as T is reduced. (d) R_C vs V_{TG}, measured at different temperatures. All data are measured in monolayer MoS$_2$ sample S-2 at $V_{BG} = 0$ V. (e) Metal-TMD Schottky contact band diagram at RT and low T, when the thermionic emission is reduced and is compensated tuning Schottky barrier at higher V_{TG}.

Figure 2.21(d) shows R_C vs V_{TG} data at different temperatures calculated using Equation 2.2 from Figure 2.21(b) and (c) data. At all temperatures, R_C vs V_{TG} data reveal a strong V_{TG} dependence, consistent with a top-gate dependent electrostatic doping of the contact regions, which in turn modulates the metal-TMD Schottky barrier width, and

ultimately determine a V_{TG} dependent R_C [Figure 2.21(e)]. The temperature dependent increase of R_C when T is reduced from 200 K to 1.5 K, at $V_{TG} > 2.5$ V, is only four-fold, indicating that the Schottky barrier width modulation largely compensates for the reduced thermionic emission at low T, as schematically depicted by the metal-MoS$_2$ Schottky barrier diagram of Figure 2.21(e). At $T = 1.5$ K in sample S-2, R_C approaches 55 k$\Omega \cdot \mu$m, a value a decade lower than the R_C probed at $T = 78$ K in top-contact, bottom-gate few-layer MoSe$_2$ sample 1 [Figure 2.10]. Recently lower contact resistance values (3.8 k$\Omega \cdot \mu$m) have been measured in Co/hBN/MoS$_2$ contact stacks, however the lower R_C is enabled by a significant increase in the fabrication complexity, namely requiring monolayer hBN identification [90].

In summary a comparison of temperature dependent four-point studies indicate that a bottom-contact, dual-gate architecture is preferable over a top-contact, bottom-gate architecture for low temperature measurements of the intrinsic properties of TMDs, given the former consistently provides low temperature, low R_C contacts [91], a principle need for magnetotransport measurement described in Chapter 3. Obtaining low temperature, low R_C contacts allows us to measure devices using DC techniques at $V_D = 10$-100 mV, and low frequency, low current lock-in techniques. This compares to measurements carried out in top-contact, bottom-gate few-layer MX$_2$ samples [Section 2.2.2], where conductance measurements at low temperature, even at high V_D, are extremely difficult because of the high contact resistance, obtained using top-contacts.

Thus far we characterized our dual-gate devices only as function of the top-gate, while the bottom-gate remained grounded. In Figure 2.22 we present two-point transfer characteristics and four-point gated conductance measurements measured as function of V_{BG} while applying a fixed V_{TG}. Figure 2.22 data are measured at $T = 1.5$ K in monolayer MoS$_2$ sample S-1, fabricated using an exfoliated flake utilizing device structure #2 and Au contacts. The device's physical dimensions are $W = 6.8$ μm, $L = 3.3$ μm. Figure 2.22(a) shows I_D vs V_{BG} data measured at V_{TG} ranging between 2 and 5 V. The bottom-gate transfer characteristics are measured $V_{TG} > 2$ V, which correspond to a V_{TG} sufficient high to effectively "turn-on" the contacts regions at $T = 1.5$ K. As the V_{TG} is progressively

increased, we observe a negative V_T shift proportional to the positive V_{TG} bias, coupled with reduced contact resistance series effect as V_{TG} increases, i.e. increased ON-current for the same overdrive at higher V_{TG}.

Bottom-gated conductance measurements (G vs V_{BG}) obtained at different positive V_{TG} and $T = 1.5$ K, allow to decouple contact resistance effects, and display a similar negative threshold voltage shift proportional to V_{TG}. A variation in the threshold voltage can be explained as follows: a positive V_{TG} (> 2 V) induces an electron concentration in the channel proportional to the top gate capacitance. In order to restore the device at threshold, namely depleted of electrons, an opposite V_{BG}, proportional to bottom-gate capacitance (C_{BG}) is required. The threshold voltage extracted from a linear extrapolation to $G = 0$ of each G vs V_{BG} trace ($V_{BG,Threshold}$) of Figure 2.22(b), is plotted as function of V_{TG}, in the inset of Figure 2.22(b). The slope of a linear fit to the $V_{BG,Threshold}$ vs V_{TG} data correspond to $C_{TG}/C_{BG} = 30$, a result consistent with the thickness of the dielectrics used (top hBN thickness 8 nm, bottom hBN thickness 24 nm, bottom SiO$_2$ thickness 285 nm) assuming $\varepsilon_{hBN} \sim 3$.
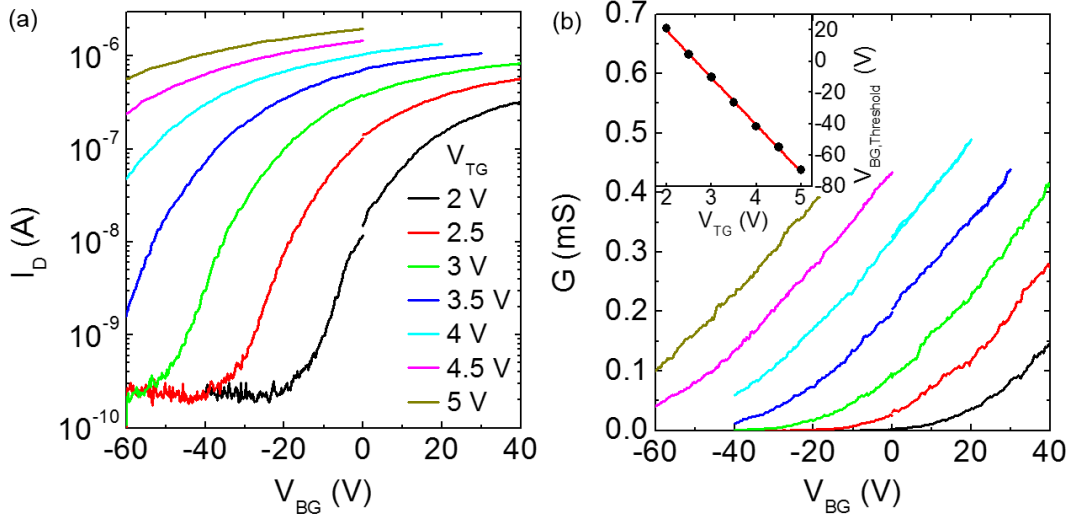
Figure 2.22 (a) I_D vs V_{BG} measured at different V_{TG} values, showing a V_T shift proportional to V_{TG}. (b) G vs V_{BG} traces measured at different V_{TG}, displaying a linear V_{BG} dependence above threshold. Inset: $V_{BG,Threshold}$ vs V_{TG} data extracted from G vs V_{BG} traces of (b), used to determine the C_{TG}/C_{BG} ratio. All data are measured in monolayer MoS$_2$ sample S-1 at $T = 1.5$ K. Panel (a) legend also applies to panel (b).
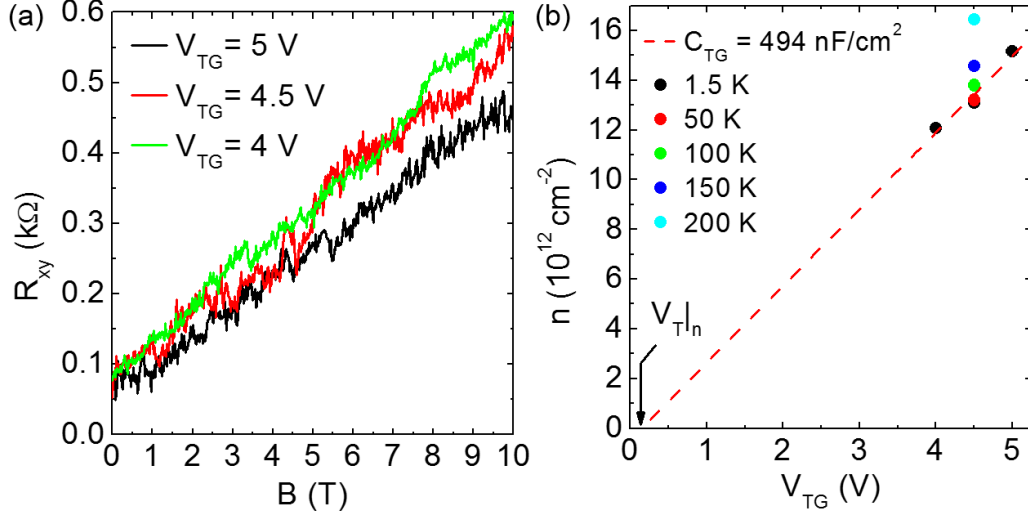
Figure 2.23 (a) R_{xy} vs B measured at $T = 1.5$ K, in a monolayer MoS$_2$ sample at different V_{TG}s. (b) n vs V_{TG} extracted from R_{xy} vs B data [panel (a)] measured at $T = 1.5$ K, and n data measured $V_{TG} = 4.5$ V at T between 50 and 200 K. All data are measured in monolayer MoS$_2$ sample S-2 at $V_{BG} = 0$ V.

A combination of Hall bar sample geometry and low T, low resistance contacts allow us to probe the Hall resistance as function of the perpendicular B-field at $T = 1.5$ K using low frequency, low current lock-in techniques, in the configuration described by Figures 1.17 and 2.21(a). Figure 2.23(a) shows R_{xy} vs B data measured at $T = 1.5$ K at different V_{TG}s in monolayer MoS$_2$ sample S-2. From the R_{xy} slope (dR_{xy}/dB) using Equation 1.10, we determine n vs V_{TG} [Figure 2.23(b)]. In a dual-gate sample, the carrier density writes:

$$n = (C_{TG}V_{TG} + C_{BG}V_{BG})\frac{1}{e} + n_0 \rightarrow n(V_{BG} = 0)$$

$$= C_{TG}(V_{TG} - V_T|_n)/e \qquad\qquad 2.4$$

where $n_0 = C_{TG}V_T/e$ is the carrier concentration at zero bias, and $V_T|_n$ is the threshold voltage for the charge density induced by the top-gate [marked in Figure 2.23(b)] . It should be noted that the correspondent measurement as a function of V_{BG}, with $V_{TG} = 0$ V, is not possible in this architecture given a fixed $V_{TG} > 0$ V is needed to "turn-on" the contacts, as highlighted in Figure 2.22. A linear fit, extrapolated to $n = 0$, of n vs V_{TG} data measured at

75

$V_{BG} = 0$ V [dashed line in Figure 2.23(b)] yields $C_{TG} = 494$ nF/cm^2, $V_{T|n} = 0.15$ V and $n_0 = -4.5 \times 10^{11}$ cm^{-2}. Electron density data measured at $V_{TG} = 4.5$ V at T between 50 and 200 K, are also shown in Figure 2.23(b). Over temperature range of ~200 K, n measured at $V_{TG} = 4.5$ V shows a 20% increase. Assuming a temperature independent C_{TG}, n measurements at higher temperatures and fixed V_{TG}, allow to determine the n_0 temperature dependence; n_0 ranges from -4.5×10^{11} cm^{-2} at 1.5 K to 2.6×10^{12} cm^{-2} at 200 K.

From the independent measurement of both G, n vs V_{TG} we obtain to G vs n data at different temperatures, using Equation 2.4, which will be used in Section 2.3.3.2 to calculate and compare field-effect and Hall mobility. It should be noted that monolayer MoS$_2$ samples of Table 2.1 are typically characterized by a $V_{T|n}$ smaller or close to 0 V at $T = 1.5$ K, thus monolayer MoS$_2$ flakes appear to be consistently unintentionally n-type doped. Unintentional electron doping that adds to electrostatic doping and enhances the carrier concentration in the contact region and may explain the low R_C measured at low temperatures in monolayer MoS$_2$ samples of Table 2.1.

2.3.3.2 Monolayer and bilayer MoSe$_2$

Mono- and bilayer MoSe$_2$ samples presented in this section are fabricated using flakes exfoliated from crystals purchased from Graphene HQ and TENN XC. Samples are fabricated utilizing bottom-contact, dual-gate structure #2 without a local bottom-gate [Figure 2.16]. For all devices discussed in this section the channel width is defined by the gate width, because the top-gates patterned around the bottom contacts are narrower than the MoSe$_2$ flakes, see examples in Figure 2.17(l) and (m). Table 2.2 presents the list of key MoSe$_2$ samples discussed in this section, which are fabricated using the same physical dimensions for gate and contacts, summarized here: $W = 3$ μm, $L = 5$ μm, $L' = 15.5$ μm, $W/L = 0.6$, $L'/L = 3.1$, and $W' = 5$ μm; W' corresponds to the contact width. Two-point measurements are carried out between D, S contacts, thus the channel length and width in this case correspond to W and L', respectively. In general, the electrical characterization of monolayer MoS$_2$ and mono-, bilayer MoSe$_2$ devices is very similar. In the following

76

discussion we will focus on the differences and similarities encountered in the characterization of the two material systems.
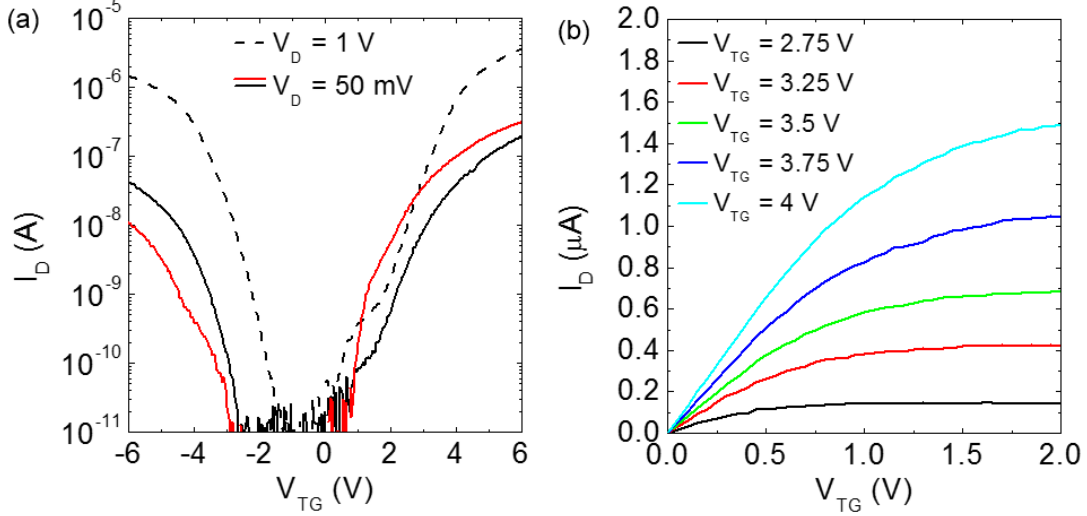
Figure 2.24: (a) I_D vs V_{TG} measured at different V_D values, showing proportional current scaling. Red and black traces label measurement on different samples, highlighting device to device variation in the ambipolar transport. (b) I_D vs V_D measured at different $V_{TG} > 0$ V, corresponding to black traces in panel (a). All data are measured in bilayer MoSe$_2$ samples at $V_{BG} = 0$ V.

Figure 2.24 shows the output and top-gate transfer characteristic for a bilayer MoSe$_2$ sample measured at RT. Figure 2.24(a) I_D vs V_{TG} data, measured at $V_D = 50$ mV and $V_D = 1$ V, exhibit ambipolar behavior where the n-branch ($V_{TG} > 0$ V) is predominant, showing the highest I_D at the same $|V_{TG}|$ compared to the p-branch ($V_{TG} < 0$ V); for either branch $I_{ON}/I_{OFF} > 10^5$ at $V_D = 1$ V. The emergence of an ambipolar behavior suggests that the metal contact Fermi level tends to pin towards mid-gap of MoSe$_2$ [61]. Two sets of I_D vs V_{TG} data measured in two different devices at $V_D = 50$ mV with comparable gate dielectric thickness and W/L [red, black traces Figure 2.24(a)], highlight the device to device variation of n-, p-branch peak I_D ratio. In the rest of our analysis we will focus exclusively on the predominant n-branch. Figure 2.24(b) I_D vs V_D data show a linear dependence at low V_D and current saturation at high V_D, consistent with observation in monolayer MoS$_2$ samples [Section 2.3.3.1]. While so far, we have discussed bilayer samples, monolayer samples show comparable RT characterization, including ambipolar

I_D vs V_{TG}. All devices presented in this section use Pd bottom-contacts. We also fabricated devices using Au or Pt bottom contacts, however they presented peak n-branch I_D equal or smaller than Pd contacted devices.
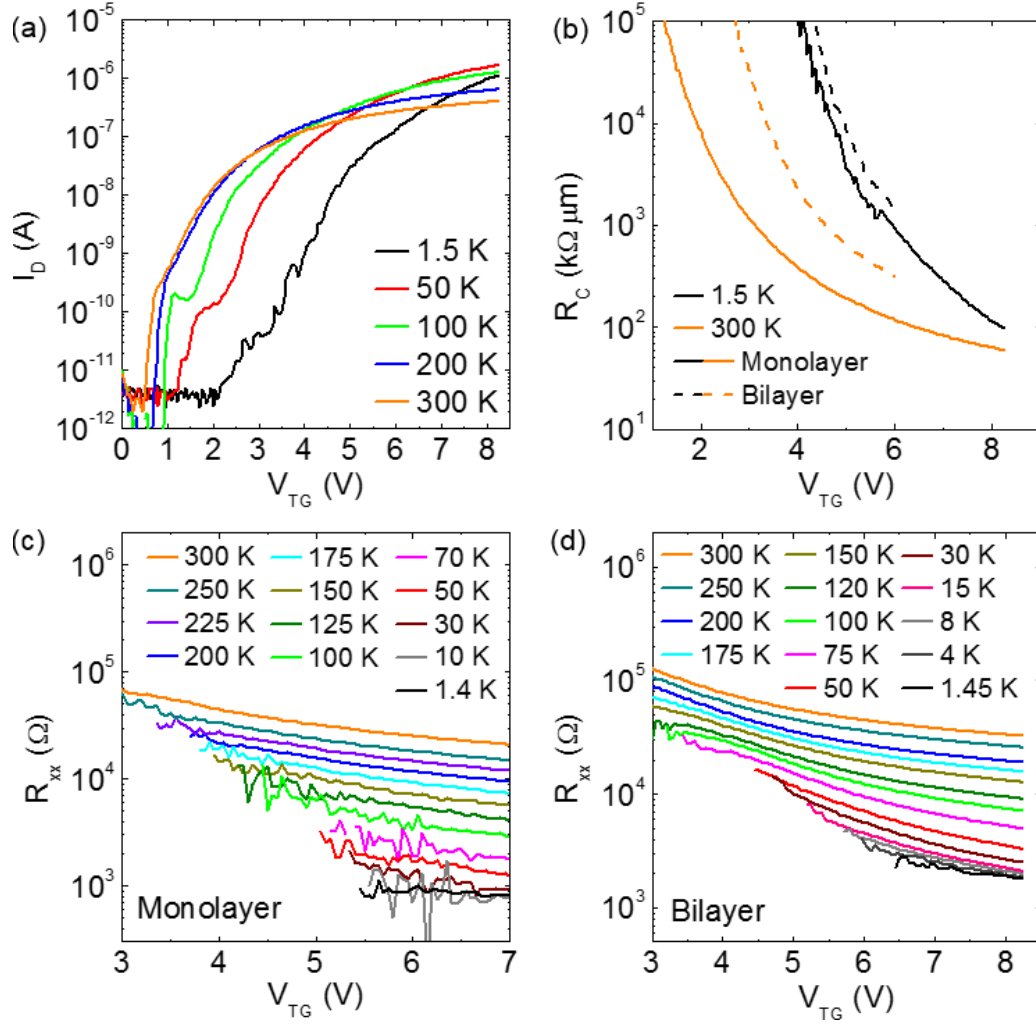
Figure 2.25: (a) I_D vs V_{TG} measured at V_D = 50 mV, and at T values between 300 K and 1.5 K, in bilayer MoSe$_2$ sample Se-1; V_T shifts at higher voltage and the peak I_D increases as T is lowered. (b) R_C vs V_{TG}, measured at 300 K and 1.5 K, for both mono- (Se-2) and bilayer (Se-1) samples. (c, d) R_{xx} vs V_{TG} measured at different T ranging from 300 K to 1.5 K in monolayer (bilayer) MoSe$_2$ sample Se-2 (Se-1). R_{xx} shows a strong temperature dependence, that weakens below $T \sim 30$ K. All data are measured at V_{BG} = 0 V.

Figure 2.25 summarizes the two-point [panel (a)] and four-point [panel (b),(c), and (d)] temperature dependence characterization of mono- and bilayer MoSe$_2$ FETs, following the same approach used for monolayer MoS$_2$ FETs [Section 2.3.3.1].

The transfer characteristics of Figure 2.25(a) are measured at various T values and $V_D = 50$ mV, in bilayer MoSe$_2$ sample Se-1 fabricated utilizing device structure #2 [Figure 2.16]. As the temperature is lowered from 300 K to 1.5 K, the I_D vs V_{TG} data show a +3 V V_T shift, and an increasing peak I_D, consistent with a temperature-dependent mobility increase. The transfer characteristic measured in monolayer samples show comparable temperature dependent V_T shift, but typically do not show any peak I_D increase, obscured likely, by higher temperature dependent R_C compared to bilayer samples. Detailed R_C measurement are described in the latter.

Four-point measurement of mono- and bilayer MoSe$_2$ samples, Se-1 and Se-2 respectively, allow to probe the four-point resistance ($R_{xx} = 1/G$) [Figure 2.25(c) and (d)] and the specific contact resistance [Figure 2.25(b)], calculated using Equation 2.2; the physical dimensions of all devices are the same and are reported at the Section outset. Specific contact resistance data measured at 300 K, 1.5 K and at $V_{BG} = 0$ V are strong function of V_{TG}, because the top-gate tunes the carrier density in contact region, effectively modulating the Schottky barrier width [Figure 2.25(b)]. The top-gate dielectric thickness is different for the two mono- and bilayer samples, but the maximum V_{TG} in each sample correspond to $n \sim 1 \times 10^{13}$ cm^{-2}. As expected, R_C increases as the temperature is lowered from 300 K to 1.5 K for both mono- and bilayer samples, because of suppressed thermionic emission. When compared at the same T and n, monolayer devices present higher R_C than bilayer devices, a behavior consistent with thickness dependent E_g in TMDs, which is largest at the monolayer limit [92]. A comparison between monolayer MoSe$_2$ [Figure 2.25(b)] and MoS$_2$ [Figure 2.21(d), at $V_{TG} = 3.5$ V] R_C data reveal that at the same $n \sim 1 \times 10^{13}$ cm^{-2}, the R_C value is one order of magnitude higher in monolayer MoSe$_2$ samples than in monolayer MoS$_2$ samples. We conclude that the metal contact Fermi level tends to pin towards the CB (midgap) in MoS$_2$, (MoSe$_2$) [61], resulting in a material dependent Schottky barrier height, consistent with unipolar (bipolar) I_D vs V_{TG} measured in monolayer

MoS$_2$ (mono- and bilayer MoSe$_2$) samples. Even though contact resistance is higher in MoSe$_2$ than in MoS$_2$ samples we can still characterize samples using small signal, low frequency lock-in amplification techniques.

Figure 2.25(c) and 2.25(d) presents the temperature dependence of R_{xx} vs V_{TG} data measured in mono- and bilayer samples, respectively and at $V_{BG} = 0$ V. When observed at constant V_{TG}, R_{xx} decreases as the temperature is lowered, which is indicative of the mobility increasing as phonon scattering is progressively suppressed, a behavior consistent with observations in MoS$_2$ samples. At lower temperatures R_{xx} becomes weakly temperature dependent, consistent with a temperature independent mobility associated with charged impurity scattering limited regime. Mobility trends evinced from R_{xx} temperature dependence are consistent with observations in few-layer samples [Section 2.2.3].

At last we note that the variation between values of the conductance ($G = 1/R_{xx}$) probed using different sets of voltage probes see a variation of most ±15% if compared to an average value, a range that holds for all MoSe$_2$ samples probed and at all temperatures.
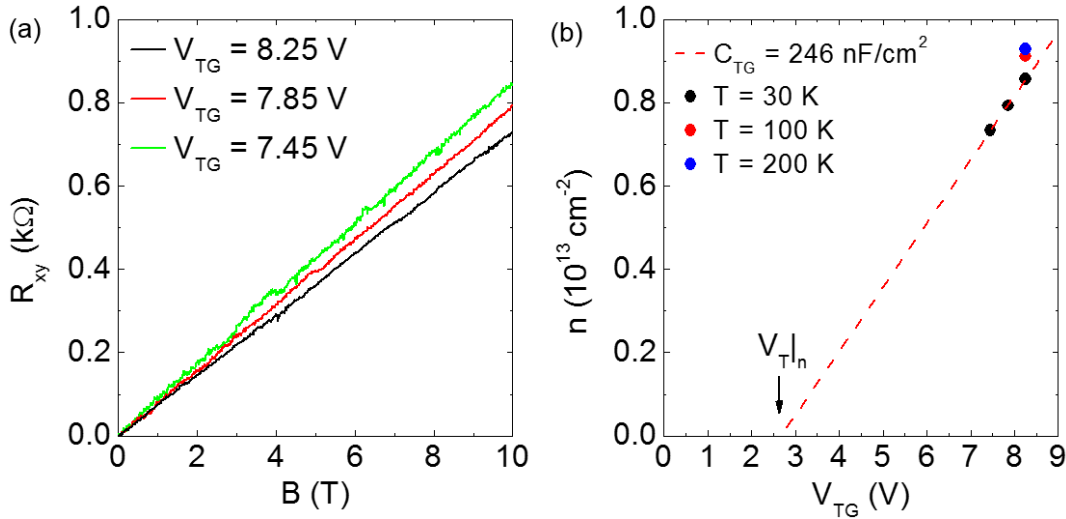
Figure 2.26: (a) R_{xy} vs B measured at $T = 30$ K, in a bilayer MoSe$_2$ sample Se-3 at different V_{TG}s. (b) n vs V_{TG} extracted from R_{xy} vs B data [panel (a)] measured at $T = 30$ K, and n data measured $V_{TG} = 8$ V at $T = 100, 200$ K. All measurements are conducted $V_{BG} = 0$ V.

All mono- and bilayer MoSe$_2$ samples are fabricated in a Hall bar geometry, which allow us to probe R_{xy} vs B, using a low frequency, low current lock-in techniques [Figure 1.17]. Figure 2.26(a) shows R_{xy} vs B measured at fixed V_{TG}, $V_{BG} = 0$ V and $T = 30$ K in bilayer MoSe$_2$ sample Se-3. From the slope of the R_{xy} vs B [Equation 1.10], we extract n vs V_{TG}, as shown in Figure 2.26(b). A linear fit, extrapolated to $n = 0$, of the n vs V_{TG} data [dashed line in Figure 2.26(b)] yields $C_{TG} = 246$ nF/cm^2, $V_T|_n = 2.7$ V and $n_0 = -1.5 \times 10^{12}$ cm^{-2}. Electron densities extracted from Hall measurement at higher temperatures (100 and 200 K) and $V_{TG} = 8$ V, show a modest increase < 10 %. As described for monolayer MoS$_2$ samples measuring n at different temperature at fixed V_{TG} allows to characterize n_0 as function of T, assuming C_{TG} is temperature independent, allowing to plot R_{xx} vs n data; n_0 ranges from -4.1×10^{12} cm^{-2} at 30 K to -3.5×10^{12} cm^{-2} at 200 K in sample Se-3 [Figure 2.26(b)]. Unlike monolayer MoS$_2$ samples, monolayer MoSe$_2$ samples typically possess a $V_T|_n > 0$ V at $T = 1.5$ K.

2.3.3.3 Field effect mobility and Hall mobility comparison

As introduced in Section 2.2.3 for few-layer TMD samples, the characterization of intrinsic mobility is a key metric to assess the material quality and characterize their transport properties, namely scattering processes. The ability to reliably estimate mobility data values hinges on the accurate determination of conductivity and carrier density. Controversy on the determination of electron mobility is not new in the 2D material community, and has been a source of confusion in early studies [63], [64]. In the following we compare field-effect, Hall mobility definitions and values, extracted from experimental data measured in bottom-contact, dual-gate monolayer MoS$_2$ and MoSe$_2$ samples presented in Section 2.3.3.1 and 2.3.3.2.

A characterization of the mobility begins probing the four-point G (or R_{xx}) as function of a gate bias (V_G), using a bottom-gate stack with a SiO$_2$ dielectric in Section 2.2.2, or a top-gate stack with hBN dielectric in Section 2.3.3. Using the physical dimension of the device (W and L), the conductivity (σ) writes:

$$\sigma = en\mu(n, T) = G\frac{L}{W} = \frac{1}{R_{xx}}\frac{L}{W} \qquad\qquad 2.5$$

where, μ is in general a function of n and T. In Section 2.2.3 we measured σ vs V_{BG}, but we did not measure the n independently. Instead we relied on the conductance (conductivity) threshold voltage ($V_T|_\sigma$) to estimate the carrier density, where $n = C_{ox}(V_{BG}-V_T|_\sigma)/e$. A linear extrapolation to $\sigma = 0$ of the measured σ vs V_{TG} defines $V_T|_\sigma$. At a fixed T, for $V_{BG} > V_T|_\sigma$ a constant n-independent field-effect mobility is obtained from Equation 2.1. We re-write Equation 2.1 as function of conductance and for top-gated devices as follows:

$$\mu_{FE} = \frac{1}{e}\frac{d\sigma}{dn} = \frac{d\sigma}{d(V_{TG} - V_T|_\sigma)}\frac{1}{C_{TG}} \qquad\qquad 2.6$$

As discussed in Section 2.3.3.1 and 2.3.3.2 for hBN encapsulated, MoS$_2$ and MoSe$_2$ based devices, C_{TG} is obtained from Hall measurements [Figures 2.23(b) and 2.26(b)], however in literature often times the top-gate capacitance is estimated as: $C_{TG} = \varepsilon_0\varepsilon_{hBN}/t_{hBN}$, where t_{hBN} is the hBN flake thickness directly measured using AFM, and ε_{hBN} values range between 3 and 4 [86], [87], [91]; C_{TG} estimates introduce yet another source of uncertainty in the μ_{FE} extraction.

A gated Hall bar geometry [Figure 1.17], coupled with measurements in perpendicular B-field, allows to independently measure n vs V_{TG}, in addition to σ vs V_{TG}, not relying anymore on $V_T|_\sigma$ do determine n. Once σ and n are both independently measured, at a given temperature, we can calculate the Hall mobility (μ_H) as follows:

$$\mu_H(n) = \frac{\sigma}{en} \qquad\qquad 2.7$$

Figure 2.27(a) shows a set of σ, n, I_D vs V_{TG} data, measured in bilayer MoSe$_2$ sample Se-3 at $T = 30$ K and $V_{BG} = 0$ V. Values of μ_{FE} and μ_H extracted from the same set of σ vs V_{TG} data are presented, clarifying the impact of field-effect and Hall mobility definitions. As introduced earlier, we begin from four-point σ vs V_{TG} data (solid black line), which are shown only for $V_{TG} > 6.5$ V, i.e. for a sufficiently high n in the contact regions such as the contacts appear ohmic, marked by a vertical dashed line. The contact behavior is captured by I_D vs V_{TG} measured at $V_D = 50$ mV (solid orange line). A linear extrapolation to $\sigma = 0$ (black dashed line) of σ vs V_{TG} data yields $V_T|_\sigma = 4.6$ V. From R_{xy} vs B measurements at

fixed V_{TG} [Figure 2.26(b)] we obtain n vs V_{TG} data (blue symbols). A linear extrapolation to $n = 0$ (blue dotted line) of n vs V_{TG} data, yields a $V_T|_n = 2.7$ V and $C_{TG} = 246$ nF/cm^2. It is evident that $V_T|_\sigma$ and $V_T|_n$ significantly differ ($V_T|_n - V_T|_\sigma = 1.9$ V). The μ_{FE} obtained from a derivative of the conductance (dashed green line), using Equation 2.7 and C_{TG} obtained from Hall data, is V_{TG} independent and overestimates μ_H (dashed red line). The μ_H, calculated using Equation 2.8, is a function of V_{TG} (n), and goes to zero for $V_{TG} < 4.6$ V $= V_T|_\sigma$, where the conductance vanishes. The overestimation of μ_{FE} stems from an underestimation of n, caused by assuming $V_T|_n = V_T|_\sigma$. It should be noted that μ_{FE} overestimating μ_H is not a function of T or specific to a material system (MoS$_2$, MoSe$_2$), as demonstrated by Figure 2.27(b), where the temperature dependence of μ_{FE} and μ_H (extracted at $n = 1.2 \times 10^{13}$ cm^{-2}) are compared for monolayer MoS$_2$ sample S-2. The field-effect mobility overestimates the Hall mobility across the whole temperature range probed. In the rest of our analysis, Section 2.3.3.4, we will focus only to Hall mobilities, as they provide a more accurate representation of the device mobility.
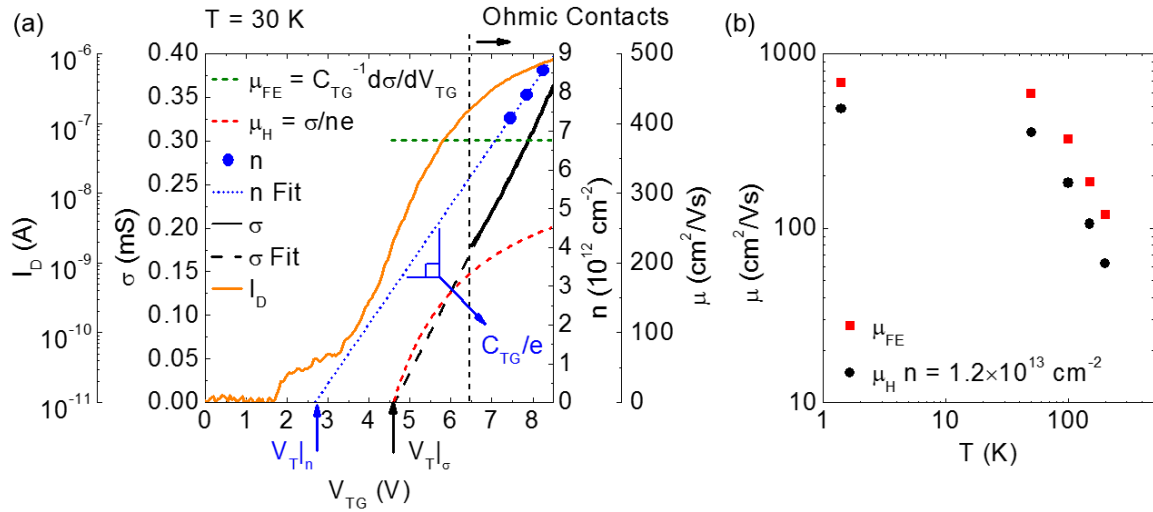
Figure 2.27: (a) σ vs V_{TG} (black solid line), $\sigma = 0$ linear extrapolation (black dashed line); n vs V_{TG} data (blue circles), $n = 0$ linear extrapolation (blue dotted line); calculated μ_H, μ_{FE} vs V_{TG} (red and green dashed lines); I_D vs V_{TG} (orange line). σ, n and I_D are all measured at 30 K in bilayer MoSe$_2$ sample Se-3. σ, $n = 0$ linear extrapolations define: $V_T|_\sigma$, $V_T|_n$. (b) μ_{FE} vs T and μ_H vs T measured at $n = 1.2 \times 10^{13}$ cm^{-2} in monolayer MoS$_2$ sample S-2, demonstrating how μ_{FE} overestimates μ_H as function of T.

2.3.3.4 Hall mobility temperature and electron density dependence

Using R_{xx}, n vs V_{TG} (G, n vs V_{TG}) data presented for MoS$_2$ samples in Section 2.3.3.1 and for MoSe$_2$ samples in Section 2.3.3.2, we extract the Hall mobility as a function of temperature [Figure 2.28] and carrier density [Figure 2.29], as discussed in the previous section. Figure 2.28 shows μ_H vs T data measured in monolayer MoS$_2$ samples (S-1, S-2, S-3) at $n = 12\times10^{12}$ cm^{-2} [panel (a)], monolayer MoSe$_2$ sample (Se-2) at $n = 12\times10^{12}$ cm^{-2} [panel (b)], and bilayer MoSe$_2$ samples at $n = 9\times10^{12}$ (Se-1, Se-3) and 12×10^{12} cm^{-2} (Se-4) [panel (b)] .
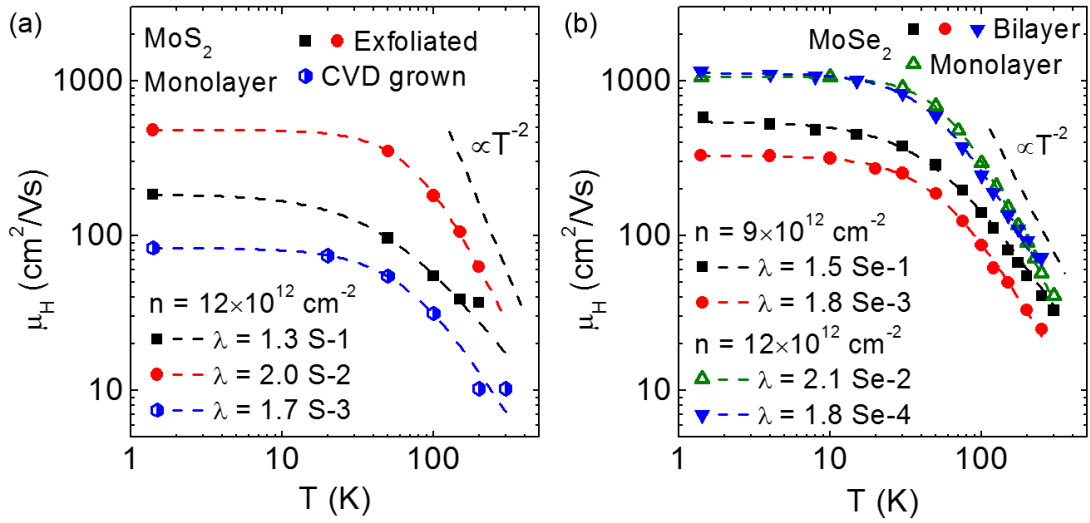
Figure 2.28   (a) μ_H vs T measured at $n = 12\times10^{12}$ cm^{-2} in exfoliated (solid symbols) and CVD grown (half-filled symbols) monolayer MoS$_2$ samples. (b) μ_{FE} vs T measured at $n = 9\times10^{12}$ and 12×10^{12} cm^{-2} in monolayer (open symbols) and bilayer (solid symbols) MoSe$_2$ samples. Dashed lines correspond to a fit of each experimental dataset to Equation 2.3. A guide for the eye shows T^{-2} power law.

The Hall mobility temperature dependence follows a similar trend in both material systems, μ_H data show a strong temperature dependence at $T > 50$ K, with μ_H increasing as the T is reduced and phonon scattering is suppressed. At $T < 50$ K the μ_H temperature dependence weakens, showing a near T independent μ_H associated to impurity scattering. Room temperature μ_H ranges between 20 and 50 cm^2/Vs for exfoliated MoS$_2$ and MoSe$_2$

samples. Comparable values of RT μ_{FE} are obtained for few-layer MX_2 samples [Figure 2.15]. A lower $\mu_H \sim 10$ cm^2/Vs is obtained for CVD-grown MoS_2 samples. First-principle calculations of intrinsic, phonon limited electron mobilities at room temperature estimate values for MoS_2 and $MoSe_2$ of 320 cm^2/Vs and 180 cm^2/Vs, respectively [93].

MoS_2 sample	λ	μ_{imp} (cm^2/Vs)	n (10^{12} cm^{-2})	$MoSe_2$ sample	λ	μ_{imp} (cm^2/Vs)	n (10^{12} cm^{-2})
S-1 Monolayer	1.3	187	12	Se-1 Bilayer	1.5	546	9
S-2 Monolayer	2.0	483	12	Se-2 Monolayer	2.1	1070	12
S-3 CVD grown Monolayer	1.7	84	12	Se-3 Bilayer	1.8	331	9
				Se-4 Bilayer	1.8	1130	12

Table 2.3: Parameters λ, μ_{imp} obtained from a fit to Equation 1.3 of each μ_{FE} vs T dataset of Figure 2.27. CVD MoS_2 was grown at UT Austin by Dr. R. Ghosh. A description of the growth techniques is found in Ref [59].

Each μ_H vs T dataset, for both material systems, is fit independently using Equation 1.3 [dashed lines in Figures 2.28(a) and 2.28(b)], which incorporates a power law dependence ($T^{-\lambda}$) to model phonon scattering and a temperature independent component (μ_{imp}) to model charged impurity scattering at low T, assuming a degenerate 2DES. For both $n = 9 \times 10^{12}$ and 12×10^{12} cm^{-2}, $T_F \sim 300$ K, a value significantly larger than temperatures where we observe a temperature independent μ_{imp}, satisfying the degenerate 2DES assumption. Parameters λ, μ_{imp} obtained from each Equation 1.3 fit to μ_H vs T data obtained from MoS_2 and $MoSe_2$ samples, are summarized in Table 2.3. Equation 1.3 fits yield a λ that ranges between 1.3 and 2.1. If we consider separately MoS_2 and $MoSe_2$ samples fabricated utilizing structure #2, where the TMD layer is sandwiched between hBN layers, with the exception on S-3 fabricated utilizing structure #1, we obtain an average $\lambda = 1.65$ for MoS_2 and $\lambda = 1.80$ for $MoSe_2$. Values of $\lambda > 1$ suggests that optical phonon scattering

dominates in the limit of high temperatures. Theory predicts $\lambda = 1.69$ in monolayer MoS_2 [76]. Values of λ, across all three monolayer MoS_2 samples probed, are consistent with $\lambda = 1.9$ obtained from μ_H vs T data measured in hBN encapsulated, CVD grown monolayer MoS_2 in Ref. [94]. Remote phonon scattering from the dielectrics surrounding the TMD layers is most likely not a factor for either dielectric configuration (hBN/hBN or hBN/SiO$_2$) [55], but it is expected to play a significant role only for high-κ dielectric environments, yielding $\lambda < 1$ [89], [95]. Comparable values of λ are also obtained from a fit to μ_{FE} vs T data measured in bottom-gated, few-layer MX_2 samples [Figure 2.15]. A comparison is reasonable because even if μ_{FE} overestimates μ_H it does not significantly alter the T dependence, as shown in Figure 2.27(a).

At the lowest temperature, phonons are frozen out, and μ_H ($T = 1.5$ K) $= \mu_{imp}$, a quantity that captures all charged impurity scattering, generated in principle by a combination of long range scatterers (Coulomb impurities) and short range scatterers (short-range atomic defects) [94]. As it is clearly visible in Figure 2.28, $MoSe_2$ samples outperform MoS_2 samples at low temperatures. We measure μ_{imp} in excess of 1000 cm^2/Vs in monolayer sample Se-2 and bilayer sample Se-4, while the highest μ_{imp} measured in MoS_2 samples is only 483 cm^2/Vs (sample S-2), less than a half compared to peak μ_{imp} in $MoSe_2$ samples [Table 2.3]. We can describe samples with higher μ_{imp} as characterized by a lower impurity (scatterer) density (n_I). For example, in Si inversion layers n_I is typically associated to the oxide charge, and in III-V 2DES n_I is associated to remote and background ionized impurities [94], [96]. For hBN-encapsulated mono- and bilayer MX_2 n_I could be associated to a variety of process variables, namely: the quality of the exfoliation crystal (limited by the growth process), the presence of surface adsorbates, which could be mitigated exfoliating and assembling samples in a glove-box, organic residues from the exfoliation tape and substrates as well as the typical bubbles/wrinkles that form once we assemble the hBN/MX_2/hBN stack [darker regions in Figure 2.17(l)].

The only grown monolayer MoS_2 sample (S-3) presents a particularly low $\mu_{imp} = 84$ cm^2/Vs, and a low RT μ_H value compared to values measured in samples S-1 and S-2. Recent literature reports have shown hBN-encapsulated, CVD grown, monolayer MoS_2

samples with μ_{imp} up to a 1000 cm^2/Vs [94]. This indicates that μ_H probed in grown monolayers based samples can match μ_H probed in exfoliated monolayers [94], however not in the sample we probed.
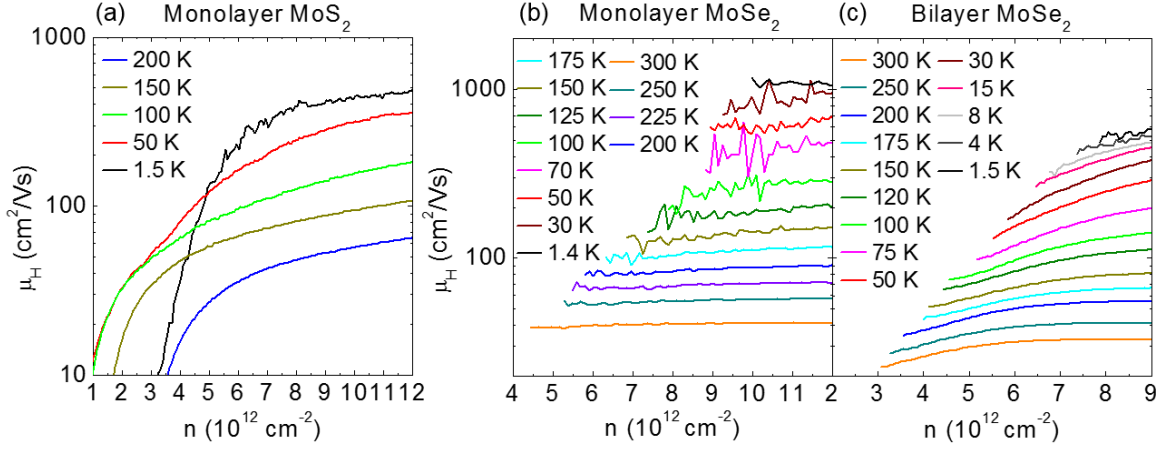
Figure 2.29: μ_H vs n measured at various T in (a) monolayer MoS$_2$ sample S-2, (b) monolayer MoSe$_2$ sample Se-2 and (c) bilayer MoSe$_2$ sample Se-1.

Figure 2.29 shows μ_H vs n measured at various temperatures in monolayer MoS$_2$ sample S-2 [panel (a)], monolayer MoSe$_2$ sample Se-2 [panel (b)], and bilayer MoSe$_2$ samples Se-1[panel (c)]. At low temperatures, all samples show a $\mu_H = \mu_{imp}$ proportional to n, a behavior consistent with a charged impurity scattering, as observed in silicon 2DESs [96]. As n increases charged impurities are increasingly screened resulting in a larger μ_H. Samples with lower μ_{imp} (higher n_I) show a stronger n dependence, e.g. samples S-2 and Se-1 in Figures 2.29(a) and 2.29(c), respectively. While in samples with higher μ_{imp}, the n dependent impurity screening is less pronounced and produces modest μ_H variation, as observed for sample Se-2 [Figure 2.29(b)] [96].

As temperature is increased and phonon scattering begins to dominate the n dependence weakens. In the high temperature limit, for samples with higher μ_{imp} [sample Se-2 Figure 2.29(b)] μ_H is near n independent in the n range probed, while samples where impurity scattering is stronger [e.g. Se-1 Figure 2.29(c)] show a more pronounced n dependence at higher T in the limit of low n. Samples show a stronger μ_H vs n dependence

at high T when the magnitude of phonon and impurity scattering limited mobilities are comparable [96], i.e. in high n_I, low n case. MoSe$_2$ samples show truncated μ_H vs n traces in Figures 2.29(b) and 2.29(c), because mobility data are shown only for carrier densities sufficiently high in the contact regions, where we obtain low resistance contacts.

As discussed in Section 2.3.3.2, MoS$_2$ samples present lower R_C compared to MoSe$_2$ samples, therefore we are able to probe μ_H at lower carrier density compared to MoSe$_2$ samples. Hall mobility data probed in monolayer MoS$_2$ sample S-2 show a disorder-driven crossover to an insulating regime at $n < 4\times10^{12}$ cm^{-2}, where μ_H increases as the T is increased [sample S-2 Figure 2.29(a)]. Similar findings are reported in monolayer MoS$_2$ [89], [90], [97] and few-layer WSe$_2$ [91] studies.

2.3.3.5 Capacitance and subthreshold swing

Our detailed electrical characterization of MoS$_2$ and MoSe$_2$ FETs using hBN dielectrics allows to characterize the properties of the dielectric, namely extract the out-of-plane dielectric constant of hBN and evaluate the sub-threshold swing scaling as function of the hBN thickness.

Figure 2.30(a) shows the inverse top or bottom gate capacitance (C^{-1}) obtained from electron density Hall measurements across multiple MoS$_2$ and MoSe$_2$ samples as function of the hBN dielectric thickness, measured with AFM. The gate capacitance consists of three capacitance components in series: the hBN capacitance, the interface capacitance (C_{int}) [98], and the quantum capacitance (C_q) therefore C^{-1} writes:

$$C^{-1} = \frac{t_{hBN}}{\varepsilon_0 \varepsilon_{hBN}} + C_q^{-1} + C_{int}^{-1} \qquad\qquad 2.8$$

A linear fit of C^{-1} vs t_{hBN} data yield a slope proportional to ε_{hBN} and an intercept that correspond to $C_q^{-1} + C_{int}^{-1}$. Fitting all C values obtained from both MoS$_2$ and MoSe$_2$ based devices at once we obtain: $\varepsilon_{hBN} = 3.2$ and $C_q^{-1} + C_{int}^{-1} = 7.25$ µF/cm^2. The interface capacitance is associated with vdW gap between the hBN and the TMD layer. In traditional 2DES and graphene, C_q is generally large and positive in the 10^{12}-10^{13} cm^{-2} carrier density range. For a spin-degenerate 2DES, with m^*/m_e ranging between 0.5 and 1, $C_q = e^2 m^*/(\pi\hbar^2)$

ranges between 30 and 70 $\mu F/cm^2$. However, in TMDs 2D systems the negative compressibility of carriers is associated with a carrier density dependent negative quantum capacitance. A detailed discussion of the phenomena is offered in Chapter 4.
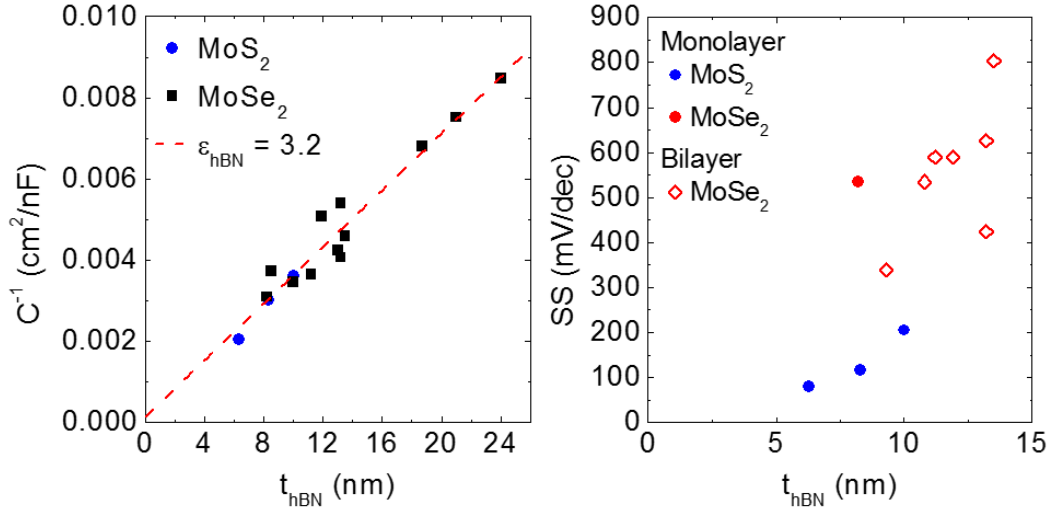
Figure 2.30: (a) C^{-1} vs t_{hBN} for MoS2 and MoSe2 samples with hBN dielectrics, the slope of the linear fit estimates the hBN out of plane dielectric constant. (b) *SS* vs t_{hBN} measured applying a V_{TG}, with $V_{BG} = 0$ V in monolayer MoS2, mono- and bilayer MoSe2 samples.

An important figure of merit for FETs in digital electronics is the subthreshold swing (*SS*), defined as [99]:

$$SS = \left(\frac{d(\log_{10} I_D)}{dV_{TG}}\right)^{-1} \qquad\qquad 2.9$$

expressed in mV/dec. Subthreshold swing values along with the threshold voltage readily capture the leakage current in the OFF-state of the transistor. Figure 2.30(a) shows SS vs t_{hBN} measured in monolayer MoS2, mono- and bilayer MoSe2 samples, when V_{TG} is swept towards positive voltages to accumulate the channel with electrons, and $V_{BG} = 0$ V. In FETs where the depletion capacitance does not play a role, e.g. a silicon-on-insulator metal-oxide-semiconductor transistor, *SS* depends on whether short channel effects (SCE) are dominant or not. The significance of SCE can be understood comparing the channel length

L with a screening length $\alpha = \sqrt{(\epsilon_{body}/\epsilon_{ox})t_{body}t_{ox}}$, where $\epsilon_{ox/body}$ and $t_{ox/body}$ are

89

the dielectric constant and thickness of the body and oxide, respectively [100]. In subthreshold, if $L \gg \alpha$, the channel potential (φ), which regulates the injection, is controlled one-to-one by V_{TG} ($d\varphi/dV_{TG} \sim 1$), therefore the subthreshold slope in this type of devices should be near ideal: $SS = \ln(10)\, k_B T/e \sim 60$ mV/dec [100]. Conversely when $L \sim \alpha$ we expect SS larger than 60 mV/dec.

In our devices the gate oxide is replaced by hBN and given $L \gg \alpha$ for Figure 2.30(b) data, one could expect a near-ideal SS independent of t_{hBN}. However, SS vs t_{hBN} data presented in Figure 2.30(b) show a marked t_{hBN} dependence with SS values ranging between 80 to 800 mV/dec, over an hBN thickness range between 5 to 15 nm. This behavior is reminiscent of SS studies in carbon nanotube Schottky barrier FETs (CN-SBFETs), where SS data measured in CN-SBFET suffer from an equivalent SCE, even for an electrostatically well-behaved devices ($L \gg \alpha$) [100]. This behavior is associated with the injection of carriers through a Schottky barrier which depends not only on the gate bias but also on the screening length, i.e. on the oxide thickness. In the first order approximation the $SS \propto a$ [100], [101], therefore we can expect an increase of the SS as the hBN and flake thickness are increased, a finding consistent with SS measured in Mo-based TMD FETs of Figure 2.30(b).

2.4 SUMMARY

In summary, we studied the fabrication and electrical characterization of molybdenum-based TMD FETs. In the first part of the chapter, we introduced a top-contact, bottom-gate architecture used to fabricate two- and four-point few-layer $MoSe_2$ and MoS_2 n-type FETs as well as ambipolar few-layer $MoTe_2$ FETs. Using four-point conductance measurements, we separate channel and contact resistance contributions, and extract the electron field-effect mobilities. The field-effect mobility shows a strong temperature dependence associated with phonon-scattering, which dominates at room temperature.

In the second part of the chapter, we introduce a new, more complex, bottom-contact, dual-gate architecture, using hBN dielectrics. Specific state of the art transfer techniques used to fabricate monolayer MoS_2, mono- and bilayer $MoSe_2$ gated Hall bars are discussed. Contact resistance measurements reveal that our bottom-contact, dual-gate architecture enables low-resistance, low-temperature ohmic contacts. Thanks to the independent measurements of the conductance and the carrier density as function of the gate bias at low temperatures, we extract both field-effect and Hall mobility. A detailed study indicates that the field-effect mobility obtained from gated conductance measurements, where the carrier density is not directly measured, overestimates the Hall mobility, obtained from combined conductance and carrier density measurements. Hall mobility measurements as function of temperature and carrier density, allow to investigate the scattering mechanisms limiting the mobility. The Hall mobility reveals a strong temperature dependence consistent with phonon scattering in the high temperature regime, above a critical temperature, as observed in few-layer devices, which saturates below a critical temperature, because of charged impurity scattering. Impurity limited mobilities increase proportionally to the carrier density and are measured in excess of 1000 cm^2/Vs in mono- and bilayer $MoSe_2$ samples.

Chapter 3: Magnetotransport of *K*-valley electrons in monolayer and bilayer MoSe₂

In this Chapter we discuss the magnetotransport of high-mobility electrons in mono- and bilayer MoSe₂. Using the "pick-up" dry transfer techniques described in Chapter 2, we assemble bottom-contact, dual-gate, MoSe₂ Hall-bars, utilizing the device structure #3 [Figure 2.16]. As discussed in the Chapter 2, hBN encapsulated samples, show impurity scattering limited Hall mobilities upwards of 1000 cm^2/Vs, at $T = 1.5$ K. High mobility samples enable the observation of Shubnikov-de Haas oscillations in perpendicular magnetic fields as low as 5 T, and quantum Hall states in high magnetic fields. The introduction of top-gated Pd bottom-contacts discussed Chapter 2 is instrumental in obtaining low-resistance, ohmic contacts at $T = 0.3$ K and in high *B*-fields, allowing to characterize samples across a large range of electron densities, using a dual-gate configuration. From the temperature dependence of the SdH oscillations we extract an electron effective mass of $0.8m_e$ in both mono- and bilayer samples. At a fixed electron density, the longitudinal resistance shows minima at filling factors that are either predominantly odd, or predominantly even, with a parity that changes as the density is tuned. Two-fold LL degeneracy and effective mass measurements indicate that electrons are hosted at a *K* point and occupy only the lower spin-split subband below a density threshold. The FFs parity transitions are a manifestation of strong electron-electron interactions in MoSe₂ 2DES. Interactions enhance the electron *g*-factor and in turn the Zeeman energy, causing the FFs to change parity as the 2DES becomes more dilute. The SdH oscillations are insensitive to an in-plane magnetic field, consistent with an out-of-plane spin orientation of electrons at the *K*-point.

3.1 Magnetotransport in group VI TMDs

As introduced in Chapter 1, group VI TMDs 1H-monolayers are direct bandgap semiconductors with band extrema at the K point, where the combination of strong SOI and broken inversion symmetry result in a spin-split bandstructure, with coupled spin and valley degrees of freedom. Conversely in bulk, bands are spin degenerate, with conduction and valence band minima are at the Q and Γ point, respectively. The material and thickness dependent bandstructure in group VI TMDs has garnered significant interest, in particular as possible host for spin related physical phenomena [16], [103]. However, experimental studies needed to validate the theoretical understanding of TMDs bandstructure are in their early stages.

To date, the bandstructures of group VI TMDs have been mostly investigated optically. The direct bandgap available at the monolayer limit, allows to probe excitonic properties. For example, exciton g-factor measurements have been reported for most group VI TMDs, probed in perpendicular B-field [104]–[107]. Other experimental techniques used to probe the bandstructure include ARPES and STS measurements. ARPES studies, which focus for undoped samples on the VB [18], [108], have been able to experimentally access spin-split bands in monolayer, and characterize the K to Γ point crossover as the number of layers is increased [Figure 1.5], [18]. STS measurements can probe the transport bandgap and access valley splitting in both conduction and valence bands (E_{KQ}, $E_{K\Gamma}$) [109]. Nonetheless values of most bandstructure parameters, for example electron and hole effective masses, are only available from theoretical calculations [12].

Magnetotransport in clean TMD samples, where clear SdH oscillations emerge, provide an alternative avenue to probe the energy-momentum dispersion at the band extrema (multiple subband occupation, effective masses), the Landau level structure, and assess the impact of electron-electron interaction via negative compressibility (discussed in Chapter 5) or enhanced Zeeman splitting. The main drawback of magnetotransport measurements, compared to different spectroscopic techniques, is sample fabrication. As introduced earlier, SdH oscillations emerge at accessible magnetic fields only in high

mobility, low disorder samples, at low temperatures. Magnetotransport investigation of gapped materials such as group VI TMDs requires to devise specific fabrication techniques in order to obtain low-temperature ohmic contacts. For these reasons, magnetotransport in TMDs lags for example optical studies.

Group VI TMDs magnetotransport studies have to date focused on WSe$_2$, where high mobility (> 4000 cm^2/Vs), hBN encapsulated samples with low-resistance Pt bottom contacts are available [91]. Shubnikov-de Haas oscillations of K-valley holes in mono- and bilayer WSe$_2$ show QHS at predominantly even or odd FFs [110]. The FF parity is a function of the hole density, revealing an interaction-enhanced Zeeman splitting [111]. Two-fold degenerate LLs indicate that holes are hosted at the K point, and populate the highest spin-split valence band, because $E_{K\Gamma}$ and $2\Delta_{vb}$ are significantly larger then the Fermi energy probed in WSe$_2$ [111]. In bilayer samples, two subbands associated with the individual WSe$_2$ layers forming the bilayer are resolved, indicating that the two layers are weakly coupled, a finding consistent with effective mass measurements which yield m^*/m_e = 0.45 in monolayer and in both subbands of the bilayer. Similarly, Γ-valley holes in few-layer WSe$_2$ present two-fold degenerate LLs consistent with a single spin degenerate minima, large effective masses (m^*/m_e = 0.89) and enhanced Zeeman splitting [112], [113], similarly to what observed for K-valley holes. Tilted field measurements reveal that WSe$_2$ K-valley holes are insensitive the parallel magnetic-field, as opposed to Γ-valley holes, indicating that at the K point the hole spin is locked perpendicular to the WSe$_2$ plane. Recently, magnetotransport studies in dual-gate trilayer WSe$_2$ samples have shown that the relative Γ-K valley hole population is tuned by the transverse electric-field. In trilayer carriers are assigned to K or Γ valley by probing their effective masses, which are comparable to monolayer (K valley) and bulk (Γ valley) WSe$_2$ holes. While magnetotransport studies have so far probed only the VB of WSe$_2$, compressibility studies of monolayer WSe$_2$ have been able to probe both CB and VB revealing comparable K-valley electron and hole effective masses, and an interaction-enhanced Zeeman splitting in the VB, but not in the CB [7].

Magnetotransport studies of electrons in group VI TMDs are more scant, and have so far been hindered by the same set of challenges discussed in Chapter 2, namely in obtaining high-mobility samples and low-temperature, low-resistance contacts. Recent efforts include the fabrication of monolayer MoS_2 hBN encapsulated Hall-bars, with graphene [94] and Co/hBN contacts [90]. Magnetotransport of monolayer MoS_2 samples is yet not fully understood, with SdH oscillations revealing a LL degeneracy between 2 and 4 [90], [94]. The unclear assignment of the LL degeneracy may stem from the interplay of almost degenerate spin-split subbands at the K point, given $2\Delta_{cb} \sim 5$ meV in monolayer MoS_2 [12]. More recently, magnetotransport measurements in bilayer MoS_2 samples, probed at $n < 4 \times 10^{12}$ cm^{-2}, show two-fold degenerate LLs, large effective masses (m^*/m_e = 0.55) and an interaction enhanced Zeeman splitting [114]. Other electron magnetotransport studies available to date have focused on in few-layer MoS_2 and WS_2 samples revealing three- or six-fold degenerate LLs, consistent with Q-valley CB minima [115]–[117].

In summary, the CB of group VI TMDs represents as largely unexplored 2DES, deserving of a more systematic investigation. It is of particular interest to characterize the occupation of different subbands associated to the Q-valley and the K-valley spin-split minima, particularly in $MoSe_2$, a TMD where magnetotransport has not yet been probed. The comparatively large effective masses probed in virtually all group VI TMDs studied thus far, strongly suggests that interaction effects may play a significant role in this class of materials, for carriers in both conduction and valence bands.

3.2 DEVICE FABRICATION

All samples discussed in this Chapter are bottom-contact, dual-gate samples fabricated using $MoSe_2$ flakes exfoliated from synthetic crystals purchased from HQ Graphene. Table 3.1 shows optical micrographs and summarizes all samples used in this study along with key measurables. All three bilayer $MoSe_2$ samples (B1, B2, B3) are fabricated using Structure #3, as outlined in Figure 2.16, sample B2 uses graphene gates in place of metal gates. Monolayer $MoSe_2$ sample A1 is fabricated using Structure #3, while

the other monolayer sample A2 uses structure #2, and correspond to sample Se-2 described Chapter 2 [Table 2.2]. Section 2.3.1 provides a detailed discussion of the processing steps, including dry transfer of 2D layers, followed to fabricate bottom-contact, dual-gate samples with metal gates. The fabrication process used for samples using graphite gates, is outlined in the latter portion of this Section. In samples A1, A2 and B1 $MoSe_2$ flakes are not etched and are larger than the top-gate, therefore the channel width is defined by the top-gate. In samples B2 and B3 the top-gate covers completely the bilayer $MoSe_2$ flake, therefore the channel width is defined by the flake size. In sample B2 the graphite gate covers a largely rectangular $MoSe_2$ flake, and in sample B1 the $MoSe_2$ flake is etched in a Hall-bar shape. In all cases L is the center to center distance between adjacent contacts and is defined by mask used to pattern bottom contacts; W and L for all samples are reported in Table 3.1.

In the following we are going to discuss specific strategies and techniques used for the fabrication of magnetotransport samples, namely discuss the device fabrication with graphene gates and the process used to select mono- and bilayer $MoSe_2$ flakes and obtain high mobility samples. Figure 3.1 details the entire fabrication process for sample with graphite gates. As introduced in Section 2.3.1 the fabrication articulates in two parts, we first assemble the bottom-gate stack, including bottom contacts, then then we assemble the top-gate stack, pick-up the $MoSe_2$ layer and complete the final structure. Dry transfers of 2D layers or stack thereof are conducted as described in Section 2.3.1 and transfer process details are omitted. We begin exfoliating natural graphite ("Flaggy Flake" from NGS Naturgraphit GmbH), until we isolate, using optical microscope and AFM, a large, uniform, and clean graphite flake 5-10 nn-thick, which would serve as bottom-gate electrode [bottom-graphite Figure 3.1(a)]. Comparably sized hBN flakes (10-20 nm-thick) are selected and dry transferred onto the bottom-graphite [Figure 3.1(b)]. Once the transfer is completed, the stack undergoes UHV anneal at 350°C to remove organic residues. A part of the bottom graphene flake is intentionally not covered by hBN, to fabricate a top-contact to the bottom graphite. Top-contacts to the bottom-graphite and bottom-contacts (Cr-Pd 3-12 nm-thick) are patterned using EBL and EBME, as show in Figure 3.1(c). After metallization, the stack undergoes an UHV anneal at 350°C to remove organic residues.

96
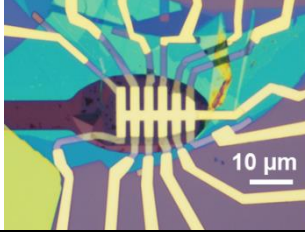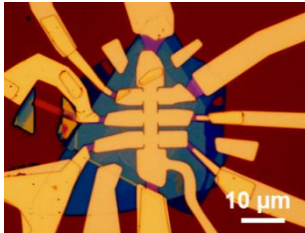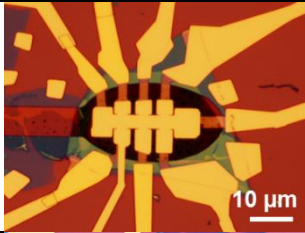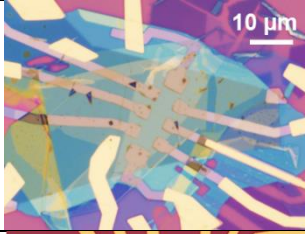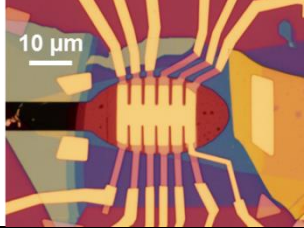
#	Type [Other names]	W, L (µm)	μ_q (cm²/Vs)	C_{TG} (nF/cm²)	C_{BG} (nF/cm²)	Optical Micrograph
A1	Monolayer, Structure #3, Gate defined Hall-bar Metal gates, [(26) BG5]	2, 3.25	1050	289	133	
A2	Monolayer, Structure #2, Gate defined Hall-bar, Metal gates, [(1) jhBN 121, Se-2 in Chapter 2]	5, 3	1100	312	-	
B1	Bilayer, Structure #3, Gate defined, Hall-bar Metal gates, [(19) BG1]	5, 3	1650	217	147	
B2	Bilayer, Structure #3, Flake defined Hall-bar Graphite gates, [(22) G1]	13, 5	2200	283	121	
B3	Bilayer, Structure #3, Etched flake Hall-bar Graphite gates, [(28) BG7]	4, 3.25	1550	269	236	

Table 3.1: List of monolayer MoSe₂ based devices discussed in Chapter 3; values of μ_q, corresponding to the mobility extracted from the *B*-field onset of the SdH oscillations, is obtained at $n \sim 5 \times 10^{12}$ cm⁻² in bilayer samples, and at $n \sim 11 \times 10^{12}$ cm⁻² in monolayer samples at $T = 0.3\text{-}1.5$ K.
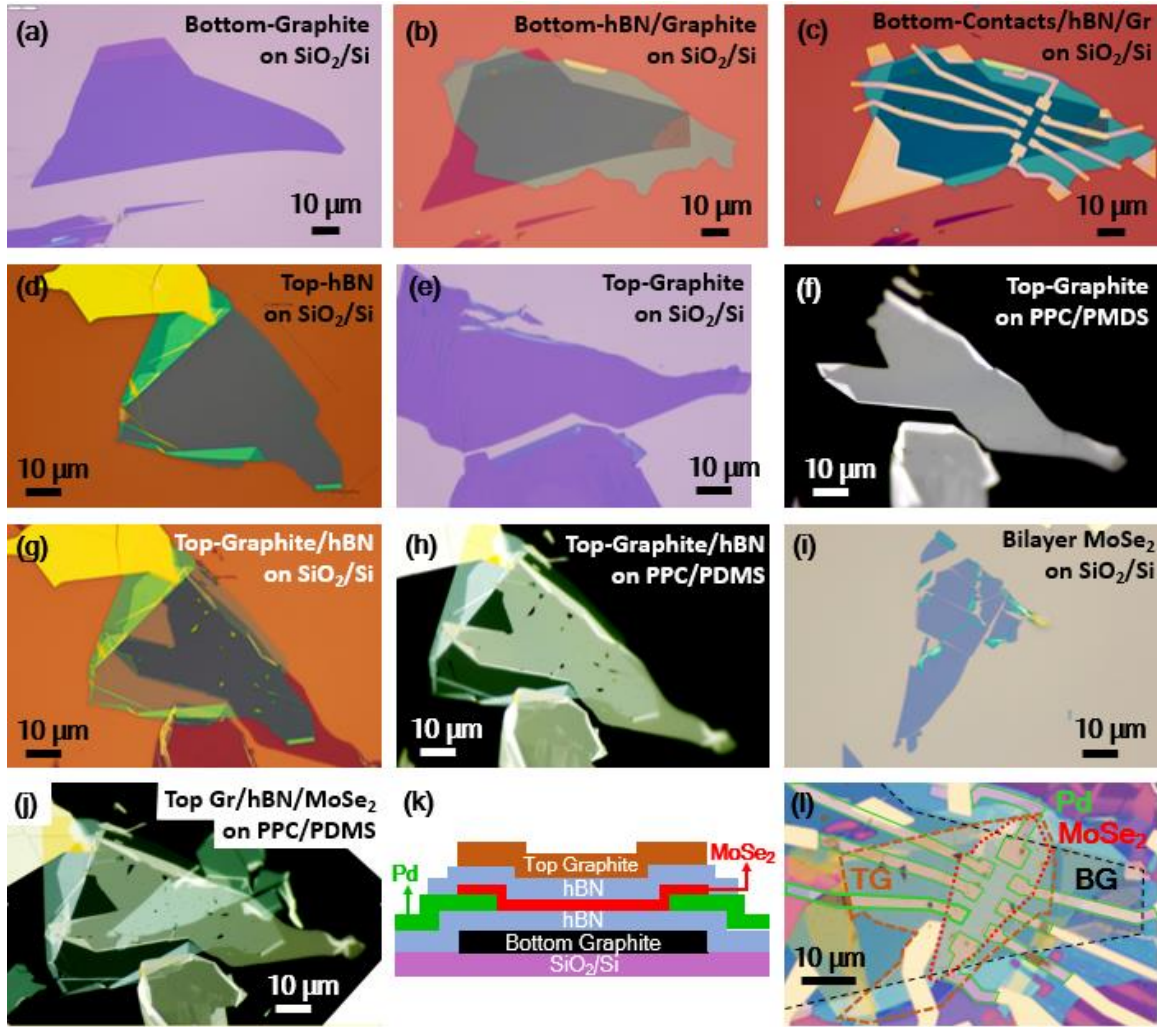
Figure 3.1: Optical micrograph showing (a) bottom-graphite exfoliated on SiO_2/Si; (b) hBN bottom-dielectric (24 nm-thick) transferred onto the bottom-graphite; (c) Cr-Pd (3-12 nm-thick) bottom-contacts and bottom-graphite top-contact patterning; (d) hBN top-dielectric (11 nm-thick) and (e) top-graphite exfoliated on SiO_2/Si; (f) top-graphite stack imaged on PPC/PDMS after pick-up; (g) top-graphite/hBN stack (h) on SiO_2/Si, after graphite transfer and (h) on PPC/PDMS after pick-up; (i) bilayer $MoSe_2$ exfoliated on SiO_2/Si; (j) top-graphite/hBN/$MoSe_2$ stack imaged on PPC/PDMS after sequential pick-up. (k) Schematic cross-section and (l) optical micrograph of a completed bottom-contact, graphite dual-gate, hBN-encapsulated $MoSe_2$ device. Outlines of different colors mark the $MoSe_2$ flake (red), Pd contacts (green), top (orange) and bottom (black) graphite gates.

Once we completed the bottom-gate stack, we exfoliate and select a hBN flake (10-15 nm-thick) which would serve as top-dielectric [top-hBN Figure 3.1(d)] and a graphite flake (5-10 nm-thick) which would serve as the top-gate electrode [top-graphite Figure 3.1(e)]. Both flakes' topography is inspected with AFM to assure uniform and clean layers. The best choice for a top-graphite layer is a flake larger than 10×20 μm^2, which is the typical size of MoSe$_2$ flakes, but smaller than the top-hBN dielectric, to avoid successive etching. Using a PPC/PDMS handle we pick-up [Figure 3.1(f)] and release the top-graphite onto the top-hBN [Figure 3.1(g)]. It should be noted that picking up bare graphite flakes, even if easier than pick-up mono- and bilayer graphene, is a low-yield process [84]. Isolated uniform flakes are easiest to pick-up. Another possibility is to pick-up graphite flakes with another hBN flake, but it adds considerable complication. After UHV anneal at 350°C, the top graphite/hBN stack topography is measured with AFM to identify wrinkle free regions [118], which will be aligned with the MoSe$_2$ flake. Using a different PPC/PMDS stamp the top-graphite/hBN stack is picked up [Figure 3.1(h)]. As introduced for the sole top-hBN in Section 2.3.1, the top-graphite/hBN stack can be released onto the exfoliated MoSe$_2$ [Figure 3.1(i)] and the whole stack can be picked up again after UHV anneal, or the MoSe$_2$ can be directly picked up. Once formed, the top-graphite/hBN/MoSe$_2$ stack on PPC/PDMS [Figure 3.1(j)] is aligned and released on the bottom gate stack [Figure 3.1(c)].

The device is completed after an UHV anneal at 350°C, patterning the contact extensions and the top-graphite top-contact using EBL and EMBE (5-30-30 nm-thick Cr-Pd-Au), and etching any potential leakage path between graphite and MoS$_2$ layers using EBL and O$_2$ RIE. Figure 3.1(k) and 3.1(l) show a cross-section schematic and optical micrograph, respectively, of the completed bilayer sample B2. To understand how each layer overlap, the cross-section schematic and the different layers outlines in the optical micrograph are marked with different colors. The fabrication process for samples with graphite gates is considerably more complex than for samples with metal gates, particularly as it concerns the fabrication of the top-gate stack. Exfoliation of graphite gates is a random process and does not provide flexible shapes to work with. Etching top- or bottom-graphite

flakes is not an option as it introduces organic residues and renders graphite pickups very difficult. Devices with metal-gates and graphite-gates show similar magnetotransport results, while graphite-gated samples show improved at low T mobility [Table 3.1]. The $MoSe_2$ flakes used to fabricate the samples discussed in this Chapter were not annealed after exfoliation, when not hBN encapsulated.
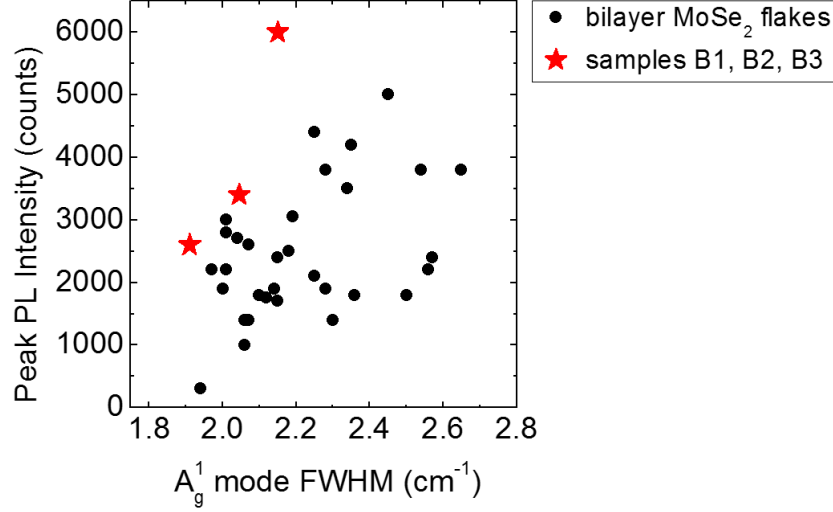
Figure 3.2: Peak PL intensity vs A^1_g mode FWHM, measured in bilayer $MoSe_2$ flakes, using an excitation wavelength of 532 nm. Counts are relative PL intensity unit for our Renishaw InVia spectrometer.

As discussed in Section 2.3.1, mono- and bilayer $MoSe_2$ flakes are identified using a combination of Raman and PL spectroscopy [Section 1.1.4.2 and 1.1.5.2] probed at RT using an excitation wavelength of 532 nm, with an excitation power ~100 µW (~10 µW) measured at the sample in Raman (PL) mode. The large variation of PL intensity between mono- and bilayer $MoSe_2$ is instrumental in the identification of flakes of different thickness. Figure 3.2 shows the peak PL intensity as a function of the A^1_g mode FWHM measured in many bilayer $MoSe_2$ samples. After probing the magnetotransport in fabricated samples, we can correlate the emergence of SdH oscillations and high mobility to the samples fabricated with $MoSe_2$ bilayer flakes that concurrently present high peak PL intensity and low A^1_g mode FWHM, as shown in Figure 3.2. Both measurable indicators correlate with material properties, namely the Raman peak width correlates with the

crystallinity [119], while stronger PL yield has been recently correlated with less defective TMD flakes, as defect sites promote non-radiative recombination [120]. For monolayer MoSe$_2$ samples we follow a similar correlation. Monolayer samples have shown SdH oscillations for peak PL intensity > 100,000 counts, and A^1_g mode FWHM < 2.2 cm^{-1}. Counts are intended as relative PL intensity unit, for comparing PL spectra measured using our Renishaw InVia spectrometer. It should be noted that typically the A^1_g mode FWHM is larger in monolayers compared to bilayers, even when measured on the same flake with different thickness terraces.

3.3 SHUBNIKOV-DE HAAS OSCILLATIONS AND QUANTUM HALL STATES

The introduction of Pd bottom contacts along with MoSe$_2$ electrostatic doping at positive V_{TG}, discussed in Section 2.3.3.2, enables n-type Ohmic contacts to mono- and bilayer MoSe$_2$, allowing us to probe R_{xx} and R_{xy} [Figure 1.17] using small signal, low-frequency lock-in techniques at temperatures down to $T = 0.3$ K, and magnetic fields up to 35 T. In one sample, monolayer A2, we were unable to use lock-in measurements, and instead adopted a quasi-AC "Delta mode" characterization technique developed by Keithley, using 6221 current source and 2182A nanovoltmeter. The transverse and longitudinal voltages are measured as the current (I) is alternated between $+I$ and $-I$ in a square wave, averaging the concurrent differential voltage reading ($+V_R$, $-V_R$) over multiple periods [121].

Figure 3.3 shows examples of R_{xx} and R_{xy} as function of the perpendicular B-field in monolayer MoSe$_2$ sample A1 [panel (a)], and bilayer MoSe$_2$ sample B1 [panel (b)], both measured at fixed electron density. The R_{xx} vs B data of Figure 3.3(a), measured at $T = 0.3$ K, $V_{TG} = 7.5$ V and $V_{BG} = -7$ V, show clear SdH oscillations developing at $B > 9$ T. The electron density: $n = 6.8 \times 10^{12}$ cm^{-2} is extracted from the R_{xy} vs B data of Figure 3.3(a), using Equation 1.10. At high B-fields we observe quantum Hall states developing at $\nu = 8$, 10, 12; where $\nu = hn/(eB_\nu)$, B_ν is the magnetic field corresponding to the QHS at filling factor ν. Magnetotransport data of bilayer in Figure 3.3(b), are measured at $T = 0.3$ K, V_{TG} = 9 V and $V_{BG} = -6$ V, and show well-defined SdH oscillations starting at $B \sim 6$ T. The

electron density is $n = 4.9 \times 10^{12}$ cm^{-2}. Similar to the monolayer case, at high B-field QHSs develop at predominantly even filling factor ($\nu = 6, 8, 10$), indicating an apparent two-fold Landau level degeneracy in both mono- and bilayer samples. From the B-field corresponding to the onset of SdH oscillations (B_q) we can extract a "quantum mobility" value: $\mu_q \sim 10^4/B_q$ in units of cm^2/Vs; $\mu_q \simeq 1100$ cm^2/Vs for monolayer sample A1, and $\mu_q \simeq 1650$ cm^2/Vs for bilayer sample B1. Values of μ_q of each sample probed in this study are included in Table 3.1.
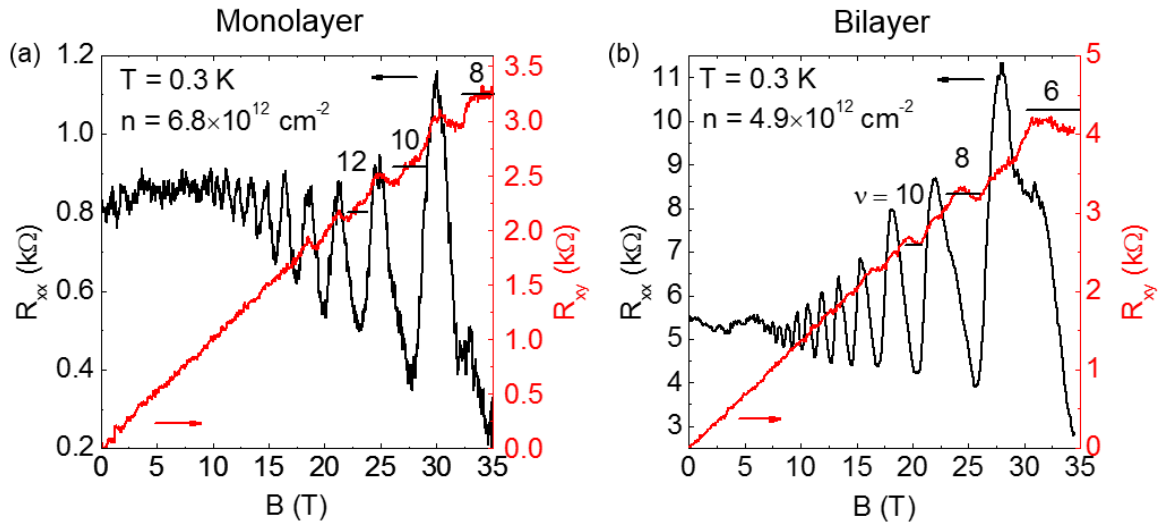
Figure 3.3: (a) R_{xx} (left axis) and R_{xy} (right axis) vs B measured at $T = 0.3$ K, (a) in monolayer MoSe2 A1 ($n = 6.8 \times 10^{12}$ cm^{-2}) and (b) in bilayer MoSe$_2$ sample B1 ($n = 4.9 \times 10^{12}$ cm^{-2}). Developing quantized R_{xy} plateaus are marked in each panel. Reprinted panels (a), (b) with permission from S. Larentis *et. al.* Phys. Rev. B 97, 201407 (2018), Ref. [102], © 2018 by the American Physical Society.

3.4 CARRIER DENSITY DEPENDENCE: LANDAU LEVEL DEGENERACY AND SUBBANDS

In this Section we study the magnetotransport at different electron densities, to characterize the LL degeneracy, and determine when and if carriers populate different subbands. We tune the electron density by varying V_{BG} at a constant V_{TG} value. This combination of gate-biases leaves the contact resistance largely unaffected. Figure 3.4 show R_{xx} vs B measured at different V_{BG}, in monolayer A1 at $V_{TG} = 8$ V, $T = 0.3$ K [panel

(a)], and in bilayer B2 at V_{TG} = 6.5 V, T = 1.5 K, respectively [panel (b)]. The SdH oscillations of Figure 3.4 are periodic as function of B^{-1}, and their frequency is proportional to the electron density of the 2DES [Section 1.2.2]. Figures 3.5(a) and 3.6(a) show the Fourier transform (FT) amplitude vs frequency corresponding to R_{xx} vs B^{-1} data of Figure 3.4(a) and 3.4(b), respectively. The FT date are obtained by first subtracting a polynomial background of the 3rd or 5th order from the R_{xx} vs B^{-1} data to center the oscillations around zero, followed by a Hamming window multiplication, and a fast FT algorithm.
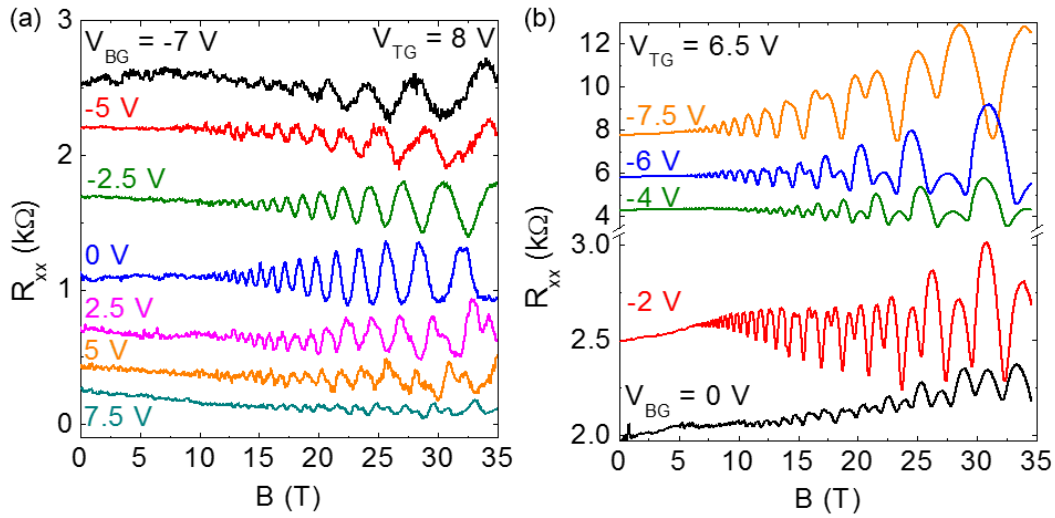
Figure 3.4: (a) R_{xx} vs B measured at various V_{BG} values, V_{TG} = 8 V, and T = 0.3 K in monolayer MoSe$_2$ A1. (b) R_{xx} vs B measured at various V_{BG} values, V_{TG} = 6.5 V, and T = 1.5 K in bilayer MoSe$_2$ B2. Traces in panels (a) and (b) are offset for clarity. Reprinted panels (a), (b) with permission from S. Larentis *et. al.* Phys. Rev. B 97, 201407 (2018), Ref. [102], © 2018 by the American Physical Society.

Figure 3.5(a) data reveal one principal V_{BG} dependent peak at a frequency f for V_{BG} ≤ 0 V. For V_{BG} > 0 V, f shows a weaker V_{BG} dependence, and a second, lower frequency peak (f') emerges, indicating a second subband is populated. Symbols in Figure 3.5(a) mark the f and f' peaks for all V_{TG} probed and FT amplitude spectra are appropriately offset to account for V_{BG} scaling. In a 2DES the carrier density-frequency relation is as follows:

$$n = g \frac{e}{h} f \qquad\qquad 3.1$$

where g is the LL degeneracy. Each subband electron density, $2\left(\frac{e}{h}\right)f$ and $2\left(\frac{e}{h}\right)f'$, and the total density $2\left(\frac{e}{h}\right)(f + f')$, along with the n values determined from the R_{xy} slope at low B-fields [Equation 1.10] are summarized as a function of V_{BG} in Figure 3.5(b). The electron density determined from the SdH oscillation frequency is obtained assuming two-fold degenerate LLs ($g = 2$). The total n displays a linear dependence on V_{BG}. At $n > 12.5 \times 10^{12}\,\mathrm{cm}^{-2}$ the second subband (f') is populated, as marked in Figure 3.5(b).
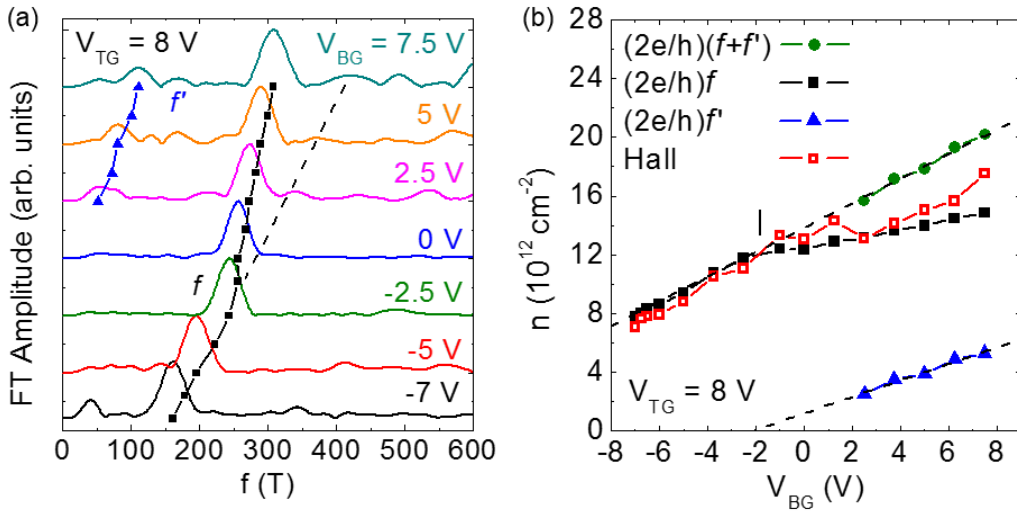
Figure 3.5: (a) Normalized FT amplitude vs frequency corresponding to R_{xx} vs B data of Figure 3.4(a). Symbols mark f (squares) and f' (triangles), including at intermediate V_{BG}. The dashed line corresponds to the linear extrapolation of f data at $V_{BG} < 0$ V. The traces in panel (a) are offset proportionally to V_{BG}. (b) n vs V_{BG} measured in monolayer MoSe$_2$ A1 at $V_{TG} = 8$ V. The onset of the upper spin-split subband population is marked, determined from the linear extrapolation of $2\left(\frac{e}{h}\right)f'$ data (dashed line). The total carrier density in the system $2\left(\frac{e}{h}\right)(f + f')$ is linearly proportional to V_{BG} and matches the linear extrapolation of $2\left(\frac{e}{h}\right)f$ data at $V_{BG} < 0$ V, when only one subband is occupied. Reprinted panels (a), (b) with permission from S. Larentis *et. al.* Phys. Rev. B 97, 201407 (2018), Ref. [102], © 2018 by the American Physical Society.

The SOI leads to a splitting of the spin-up and spin-down states at the K point in TMDs. This splitting is ≈ 0.2 eV and ≈ 25 meV for monolayer $MoSe_2$ VB [16] and CB [12], [122], [123], respectively. We associate the peaks f and f' in Figure 3.5 with the population of the lower and upper CB spin-split bands of monolayer $MoSe_2$, respectively. The deviation between $2\left(\frac{e}{h}\right)(f + f')$ obtained from FT and Hall data at $V_{BG} > 0$ V in Figure 3.5(a), may be associated to a mobility difference between the two subbands [124], [125].
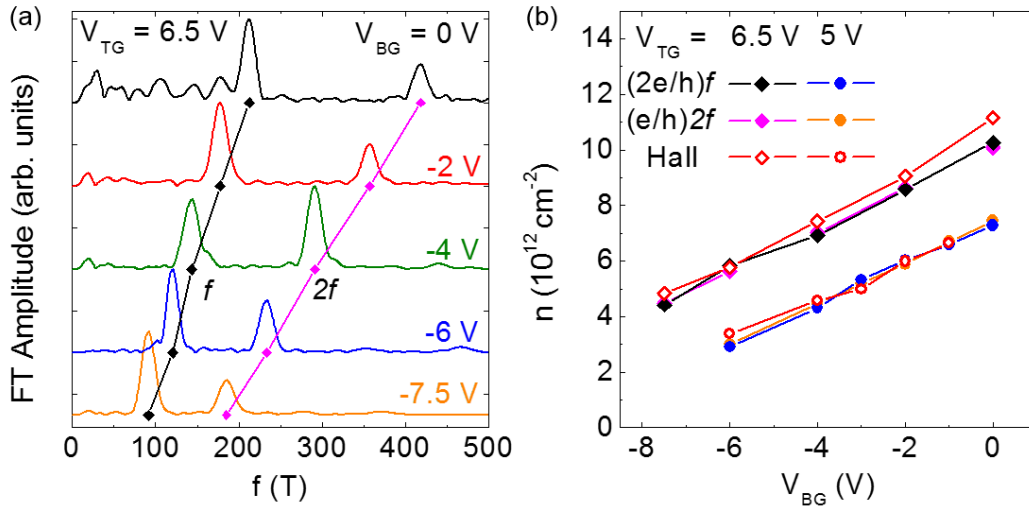
Figure 3.6: (a) Normalized FT amplitude vs frequency corresponding to R_{xx} vs B data of Figure 3.4(b). Black and pink symbols mark f and $2f$, respectively. The traces in panel (a) are offset proportionally to V_{BG}. (b) n vs V_{BG} measured in bilayer $MoSe_2$ B2 at $V_{TG} = 6.5$ V (diamonds) and $V_{TG} = 5$ V (circles). Solid (open) symbols correspond to n determined from FT (R_{xy}) data. Reprinted panels (a), (b) with permission from S. Larentis *et. al.* Phys. Rev. B 97, 201407 (2018), Ref. [102], © 2018 by the American Physical Society.

Figure 3.6(a) data, corresponding to bilayer $MoSe_2$, reveal one principal peak at a frequency f, and its second harmonic ($2f$) indicating a single subband is occupied. The f value increases linearly with V_{BG}, consistent with FT data of monolayer $MoSe_2$, presented in Figure 3.5(a), where only the lowest spin-split subband populated. Figure 3.6(b) shows a comparison between electron densities calculated using the f and $2f$ values of Figure 3.6(a), $2\left(\frac{e}{h}\right)f$ and $\left(\frac{e}{h}\right)2f$, respectively, and n values determined from the R_{xy} slope at low

105

B-fields as a function of V_{BG} [Equation 1.10]. The agreement between *n* obtained from Hall and FT data for bilayer samples confirms the two-fold LL degeneracy (*g* = 2), also consistent with monolayer data of Figure 3.5(b).

3.5 ELECTRON EFFECTIVE MASS

Using magnetoresistance measurements, we measure the electron effective mass in mono- and bilayer MoSe$_2$. The effective mass represents a key bandstructure property and determines the electron transport properties. Comparing the *m** of MoSe$_2$ with other known 2D systems, we can gauge the relative strength of electron-electron interaction in this 2DES. For example considering only the exchange contribution to account for many-body effects, on top of the non-interacting kinetic energy, a 2D system with heavier *m** would see stronger interaction effects compared to a system with lighter *m**, at the same carrier density.

Figure 3.7(a) shows the SdH oscillations temperature dependence at $n = 4.9 \times 10^{12}$ cm^{-2} for bilayer MoSe$_2$ sample B1, displaying a clear reduction in the oscillations amplitude (ΔR_{xx}) as the *T* is increased. From *T* dependence of the ΔR_{xx} we can extract the electron effective mass, as ΔR_{xx} is proportional to the Dingle factor [126]:

$$\Delta R_{xx} \propto \frac{\xi}{sinh\ \xi}; \quad \text{where } \xi = \frac{2\pi^2 k_B T m^*}{\hbar e B} \qquad 3.2$$

To extract *m** we first obtain the FT amplitude spectra [Figure 3.7(b)], for the R_{xx} vs *B* data of Figure 3.7(a). The FT amplitude spectra is obtained as discussed in Section 3.4, and features a decreasing amplitude as *T* is increased. A band pass filter centered around *f* , corresponding to shaded region of Figure 3.7(b), is applied to FT data to eliminate other frequency components. Figure 3.7(c) shows ΔR_{xx} vs B^{-1} data at different *T*, obtained by applying an inverse FT algorithm to the filtered FT amplitude spectra of Figure 3.7(b). At fixed *B* fields corresponding to the oscillation peaks of Figure 3.7(c), we obtain ΔR_{xx} vs *T* datasets, shown in Figure 3.7(d), which are then fit to the Dingle factor [Equation 3.2], to obtain *m** values. We repeat the same procedure to characterize the *m** at different electron densities and across different mono- and bilayer samples.
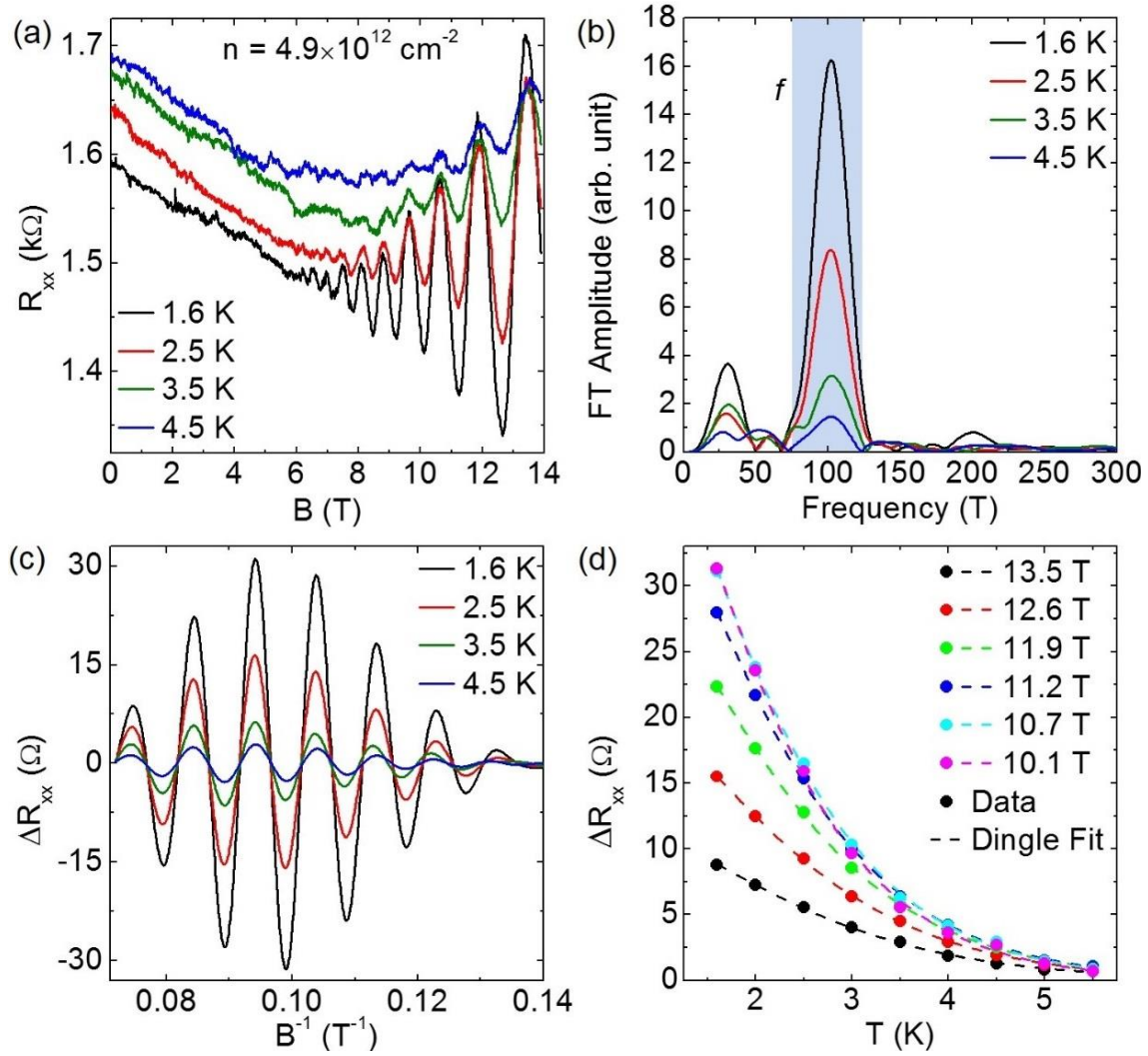
Figure 3.7: (a) R_{xx} vs B measured at various T values, at $n = 4.9 \times 10^{12}$ cm^{-2} in bilayer MoSe$_2$ B1. (a) FT amplitude vs frequency obtained from R_{xx} vs B^{-1} data of panel (a). (c) ΔR_{xx} vs B^{-1} calculated from the inverse FT of panel (a) data, using a bandpass filter centered around f [shaded region in panel (b)]. (d) ΔR_{xx} vs T at different fixed B (symbols), which coincide with the peaks of ΔR_{xx} vs B^{-1} data of panel (c). Dingle factor fit to the experimental data (dashed lines). Reprinted panels (a)-(d) with permission from S. Larentis *et. al.* Phys. Rev. B 97, 201407 (2018), Ref. [102], © 2018 by the American Physical Society.

Figure 3.8 shows m^*/m_e vs B data for monolayer A1 and bilayer B1, B2 at n ranging between 4.9−12.4×10^{12} cm^{-2}, where only the lower spin-split CB at the K point is probed. The average $m^*/m_e = 0.8$ is largely insensitive to n and B. Error bars represent the 95% confidence bounds of the Dingle factor fit. Theoretical calculations of m^*/m_e,

underestimate the experimental value and range between $0.50 - 0.56$ [12], [122]. The measured effective mass value is comparatively large, even when compared to other group IV TMDs. For example, K-valley effective masses measured for holes in mono-, bilayer WSe_2 and electrons in bilayer MoS_2 reveal $m^*/m_0 = 0.45$ [110], and 0.55 [114], respectively.

The measured m^* values, and the corresponding density of states ($m^*/\pi\hbar^2$) allows us to determine the CB spin-splitting ($2\Delta_{cb}$) in monolayer $MoSe_2$. Considering the threshold density for the population of the upper CB subband $n_T = 12.5 \times 10^{12}\,cm^{-2}$ [Figure 3.5(b)], we obtain $2\Delta_{cb} = n_T \cdot \pi\hbar^2/m^* = 37$ meV, a value comparable to, albeit larger than theoretical calculations (≈ 25 meV) [12], [20], [122], [123].
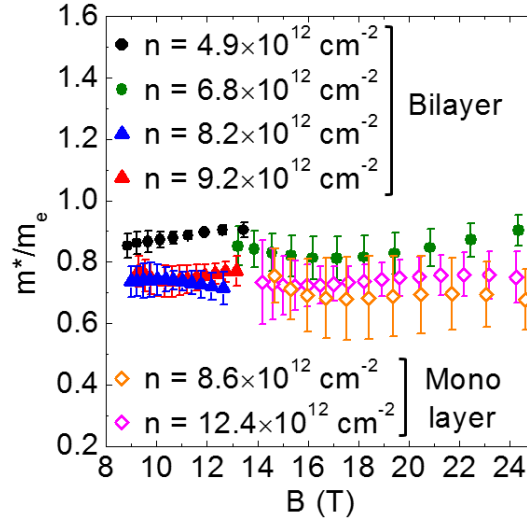
Figure 3.8: m^*/m_e vs B measured at different n in monolayer $MoSe_2$ A1 ($\diamond$), bilayer $MoSe_2$ B1 ($\bullet$), and B2 ($\blacktriangle$). Reprinted figure with permission from <u>S. Larentis et. al. Phys. Rev. B 97, 201407 (2018)</u>, Ref. [102], © 2017 by the American Physical Society.

3.6 K-VALLEY ELECTRONS

Bandstructure calculations indicate that for $MoSe_2$ CB minima are expected to be at the K point in monolayer [Figure 1.4], and at the Q point in bulk [Figure 1.5] [4], [8]. The data of Figures 3.5, 3.6 and 3.8 allow us to unambiguously determine the CB minima in mono- and bilayer $MoSe_2$. The two-fold LL degeneracy observed in both mono- and

bilayer MoSe$_2$ samples is consistent with CB minima at the K point, as SdH oscillations of carriers at the Q point would show three- or six-fold degenerate LLs [115]–[117]. The similar m^* values measured for both mono- and bilayer MoSe$_2$ further support this conclusion [Figure 3.8]. In group VI TMD bilayers, the weak inter-layer coupling of K-valley carriers leads to two distinct subbands for each layer [110], with densities that can be independently controlled by V_{TG} and V_{BG}. For $V_{TG} > 0$ V and $V_{BG} \leq 0$ V only the top layer is populated, and the bilayer MoSe$_2$ can be effectively treated as a monolayer. The absence of a beating pattern in bilayer MoSe$_2$ SdH oscillations up to $n = 11.0 \times 10^{12}$ cm^{-2} [Figure 3.4(b)] indicates the electrons populate the lower spin-split subband of the top layer.

The two-fold degenerate LLs structure observed in mono- and bilayer MoSe$_2$ samples, when only the lower K-valley spin-split subband is populated, is notably different from what is observed in monolayer graphene, a 2D material with band extrema at the K-point and hexagonal lattice, where four-fold, spin and valley degenerate, LLs are observed [Section 1.2.2.1], [52]. In group VI TMD monolayers a combined effect of broken inversion symmetry and strong SOI lifts spin-valley degeneracy, observed graphene, i.e. spin-splits bands, and yields carriers with coupled spin and valley degrees of freedom at the K point, which in perpendicular B-field result in two-fold degenerate LLs, as is also reported for holes mono- and bilayer WSe$_2$ [110]. Our results highlight a symmetry between spin-valley coupled conduction and valence bands, which is exploited in valley selective optical studies [Figure 1.4(c) and 1.4(d)], [106]. It should be noted that in hole doped group VI TMDs, where $2\Delta_{vb} >> 2\Delta_{cb}$ the population of the lower spin-split band at the K point in the VB is out of reach using electrostatic gating. Given $E_{K\Gamma} < 2\Delta_{vb}$, the population of a second subband at Γ point is more likely in few-layer, hole doped group VI TMDs [Table 1.3].

3.7 ELECTRON DENSITY DEPENDENT FILLING FACTOR SEQUENCE

Now we turn to the investigation of the filling factor sequence as function of the electron density in both mono- and bilayer MoSe$_2$. We define an FF sequence to be even

or odd, when R_{xx} minima occur predominantly at even or odd FFs. Recent group VI TMDs magnetotransport studies indicate that a an interaction enhanced Zeeman splitting determines a density dependent variation of FF sequence parity [111], [113], [114]. Interaction effects are expected to be significant, in the range of carrier densities probed here, in both electron and hole doped group VI TMDs 2D systems with comparably large m^*, including MoSe$_2$.

Figure 3.9(a) shows R_{xx} vs ν at different n values between $2.9 - 11.0 \times 10^{12}\,\text{cm}^{-2}$, measured at $T = 1.5$ K in bilayer B2. At a high carrier density, $n = 11.0 \times 10^{12}\,\text{cm}^{-2}$, R_{xx} shows strong minima at odd FFs. and As n is reduced to $8.6 \times 10^{12}\,\text{cm}^{-2}$ we observe developing R_{xx} minima at even FFs. At $n = 7.0 \times 10^{12}\,\text{cm}^{-2}$, the R_{xx} minima at odd and even FFs are of equal strength up to $\nu = 36$, marking the transition between odd and even FF sequences. As n is further lowered to $5.6 \times 10^{12}\,\text{cm}^{-2}$ the FF sequence turns predominantly even, with R_{xx} minima at odd FFs becoming less prominent. At $n = 4.5 \times 10^{12}\,\text{cm}^{-2}$ R_{xx} minima at odd FFs are absent. At the lowest $n = 2.9 \times 10^{12}\,\text{cm}^{-2}$ the FF sequence turns odd, evidence of another FF sequence parity variation, from even to odd. For R_{xx} vs B data that resolve all FFs (e.g. at $n = 7.0 \times 10^{12}\,\text{cm}^{-2}$), the FT amplitude spectra shows a strong second harmonic $(2f)$, with an amplitude comparable or higher than f, as shown in Figure 3.6(a) data at $V_{\text{BG}} = -4$ V.

Figure 3.9(a) illustrates FF sequence parity transitions as function of the carrier density. However in our samples a set of gate biases (V_{TG} and V_{BG}) concomitantly determine the electron density and the transverse electric-field (E) parallel to the MoSe$_2$ crystal c-axis. In order to confirm that FF sequence parity transitions are a carrier density dependent effect we should verify whether or not the FF sequence is also a function of the transverse E-field, defined as follows:

$$E = \frac{|C_{TG}V_{TG} - C_{BG}V_{BG}|}{2\epsilon_0} \qquad 3.3$$
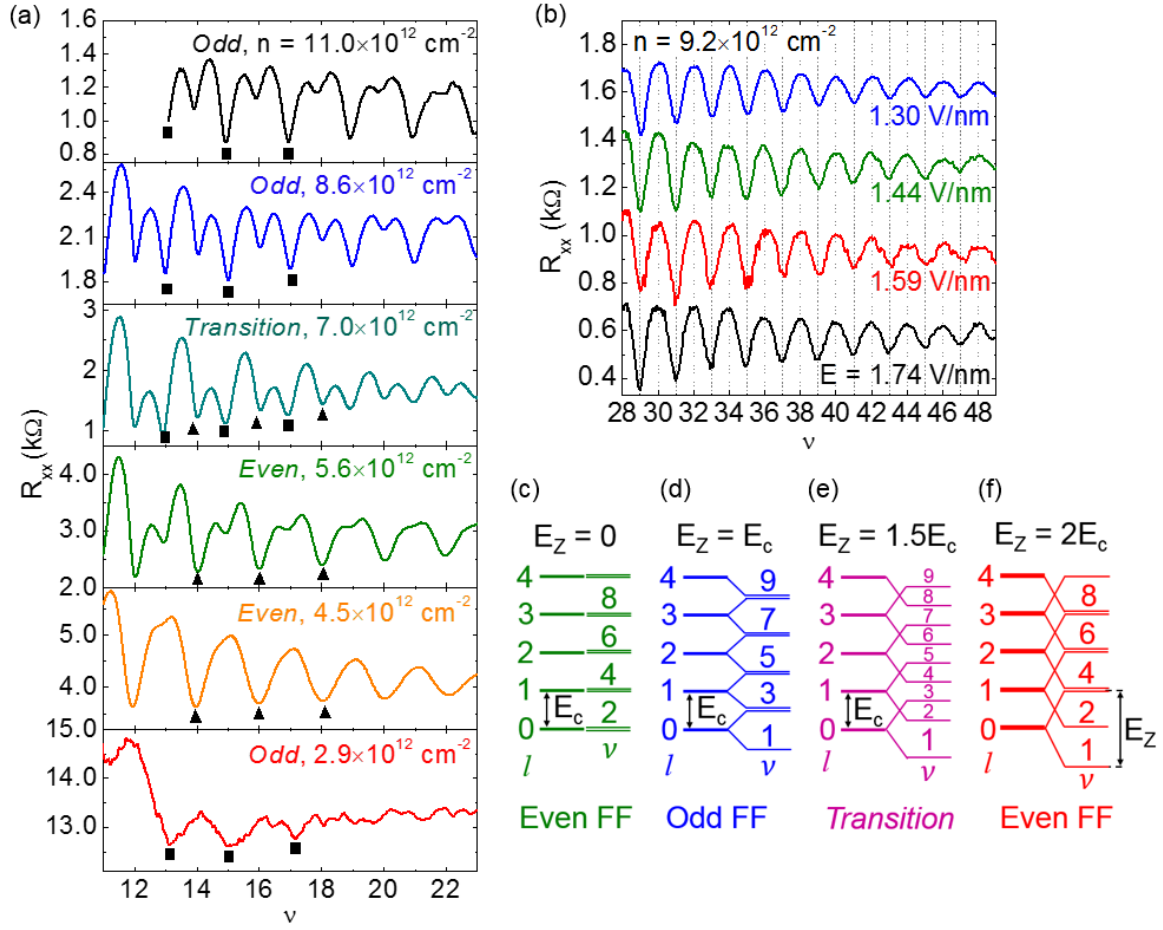
Figure 3.9: (a) R_{xx} vs ν measured at n values between $2.9-11.0\times10^{12}$ cm^{-2}, $T = 1.5$ K in bilayer MoSe$_2$ B2. The FF sequence undergoes parity transitions at $n = 7.0 \times 10^{12}$ cm^{-2}, and $n = 4.0 \times 10^{12}$ cm^{-2}. The triangles (squares) mark R_{xx} minima at even (odd) FFs. (b) R_{xx} vs ν measured in bilayer MoSe$_2$ B2 at $T = 1.5$ K and $n = 9.2 \times 10^{12}$ cm^{-2}, and at different E-fields. The traces are offset for clarity. LL structure obtained using Equation 3.5 for $E_Z = 0$ (c), $E_Z = E_c$ (d), $E_Z = 1.5E_c$ (e) and $E_Z = 2E_c$ (f); E_Z/E_c determines the FF sequence parity. Reprinted panels (a), (b) with permission from S. Larentis *et. al.* Phys. Rev. B 97, 201407 (2018), Ref. [102], © 2018 by the American Physical Society.

Figure 3.9(b) shows R_{xx} vs ν measured at different E ranging between $1.30 - 1.74$ V/nm, at a fixed $n = 9.2 \times 10^{12}$ cm^{-2}, and $T = 1.5$ K in bilayer MoSe$_2$ B2. The R_{xx} minima are insensitive to changes in the transverse E-field, suggesting an E-field independent band and LL structure in the range of values probed here. For R_{xx} vs ν data of Figure 3.9(a) the E-field varies between 1.17 and 1.64 V/nm, an E-field range comparable with Figure 3.9(b)

data, indicating that indeed FF sequence parity transitions are a carrier density dependent effect. A similar E-field insensitivity is also observed for mono- and bilayer WSe$_2$ [111]. Conversely, magnetotransport studies in trilayer WSe$_2$ have shown SdH oscillations which respond to the E-field, stemming from an E-field tunable population of Γ and K valleys [127].

To better understand the n-dependent FF sequence, we write the Landau level energies for the conduction band, including both cyclotron and Zeeman terms, as introduced in Section 1.2.2:

$$E_{l,\tau s} = \tau s \Delta_{cb} + \left(l + \frac{1}{2}\right) E_c + \frac{s g_s \mu_B B}{2} + \frac{\tau g_v \mu_B B}{2} \qquad 3.4$$

where $l = 0, 1, 2, \ldots$ is the LL orbital index, $s = \pm 1$ corresponds to the electron spin ↑ and ↓, $\tau = \pm 1$ labels K and K' valleys, $E_c = \hbar \omega_c$ is the cyclotron energy, $\mu_B = e\hbar/(2m_e)$ is the Bohr magneton, and g_v, g_s are the valley and spin g-factors, respectively. The $\tau s \Delta_{cb}$ term describes the spin-split CB minima [Figure 1.4(c)], where the LLs originate. The $\tau s = \pm 1$ doublets lead to two LL fan diagrams with an energy separation of $2\Delta_{cb}$ at $B = 0$ T. We assume that electrons reside in the lowest spin-split band ($\tau s = -1$), where the total, spin and valley LL Zeeman energy is $E_Z|_{\tau s=-1} = g^* \mu_B B$; $g^* = g_v - g_s$ is the effective g-factor for LLs of the lowest CB spin-split subband. The LL energies of the $\tau s = -1$ group write:

$$E_{l,\tau s} = \left(l + \frac{1}{2}\right) E_c + \frac{\tau g^* \mu_B B}{2} \qquad 3.5$$

Here we use the single-band model convention in which all LLs are two-fold degenerate in absence of Zeeman splitting, as shown by the LL structure of Figure 3.9(c) [122], [128]. Using a model in which the $l = 0$ is non-degenerate, is equivalent to g^* offset by $2m_e /m^*$ [104]. From now on, we relabel $E_Z|_{\tau s=-1} = E_Z$. Using Equation 3.5 we construct the LL energy diagrams of Figure 3.9(d) to 3.9(f), obtained for different values of $E_Z = 1, 1.5, 2$. In absence of Zeeman splitting ($E_Z = 0$) the FF sequence would even [Figure 3.9(c)]. Using this model we can explain the FF sequence parity transitions with a variation in the Zeeman-to-cyclotron energy ratio. A LL structure characterized by an even (odd) E_Z/E_c value corresponds to SdH oscillations with R_{xx} minima at even (odd) FFs [Figure 3.9(d)

and (e)]. A half integer E_Z/E_c value corresponds a FF sequence where all FFs are resolved (spin resolved sequence) which we denote as a transition sequence [Figure 3.9(a) and 3.9(e)]. For $E_Z/E_c = 2$ we obtain an even FF sequence, however we distinguish integer $\nu = 1, 2$ [Figure 3.9(f)], where the two lowest occupied LLs have the same spin orientation. The observation of R_{xx} minima at integer FFs in magnetotransport data is discussed in Section 3.9.

Figure 3.9(a) data reveal a B-field independent FF sequences at a fixed n, indicating that E_Z/E_c does not vary with the B-field. The FFs parity transitions can be explained by an n-dependent E_Z/E_c, or equivalently by an n-dependent, interaction enhanced g^*. Consistent with the large effective mass probed in this 2D system, electron-electron interaction effects are expected to enhance g^* as n is reduced, as reported in Si [129], [130], GaAs [131], AlAs [132], and WSe$_2$ [111]–[113], [133] 2D systems. In the following Sections we will attempt to determine g^* values for our K-valley MoSe$_2$ 2DES. Traditional methods used to probe the g-factor include: magnetotransport in tilted magnetic field [Section 3.8], and polarization field measurements [Section 3.9].

3.8 TILTED FIELD EXPERIMENTS

Magnetotransport in magnetic fields tilted at an angle (θ) from the 2D plane normal [Figure 3.10 inset] has been traditionally employed to probe the Zeeman splitting in 2D systems [129]. In a tilted magnetic field E_c is proportional to the B-field component perpendicular to the plane, while E_Z is proportional to the total magnetic field (B_T). Probing the sample magnetoresistance at various θ and at a fixed n, allows to tune the Zeeman-to-cyclotron ratio ($E_Z/E_c \propto 1/\cos\theta$). At specific coincidence angles, corresponding to integer values of E_Z/E_c the FF sequence is expected to change parity, i.e. oscillations minima would become maxima and vice versa, allowing to determine a g-factor value [129].

Figure 3.10 shows R_{xx} vs B at various θ values and $n = 4.5 \times 10^{12}$ cm^{-2} in bilayer B2. At $\theta = 0°$ the FF sequence is predominantly even, and remains unchanged for all θ values, indicating that E_Z is insensitive to the parallel magnetic field component ($B_∥$), i.e. E_Z/E_c remains constant and $E_Z \propto (B_T \cos\theta) = B$. These findings contrast observations in Si

[129], [130], GaAs [131], AlAs [132], and few layer WSe_2 [112], [113] 2D systems, but agree with observations in trilayer MoS_2 [116], and mono- and bilayer WSe_2 [111], where the combination of strong SOI and band extrema away from the Brillouin zone center locks the carrier spin perpendicular to the 2D system. Even tough tilted-field measurements inform us on the direction of the electron's spin at the K point, they cannot be used to quantitatively determine the g-factor.
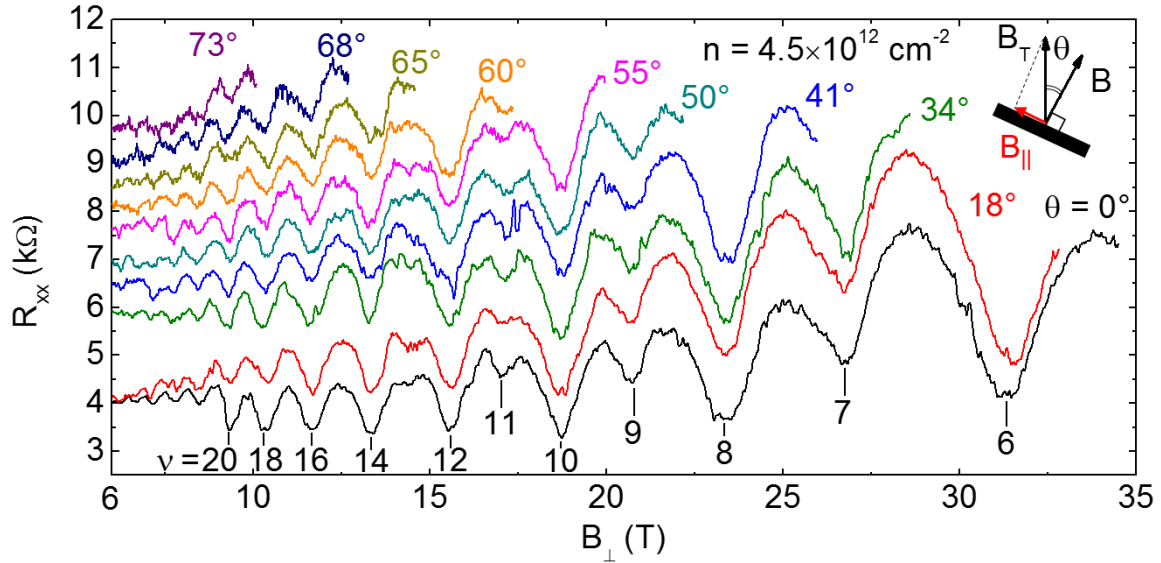
Figure 3.10: R_{xx} vs B measured at different θ, at $n = 4.5 \times 10^{12}\,cm^{-2}$, and $T = 1.5$ K in bilayer B2. The traces are offset for clarity. Inset: sample orientation schematic and B, B_T and $B_\parallel$ definitions. Reprinted figure with permission from S. Larentis *et. al.* Phys. Rev. B 97, 201407 (2018), Ref. [102], © 2018 by the American Physical Society.

3.9 G-FACTOR AND SPIN POLARIZATION

A quantitative determination of g^* as a function of the electron density is possible using FF sequence parity data [Figure 3.9(a)], or the spin-polarization field measurements [Figure 3.11].

Figure 3.11 shows examples of R_{xx} vs B data measured in bilayer B3 at low n values and $T = 0.3$ K. Two noteworthy features can be identified in this R_{xx} vs B dataset. First an even to odd transition is observed between $n = 4.7 \times 10^{12}$ and $3.4 \times 10^{12}\,cm^{-2}$, consistent with Figure 3.9(a) data. Second, for $n < 4.0 \times 10^{12}\,cm^{-2}$ SdH oscillations show R_{xx} minima

at odd FFs (v = 11, 9, 7), while above a density-dependent magnetic field (B_p), marked in Figure 3.11, consecutive integer FFs are observed (v = 5, 4, 3). To explain the emergence of consecutive FF, Figure 3.12(a) illustrates three different LL structures, obtained using Equation 3.5, where the E_c and E_Z contributions are shown separately. Each LL structure is obtained for different E_Z/E_c = 5, 4, 3, associated with increasing electron density, resulting in FF sequences of different parity. In each diagram of Figure 3.12(a), a number of LLs corresponding to the E_Z/E_c value are non-degenerate and of the same spin orientation. The emergence of R_{xx} minima at integer FFs in Figure 3.11 is associated with the occupation of these spin-polarized LLs. For a LL structure obtained for $E_Z/E_c = i$, the highest integer FF is $v = i$ [Figure 3.12(a)].
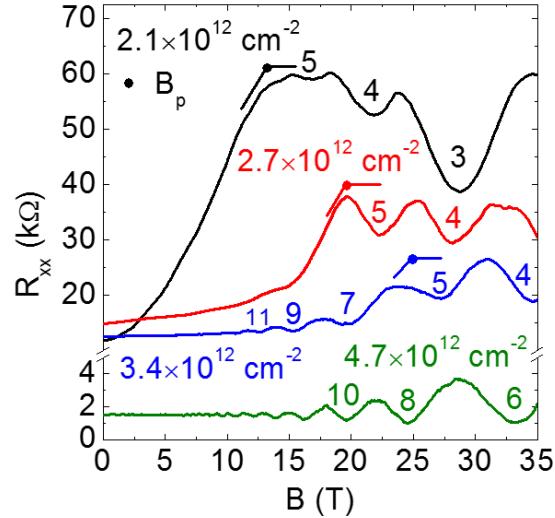
Figure 3.11: R_{xx} vs B measured at n between $2.1 - 4.7 \times 10^{12}$ cm^{-2} cm , $T = 0.3$ K in bilayer B3. At $n < 4.0 \times 10^{12}$ cm^{-2}, integer FFs associated with spin polarized LLs emerge. An even-to-odd parity variation is also identified between $n = 4.7 \times 10^{12}$ and 3.4×10^{12} cm^{-2}, consistent with Figure 3.9(a) data. Reprinted figure with permission from S. Larentis *et. al.* Phys. Rev. B 97, 201407 (2018), Ref. [102], © 2018 by the American Physical Society.

Figures 3.12(b) and 3.12(c) summarize the FF sequence parity electron density dependence in all mono- and bilayer samples, respectively. Over a density range that spans close to one order of magnitude of carrier density, between 2.0×10^{12} cm^{-2} and 12.0×10^{12} cm^{-2}, we distinguish two FF parity transitions: odd to even and even to odd, as the electron

density is increased, for both mono- and bilayer data. It should be noted that the FF sequence parity carrier density dependence is consistent across multiple samples and cooldowns.
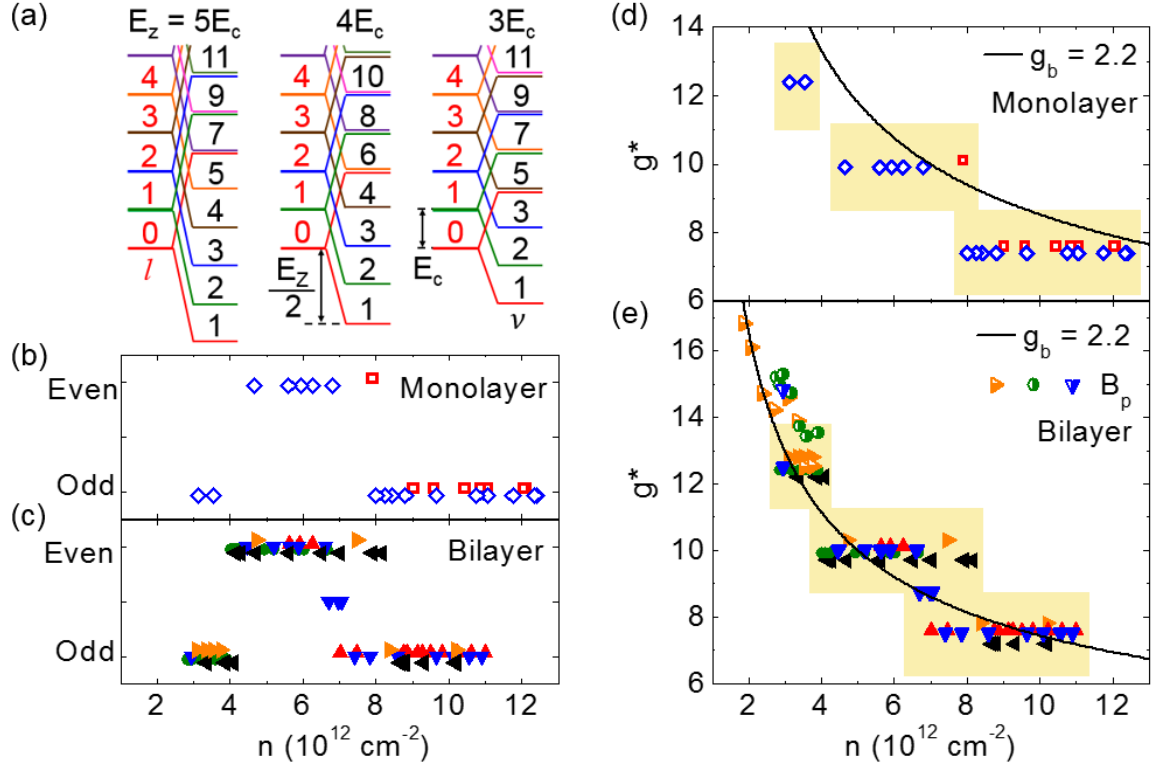
Figure 3.12: (a) LLs structure highlighting the interplay between E_Z and E_c. Consecutive integer ν are associated with LLs of same spin orientation. (b), (c) FF sequence parity vs n in mono- and bilayer MoSe$_2$ samples, respectively. Symbol legend: monolayer A1 ($\diamondsuit$), A2 ($\circ$); bilayer B1 ($\bullet$), B2 ($\blacktriangle$,$\blacktriangledown$), B3 ($\blacktriangleleft$,$\blacktriangleright$), $\blacktriangle$,$\blacktriangledown$ and $\blacktriangleleft$,$\blacktriangleright$ label different cooldowns. (d), (e) g^* vs n in mono- and bilayer MoSe$_2$, respectively (symbols), obtained from FF sequence data [panel (b), (c)] and B_p data [Figure 3.11]; fit of the calculated χ/χ_0 to the experimental g^* vs n data using $g_b = 2.2$ (solid line). The shaded regions in panel (d) and (e) indicate the g^* error bar $\Delta g^* = \pm m_e/m^*$. Symbols in panel (b) through (d) are slightly offset for clarity. Reprinted panels (a)-(e) with permission from S. Larentis *et. al.* Phys. Rev. B **97**, 201407 (2018), Ref. [102], © 2018 by the American Physical Society.

In order to determine the g^* from the density dependent FF sequence data we need to assign an E_Z/E_c value to each of the three group of FF sequences (odd, even, odd).

Comparing the diagram of Figure 3.12(a) obtained with $E_Z/E_c = 5$ and the FF sequence (ν = 4, 5, 7, 9, 11…) associated to R_{xx} vs B data measured at $n = 3.4 \times 10^{12}$ cm^{-2} in bilayer B3 [Figure 3.11], allows us to assign to the lowest electron density FF sequence parity group of Figure 3.12(c) an $E_Z/E_c = 5$. The observation of consecutive integer FFs above B_p, associated with spin polarized LLs [Figure 3.11 and 3.12(a)] allows to unambiguously assign the E_Z/E_c value. We were able to distinguish odd FFs and integer FFs at $\nu \leq 5$, at n < 3.4×10^{12} cm^{-2}, consistently across all three bilayer samples probed and in one monolayer sample (A1). As n is increased, each FF sequence transition is associated with a decrease in E_Z equal to E_c [Figures 3.12(a), 3.12(b) and 3.12(c)], consistent with a decreasing g^* as the 2D system becomes less dilute. A filling factor sequence associated with a transition [Figure 3.9(a)] is assigned to a half integer E_Z/E_c value. Once we assign an $i = E_Z/E_c$ value to each FF sequence group [Figures 3.12(b) and 3.12(c)], namely $i = 5$, 4, 3, in order of increasing electron density, we can convert E_Z/E_c in a g-factor as follows:

$$i = \frac{E_Z}{E_c} = \frac{g^* \mu_B B}{\hbar \omega_c} = \frac{g^* \frac{e\hbar}{2m_e} B}{\frac{\hbar e B}{m^*}} \rightarrow g^* = 2 \frac{m_e}{m^*} i \qquad 3.6$$

Figures 3.12(d) and 3.12(e) show g^* vs n data for both mono- and bilayer samples, respectively, obtained from Figures 3.12(b) and 3.12(c) data using Equation 3.6. As discussed in Section 3.7, to each FFs sequence labeled odd (even) corresponds an odd (even) E_Z/E_c ratio within a $\pm 1/2$ window, which determines a g^* error bar (Δg^*) of $\pm m_e/m^*$, corresponding to the shaded regions of Figures 3.12(d) and 3.12(e).

As introduced in Section 3.8, tilted and parallel field experiments have been used to probe the Zeeman splitting in traditional 2DES (e.g. III-V systems), because in these systems $E_Z \propto B_T$. Magnetotransport measurements conducted at $\theta = 90°$, a case where $B_T = B_\parallel$, probe the Zeeman energy in absence of any cyclotron response. The Zeeman coupling splits the spin-up and -down subbands as shown in Figure 3.13, leading to a spin polarized 2DES, in which the electron densities associated each spin are different. The spin polarization is defined as $\xi = (n^\uparrow - n^\downarrow)/n$, where $n^{\uparrow/\downarrow}$ are the spin-up or -down electron

densities. At the onset of full spin polarization $B_T = B_p$ ($\xi = 1$), and E_Z is equal to the Fermi energy (E_F), and the spin polarization field (B_p) writes:

$$n\frac{2\pi\hbar^2}{m^*} = E_F = g^*\mu_B B_p \rightarrow B_p = \frac{2hn}{eg^*\dfrac{m^*}{m_e}} \qquad 3.7$$

At $\xi = 1$ the Fermi energy is calculated using a density of states ($m^*/2\pi\hbar^2$) associated with a spin polarized band, where the spin degeneracy is absent. In parallel B-field experiments ($\theta = 90°$) the onset of spin polarization at B_p is marked by saturation of the positive magnetoresistance (MR), as observed in Si, GaAs and AlAs 2D systems [130], [132], [134].
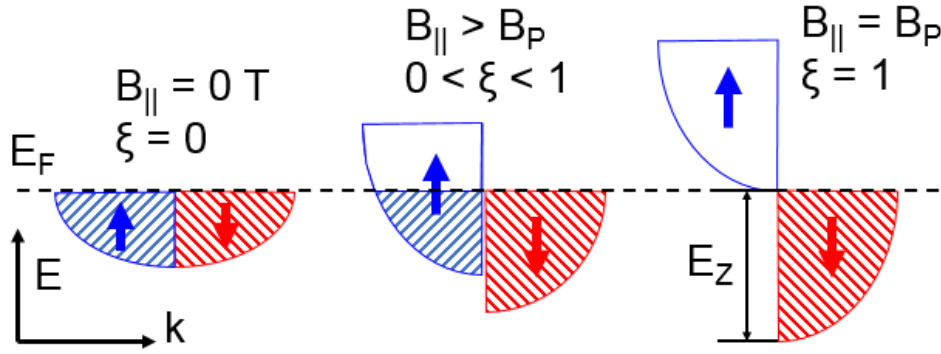
Figure 3.13: Sketches of spin ↑ and ↓ subbands population as a function of the parallel B-field ($B_\parallel$). To $B_\parallel = B_p$ correspond to the onset of spin polarization ($\xi = 1$).

Alternatively, in high mobility samples B_p can be probed using magnetotransport measurements in nearly parallel field. A constant B_T parallel to sample is applied at first, then small samples rotations are performed around $\theta = 90°$, inducing a perpendicular B-field sufficiently large to probe SdH oscillations, leaving $B_\parallel$ virtually unchanged for small angle rotations. A FT analysis of SdH oscillations yields the carrier density of subbands associated to each spin, allowing to directly measure ξ, thus determine the B_p [134].

In our samples a parallel B-field does not induce any positive MR response because it does not couple to the spin of electrons hosted at the K-valley in MoSe$_2$. Similar observations are also reported for mono- and bilayer WSe$_2$ [111]. However the observation of R_{xx} minima at integer FFs at $B > B_p$ and low n, associated with spin-polarized LLs

[Figure 3.11], is accompanied by a pronounced positive MR background superimposed onto the SdH oscillations for $B < B_p$. The positive MR saturation at perpendicular B-field greater than B_p in bilayer MoSe$_2$ samples [Figure 3.11] is reminiscent of parallel B-field-induced spin polarization in Si, GaAs and AlAs 2D systems [130], [132], [134].

At low electron density the B_p vs n measurements provide a separate method to probe g^* vs n. The g^* values obtained from B_p measurements, across all three bilayer samples, using Equation 3.7 are summarized in Figure 3.12(e) along with g^* vs n data obtained from FF sequence parity data. Values of g^* probed in both mono- and bilayer MoSe$_2$ samples, obtained with both methods [Figure 3.12(d) and 3.12(e)], show significant interaction enhancement as the 2DES becomes more dilute. In absence of interactions the g-factor would be density independent and equal to the band g-factor (g_b), a value determined by the bandstructure of the material. It should be noted that while g^* datasets obtained from FF sequence parity and B_p data in bilayer samples show good agreement, they are obtained at different spin polarization. Filling factor sequence parity data are obtained at $0 < \xi < 1$, and B_p values are by definition are obtained at $\xi = 1$.

3.10 SPIN SUSCEPTIBILITY CALCULATIONS

In a 2DES, in the limit of zero temperature the effect of Zeeman splitting is captured by the spin polarization. The ratio of spin polarization induced by a weak magnetic field is measured by the spin susceptibility (χ), which writes [131], [135], [136]:

$$\chi \equiv \left.\frac{\partial \xi n}{\partial B}\right|_{B=0} = \frac{-g_b \mu_B n}{2} \left(\left.\frac{\partial^2 \epsilon(n,\xi)}{\partial \xi^2}\right|_{\xi=0}\right)^{-1} \qquad 3.8$$

where $\epsilon(\xi)$ is the ground state energy per particle as function of the spin polarization. For a non-interacting 2DES it corresponds to:

$$\epsilon_0(n,\xi) = \frac{\hbar^2 \pi n}{\zeta m^*}(1 + \xi^2) \qquad 3.9$$

where ζ is the product of valley and spin degeneracy, which in this Section we assume equal to 2. Such description is suitable for spin-degenerate electrons as in GaAs, and TMD 2DESs where only the lower spin split CB at the K (K') point is populated [Section 1.2.1].

Using Equation 3.8 and 3.9 we can determine the spin susceptibility (χ_0) in a non-interacting 2DES:

$$\chi_0 = \frac{-g_b\mu_B n}{2}\left(\frac{\partial^2 \epsilon_0(n,\xi)}{\partial \xi^2}\bigg|_{\xi=0}\right)^{-1} = -\frac{g_b m^* \mu_B}{2\pi\hbar^2} \qquad 3.10$$

To model g-factor experimental data, it is of interest to obtain the spin susceptibility interaction enhancement χ/χ_0. In an interacting system, χ is calculated including the exchange (ϵ_{ex}) and correlation (ϵ_c) contributions to $\epsilon(\xi)$. The spin susceptibility enhancement writes [135]:

$$\frac{\chi}{\chi_0} = \frac{\dfrac{\partial^2 \epsilon_0(r_s,\xi)}{\partial \xi^2}\bigg|_{\xi=0}}{\dfrac{\partial^2 \epsilon(r_s,\xi)}{\partial \xi^2}\bigg|_{\xi=0}} = \frac{\dfrac{\partial^2 \epsilon_0(r_s,\xi)}{\partial \xi^2}\bigg|_{\xi=0}}{\dfrac{\partial^2 (\epsilon_0(r_s,\xi) + \epsilon_{ex}(r_s,\xi) + \epsilon_c(r_s,\xi))}{\partial \xi^2}\bigg|_{\xi=0}} \qquad 3.11$$

Energy per particle contributions ($\epsilon_0, \epsilon_{ex}, \epsilon_c$) are expressed as function of the spin polarization, and of the dimensionless inter-particle distance $r_s = 1/(a_B^* \sqrt{\pi n})$, which is proportional to the ratio of interaction to kinetic energy in continuum electron gas models [135]; where $a_B^* = a_B\left(\frac{\kappa m_e}{m^*}\right)$ is the effective Bohr radius, κ is the effective dielectric constant, and $a_B = \frac{4\pi\epsilon_0 \hbar^2}{m_e e^2}$ is the Bohr radius. In a 2D system at the interface between two dielectrics κ writes:

$$\kappa(t,b) = \frac{\left[\left(\epsilon_t^{\|}\epsilon_t^{\perp}\right)^{1/2} + \left(\epsilon_b^{\|}\epsilon_b^{\perp}\right)^{1/2}\right]}{2} \qquad 3.12$$

where $\epsilon_{t(b)}^{\perp/\|}$ is the the top (bottom) relative dielectric constant with respect to the 2D plane normal. For monolayer MoSe$_2$ samples $\kappa = \kappa(\text{hBN, hBN}) = 4.55$, where $\epsilon_{hBN}^{\perp} = 6.9$ [137], $\epsilon_{hBN}^{\|} = 3$ [Figure 2.30]. For bilayer MoSe$_2$ the dielectric environment for electrons in top layer is altered by the depleted MoSe$_2$ bottom layer, for which the following average is used $\kappa = [\kappa(\text{hBN, hBN}) + \kappa(\text{hBN, MoSe}_2)]/2 = 5.38$, where $\epsilon_{MoSe_2}^{\perp} = 15.5$ [3], [46], $\epsilon_{MoSe_2}^{\|} = 4$ [138].

While the kinetic and exchange contributions to the energy per electron can be evaluated analytically, the correlation contribution has to be calculated numerically. Reference [139] presents quantum Monte Carlo (QMC) correlation energy calculations, which are parametrized to obtain an analytic expression of $\epsilon_c(r_s, \xi)$. The second derivative as function of the spin polarization of $\epsilon_c(r_s, \xi)$, as provided by the QMC parametrization, which we need to calculate the χ/χ_0, is proportional to the analytical function $\alpha_1(r_s)$ [139]:

$$\left.\frac{\partial^2 \epsilon_c(r_s, \xi)}{\partial \xi^2}\right|_{\xi=0} = 4\alpha_1(r_s) \qquad\qquad 3.13$$

which writes as follows:

$$\alpha_1(r_s) = A_1 + (B_1 r_s + C_1 r_s^2 + D_1 r_s^3) \times ln\left(1 + \frac{1}{E_1 + F_1 r_s^{3/2} + G_1 r_s^2 + H_1 r_s^3}\right) \quad 3.14$$

where $\alpha_1(r_s)$ is expressed in effective Rydberg units [Ry* = $m^*/(m_e \kappa^2)$ Ry; Ry = 13.6 eV], and A_i, B_i… are parameters specified in Table 3.2 [135].

A_i	0.117331
B_i	-3.394×10^{-2}
C_i	-7.66765×10^{-3}
E_i	0.4133
F_i	0
G_i	6.68467×10^{-2}
H_i	7.799×10^{-2}
$D_i = -A_i H_i$	-9.15064×10^{-5}

Table 3.2: Set of α_1 parameters quoted from Ref. [139].

Using the χ/χ_0 definition [Equation 3.11], the analytical expressions of $\epsilon_0(r_s, \xi) = Ry^*(1 + \xi^2)/r_s^2$ [Equation 3.9], [135], $\epsilon_{ex}(r_s, \xi)$, which writes [135]:

$$\epsilon_{ex}(r_s, \xi) = -\frac{8\sqrt{2}}{3\pi r_s} \frac{(1 + \xi)^{\frac{3}{2}} + (1 - \xi)^{\frac{3}{2}}}{2} Ry^* \qquad\qquad 3.15$$

and Equation 3.13 obtained from the QMC parametrization for [139], we write:

$$\frac{\chi}{\chi_0}(r_s) = \left[1 - \frac{\sqrt{2}}{\pi} r_s + 2r_s^2 \alpha_1(r_s)\right]^{-1} \qquad\qquad 3.16$$

Figure 3.14 shows the calculated χ/χ_0 vs r_s, for all $r_s > 0$, $\chi/\chi_0 > 1$. The spin susceptibility enhancement of Equation 3.16 applies to a 2DES with zero layer thickness, in the limit of zero temperature, and in the absence of disorder [136], [139].
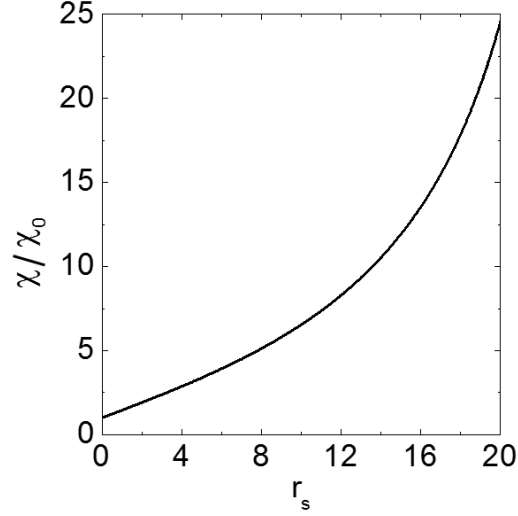
Figure 3.14: χ/χ_0 vs r_s obtained using a QMC parametrization of the correlation energy introduced in Ref. [139] for an ideal 2DES at $T = 0$ K, in absence of disorder.

The spin susceptibility enhancement is a quantity that was introduced to allow for an effective comparison with the experimental data, in fact we can express χ/χ_0 as follows [131], [135], [136]:

$$\frac{\chi}{\chi_0} = \frac{g^* m^*}{g_b m_b}$$

3.17

where g^* and m^* are the effective values probed experimentally and correspond to quasiparticle values that in principle are density dependent; g_b and m_b correspond to the g-factor and effective mass band values, used in the r_s expression and in the spin susceptibility definition [Equation 3.10] [132], [136]. Using Equation 3.17, χ/χ_0 calculations of Figure 3.14 [139] are compared with $g^* m^*$ data, normalized using band values, probed using tilted-field and spin polarization measurements in GaAs [131] and AlAs [132] 2DES, showing good agreement. Because our experimental investigation shows a largely n-independent MoSe$_2$ K-valley effective mass in the range of n probed

[Figure 3.8] we assume $m_b = m^*$, and Equation 3.17 becomes $\frac{\chi}{\chi_0} = \frac{g^*}{g_b}$. A comparison between the experimental g^* and the calculated χ/χ_0 [Figure 3.14] requires a g_b value, which has not yet been established for MoSe$_2$ [122], [128], [140]. A fit of the calculated χ/χ_0 [Figure 3.14], [139] to the experimental g^* vs n data yields a $g_b = 2.2$ for both mono- [Figure 3.12(d)] and bilayer [Figure 3.12(e)] data. A similar fit to the experimental g^* vs n data probed in mono- and bilayer WSe$_2$ 2D K-valley holes yields $g_b = 6.8$ [111]. Such a fit implicitly assumes that χ/χ_0 calculations [139] approximate well the interaction enhancement of g^* in MoSe$_2$ as in other 2D systems [131], [132], [136], and that disorder effects are negligible.

The g^* interaction enhancement observed in mono- and bilayer MoSe$_2$ 2DES is consistent with experiments in mono- and bilayer WSe$_2$ holes [111], and bilayer MoS$_2$ electrons [114] 2D systems over a comparable carrier density range. The g^* enhancement probed in III-V systems (GaAs and AlAs) is also well captured by the same χ/χ_0 [Figure 3.14], but emerges at carrier densities significantly smaller, of the order $\sim 10^{10}$ cm^{-2} in GaAs [131], [141] and $\sim 10^{11}$ cm^{-2} in AlAs [132]. Many-body effects are present at higher densities in group VI TMDs because of the large effective masses and the low-κ dielectric environment of hBN compared to III-V systems. This renders group VI TMDs an interesting host for studies of correlated phenomena.

3.11 SUMMARY

In summary, we report magnetotransport studies in high mobility mono- and bilayer MoSe$_2$ samples. Samples are fabricated utilizing a bottom-contact, dual-gate architecture, with hBN dielectrics and Pd contacts. The SdH oscillations temperature dependence allows to probe an electron effective mass of $0.8m_e$ in both mono- and bilayer samples. The FT analysis of SdH oscillations measured at different bottom-gate biases, coupled with effective mass measurements, indicate that electrons reside at the K point. The SdH oscillations reveal a density dependent FF sequence which is insensitive to a perpendicular electric field and to a parallel magnetic field, indicating that the electron's spin is locked

perpendicular to the MoSe$_2$ plane. The interplay between cyclotron and Zeeman energy, along with an interaction enhanced, density dependent g-factor explains the FF sequence odd-to-even transitions. Both FF sequence parity data and spin polarization field measurements are used to determine the interaction enhanced g-factor. A comparison of the experimental $g*$ with spin susceptibility enhancement calculations estimates the band g-factor. The findings presented in this Chapter clarify the LL structure of K-valley electrons in MoSe$_2$ and highlight the role of interactions in this large effective mass 2D system.

Chapter 4: Band Offset and Negative Compressibility in Graphene-MoS₂ Heterostructures

Magnetotransport studies of TMDs discussed in Chapter 3 have revealed that group VI TMDs are hosts to comparatively heavy carriers, with effective masses as high as $0.8m_e$ for K-valley electrons in mono- and bilayer MoSe$_2$ [Chapter 3] and $0.9m_e$ for Γ-valley holes in few-layer WSe$_2$ [112]. Large effective masses suggest that electron-electron interaction effects are expected to be significant in these class semiconductors, even at relatively large electron densities. Indeed the investigation of Zeeman splitting in group VI TMDs 2D systems revealed a strong g-factor enhancement, a signature of interaction effects, for carrier densities as high as 1×10^{13} cm^{-2} [111], [Section 3.9]. The interaction enhanced g-factor is modeled introducing the spin susceptibility, a derivative of the ground state energy with respect to the spin polarization [135]. Another way to probe of electron-electron interactions in a system is to study its compressibility. The electronic compressibility is proportional to the rate of change of the carrier concentration with chemical potential, i.e. the thermodynamic density of states. In analogy to the definition of the spin susceptibility, the compressibility corresponds to the ground state energy derivative with respect to the carrier density [135]. Experimentally we can probe compressibility using two 2D layers in close proximity where a carrier density variation in one layer acts as a probe for the chemical potential in the other. In a 2D system where we probe negative compressibility, the chemical potential decreases as we increase the carrier density, because electron-electron interaction effects are predominant in the carrier density range studied.

In this chapter, we report the combined experimental and theoretical investigation of electron density partitioning in graphene-MoS$_2$ heterostructures. Four-point

measurements of the heterostructure conductivity as a function of the bottom-gate bias show ambipolar characteristics, along with a clear saturation on the electron branch. Measurements of the graphene layer carrier concentration using magnetotransport reveal that the conductivity saturation is associated with carrier-population onset of the conduction band of the lower mobility MoS_2 layer. Experimental data from heterostructures with different MoS_2 thicknesses allows us to extract the band offset between the MoS_2 conduction band and the graphene charge neutrality point. Surprisingly, the carrier density in graphene decreases with increasing bottom-gate bias once electrons populate the MoS_2 layer, a finding associated with the negative compressibility of the MoS_2 electron system [135], [143]. To interpret our results, the graphene-MoS_2 charge-partitioning problem is solved using the thermodynamic equilibrium condition that the chemical potentials of the two layers electrons are equal. We find that the observation of decreasing graphene density as a function of the bottom-gate bias, above the critical voltage for MoS_2 occupation, is a direct result of exchange and correlation energy contributions to the ground state energy, determined using the random phase approximation (RPA), to the many-body chemical potential of MoS_2. A model for disorder is also introduced to account for reduced magnitude of interaction effects near the MoS_2 population threshold.

4.1 INTRODUCTION

4.1.2 Graphene-MoS₂ heterostructures

A variety of graphene-MoS_2 or graphite-MoS_2 vertical heterostructures, similar to the heterostructure presented in this chapter, have been investigated in literature. Notable examples include memory devices based on graphite floating gates, for charge based storage [144], [145] and optoelectronic devices characterized by high photoresponsivity and gated persistent photoconductivity [146]. However, to date, the most investigated graphene- or graphite-MoS_2 heterostructures use the carbon layer as a contact to the TMD layer, in place of a metal, i.e. the graphite/graphite layer covers MoS_2 only partially. As discussed in Chapter 2, obtaining low resistance contacts to mono- and few-layers TMDs

at both room and low temperatures has proven to be a significant engineering challenge. The lack of low resistance contacts limits the performances of TMD FETs [147], [148]. For this reason, the fabrication of low resistance contacts has been intensely researched.

Monolayer graphene contacts appear promising because of their tunable work-function and because they may act as de-pinning layer, for metal contacts [149]. Both monolayer graphene- or thicker graphite layers have been used to fabricate n-type contacts to MoS_2 using two different integration approaches shown in Figure 4.1. One option consist in first patterning the graphene onto the bottom gate dielectric, and then transferring the MoS_2 on the bottom graphene contacts [Figure 4.1(a)], [86], [150], [151]. Another option uses transfer techniques to sequentially pick up the top-hBN (optional), and the patterned graphene/graphite which are released on the MoS_2 layer, previously exfoliated on the bottom-gate dielectric [Figure 4.1(b)], [86], [94], [151]–[153]. Graphene/graphite contacts and gate electrodes, along with hBN dielectrics, are also used to integrate all 2D material n-type MoS_2 FETs, on flexible and transparent substrates [65], [152].
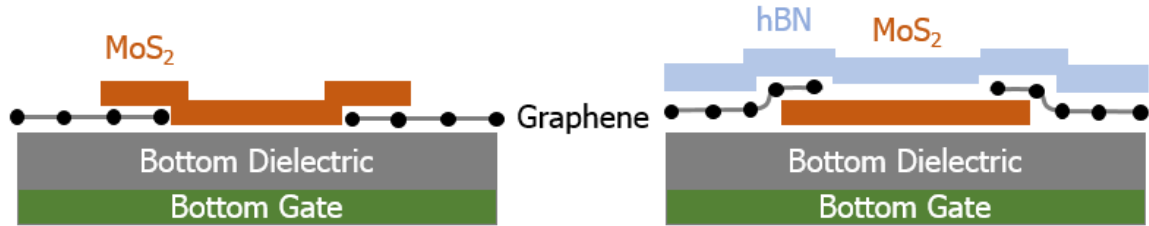
Figure 4.1: Cross-sectional schematics of MoS_2 FETs fabricated using graphene contacts. Devices are assembled: (a) transferring of the MoS_2 layer on patterned graphene contacts, (b) picking up sequentially the hBN and the pre-patterned graphene/graphite contacts and releasing them on MoS_2 exfoliated on the bottom dielectric.

Graphene contacts to MoS_2 inject electrons efficiently, in either configuration of Figure 4.1, even at low temperatures ($R_C \sim 10$ kΩ·µm at $T = 1.5$ K [94]), suggesting that graphene's Dirac point and the conduction band edge of MoS_2 are energetically close. A quantitative understanding of the graphene-MoS_2 contact is therefore necessary. It should be noted that while metal-MoS_2 contacts appear promising to resolve the contact bottleneck

in the development of TMD FET, less complex architectures based on metal bottom contacts [Chapter 2], [91], have shown comparable contact resistance values at low temperatures.

4.1.2 Negative compressibility of a two-dimensional electron systems

The ground state energy per electron of an interacting systems writes, as introduced in Chapter 3, as the sum of the kinetic energy, describing the non-interacting 2D system, and the first and second order interaction corrections, corresponding to exchange and correlation contributions, which accounts for the Coulomb interaction in the system:

$$\epsilon = \epsilon_0 + \epsilon_{ex} + \epsilon_c \qquad\qquad 4.2$$

while the ground state energy can be calculated theoretically, it is not directly measurable quantity [135]. However the derivates of the ground state energy with respect to the carrier density or the spin polarization can be related to measurable quantities. In Chapter 3 we studied the spin susceptibility, which corresponds to the second derivative of ϵ with respect to the spin polarization. In this chapter we will focus on a different quantity, the compressibility (K) or its inverse the bulk modulus (β), which corresponds to the second derivate of ϵ with respect to the carrier density, and writes as follows [135]:

$$\frac{1}{K} = \beta = n^2 \frac{\partial}{\partial n}\left(\frac{\partial(n\,\epsilon)}{\partial n}\right) \qquad\qquad 4.2$$

A more convenient expression for K is written as a function of the chemical potential, μ and alternatively of the quantum capacitance, $C_q = e^2 \frac{\partial n}{\partial \mu}$ [135]:

$$\frac{1}{K} = n^2 \frac{\partial \mu}{\partial n} = \frac{n^2 e^2}{C_q} \qquad\qquad 4.3$$

An intuitive way to measure the compressibility, or $\partial\mu/\partial n$, is a carrier density dependent capacitance (C) measurement. If we consider a gated 2DES classically the measured capacitance is the dielectric capacitance $C_{ox} = \varepsilon_0\varepsilon_r/d$; where d is the dielectric thickness and ε_r is the relative permittivity. However, to a variation of carrier density in the

2DES corresponds a variation of its chemical potential, which in terms of capacitance corresponds to a C_q that adds in series to C_{ox} [135]. The total capacitance per unit area, in general density dependent, reads:

$$C = \left(C_{ox}^{-1} + C_q^{-1}\right)^{-1} = \frac{\varepsilon_0 \varepsilon_r}{d + \frac{\varepsilon_0 \varepsilon_r}{e^2}\left(\frac{\partial \mu}{\partial n}\right)} = \frac{\varepsilon_0 \varepsilon_r}{d + \gamma} \qquad 4.4$$

where the screening length is defined as follows: $\gamma = \frac{\varepsilon_0 \varepsilon_r}{e^2}\left(\frac{\partial \mu}{\partial n}\right)$. Depending on the sign of $\partial \mu / \partial n$, the quantum capacitance contribution may reveal an enhancement (negative C_q, K) or a reduction (positive C_q, K) of the C value, by a factor of $\left(1 + C_q/C_{ox}\right)^{-1}$. In a non-interacting system, both K and C_q are positive. For spin degenerate 2DES, where the ground state energy is only the kinetic contribution from individual states, C_q writes:

$$C_q = e^2 \frac{\partial n}{\partial \mu} = \frac{e^2 m^*}{\pi \hbar^2}; \quad \frac{\partial \mu}{\partial n} = \frac{\pi \hbar^2}{m^*} \qquad 4.5$$

Therefore the emergence of a C enhancement, i.e. negative K and C_q, is associated with a regime where many-body effects are dominant.

The outlined capacitive measurement is in principle simple, but of difficult execution. In GaAs systems d is typically few hundred nm, while γ value is comparable to the effective Bohr radius ($a_B^*/4$ ~2.5 nm in GaAs). Typical values of C, for device sizes of 200×200 µm^2 [143], are in the pF range, and the quantum capacitance contribution accounts only for a very small percentage of measured the C, only few aF. The C_{ox} dominance coupled with a requirement for a very accurate measurement, may render this measurement technique impractical, obscuring the sign and magnitude of C_q. However, in the limit of thin dielectrics (~10 nm-thick), where d is comparable with γ, low frequency C-V measurements in black phosphorus [154], and in LaAlO$_3$/SrTiO$_3$ [155] 2DES have shown C enhancement near the population threshold.
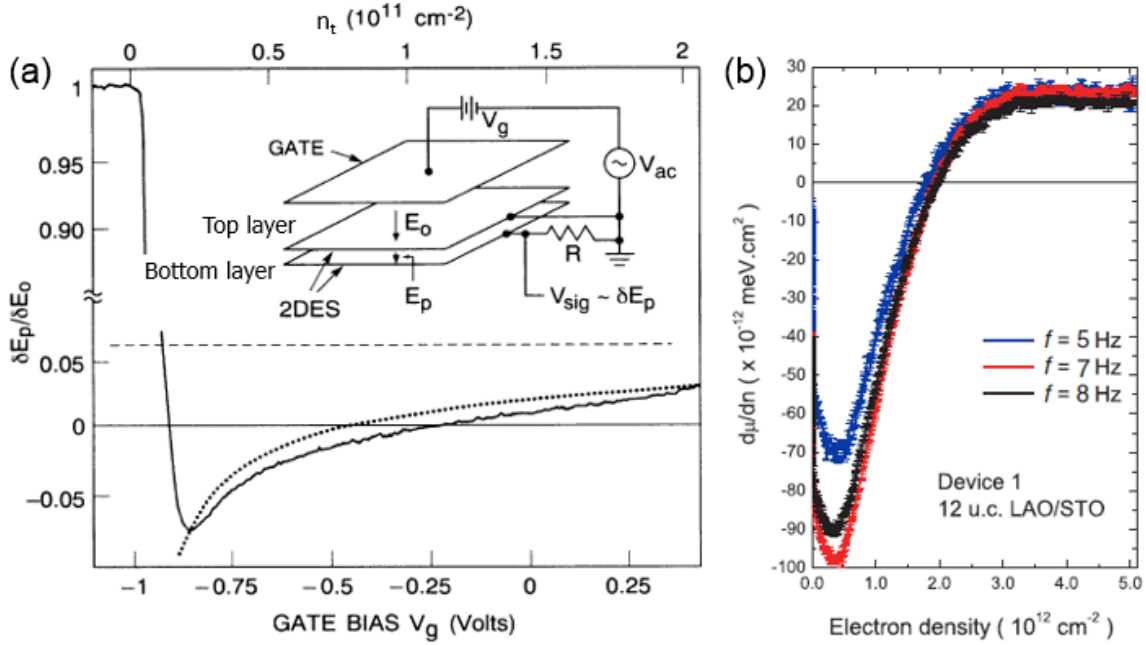
Figure 4.2: (a) $\delta E_p/\delta E_0 \propto \partial\mu/\partial n$ measured as function of V_g and n_t, in a GaAs double quantum well system at $T = 1.2$ K. Horizontal dashed line represents the non-interacting result [Equation 4.5]. Dotted line represents a calculation including exchange and correlation contributions [156]; $n_{Critical} \sim 1 \times 10^{11}$ cm^{-2} marks the n_t at which the K changes sign. At $n_t < 1.6 \times 10^{10}$ cm^{-2} interaction effects are obscured by disorder and K becomes again positive. Inset: sample and biasing schematic. Reprinted with permission from J.P. Eisenstein, L.N. Pfeiffer and K.W. West, Phys. Rev. Lett. 68, 674 (1992), Ref. [157], © 1992 by the American Physical Society. (b) $\partial\mu/\partial n$ vs n obtained from penetration field measurements in a LaAlO$_3$/SrTiO$_3$ system, at $T = 4.2$ K and different frequencies (5-8 Hz). For this 2DES, $n_{Critical} \sim 1.5 \times 10^{12}$ cm^{-2}. From L. Li *et al.* Science 332, 825 (2011), Ref. [155]. Reprinted with permission from AAAS.

A more sensitive technique, introduced by Eisenstein *et al.* [143], [157], relates the compressibility ($\partial\mu/\partial n$) to the penetration electric field (E_p) between two GaAs quantum wells kept at the same electrochemical potential. Each well or layer is an independent 2DES, and the separation between the two wells is $a \propto C_{IL}$, the interlayer capacitance. The measurement setup is shown in the inset of Figure 4.2(a). Similar to a C-V measurement a small AC modulation (δV), on top of a fixed DC bias (V_g) is applied to a gate. The DC bias is swept to vary the total carrier density in the two layers. In addition to monitoring the

gate-charge variation ($\delta n_t + \delta n_b \propto \delta E_0$), as in a C-V measurement, the electron density variation in the bottom layer ($\delta n_b \propto \delta E_p$) is also monitored; δn_t (δn_b) is electron density variation in the top (bottom) layer, marked in Figure 4.2(a) inset, and δE_0 (δE_p) is electric field variation between the gate (top layer) and the top (bottom) layer. In effect, values of δn_b or δE_p depend on the screening by the top layer, and are an indirect measurement on the chemical potential in the top layer. An analysis of the equivalent capacitor network, modeling the double layer system, is useful to understand the merit of this technique. Solving for δn_b as function of the total charge variation, allows to directly access $\partial \mu / \partial n$:

$$\delta n_b = \frac{C_{q,t}^{-1}}{C_{q,t}^{-1} + C_{q,b}^{-1} + C_{IL}^{-1}} (\delta n_t + \delta n_b) \qquad \text{4.6a}$$

$$\frac{\delta E_p}{\delta E_0} = \frac{\delta n_b}{\delta n_t + \delta n_b} = \frac{\gamma_t}{\gamma_t + \gamma_b + a} \approx \gamma_t \propto \frac{\partial \mu}{\partial n_t} \qquad \text{4.6b}$$

where $C_{q,t}$, $C_{q,b}$ (γ_t, γ_b) are top and bottom layer quantum capacitances (screening lengths). In Equation 4.6b each capacitance component is expressed in terms of its dielectric or screening length (a or γ). In GaAs double layers used in References [143], [157], $a = 37.5$ nm and γ for non-interacting electron is $a_B^*/4 \sim 2.5$ nm, therefore $\delta E_p / \delta E_0$ is proportional to $\partial \mu / \partial n_t$. Figure 4.2(a) shows $\delta E_p / \delta E_0$ measured as function of V_g in GaAs/AlGaAs double layer systems. Separate penetration field measurements in constant perpendicular *B*-field are conducted to convert V_g in n_t. Recently Dultz at al. [158] introduced an analogous approach employing a double gated single 2DES, a technique used to measure $\partial \mu / \partial n$ vs *n* in a LaAlO$_3$/SrTiO$_3$ 2DES system [155], as shown in Figure 4.2(b).

In both GaAs [Figure 4.2(a)] and LaAlO$_3$/SrTiO$_3$ [Figure 4.2(b)] data two compressibility regimes can be distinguished, below and above critical density ($n_{\text{Critical}} = 1 \times 10^{11}$ cm^{-2} for the GaAs system and $n_{\text{Critical}} = 2 \times 10^{12}$ cm^{-2} for the LaAlO$_3$/SrTiO$_3$ system) where the 2DES probed show negative *K* at $n < n_{\text{Critical}}$ and positive *K* at $n < n_{\text{Critical}}$. The emergence of these two regimes of compressibility for both systems discussed, can be interpreted by extending the non-interacting picture, where $\partial \mu / \partial n$ is constant and density

independent [Equation 4.5, dashed line in Figure 4.2(a)], to include electron-electron interactions.

To the first order Coulomb interaction effects can be modeled to include an additional exchange term (Hartee-Fock approximation) in addition to the kinetic energy. The $\partial\mu/\partial n$ value for a spin degenerate system, including the kinetic and exchange contributions reads:

$$\frac{\partial\mu}{\partial n} = \frac{\partial}{\partial n}\left(\frac{\partial(n\,\epsilon_0 + n\,\epsilon_{ex})}{\partial n}\right) = \frac{\pi\hbar^2}{m^*} - \sqrt{\frac{2}{\pi}}\frac{e^2}{4\pi\varepsilon_0\varepsilon_r}n^{-\frac{1}{2}} \propto \frac{1}{K} \qquad 4.7$$

While at very high density the $\partial\mu/\partial n$ approaches a single-particle result, at a sufficiently low carrier density value, depending on dielectric environment and the carrier effective masses, the exchange term exceeds the kinetic term. In this approximation, for $n < \left(\frac{4m^*e^2\sqrt{2}}{h^2\varepsilon_0\varepsilon_r\sqrt{\pi}}\right)^2 = n_{Critical}$, the 2DES exhibit negative compressibility and $\partial\mu/\partial n$ becomes negative, decreasing as $\propto -n^{-1/2}$. The large difference in critical density between the two material systems presented in Figure 4.2 is to be attributed to effective mass ($n_{Critical} \propto m^{*2}$) and dielectric environment ($n_{Critical} \propto 1/\varepsilon_r^2$) difference. At low densities, below 1.6 $\times 10^{10}$ cm^{-2} in GaAs samples another change in the compressibility sign is observed, which departs from the $\partial\mu/\partial n \propto -n^{-1/2}$ dependence. This is indicative of a regime where the disorder prevails over electron-electron interactions.

4.2 DEVICE FABRICATION

The graphene-MoS$_2$ heterostructures studied in this Chapter consist of monolayer graphene transferred onto a few-layer MoS$_2$ flake exfoliated onto a SiO$_2$/Si substrate, where the highly doped Si serves as bottom-gate. A 3D sketch of the completed device including metal contacts is shown in Figure 4.3(a). To fabricate graphene-MoS$_2$ samples, we first exfoliate commercially available MoS$_2$ crystals (SPI Inc., 2D semiconductors) onto a 285 nm thick SiO$_2$/Si substrate, as described in Section 1.1.3.1. The exfoliated flakes are annealed in ultra-high vacuum (UHV) at 350°C for 6 hours, to remove tape residues. Figure

4.3(b) shows the AFM topography of an annealed MoS$_2$ flake, free of residues. In order to transfer graphene on MoS$_2$ we will employ a different technique compared to the PDMS/PCC transfer outlined in Section 2.3.1. As we discussed in Section 3.2, a direct pick-up of graphene using PPC is unsuitable, as it has particularly low yield. Graphene monolayers are instead directly exfoliated from natural graphite onto a Si substrate coated with a PMMA/polyvinyl alcohol (PVA) stack [Figure 4.3(c) inset]. Typical thicknesses of the PMMA/PVA stack are 750/70 nm. A low power O$_2$ plasma etching (30 W – 5-10 s) is performed to increase monolayer graphene yield exfoliation. Figure 4.3(c) shows a graphene flake exfoliated on PMMA/PVA, highlighting the typical contrast of a monolayer under optical microscope. Using a green filter fitted on the microscope or filtering the spectra during the image postprocessing helps to enhance the contrast and identify monolayer flakes. The PMMA layer used here effectively plays a similar role of the PCC layer discussed in Section 2.3.1. However in this technique flakes are not picked up from SiO$_2$/Si substrates, but are instead directly exfoliated on PMMA/PVA stacks.

Once we isolated a suitable monolayer graphene flake and verified its thickness using Raman spectroscopy [159], the polymer coated Si subtrates are placed floating on deionized water [Figure 4.3(d)]. The water soluble PVA interlayer is then dissolved, while the bare Si substrate sinks separating from the PMMA membrane. The PMMA membrane is then fished out, and centered onto a perforated custom glass mask [78]. The hollow region is centered around the desired monolayer [Figure 4.3(e)]. Using a mask-aligner with a custom heated stage, the glass/membrane assembly is aligned and brought into contact with the target MoS$_2$ flake [Figure 4.3(e)]. Different substrate temperatures (RT, 45 °C) set before contact, do not impact the result of the transfer and the electrical characteristic of the device. After the membrane is brought into contact, to favor adhesion, the substrate temperature is raised to 85 °C. Using a scalpel, the PMMA membrane is severed around the edge of the glass mask hollow region, to decouple it from the substrate. After the transfer process is completed the PMMA membrane is then dissolved in acetone overnight. This wet-transfer technique, using a PVA layer to decouple the PMMA membrane from the Si substrate, was initially introduced by Dean *at el.* [78]. Figure 4.3(f) shows the AFM

micrograph of a monolayer graphene/MoS$_2$ stack assembled during the transfer process, after PMMA removal, and 6-hour UHV anneal at 350°C. The transferred graphene displays some ripples or wrinkles, which are typical of mono- and few-layer graphite layers transferred on TMDs and hBN substrates [160].
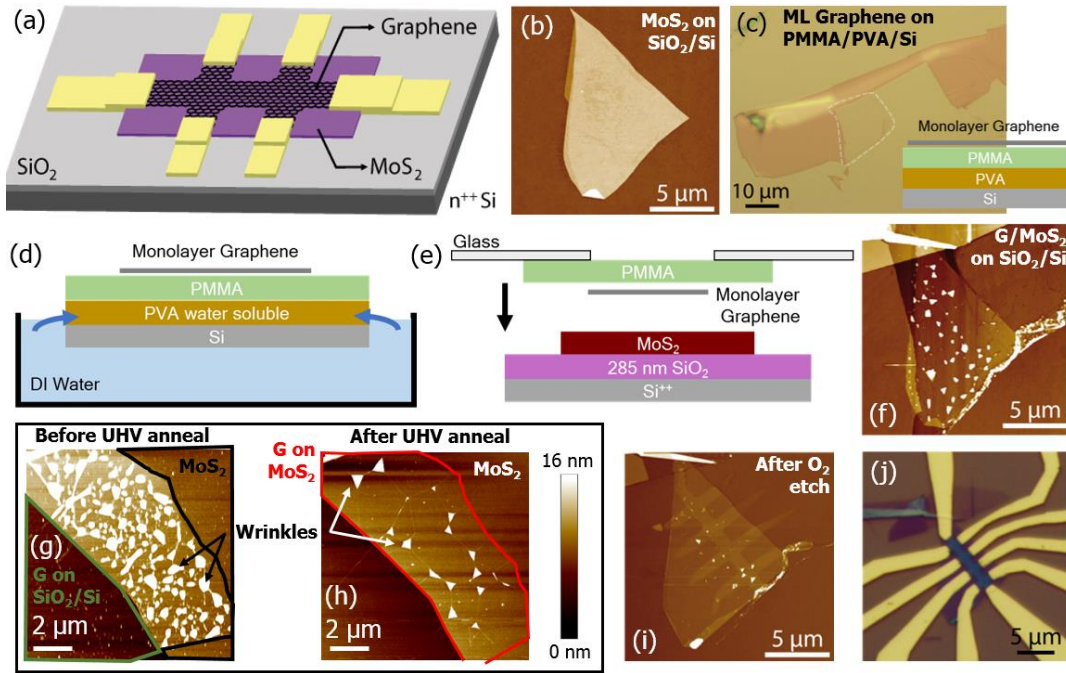
Figure 4.3: (a) Schematic representation of the graphene-MoS$_2$ heterostructure. (b) AFM topography of a MoS$_2$ flake exfoliated on SiO$_2$/Si substrate, after UHV anneal at 350° C. (c) Few-layer graphite flake exfoliated on PMMA/PVA, monolayer region is highlighted. Inset: cross sectional schematic of Si wafer coated with PMMA/PVA. Cross-sectional schematic describing: (d) separation of PMMA membrane, supporting graphene, and the Si substrate, dissolving the PVA layer in deionized water and (e) the transfer setup used to transfer graphene on MoS$_2$, using a hollow glass mask to support the PMMA membrane. (f) AFM topography of monolayer graphene transferred on the same flake as in (b), after UHV anneal. Note the presence of ripples on the graphene surface. (g), (h) AFM topography of graphene transferred on SiO$_2$ and MoS$_2$ to highlight the effect of UHV anneal on graphene wrinkles. AFM topographies refer to a different sample than in (f). (i) AFM topography of the graphene-MoS$_2$ heterostructure after the graphene Hall bar is patterned and the device is UHV annealed. (e) Optical micrograph of the completed device with Ni/Au contacts. Panels (a)-(c),(f),(i),(j) reprinted with permission from S. Larentis *et al.* Nano Letters 14, 2039, Ref. [142]. © 2014 American Chemical Society.

134

Figures 4.3(g) and 4.3(h) show AFM micrographs of a different graphene/MoS$_2$ heterostructure, before and after a 6-hour UHV anneal at 350°C, respectively, where three different regions can be individuated: bare MoS$_2$ on SiO$_2$/Si (black outline), graphene/MoS$_2$ on SiO$_2$/Si (red outline) and graphene on SiO$_2$/Si. Two noteworthy findings are featured in Figures 4.3(g) and 4.3(h). First, after transfer and before annealing the surface of graphene/MoS$_2$ is covered by a large density of wrinkles, associated to segregation of hydrocarbons below the surface of graphene [160]. Notably these wrinkles are absent for graphene transferred on SiO$_2$, only small "dots", contaminants can be distinguished. Second, after annealing the density of wrinkles in the graphene/MoS$_2$ is drastically reduced, leaving large areas up to a few µm in diameter wrinkle free [78]. Annealing in UHV is also beneficial for bare graphene on SiO$_2$/Si in fact, surface contaminants [small "dots" in Figure 4.3(g)] are removed from the graphene surface.

Electron beam lithography (EBL), O$_2$ plasma etching are used to define a graphene Hall bar in a ripple-free region as shown in Figure 4.3(i). The graphene-MoS$_2$ stack is UHV annealed once again, using the same recipe, to remove PMMA residues and further reduce the number of wrinkles. A second EBL step followed by e-beam evaporation of Ni/Au and lift off is used to define the Ni-Au metal contacts (30-30 nm-thick). Figure 4.3(j) shows an optical micrograph of a completed device.

Raman spectra of device regions with and without graphene, obtained using 532 nm excitation wavelength, is shown in Figure 4.4(f), to confirm the successful transfer. The Raman spectra measured in the graphene-MoS$_2$ region exhibit four different peaks corresponding to MoS$_2$'s the E^1_{2g} and A_{1g} modes, as well as the G and 2D modes for graphene. The presence or absence of G and 2D modes, label region with or without graphene.
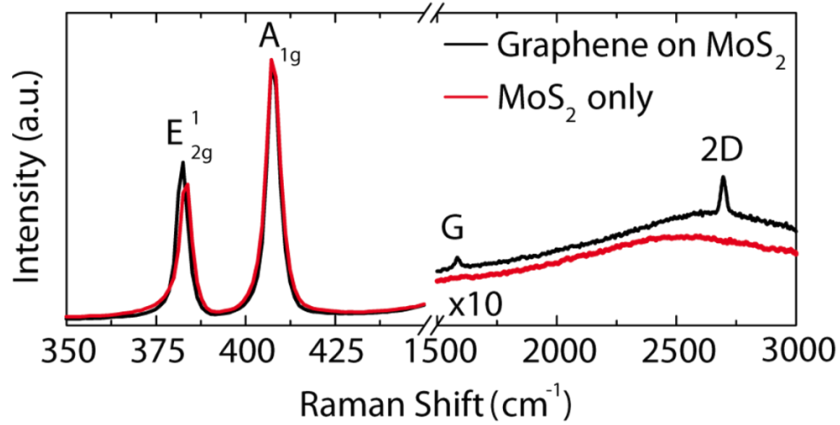
Figure 4.4: Raman spectra of device regions with and without graphene, obtained using 532 nm excitation wavelength. Reprinted with permission from S. Larentis *et al.* Nano Letters 14, 2039, Ref. [142]. © 2014 American Chemical Society.

4.3 ELECTRICAL CHARACTERIZATION AND TEMPERATURE DEPENDENCE

In this section we describe the four-point, bottom-gate characterization of the heterostructure conductivity (σ). Multiple samples have been measured at RT and temperatures down to $T = 1.5$ K, using both semiconductor parameter analyzer and low current, low frequency lock-in techniques, obtaining consistent results. Figure 4.5(a) shows σ vs V_{BG} at different temperatures ranging between 4.5 K and 295 K. The conductivity reaches a minimum at a gate bias value (V_D), which we identify with charge neutrality in the graphene sheet. For $V_{BG} < V_D$ σ decreases with increasing V_{BG}, indicating holes populate the heterostructure, conversely for $V_{BG} > V_D$ σ increases with increasing V_{BG}, consistent with electrons populating the heterostructure. While this ambipolar behavior is characteristic of graphene, the σ vs V_{BG} data of Figure 4.5(a) show a clear particle-hole asymmetry characterized by saturation at a positive threshold gate bias (V_{TH}), which becomes more sharply defined at reduced temperature.
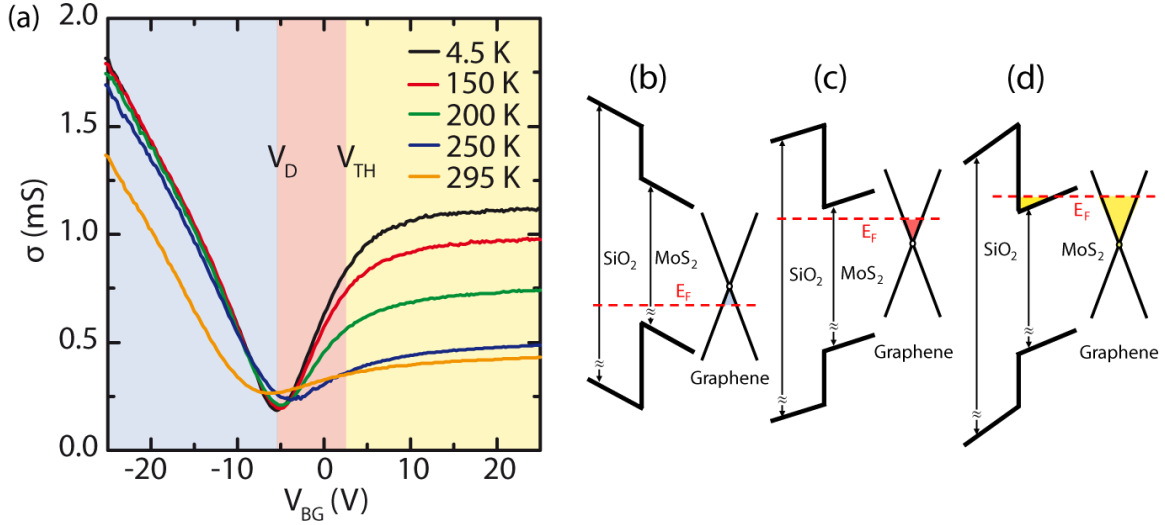
Figure 4.5: (a) σ vs V_{BG} measured at different T ranging from 4.5 K to 295 K. The electron branch shows a clear saturation of σ for $V_{BG} > V_{TH}$. The different shaded areas correspond to the band diagrams in (b), (c) and (d). (b), (c) Band diagram of the heterostructure for $V_{BG} < V_{TH}$ ($V_D < V_{BG} < V_{TH}$) when holes (electrons) are induced in the graphene layer. (d) Band diagram for $V_{BG} > V_{TH}$ when electrons are induced in the MoS$_2$ conduction band. Reprinted with permission from S. Larentis *et al.* Nano Letters 14, 2039, Ref. [142]. © 2014 American Chemical Society.

We interpret Figure 4.5(a) data using the band structure diagrams of Figures 4.5(b) to 4.5(d). For $V_{BG} < V_D$ gate-induced carriers are added to the graphene valence band [Figure 4.5(b)]. For $V_D < V_{BG} < V_{TH}$ the carriers are added to the graphene conduction band [Figure 4.5(c)]. For $V_{BG} < V_{TH}$ the chemical potential in graphene is lower than the MoS$_2$ conduction band edge. At a sufficiently large gate bias, the increase in the chemical potential of electrons in graphene coupled with the electric field induced band bending brings the bottom of the conduction band of MoS$_2$ into alignment with the graphene chemical potential. For $V_{BG} > V_{TH}$ carriers are added to the MoS$_2$ conduction band [Figure 4.5(d)]. The total carrier density (n_{Tot}) summed over graphene (n_G), and MoS$_2$ (n_{MoS_2}) systems satisfies:

$$n_{Tot} = n_G + n_{MoS_2} = \frac{C_{ox}}{e}(V_{BG} - V_D) \qquad 4.8$$

where C_{ox} is the bottom-gate oxide capacitance. Because the separation between the bottom gate and the heterostructure is much larger than the typical electronic screening lengths of

137

either MoS$_2$ or graphene, quantum capacitance contributions to the total capacitance are negligible. Indeed, the graphene quantum capacitance at a density of 10^{11} cm^{-2} is approximately two orders of magnitude larger than the 285 nm thick SiO$_2$ dielectric capacitance, and can be neglected as a series contribution.

We attribute the conductivity saturation beyond V_{TH} to the lower MoS$_2$ mobility compared to graphene. The graphene field-effect mobility [defined by Equation 2.6], extracted from Figure 4.5(a) data for both electron and hole branches at $V_{BG} < V_{TH}$ and at $T = 4.5$ K is 8,000 cm^2/Vs. At RT the μ_{FE} extracted for $V_{BG} < V_D$ is reduced to 6,000 cm^2/Vs. In contrast, the field-effect electron mobilities measured in separate four-terminal MoS$_2$ devices are more to an order of magnitude lower at low temperatures [89], [97], [161]. Our T dependent four-point measurements, of top-contact, bottom-gate few-layer MoS$_2$ samples, reported in Section 2.2.2.2 reveal $\mu_{FE} = 50$ cm^2/Vs at room temperature, which increases up to 800 cm^2/Vs at $T = 4$ K. These findings are consistent with measurements of the MoS$_2$ conductivity, in separate devices, ranging between 30 µS at RT to 300 µS at $T = 4$ K in the ON state [Section 2.2.2.2], [89], [97], [161], not large enough to provide significant parallel conduction in our heterostructure.

We remark that the carrier mobility in graphene supported by MoS$_2$ is significantly lower than that of graphene supported by hBN [78], even though the heterostructure fabrication techniques are very similar. The maximum μ_{FE} value probed in graphene-MoS$_2$ heterostructures is 13,000 cm^2/Vs at $T = 1.5$ K, while graphene-hBN heterostructures show μ_{FE} in excess of 10^5 cm^2/Vs at comparable temperatures [78].

4.4 MAGNETOTRANSPORT

To substantiate the conductance measurements presented in the previous section, we probe the carrier density in the system using magnetotransport. Here we measure the longitudinal and Hall resistance, simultaneously, as function of perpendicular B-field at $T = 1.5$ K, as shown in Figure 1.16, using lock-in techniques. Similar results are obtained across multiple samples.
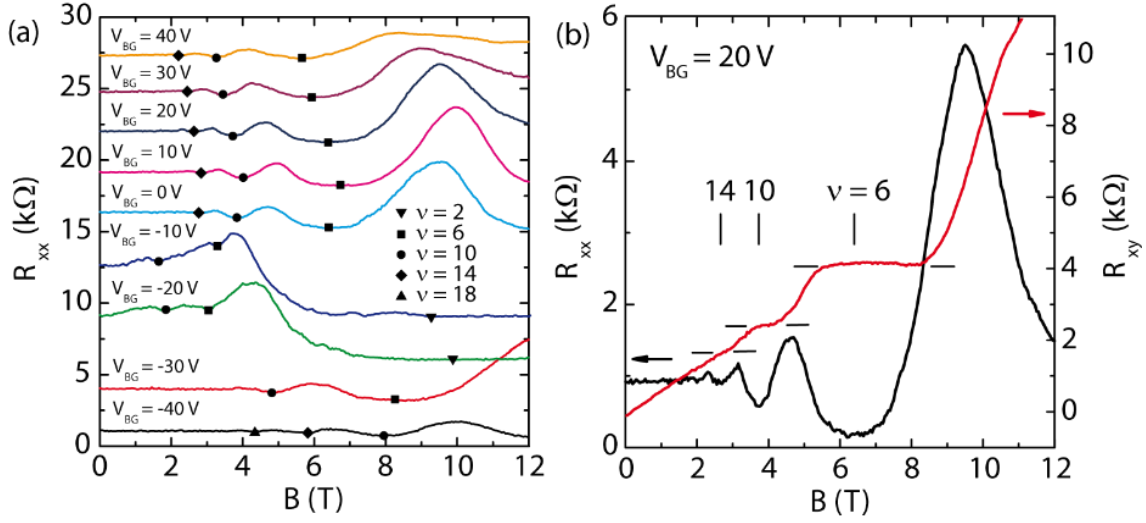
Figure 4.6: (a) R_{xx} vs B measured at different V_{BG} and at T = 1.5 K (solid lines). The symbols mark the R_{xx} oscillation minima position and the corresponding ν. Traces are offset vertically for clarity. (b) R_{xx} and R_{xy} vs B measured at V_{BG} = 20 V. The QHSs corresponding filling factors are marked. Reprinted with permission from S. Larentis *et al.* Nano Letters 14, 2039, Ref. [142]. © 2014 American Chemical Society.

Figure 4.6(a) shows R_{xx} vs B measured at different V_{BG} values and at T = 1.5 K. For this sample the V_{BG} value at charge neutrality in this device is V_D = -15 V. R_{xx} data display Shubnikov-de Haas oscillations for B fields as low as 2 T, and follow a quantum Hall state sequence with filling factors v = ±2, 6, 10, 14, 18 that can be attributed to monolayer graphene, as described in Section 1.2.2.1 [162]. Figure 4.6(b) shows an example of R_{xx} and R_{xy} vs B data measured at V_{BG} = 20 V, with the corresponding QHS filling factors v = +6, 10, 14 marked. The carrier density in graphene at a fixed V_{BG}, is extracted from the R_{xx} oscillations minima using: $n_G = v B_v e/h$ where B_v is the magnetic field corresponding to the QHS at filling factor v, marked in Figure 4.6(a). Because separate magnetotransport measurements on few-layer MoS_2 samples do not show SdH oscillations at comparable B-fields, we associate the R_{xx} minima exclusively with QHSs in graphene. The MoS_2 carrier density (n_{MoS_2}) can be inferred using the experimentally determined n_G values and the total density calculated using Equation 4.8.
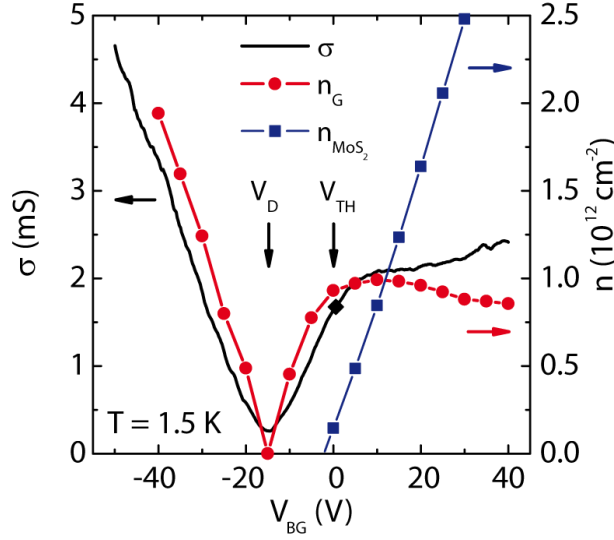
Figure 4.7: σ vs V_{BG} measured at $B = 0$ T and at $T = 1.5$ K (black line, left axis), n_G vs V_{BG} (red symbols, right axis) extracted from the SdH oscillations measured at different V_{BG} of Figure 4.6(a), and n_{MoS_2} vs V_{BG} (blue symbols, right axis) obtained as the difference between the total density and n_G [Equation 4.8]; σ and n_G both saturate for $V_{BG} > V_{TH}$, as the MoS$_2$ becomes populated. The n_G decreases for $V_{BG} > V_{TH}$ showing evidence of negative compressibility in the MoS$_2$ 2DES. Reprinted with permission from S. Larentis *et al.* Nano Letters 14, 2039, Ref. [142]. © 2014 American Chemical Society.

Figure 4.7 shows n_G and n_{MoS_2} vs V_{BG}, along with the σ vs V_{BG} data measured at $B = 0$ T. Two main findings are apparent from Figure 4.7. First, the n_G vs V_{BG} data shows a clear feature at V_{TH}, concomitant with the saturation of σ vs V_{BG} data. A comparison of the σ and n_G data allows to precisely assign V_{TH} [marked by a black symbol in Figure 4.7] as the voltage at which σ vs V_{BG} data depart from the linear trend. The concomitant saturation of σ and n_G is consistent with our description of the heterostructure, consisting of two parallel channels, graphene and MoS$_2$ with significantly different mobilities. Secondly, and perhaps most surprisingly, the carrier density in graphene decreases with increasing bottom-gate bias for $V_{BG} > V_{TH}$, a finding that can be explained accounting for the exchange and correlation energy influence on the many-body chemical potential of MoS$_2$. In the following, we will further discuss these two findings.

4.5 Band offset

Once we have determined a criterion to assign V_{TH}, as voltage at which the onset of n_G saturation begins [Section 4.4], we extract V_{TH} from σ vs V_{BG} data in heterostructures with different MoS$_2$ thickness to determine the graphene-MoS$_2$ band alignment.

Figure 4.8(a) shows the heterostructure band diagram at flat-band: $V_{BG} = V_D$, and $n_G = 0$. We introduce here the band offset (ΔE_C) as the energy separation between the graphene's charge neutrality point and the MoS$_2$ conduction band edge, marked in red in Figure 4.8(a). In order for the MoS$_2$ to be populated with electrons, the MoS$_2$ conduction band edge has to be brought into alignment with the chemical potential in graphene. In a gated structure, this can be accomplished thanks to the increase in graphene chemical potential at $V_{BG} > V_D$, along with the electrostatic band bending of the MoS$_2$ conduction band. Figure 4.8(b) shows a band diagram for the threshold condition ($V_{BG} = V_{TH}$), above which MoS$_2$ is populated with electrons. At threshold, the graphene's chemical potential and the MoS$_2$ band bending contributions are marked in Figure 4.8(b) in blue and green, respectively. At $V_{BG} \geq V_{TH}$, equilibrium is achieved between graphene and MoS$_2$ systems when their chemical potentials, including electrostatic band bending and exchange-correlation contributions, are equal:

$$\mu_G(n_G) = \mu_{MoS_2}(n_{MoS_2}) + \Delta E_C - \frac{e^2 t_{MoS_2}}{\epsilon_{MoS_2}^{\parallel} \epsilon_0} n_G \qquad 4.9$$

here, $\mu_G(n_G)$ and $\mu_{MoS_2}(n_{MoS_2})$ are the graphene and MoS$_2$ chemical potentials at carrier densities n_G and n_{MoS_2}, measured from graphene's neutrality point and MoS$_2$ conduction band edge, respectively; t_{MoS_2} and $\varepsilon_{MoS_2}^{\parallel}$ are respectively the MoS$_2$ thickness and relative dielectric constant parallel to the c-axis. The graphene chemical potential writes $\mu_G(n_G) = \hbar v_F \sqrt{\pi n_G}$, where v_F is the Fermi velocity in graphene.
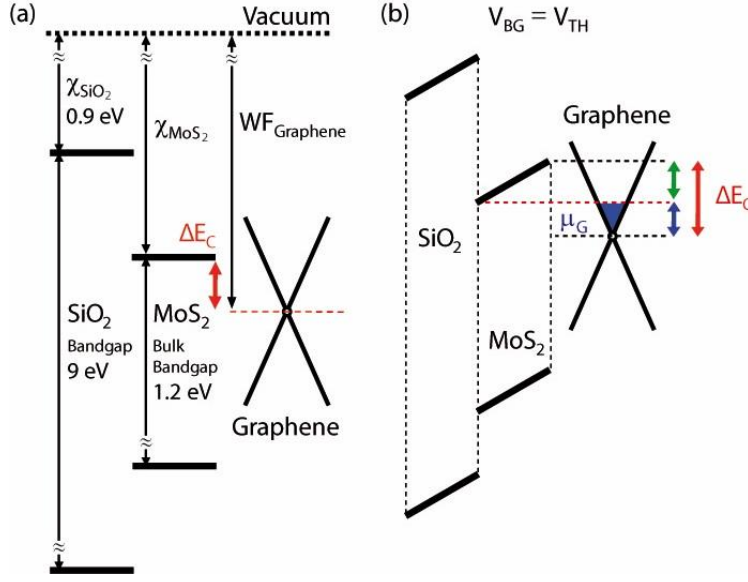
Figure 4.8: (a) Band diagram at flat band ($V_{BG} = V_D$, $n_G = 0$) in the graphene-MoS$_2$-SiO$_2$ heterostructure, constructed using data from [163]–[165]. (b) Band diagram at threshold for MoS$_2$ population ($V_{BG} = V_{TH}$, $\mu_{MoS_2} = 0$). The chemical potential of graphene is brought in alignment to the MoS$_2$ CB edge; μ_G and band bending contribution [Equation 4.9] are marked in blue and green respectively. In both panels ΔE_C is marked in red. Panel (a) reprinted with permission from S. Larentis *et al.* Nano Letters 14, 2039, Ref. [142]. © 2014 American Chemical Society.

The last term in Equation 4.9 accounts for the electrostatic band bending of the MoS$_2$ conduction band edge, assuming that t_{MoS_2} is the effective interlayer separation between graphene and the occupied states in our few-layer MoS$_2$ samples. We justify this assumption in the discussion that follows. Interlayer coupling in TMDs is weak, as indicated by the small energy width ($\approx$ 30-40 meV) of bulk MoS$_2$ conduction bands along the high symmetry direction K-H [Figure 1.3(b)], as shown by DFT calculations [22], [166]. At the onset of MoS$_2$ population the transverse electric field induced by the graphene carrier density $n_G = 0.8 \times 10^{12}$ cm^{-2} [at $V_{BG} = V_{TH}$, Figure 4.7] creates a potential drop across neighboring MoS$_2$ layers of 25 meV, comparable to the interlayer hopping energy scale. We thus choose to model our results by approximating the MoS$_2$ band structure as a set of uncoupled monolayers. Using a MoS$_2$ density of states of 3.6×10^{14} eV$^{-1}\cdot$cm^{-2} yields

a minimum n_{MoS_2} for the second MoS$_2$ band (layer) to be occupied of 9×10^{12} cm^{-2}. For smaller n_{MoS_2}, electrons occupy only the layer with lowest electrical potential, i.e. the layer furthest from graphene and closest to the gate.

The opposite limit of this approximation is to neglect the potential drop across neighboring layers of MoS$_2$ and model the carriers as occupying the lowest sub-band of a few-layer system. The principle change to our analysis would be to reduce the effective value of the graphene-MoS$_2$ separation. For example, the calculated sub-band energy splitting near the conduction band minimum in six-layer MoS$_2$ is $\approx$ 0.1 eV [19], a value corresponding to a MoS$_2$ carrier density of nearly 4×10^{13} cm^{-2} necessary to occupy the second sub-band, obtained using the same density states used above. These considerations validate the approximation we use, namely treating MoS$_2$ as a single sub-band 2DES.

Figure 4.9(a) shows σ vs V_{BG} data for graphene-MoS$_2$ heterostructures with different MoS$_2$ thicknesses, measured at temperatures between 1.4 K and 10 K. The MoS$_2$ population threshold is marked on each trace, which corresponds to the band alignment presented in Figure 4.9(b). Experimental V_{TH} - V_D values as a function of MoS$_2$ sample thickness t_{MoS_2} are summarized in Figure 4.9(b). Error bars corresponds the uncertainty of AFM measurements used to probe the MoS$_2$ thickness, and of the V_{TH} extraction, using a linear fit of σ vs V_{BG} data. Thicker MoS$_2$ layers are populated at a lower n_G, threshold, i.e. V_{TH} - V_D, because the band bending term in Equation 4.9 [marked in blue in Figure 4.8(b)] makes up for a bigger portion of ΔE_C as t_{MoS_2} is increased.

Figure 4.9(b) data can be fitted to extract ΔE_C using Equation 4.9, where $n_G = \frac{C_{ox}}{e}(V_{TH} - V_D)$ and μ_{MoS_2} is set to zero. The fit to the experimental data, assuming the experimental C_{ox} = 12.1 nF/cm^2 value, and a theoretical $\varepsilon_{MoS_2}^{\parallel}$ = 4 [167], yields ΔE_C = 0.29 eV [Figure 4.9(b)]. We note that given the MoS$_2$ bandgap depends on thickness as the monolayer limit is approached [92], the extracted ΔE_C value is most accurate for thicker samples. Band alignment calculations show that for MoS$_2$ the CB edge energy and bandgap are thickness independent at t_{MoS_2} > 4 layers [19], [92], a finding consistent with our choice of considering only samples thicker than 6 layers.
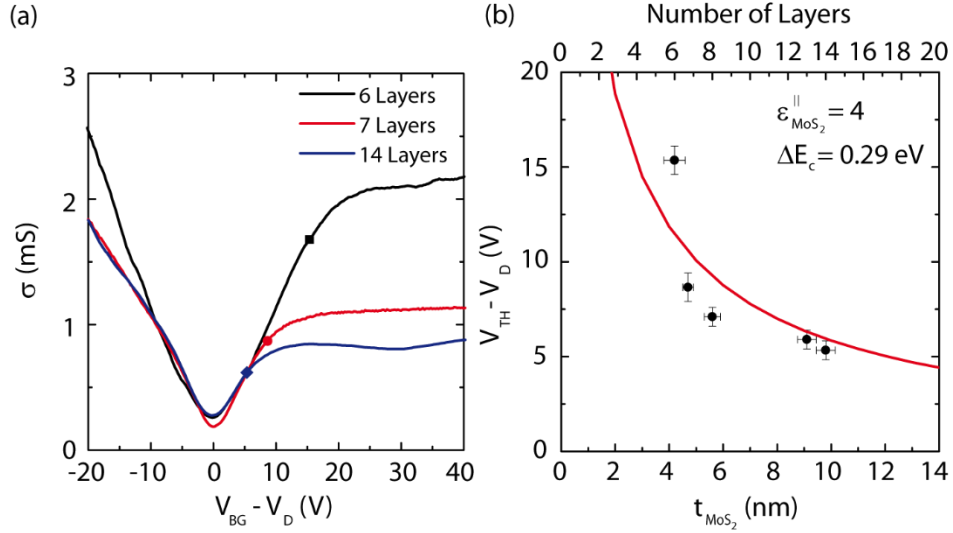
Figure 4.9: (a) σ vs V_{BG} measured in samples with different t_{MoS_2}, namely 6, 7 and 14 layers (solid lines), measured at temperatures between 1.5 - 10 K. Symbols mark the extracted V_{TH} value for each trace. (b) $V_{TH} - V_D$ vs t_{MoS_2} (bottom axis) and number of layers (top axis) data (symbols) obtained from σ vs V_{BG} data of panel (a), showing a $V_{TH} - V_D$ increase for decreasing t_{MoS_2}; fit (red line) to the experimental data using Equation 4.9 and $\mu_{MoS_2} = 0$, yields ΔE_C = 0.29 eV, for $\varepsilon^{\parallel}_{MoS_2} = 4$. Horizontal and vertical error bars indicate the uncertainty of AFM MoS$_2$ thickness measurement and V_{TH} extraction, respectively. Reprinted with permission from S. Larentis *et al.* Nano Letters 14, 2039, Ref. [142]. © 2014 American Chemical Society.

Using the experimental value for monolayer graphene work function 4.57 ± 0.05 eV [163], [164], and the band offset value obtained from the fit we calculate the MoS$_2$ electron affinity, $E_{EA,MoS_2} = 4.28$ eV, and assuming a bulk $E_g = 1.2$ eV for MoS$_2$, obtained from optical (PL [1] and photocurrent [10]) and STS [168] measurements, we estimate the valence band offset (ΔE_C) as the energy separation between the graphene charge neutrality point and the MoS$_2$ valence band edge, $\Delta E_V = 0.91$ eV. A similar band offset investigation has been carried out using monolayer graphene and few-layer WSe$_2$ heterostructures [98], yielding $\Delta E_C = 0.54$, $\Delta E_C = 0.77$ eV and $E_{EA,WSe_2} = 4.06$ eV. The band alignment picture for monolayer graphene [163], few-layer MoS$_2$ and WSe$_2$ [98], is presented in Figure 4.10. In addition to experimental data obtained from graphene-TMD heterostructures, Figure 4.10 presents band alignment data obtained from photoemission experiments, described in

Ref. [165], on bulk MoS_2 [169], and WSe_2 [170] samples, and band alignment calculations for bulk MoS_2 and WSe_2 [92]. Monolayer MoS_2 and WSe_2 band alignment data are also included in Figure 4.10 for comparison. Two sets of DFT calculations obtained using different exchange-correlation functionals are shown [92].
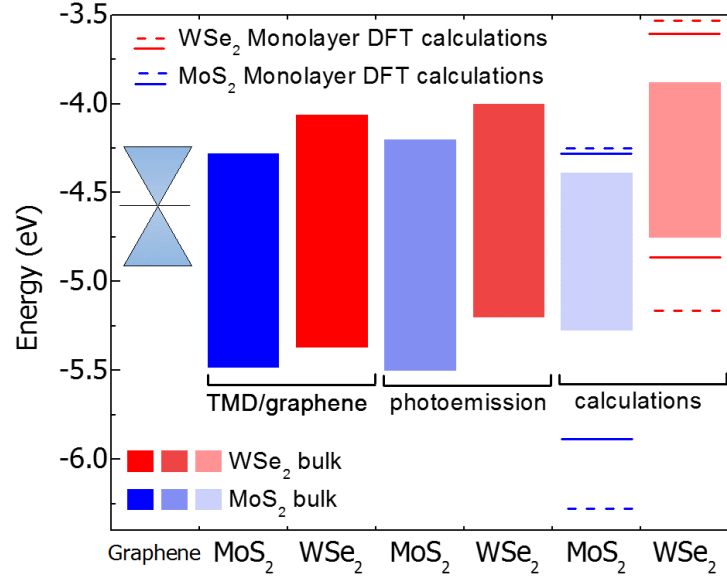
Figure 4.10: Band alignment data for graphene (experimental [163]), MoS_2 and WSe_2. MoS_2 (WSe_2) experimental data are obtained from graphene-TMD heterostructures discussed in this Section (in Ref. [98]), and photoemission band alignment measurements of Ref. [169] ([170]); ΔE_V for graphene-MoS_2 data is obtained using experimental bulk MoS_2 E_g data [1], [10], [168]. Band alignment DFT calculations for bulk $MoSe_2$ and WSe_2 (solid boxes), and monolayer $MoSe_2$ and WSe_2 (solid and dashed lines) [92]. Monolayer calculations are obtained using two different exchange-correlation functionals [92].

Figure 4.10 indicates that photoemission experiments in bulk TMDs are in good agreement with data obtained from graphene-TMD heterostructures, while bulk TMD calculations appear to underestimate the materials' bandgap, showing better agreement with MoS_2 experimental data. Other GW calculations tend to produce larger E_g, as discussed in Chapter 1 [171]. The ΔE_C values for bulk MoS_2 obtained from photoemission experiments (0.37 eV) and from DFT calculations (0.17 eV) are both consistent with ΔE_C = 0.29 eV experimentally determined in our study. Band alignment calculations in Figure

4.10 indicate that as the thickness is decreased from bulk to monolayer, the bandgap enlargement in MoS$_2$ is mostly correlated with an increase of ΔE_V, while for WSe$_2$ a more uniform increase of ΔE_C and ΔE_V is expected.

Accurate measurements of the band alignment of TMDs, i.e. measuring ΔE_C, ΔE_V and E_{EA} play an important role in the design and modeling of TMD double-layers, heterostructures formed stacking two different TMDs separated by a dielectric layer [172], are graphene double layers where the TMD material serves as a barrier [173], [174]. For graphene double layers TMDs are preferable barriers compared to hBN, because the smaller bandgap leads to higher tunneling currents [173], [174]. In particular few-layer WSe$_2$ has favorable band alignment with monolayer graphene, where the charge neutrality point of graphene aligns with the WSe$_2$ midgap [98].

4.6 MANY-BODY CHEMICAL POTENTIAL AND CHARGE PARTITIONING PROBLEM

The many-body chemical potential for the MoS$_2$ layer is calculated from the ground state energy per particle, including kinetic, exchange and correlation contributions, differentiating the $n \, \epsilon$ product:

$$\epsilon(n) = \epsilon_0(n) + \epsilon_{ex}(n) + \epsilon_c(n), \ \ \mu(n) = \frac{\partial \big(n \, \epsilon(n) \big)}{\partial n} \qquad 4.10$$

Even though Equation 4.10 is expressed as function of as function of n, calculations of the ϵ are often carried out as function of the parameter r_s, defined in Section 3.10, which through the effective Bohr radius includes contributions from m^* and κ [Equation 3.12], capturing the effects of the dielectric environment and the crystal hosting the 2DES. In the following we write expressions for $\epsilon_0, \epsilon_{ex}$ and ϵ_c, for a generic multivalley 2DES, where ζ_s and ζ_v are spin and valley degrees of freedom, respectively. In this discussion we assume that inter-valley electron-electron scattering is strongly suppressed relative to intra-valley scattering by the long range of the Coulomb potential. A condition satisfied at low n, where the Fermi wavevector (k_F) is much smaller than the inverse lattice constant. The valley degree of freedom then enters our interaction energy expressions only as an effective

146

degeneracy factor. The kinetic and exchange energy per electron expressions are analytical write as follows:

$$\epsilon_0 = \frac{2Ry^*}{r_s^2 \zeta_s \zeta_v} \qquad \text{4.11}$$

$$\epsilon_{ex} = -\frac{16}{3\pi (\zeta_s \zeta_v)^{\frac{1}{2}}} \left(\frac{Ry^*}{r_s} \right) \qquad \text{4.12}$$

where Ry^* is the reduced Rydberg energy (Ry) defined as follows:

$$Ry^* = Ry \frac{m^*/m_e}{\kappa^2} = \frac{m^*/m_e}{\kappa^2} 13.6 \; eV, \qquad Ry = \frac{m_e e^4}{8\varepsilon_0^2 h^2} = 13.6 \; eV \qquad \text{4.13}$$

To evaluate the correlation energy per particle we follow the common procedure of combining coupling-constant integration with the fluctuation-dissipation relationship between the density structure factor and the RPA density response function [135]. The correlation energy per electron can be isolated and written as an integration over the dimensionless wavevector, q, frequency, ω, and the imaginary axis Lindhard function, $\bar{\chi}(q, i\omega)$ [135]:

$$\epsilon_c = \frac{4}{(\zeta_s \zeta_v)^2} \left(\frac{Ry^*}{\pi r_s^2} \right) \int q \, dq \int d\omega \left(r_s \frac{(\zeta_s \zeta_v)^{\frac{3}{2}}}{2q} \overline{\chi}(q, i\omega) + ln \left(1 - r_s \frac{(\zeta_s \zeta_v)^{\frac{3}{2}}}{2q} \overline{\chi}(q, i\omega) \right) \right) \quad \text{4.14}$$

From an array of n values, converted in array of r_s, all three ϵ components are calculated. Equations 4.11 and 4.12 are evaluated analytically to obtain $\epsilon_0, \epsilon_{ex}$, while Equation 4.14 integral is calculated numerically to obtain ϵ_c using Simpson's rule, with the change of variables for q and ω, and an expression of $\bar{\chi}$ presented in Reference [135]. While the kinetic energy is positive, both the exchange and correlation energies of the 2DES are negative and reduce the total energy per particle. Using the calculated ground state energy per electron and Equation 4.10 we obtain the chemical potential.

We model the only occupied MoS$_2$ conduction subband (layer) closest to the SiO$_2$ dielectric, as introduced in Section 4.5, with a two-valley two-dimensional electron system using the following parameters $\zeta_s = 2$, $\zeta_v = 2$, $m^* = 0.43 m_e$ [175] and $\kappa(\text{MoS}_2, \text{SiO}_2) =$

5.63. The dielectric constant reflects the anisotropy of the dielectric environment surrounding the occupied MoS2 band (layer), namely SiO2 dielectric and unoccupied MoS2 layers; κ(MoS2, SiO2) is obtained using Equation 3.12, where $\varepsilon_{MoS2}^{\parallel} = 4$ [167], $\varepsilon_{MoS_2}^{\perp} = 13.5$ [167] and $\varepsilon_{SiO2}^{\parallel} = \varepsilon_{SiO2}^{\perp} = 3.9$ [99], parallel and perpendicular directions are defined with respect to the c-axis of MoS2. Using these effective mass and dielectric environment values we obtain $Ry^* = 184$ meV and $a_B^* = 6.9$ Å. The product of the MoS2 Fermi surface diameter ($2k_F$) and the MoS2 layer thickness can be used to assess both the relevance of the dielectric screening in the vacuum region, as well as correlations between MoS2 and graphene electrons [176]. For carrier densities large enough that the influence of disorder on the MoS2 chemical potential is minimal, we find $2k_F\,t_{MoS_2} \approx 3$ - 6 implying a negligible role for this remote part of the MoS2 2DES environment.

Figure 4.11 shows the calculated μ_{MoS_2} vs n_{MoS_2} illustrating the contribution of exchange and correlation to the chemical potential of the MoS2 layer. The MoS2 chemical potential calculated using three different approximations is shown. First, a single particle chemical potential is presented, which includes the kinetic or density of states (DOS) contribution ($\epsilon = \epsilon_0$). Second, the Hartee-Fock approximation is presented, including the kinetic and exchange contributions ($\epsilon = \epsilon_0 + \epsilon_{ex}$). Third, the full RPA result is presented including kinetic, exchange and correlation contributions ($\epsilon = \epsilon_0 + \epsilon_{ex} + \epsilon_c$). In the entire range of n_{MoS_2} experimentally accessible, up to 4×10^{12} cm^{-2}, the many-body contribution to the chemical potential is negative and much larger than the kinetic energy contribution, i.e. the MoS2 2DES is negative compressible for all n_{MoS_2} probed. Chemical potential calculations for a system with a single valley degree of freedom ($\zeta_v = 1$) show a full RPA result that is comparable, albeit smaller, in absolute value, than the two-valley 2DES result, for n values considered in Figure 4.11.

It noteworthy to compare Figure 4.2(a) data, where the GaAs 2DES transitions between negative and positive compressibility regimes at ~1 $\times$ 10^{11} cm^{-2}, and the MoS2 chemical potential calculations of Figure 4.11. We observe how calculations predict a

negative compressible MoS_2 2DES at n 40 times larger than in GaAs, a finding explained by the lower m^* and larger κ of GaAs.
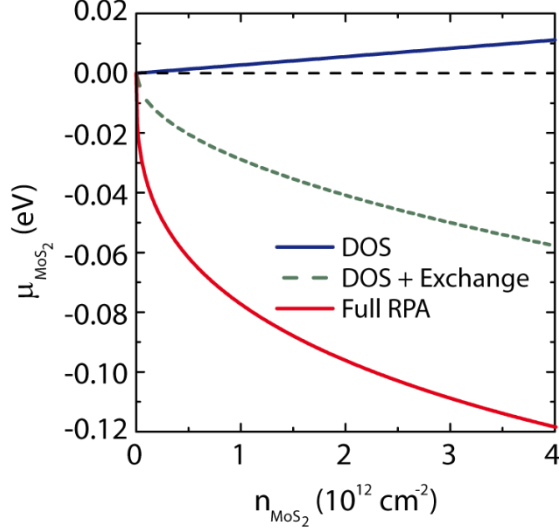
Figure 4.11: μ_{MoS_2} vs n_{MoS_2} showing the single-particle (DOS) contribution to μ_{MoS_2} (blue), the DOS and exchange contribution (dashed green), and the full RPA result (red), including DOS, exchange, and correlation contributions, calculated for a 2DES with $\zeta_s = 2$ and $\zeta_v = 2$, $m^* = 0.43m_e$ and $\kappa(MoS_2, SiO_2)$ = 5.63. Reprinted with permission from S. Larentis *et al.* Nano Letters 14, 2039, Ref. [142]. © 2014 American Chemical Society.

For completeness, we have used a similar procedure to calculate the RPA ground state energy per particle of doped graphene. This calculation evaluates expressions given in Reference [177], using a dielectric constant of $\kappa(\text{Vacuum}, MoS_2) = 4.2$, obtained using Equation 3.12, to reflect the anisotropy of graphene's dielectric environment. Correlation and exchange contributions in graphene act oppositely, and the overall interaction effect is smaller in relative terms. Calculations shows that near the graphene density saturation, its many-body chemical potential is accurately approximated by the non-interacting expression $[\mu_G(n_G) = \hbar v_F \sqrt{\pi n_G}]$, where v_F is approximately 20% larger with respect to the bare value $v_{F0} = 1 \times 10^8$ cm/s, in close agreement with recent experimental results, which report $v_F = 1.15 \times 10^8$ cm/s [83].
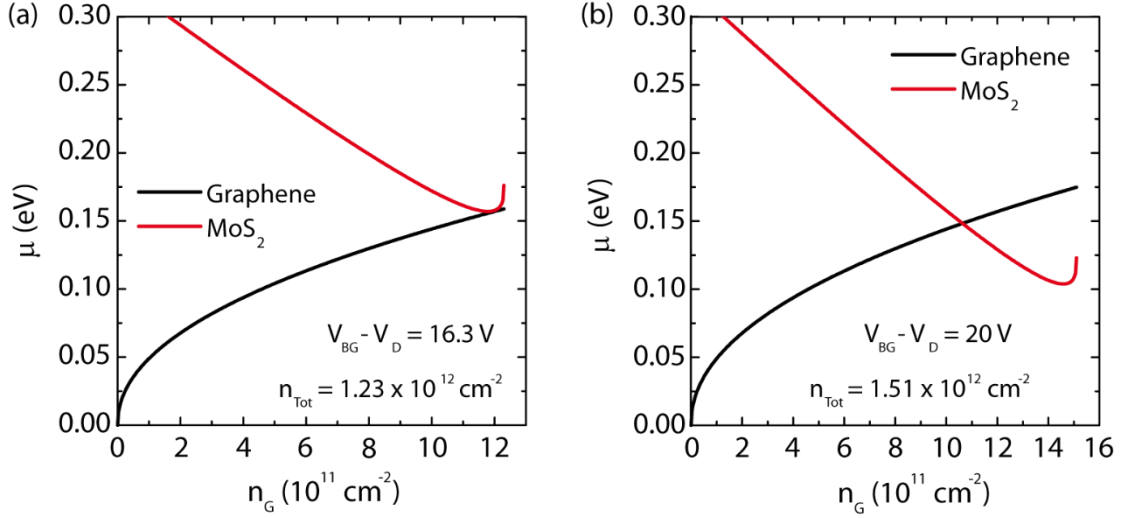
Figure 4.12: Graphene and MoS$_2$ chemical potentials vs n_G at fixed n_{Tot}, showing μ_G (black), and the RHS of Equation 4.9 (red). Panel (a) corresponds to $n_{Tot} = 1.23 \times 10^{12}$ cm^{-2} (V_{BG} = 16.3 V), and panel (b) to $n_{Tot} = 1.5 \times 10^{12}$ cm^{-2} (V_{BG} = 20 V). Calculations in both panels are performed for a heterostructure with t_{MoS_2} = 4.2 nm, and using the full RPA μ_{MoS_2} shown in Figure 4.11 and ΔE_C = 0.41 eV. Reprinted with permission from S. Larentis *et al.* Nano Letters 14, 2039, Ref. [142]. © 2014 American Chemical Society.

Using the calculated MoS$_2$ chemical potential [Figure 4.11] we solve Equation 4.9 for different values of total density in the system ($n_{Tot} = n_G + n_{MoS_2}$). In Figure 4.12(a) and 4.12(b) we plot the LHS (μ_G, black line) and RHS (red line) of Equation 4.9, as a function of n_G, at two $n_{Tot} = 1.23 \times 10^{13}$ (V_{BG} = 16.3 V) and 1.51×10^{13} cm^{-2} (V_{BG} = 20 V), using t_{MoS_2} = 4.2 nm and ΔE_C = 0.41 eV. The t_{MoS_2} value used corresponds to the t_{MoS_2} of the graphene-MoS$_2$ heterostructure probed in Figure 4.7. The equilibrium condition for charge partitioning corresponds to the intersection of the two traces, where Equation 4.9 is satisfied. Note that the RHS of Equation 4.9, depends not only on μ_{MoS_2}, but also on the band offset between graphene's Dirac point and MoS$_2$ CB edge, as well as the band bending in the MoS$_2$ layer proportional to n_G. The n_{Tot} value used in Figure 4.12(a) corresponds to the threshold for MoS$_2$ population. We remark here that in a limited range of $n_{Tot} > 1.23 \times 10^{13}$ cm^{-2}, past the threshold for the MoS$_2$ layer population, Equation 4.9 has two solutions for n_G and n_{MoS_2}, suggesting a possible charge bistability. We find that the

solution with the smaller n_{MoS_2} value occurs at a maximum in energy per volume, whereas the solution at larger n_{MoS_2} occurs at a minimum and is therefore energetically favorable. The possibility of two solutions is to be attributed solely to the negative many-body chemical potential.

To compare theory and experiment, Figure 4.13 shows n_G vs V_{BG} data at $V_{BG} > V_D$ obtained from magnetotransport experiments (symbols) [Figure 4.6(a) and 4.7] and calculations obtained from the charge partitioning equation. To illustrate the role of exchange and correlation, Figure 4.13 includes the calculated n_G vs V_{BG} neglecting (dashed red) and including (dark blue) the electron-electron interaction contributions to μ_{MoS_2}. The reduction in graphene density above the threshold for MoS_2 occupation is a direct result of electron-electron interactions and is well captured by our RPA theory for the many-body chemical potentials of MoS_2. Calculations assume a $\Delta E_C = 0.41$ eV, in order for the many-body calculations to match the experimental $n_G = 8.6 \times 10^{11}$ cm^{-2} at $V_{BG} = 40$ V. A non-interacting picture, including the sole DOS contribution to μ_{MoS_2}, cannot model the observed decrease in n_G, instead predicting an increasing n_G as the MoS_2 layer is populated. Many-body theoretical results indicate a small discontinuous change in the n_G ($\sim 3 \times 10^{10}$ cm^{-2}) at the onset of MoS_2 occupation. Figure 4.12(a) data explain well this feature, where the onset of the MoS_2 population is not gradual as it would be in a non-interacting picture, but sudden.

Graphene carrier density calculations obtained using a many-body μ_{MoS_2}, and experimental data agree well at high V_{BG} (high n_{MoS_2}), but depart near $V_{BG} = V_{TH}$ (limit of $n_{MoS_2} \to 0$). The difference between experimental data and calculations can be explained by considering the impact of disorder in the MoS_2 layer, which may dominate at low n_{MoS_2}. Similar observations were made in GaAs 2DES where at carrier densities below 1.6×10^{10} cm^{-2} disorder obscures the many body effect [Figure 4.2(a)], causing the compressibility to change sign and become positive [143], [157].
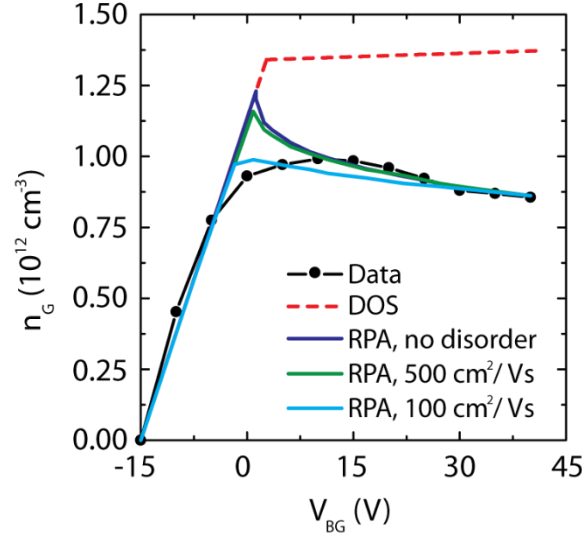
Figure 4.13: Theoretical and experimental comparison of n_G vs V_{BG} in a graphene-MoS$_2$ with $t_{MoS_2} = 4.2$ nm. Black symbols are experimental data extracted from SdH oscillations in Figure 4.6(b), also shown in Figure 4.7. The lines represent calculations performed using only the single-particle contribution (DOS) to μ_{MoS_2} (dashed red), including many-body interactions using the full RPA result, but not disorder (solid dark blue), using the full RPA result including disorder assuming a MoS$_2$ mobility of 500 cm^2/Vs (green) and 100 cm^2/Vs (light blue). Reprinted with permission from S. Larentis *et al.* Nano Letters 14, 2039, Ref. [142]. © 2014 American Chemical Society.

4.7 DISORDER

To improve the agreement between experimental data and calculated results [Figure 4.13], we include a model for disorder. Using a typical few-layer MoS$_2$ low temperature mobility value of 500 cm^2/Vs, which corresponds to a scattering time $\tau = \mu m^*/e = 1.2 \times 10^{-13}$ s, we obtain a disorder energy scale $\Gamma_{dis} = \hbar/\tau = 5.4$ meV. When the Fermi energy in MoS$_2$ is comparable or less then Γ_{dis}, we can expect disorder to play a significant role. Because of the large effective mass the MoS$_2$ Fermi energy is lower than 5.4 meV for n_{MoS_2} $< 2 \times 10^{12}$ cm^{-2}, a sizeable fraction of the density range experimentally accessible.

To quantitatively account for the influence of disorder in MoS$_2$, we extend the single particle model for the MoS$_2$ chemical potential introducing a phenomenological approximation for the density of states of disordered MoS$_2$ (g_{dis}):

$$g_{dis}(E) = \frac{g_0}{2}\left(tanh\left(\frac{E - E_c}{\Gamma_{dis}}\right) + 1\right) \qquad\qquad 4.15$$

For electron energies well above the band edge, g_{dis} corresponds to the density of states in absence of disorder: $g_0 = 2m^*/(\pi\hbar^2)$. At energies close to the CB band edge, $E_c \pm 2\Gamma_{dis}$, Equation 4.15 captures the gradual, increase of the density of states in a disordered system [178]. The single-particle contribution to the chemical potential including disorder (μ_{dis}) modeled by the density of state of Equation 4.15 is:

$$\mu_{dis}(n_{MoS2}) = \frac{\Gamma_{dis}}{2}\ln\left(exp\left(\frac{2\,n_{MoS2}}{g_0\,\Gamma_{dis}}\right) - 1\right) \qquad\qquad 4.16$$

Because $\mu_{dis}(n_{MoS2})$ increases rapidly with n_{MoS_2} at low carrier densities, disorder counteracts in part the otherwise dominant influence of exchange and correlation on the chemical potential in the low carrier density limit.

We solve the charge partitioning problem [Equation 4.9] using the full RPA chemical potential, where we replace the kinetic energy contribution to the chemical potential, red trace in Figure 4.11, with Equation 4.16. In Figure 4.13 we compare calculations of n_G vs V_{BG} including and neglecting disorder. Two calculations for disorder are included, assuming a MoS$_2$ mobility of 500 cm^2/Vs (Γ_{dis} = 5.4), and 100 cm^2/Vs (Γ_{dis} = 26.9). Both calculations fit n_G data at V_{BG} = 40 V, using ΔE_C = 0.41 eV and 0.42 eV, respectively. At this large V_{BG} disorder in the MoS$_2$ plays a relatively weak role, and for this reason we obtain values comparable with the disorder-free theory. When disorder is included, the discontinuous drop in graphene density at the onset of MoS$_2$ occupation no longer occurs, and the maximum graphene density achieved prior to MoS$_2$ occupation is reduced, both improving agreement with experiment.

4.8 DEVICE APPLICATIONS

Lastly, we comment on the relevance of these results for potential device applications. Capacitance enhancement through gate dielectric thickness scaling and oxide engineering has been one of fundamental drivers for ON-current improvement in FETs. Capacitance enhancement is not the sole requirement, because devices should also show a

sufficiently low gate-leakage. A solution to satisfy this trade-off, implemented by Intel at the 45 nm node [179], was the introduction of high-κ dielectrics, when scaling of the SiO_2 gate thickness had reached its limit. Quantum effects, such as positive C_q and inversion layer thickness, generally add a positive series capacitance to the dielectric capacitance, reducing the total gate stack capacitance, thus negatively affecting the FET performance. Negative compressibility of MoS_2 electrons on the other hand translates into a negative C_q. The negative C_q will add in series to the oxide capacitance, as shown in Figure 4.14 schematic, potentially enabling MoS_2 FETs with a gate capacitance larger than the dielectric capacitance. For example, an increased gate stack capacitance would allow to increase the threshold voltage, reducing the off-current, while preserving the same ON-current performance.
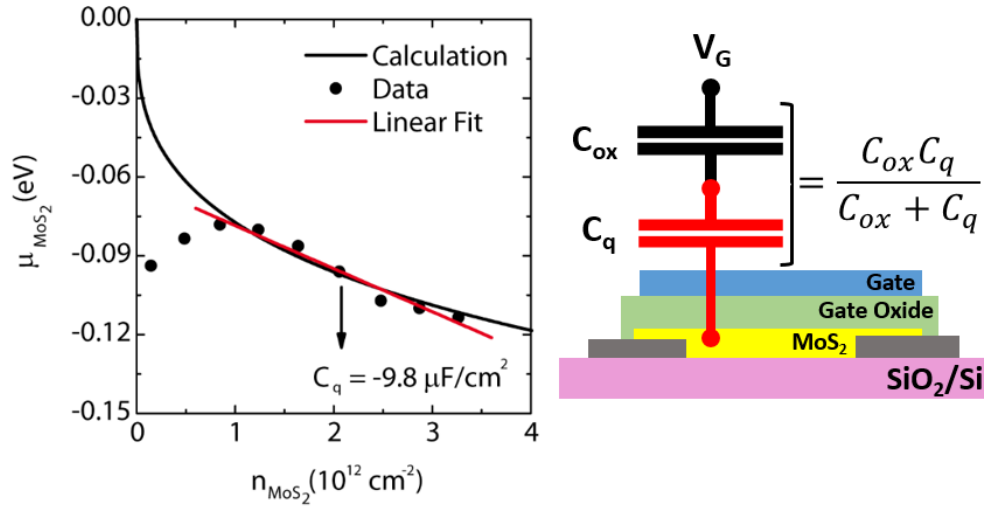
Figure 4.14: μ_{MoS_2} vs n_{MoS_2} extracted from measured n_G data of Figure 4.7 using Equation 4.9 (symbols), and calculated values (black line) including kinetic, exchange and correlation energy contributions. The inverse slope of μ_{MoS_2} vs n_{MoS_2} data (red line) yields a C_q = -9.8 µF/cm^2, for a n_{MoS_2} between 1-3 × 10^{12} cm^{-2}.

Figure 4.14 shows the experimental μ_{MoS_2} vs n_{MoS_2}, extracted from the measured n_G values of Figure 4.7 using Equation 4.9. The experimental data are in good agreement with the calculated μ_{MoS_2}, including interaction contributions. Only at lower MoS_2 densities $n_{MoS_2} < 1 \times 10^{12}$ cm^{-2}, experimental data and calculation diverge, suggesting a

regime dominated by disorder, as discussed in Section 4.7. A linear fit of the μ_{MoS_2} vs n_{MoS_2} data in an n_{MoS_2} range between 1 - 3 $\times 10^{12}$ cm^{-2}, yields a C_q = - 9.8 μF/cm^2. The absolute value of C_q corresponds to the capacitance of a 0.35 nm thick SiO$_2$ dielectric. MoS$_2$'s negative C_q would enable a larger total gate capacitance only in aggressively scaled FET, with equivalent SiO$_2$ oxide thicknesses < 4 nm, for an improvement of at least 10%. Assuming a C_{ox} = $|C_q|$/2 in series with C_q, the total capacitance would see an 100% enhancement, in a system characterized by negative compressibility (C_q < 0), e.g. MoS$_2$, while it would decrease by 1/3 in an equivalent system with positive C_q. While the implementation of negative capacitance appears promising from a device standpoint, negative compressibility has only been demonstrated to date at cryogenic temperatures [108], [154], [155], [157].

4.9 SUMMARY

In summary, we investigate the electrical properties and the carrier distribution in a graphene-MoS$_2$ heterostructure. The conductance-density dependence reveals a marked saturation on the electron branch, associated with the onset of MoS$_2$ conduction band population. This observation allows the graphene-MoS$_2$ band offset to be extracted from the data. Magnetotransport measurements show a surprising decrease of the graphene electron density with gate bias beyond the MoS$_2$ population threshold, a finding that highlights the negative compressibility of the MoS$_2$ electron system. Using the random phase approximation for the exchange-correlation contribution to the chemical potentials of MoS$_2$ and graphene, we solve for the density distribution as a function of bottom-gate voltage (i.e. total density). The decrease in graphene density at large gate voltage is due entirely to interaction effects. We are able to account quantitatively for features at the onset of MoS$_2$ population including a density of states contribution to the chemical potential for disordered MoS$_2$. Theoretical calculations are in good agreement with experiment and demonstrate that the MoS$_2$ electron gas is strongly correlated.

Chapter 5: Monolayer MoTe$_2$ Field-Effect Transistors for Integrated Circuits

Transition metal dichalcogenides are of interest for next generation switches, but the lack of low resistance electron and hole contacts in the same material, has hindered the development of complementary field-effect transistors and circuits. As discussed in Chapter 2, for either top- or bottom-contact architectures the contact resistance is a function of the gate bias, limiting the device performance. Despite the significant contact resistance reduction obtained introducing bottom-contacts, achieving low resistance contacts independent on the gate bias, i.e. introducing a gate independent doping, for either type of carriers is still an intensely investigated topic.

In this chapter, we report the fabrication of an air stable monolayer MoTe$_2$ transistors fully encapsulated in hexagonal boron-nitride. In order to effectively inject carriers in either conduction or valence band, local contact-gates are used to induce a large carrier concentration in the proximity of the metal-TMD contact. Electrostatically doping the contacts regions allows for reduced contact resistance, independent of the channel gating, enabling reconfigurable electron or hole injection depending on contact-gate bias polarity. The introduction of a multi-gate scheme with local bottom- and plunger-gates, along with the contact specific gates, allows for decoupling and control of the gate dependent contact resistance, channel resistance, and device threshold voltage tuning, independent of the unintentional flake doping. This multi-gate scheme is used to design a complementary inverter and a diode, showing potential for its use in integrated circuits and optoelectronic devices.

5.1 INTRODUCTION

Group VI TMDs have, to date, due to their semiconducting properties, drawn significant interest as candidate materials for the integration of next-generation switches and optoelectronic devices [6]. Both thickness scaling and large bandgap [Table 1.2] are attractive features to integrate low power, scaled devices, with optimal gate control [181]. The availability of different material and thickness dependent bandgaps spanning the red and near infrared spectra, as well as the availability of a direct energy bandgap at the monolayer limit, is of interest for optoelectronic applications [65], [181], [182]. Despite their apparent potential, group VI TMDs based FETs are currently limited by moderate mobilities, lower than what initially suggested [64], [89], and Schottky contacts that influence the performance of the device in both ON and OFF state [91], [147], as discussed in Chapter 2. Because of contact and mobility limitations, TMD FETs are not yet up to par with present day technology, and appear to be more suited for more-than-Moore applications, namely low cost, flexible integrated circuits (IC) as well as light-emitters, detectors and sensors [182], [183]. In particular, TMD-based logic might be of interest in applications, such as the internet of things, where performance may be sacrificed in exchange of lower fabrication cost, integration on ubiquitous substrates or back end of the line integration in hybrid platforms [65]. While more-than-Moore applications may appear more suitable for TMDs [65], at least in the short term, most TMD-based devices, circuits, logic and optoelectronic devices have so far been limited by the availability of reliable, low resistance contacts for both electrons and holes in the same TMD material [62].

Among group VI TMDs, MoS_2 has so far been the most investigated, in part because mineral crystals are available, and exfoliated flakes are stable for long periods of time. However the main reason for its popularity is the availability of low resistance contacts for electron injection, securing good n-type performance such as large I_{ON}/I_{OFF} and moderate intrinsic mobilities [89], [148]. Recently, WSe_2 based p-FETs have outperformed their MoS_2 counterparts, thanks to low resistance Pt bottom-contacts for hole injection, showing room temperature mobility > 100 cm^2/Vs [91], [110]. While both MoS_2

n-type and WSe$_2$ *p*-type based FETs have shown promising performance, it is important to be able to integrate both *p*- and *n*-type transistors in the same TMD material. Hybrid structures where *p*- and *n*-type transistors are integrated on different TMDs [184] would greatly complicate both integration, growth and transfer efforts. The availability of both *p*- and *n*-type FETs in same material would enable complementary architectures, as opposed to pseudo *n*-MOS [151], which require only one type of transistor. Possible solutions to integrate complementary FETs in the same TMD include a number of doping techniques relying on chemical doping (K, NO$_2$) [185], [186], organic molecules [187], or sub-stoichiometric oxides [58]. Another route is electrostatic doping, achieved through gating [188]. In this approach, a set of buried or overlapping split gates are biased at different, opposite voltages allowing to define spatially controlled *p*- (hole) or *n*- (electron) type doped regions, enabling diverse device structures, e.g. *p-n* diodes based on carbon nanotubes [189]–[191]. To utilize this doping scheme, the semiconductor needs to exhibit ambipolar behavior, namely contacts should be able to inject both electron and holes depending on the gating polarity.

Figure 5.1 shows a calculated band alignment diagram for monolayer Mo and W based TMDs (1H) at the *K* point, obtained from DFT calculations using Perdew-Burke-Ernzerhof (PBE), and Heyd-Scuseria-Ernzerhof (HSE) approximations for the exchange–correlation energy functional [92]. Two sets of CB and VB edges are presented, solid and dashed lines in Figure 5.1, depending on the type of approximation used, PBE or HSE. Comparing TMDs with the same transition metal, as the chalcogen atomic number increases (S to Te) we observe decreasing bandgap and electron affinity, for either approximation. Using this calculated band alignment, we can select a favorable candidate for ambipolar injection. MoTe$_2$ appears to be a good option, being characterized by an intermediate $E_{EA} \sim 3.8$ eV as shown in Figure 5.1, and narrower $E_G = 1.1$ eV [11], obtained from PL measurements, compared to monolayer WSe$_2$ ($E_{EA} = 3.5$ eV, $E_G = 1.7$ eV, [10]), and monolayer MoS$_2$ ($E_{EA} \sim 4.3$ eV, $E_G = 1.8$ eV [Figure 1.15]), typically employed to fabricate *n*- and *p*-type FETs respectively.

158
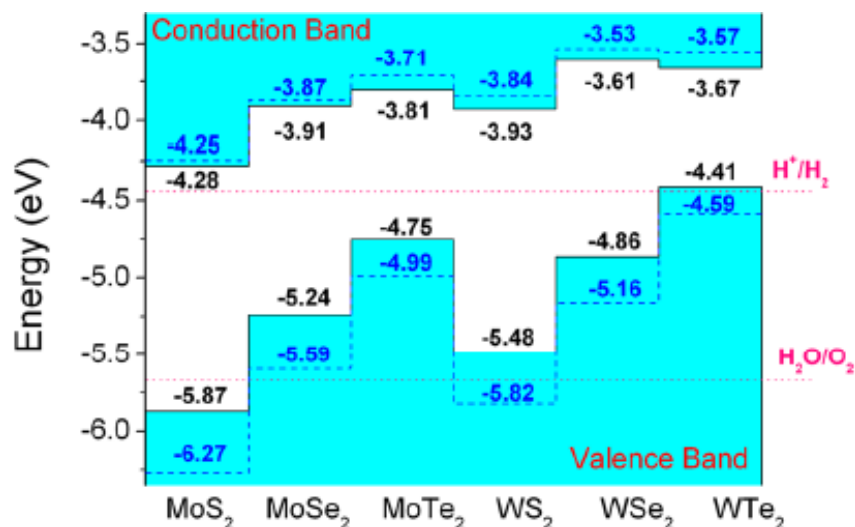
Figure 5.1: Calculated *K* point band alignment for monolayer group VI TMDs (1H). Solid (dashed) lines correspond to DFT results obtained using the PDE (HSE) approximation. Horizontal dotted lines indicate the water reduction (H^+/H_2) and oxidation (H_2O/O_2) potentials. The vacuum level is taken as zero reference for the energy. Reprinted from Kang *et al.* Appl. Phys. Lett. 102, 012111 (2013). Ref. [92], with the permission of AIP Publishing.

In addition, 2D materials electrical properties are often sensitive to environmental and processing conditions. Organic residues and chemical adsorbate contamination [192], atmospheric degradation [193], etching reactivity, and metal contact deposition instability [91], [148], can all degrade FETs performance, impacting devices' contact resistance, carrier mobility and threshold voltage. The high surface-to-volume ratio, typical of 2D materials, renders them particularly sensitive to contaminant molecules and doping. This is an inherent reliability and process integration challenge, which enables on the flip side chemical sensing properties [183]. To address the sensitivity to process and environmental conditions, in Chapter 2 we have described the evolution of TMD FETs integration. First, we introduced top-contact, bottom-gate architectures, where the channel is exposed to the environment and process conditions, then we introduced more complex bottom-contact, dual-gate architectures, which use hBN dielectrics to encapsulate the channel material.

Bulk $MoTe_2$ and thick exfoliated flakes are typically stable in ambient. However few-layer $MoTe_2$ flakes are more sensitive to processing as compared to MoS_2 and $MoSe_2$

layers [Section 2.2.2.3]. At the monolayer limit MoTe$_2$ is extremely sensitive to atmospheric interaction, showing signs of degradation in ambient [194]. This renders the fabrication of monolayer MoTe$_2$ devices, where the channel is not encapsulated, extremely challenging [184], [195]. Stable encapsulation techniques are necessary in order to fabricate reliable devices. For these reasons MoTe$_2$ FETs studies have focused to date only on few-layer flakes. Different reports in literature show predominant *p*-type [184] or ambipolar [196] transfer characteristics in few-layer MoTe$_2$ FETs fabricated using exfoliated flakes. Devices fabricated with few-layer MoTe$_2$ flakes with phase engineered 1T' contacts, present instead predominantly *n*-type transfer characteristics [197]. The absence of studies focusing on the fabrication, addressing the environmental instability challenge, and the electrical characterization of monolayer MoTe$_2$ FETs has prompted our investigation.

5.2 Device fabrication

We fabricate our encapsulated MoTe$_2$ FETs by forming a vertical hBN-MoTe$_2$-hBN stack, as shown in Figure 5.2. Using a two-step process, we first stack the top-hBN dielectric onto the monolayer MoTe$_2$, then we place the stack on a set of high work-function metal contacts pre-patterned on the bottom-hBN dielectric. The detailed fabrication process for a bottom-contact, dual-gate structure has been described in Section 2.3.1, and is shared between devices made with different TMDs. All transfers are performed using PPC/PDMS stamps [Figure 2.17(a)]. Details specific to the fabrication of MoTe$_2$ devices will be highlighted in the following. Monolayer MoTe$_2$ flakes are exfoliated from commercially available crystals from HQ Graphene (typical size ~1cm^2). Monolayers are isolated using optical contrast and Raman spectroscopy, as described in Section 1.1.4.3. To avoid possible atmospheric degradation [Figure 5.2(a)], hBN flakes (~5-15 nm) are aligned and released on the monolayer MoTe$_2$ region [Figure 5.2(b)] right after isolation. The typical amount of time between monolayer isolation and encapsulation, when the flake is exposed to air is at most 30 minutes.
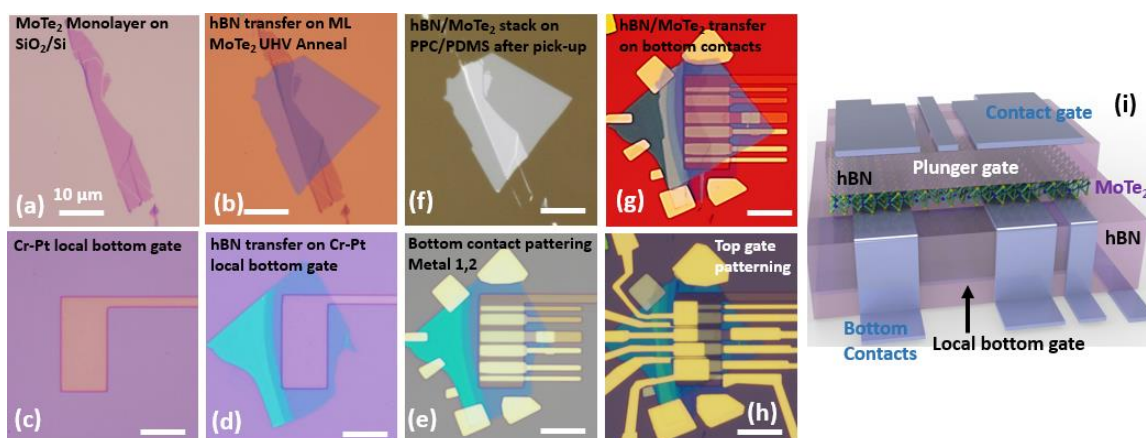
Figure 5.2: Optical micrographs showing: (a) monolayer MoTe$_2$ exfoliated on SiO$_2$/Si; (b) hBN/MoTe$_2$ stack formed immediately after exfoliation, to protect MoTe$_2$ from atmospheric degradation; (c) Cr-Pt (2-9 nm-thick) local bottom-gate, defined on a different SiO$_2$/Si; (d) Cr-Pt local bottom-gate underneath the bottom hBN dielectric (~10-20 nm-thick); (e) bottom-contacts patterning, using two sets of high WF metals (~15 nm-thick), onto bottom hBN; (f) hBN/MoTe$_2$ stack on PPC/PDMS after pick-up; (g) hBN/MoTe$_2$ stack released on the patterned bottom-contacts, after UHV anneal; (h) the final device, after top-gate pattering in alignment with the underlying contacts. (i) 3D illustration of the top section of the completed device in panel (h). Reprinted with permission from S. Larentis *et al.* ACS Nano 11, 4832, Ref. [1]. © 2017 American Chemical Society.

Once the monolayer MoTe$_2$ flake is hBN-encapsulated, we can proceed to pattern the bottom-gate stack and the bottom-contacts. To form the bottom-gate stack, we first pattern a Pt local bottom-gate on a different SiO$_2$/Si substrate [Figure 5.5(c)], which we then cover with the bottom hBN dielectric (~10-20 nm-thick), as shown in Figure 5.2(d). Multiple sets of metal contacts are then patterned on the bottom hBN [Figure 5.2(e)]. In this study, we considered Ni, Pd, Pt, and Au contacts; all deposited metals except Ni use a ~ 3 nm-thick Cr adhesion layer. The typical thickness of the evaporated metal measured with AFM ranges between 10 and 20 nm. It should be noted that all metal used have high WF > 5 eV [85], a precaution taken to avoid oxidation of the metal contacts. Particular attention is paid to the metal interface quality, which along with the metal-TMD band line-up will ultimately determine the carrier injection efficiency, hence the contact resistance. After patterning and annealing in UHV at 350°C, the metal contact topography is probed

with AFM to ensure interfaces are free of organic residues, e.g. PMMA. Once the bottom-gate stack is completed along with the bottom-contacts, the hBN/MoTe$_2$ stack is annealed in UHV at 350°C. This treatment improves the van der Waals bonding between MoTe$_2$ and hBN, allowing for the entire stack to be picked up at once [Figure 5.2(f)], even if the stack has been formed several days earlier. Only the MoTe$_2$ portions outside the hBN, environmentally degraded, are left behind. The hBN/MoTe$_2$ stack is then aligned and transferred on the pre-patterned high WF metal contacts, as shown in [Figure 5.2(f)]. Finally, top-gates and contact extensions are defined in alignment with the underlying contact electrodes [Figure 5.2(h)]. Figure 5.2(i) illustrates the completed hBN encapsulated MoTe$_2$ device.

5.3 MoTe$_2$ air stability

The air stability of exfoliated 2D layers varies significantly from one material to another. While graphene and hBN do not show visible degradation in ambient over a period of many months, black phosphorus degrades in a few days [198]. Sulfur and selenium-based TMD monolayers are characterized by an intermediate air stability compared to graphene and black phosphorus, and are prone to environmental degradation over a period of several weeks to months [193]. Monolayer MoTe2 flakes on the other hand has shown to be considerably more unstable, showing clear signs of degradation resulting from interaction with atmospheric O$_2$ [194]. A significant variation of optical contrast and the Raman spectra intensity capture this interaction [194].

Figures 5.3(a) to 5.3(c) and 5.3(d) to 5.3(g) show two different sets of optical micrographs illustrating the optical contrast evolution of two MoTe$_2$ flakes as a function of time after the exfoliation, including a monolayer MoTe$_2$ partially covered with hBN. While the optical contrast variation with time, associated with the MoTe$_2$ flake degradation is different for each individual exposed flake, the results generally show an optical contrast that drops monotonically until the flake becomes invisible under optical microscopy. On the other hand, hBN-encapsulated MoTe$_2$ flakes [Figures 5.3(a) to 5.3(c)] and thicker MoTe$_2$ flakes [Figures 5.3(a) to 5.3(g)] do not display appreciable optical contrast variation

during the same timeframe. While optical contrast variation provides a qualitative estimate of the degradation process, Raman spectroscopy offers a more systematic way to track it and verify the hBN encapsulation effectiveness in preventing it.
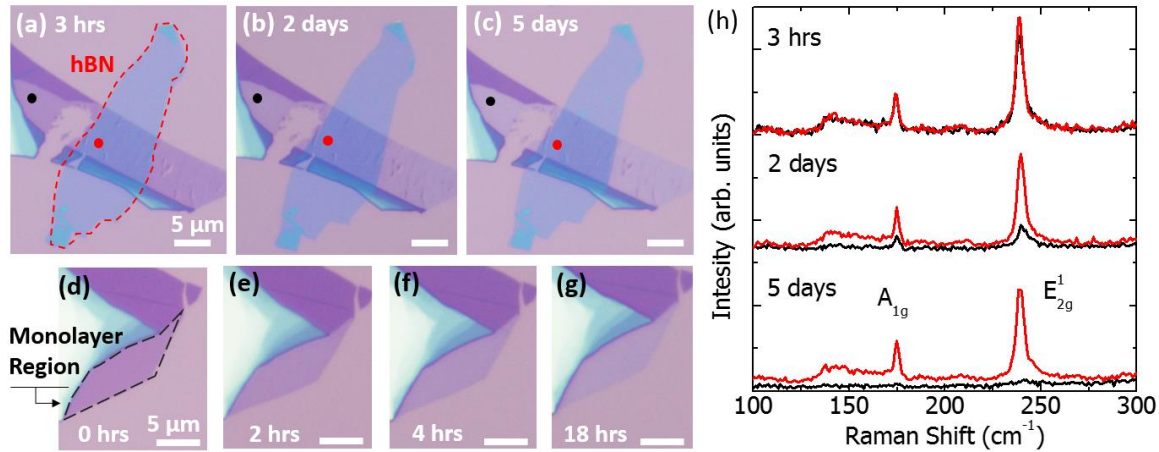
Figure 5.3: (a)-(c) Optical micrographs of a MoTe$_2$ flake taken over the course of 5 days. A section of the monolayer region is hBN-encapsulated (red dot), The optical contrast decreases with time in the exposed monolayer region (black dot). (d)-(g) Similar set of optical micrographs taken over the course of 18 hours for a different MoTe$_2$ flake, showing a different time-dependent optical contrast variation for the monolayer region, marked in (d), compared to the exposed monolayer region (black dot) in (a)-(c). (h) Raman spectra of different monolayer MoTe$_2$ regions, marked in panels (a)-(c), and their evolution with time. The red (black) traces represent the encapsulated (exposed) region. Reprinted with permission from S. Larentis *et al.* ACS Nano 11, 4832, Ref. [1]. © 2017 American Chemical Society.

Figure 5.3(h) shows the Raman spectra of the corresponding monolayer MoTe$_2$ regions highlighted in Figures 5.3(a) to 5.3(c), measured using a 532 nm laser excitation, a 100X objective lens and an excitation power, measured at the sample ~100 μW. The measured Raman spectra presents the typical monolayer MoTe$_2$ signature, also discussed in Section 1.1.4.3, characterized by two peaks at 174 cm^{-1} and 239 cm^{-1} corresponding to the A$_{1g}$ and E$^1_{2g}$ modes, respectively. The absence of the B$^1_{2g}$ mode typically observed at 290 cm^{-1} in thicker flakes, confirms that we are probing a monolayer region [11], [194]. The red traces in Figure 5.3(h) correspond to spectra measured in hBN-encapsulated,

monolayer MoTe$_2$ regions [red dot, Figures 5.3(a) to 5.3(c)], while the black traces are measured in exposed monolayer regions [black dot, Figures 5.3(a) to 5.3(c)]. The encapsulated MoTe$_2$ spectra show little variation over time, with both peaks remaining clearly visible and their intensity unchanged, whereas exposed regions show a dramatic reduction in the peaks' intensity, until no Raman signature is detected, for a measurement carried out 5 days after the flakes had been exfoliated.

The intensity ratio of monolayer MoTe$_2$ E^1$_{2g}$ and Si 520 cm^{-1} peaks ($I_{E^1_{2g}}/I_{Si}$) measured as a function of time allows us to systematically track the flake degradation. Figure 5.4 shows multiple datasets of $I_{E^1_{2g}}/I_{Si}$ measured as function of time, acquired from seven different monolayer MoTe$_2$ flakes, including both exposed and encapsulated regions. Between successive Raman spectra measurements the flakes are left in atmosphere. Figures 5.4(a) and 5.4(d) present $I_{E^1_{2g}}/I_{Si}$ data as function of time measured at different excitation powers 100 µW in panel (a) and 20 µW in panel (d). In each of the seven datasets $I_{E^1_{2g}}/I_{Si}$ drops quickly, by more than half in less than 24 hours, independently of excitation power. Each flake is characterized by a different $I_{E^1_{2g}}/I_{Si}$ decay rate, a finding consistent with the time-dependent optical contrast variation observed in Figure 5.3, which is also sample dependent.

Figures 5.4(b) and 5.4(e) present $I_{E^1_{2g}}/I_{Si}$ data as a function of time measured in partially encapsulated monolayer MoTe$_2$ flakes, at different excitation power, 100 µW in panel (b) and 20 µW in panel (e). The red and black datasets refer to areas where monolayer MoTe$_2$ is encapsulated or exposed, respectively. Encapsulated (red dot) and exposed (black dot) regions are marked accordingly on the optical micrographs of Figures 5.4(c) and 5.4(f). For hBN-encapsulated regions the measured $I_{E^1_{2g}}/I_{Si}$ remains unchanged for an extended period of over 250 hours, while $I_{E^1_{2g}}/I_{Si}$ measured in an exposed region of the same flake shows a significant drop, greater than tenfold, in the same timeframe independent of the excitation power. The optical contrast and Raman spectroscopy data confirm that monolayer MoTe$_2$ flakes have a short lifetime in ambient, and that hBN

encapsulation proves effective in preventing oxidation, and may represent a viable strategy to for the fabrication of monolayer MoTe$_2$ based electronic devices. It is therefore critical to encapsulate the flakes as soon as possible after the exfoliation, given the short monolayer lifetime. As discussed in the previous section monolayer are encapsulated within 30 minutes from the exfoliation.
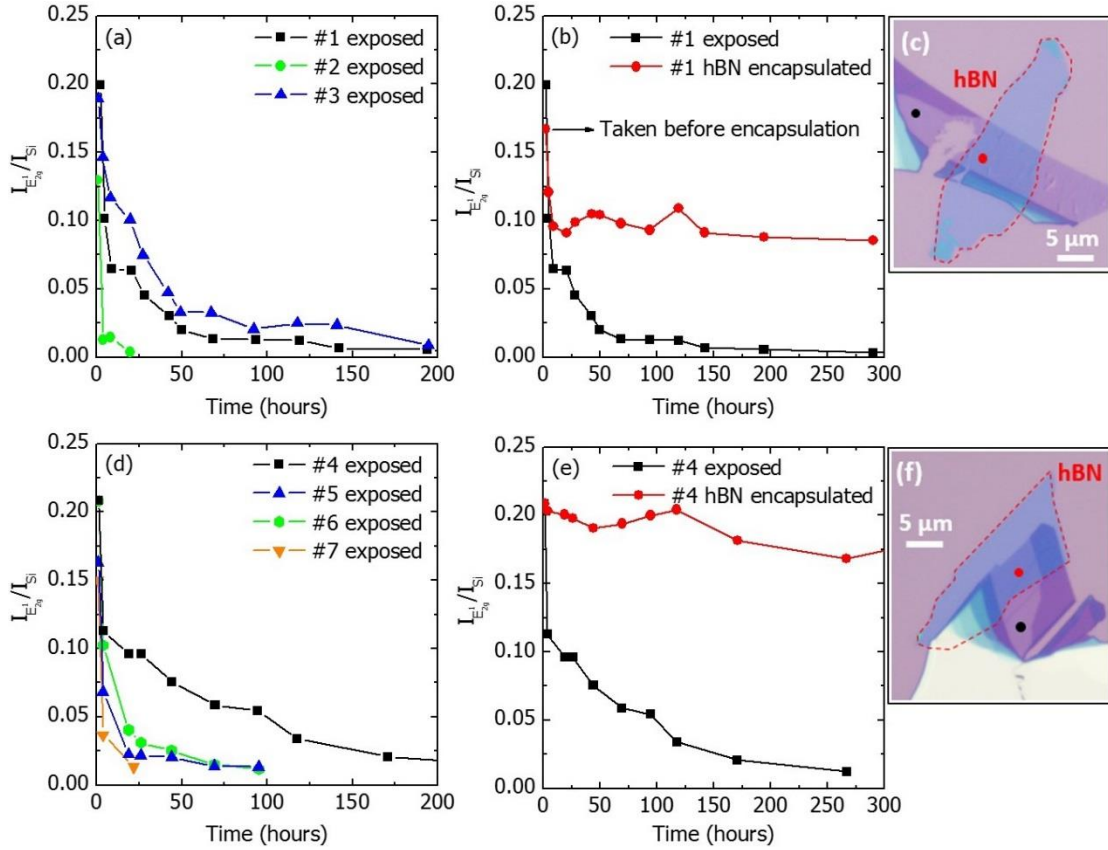
Figure 5.4: (a), (d) $I_{E_{2g}^1}/I_{Si}$ measured as a function of time in different monolayer MoTe$_2$ flakes, using an excitation power of 100 μW in panel (a), 20 μW in panel (d). Each flake is characterized by a different $I_{E_{2g}^1}/I_{Si}$ decay rate. (b), (e) $I_{E_{2g}^1}/I_{Si}$ measured as a function of time, showing a decaying (constant) $I_{E_{2g}^1}/I_{Si}$ over time for the exposed (encapsulated) regions marked in panel (c) and (f), respectively, measured using an excitation power of 100 μW in panel (b) and 20 μW in panel (e). (c), (f) Optical micrographs of partially encapsulated monolayer MoTe$_2$ flakes, red (black) dots mark the encapsulated (exposed) regions. Reprinted with permission from S. Larentis *et al.* ACS Nano 11, 4832, Ref. [1]. © 2017 American Chemical Society.

5.4 DUAL-GATE FETs ELECTRICAL CHARACTERIZATION

Once we established that hBN-encapsulated monolayer MoTe$_2$ flakes are stable, we fabricated dual-gate, bottom-contact, hBN-encapsulated MoTe$_2$ devices. We first examine devices characterized by a top-gate and a local bottom-gate, as illustrated in Figure 5.5(b) inset. The top-gate overlaps both channel and contact regions, while the bottom-gate is patterned underneath the channel and the bottom-contacts, as shown in Figures 5.5(a) and 5.5(b) insets. Tuning the V_{TG} induces carriers in both the channel and contact regions. Carriers induced in the contact region, at the TMD-metal interface, modulate the contact Schottky barrier determining electron and hole injection, which in turn determine the contact resistance [91]. Conversely, tuning the bottom-gate bias (V_G) solely induces carriers in the channel, because of screening by the bottom-contacts.

5.4.1 Metal contact dependence

Figures 5.5(a) and 5.5(b) show the top-gate transfer characteristic (I_D vs V_{TG}) at different $V_D = 0.1$ V and 1 V, while $V_G = 0$ V, for a set of four different high WF metal contacts, Ni, Pd, Au, and Pt. All traces are obtained from the same multi-contact device fabricated using a single monolayer MoTe$_2$ flake. Each pair of metal contacts define a device with channel length $L = 0.75$ µm and a width $W = 3.5$ µm, defined by the top-gate. The device's physical dimensions (W, L) are marked in Figure 5.5(b) inset. The top hBN dielectric is 11.8 nm-thick ($t_{hBN,top}$). The I_D vs V_{TG} data display ambipolar behavior, resulting from V_{TG} modulating both the contact and channel regions, and injecting electrons for positive V_{TG} (n-branch) and holes for negative V_{TG} (p-branch). For all metal contacts examined here, the I_D vs V_{TG} data for the p-branch show a high $I_{ON}/I_{OFF} > 10^6$ at $V_D = 1$ V, comparable with other TMDs [91], [148], while n-branches I_{ON}/I_{OFF} ratios are about two orders of magnitude lower for Ni, Au, and Pt metal contacts. For Pd metal contacts, the n-branch $I_{ON}/I_{OFF} > 10^5$ at $V_D = 1$ V, revealing comparable injection for electron and holes. Few-layer MoTe$_2$ devices, discussed in Section 2.2.2.3 are also characterized by ambipolar transfer characteristics. However, for these devices the n-branch is dominant, showing a

higher I_{ON}/I_{OFF} ratio compared with the *p*-branch, for a V_{BG} range of ±40 V and using a 285 nm-thick SiO_2 dielectric. The emergence of a predominant *n*-branch is independent of metal contacts used, as both high WF metals, e.g. Ni (5.1 eV) and lower WF metals, e.g. In (4.1 eV), show similar results.
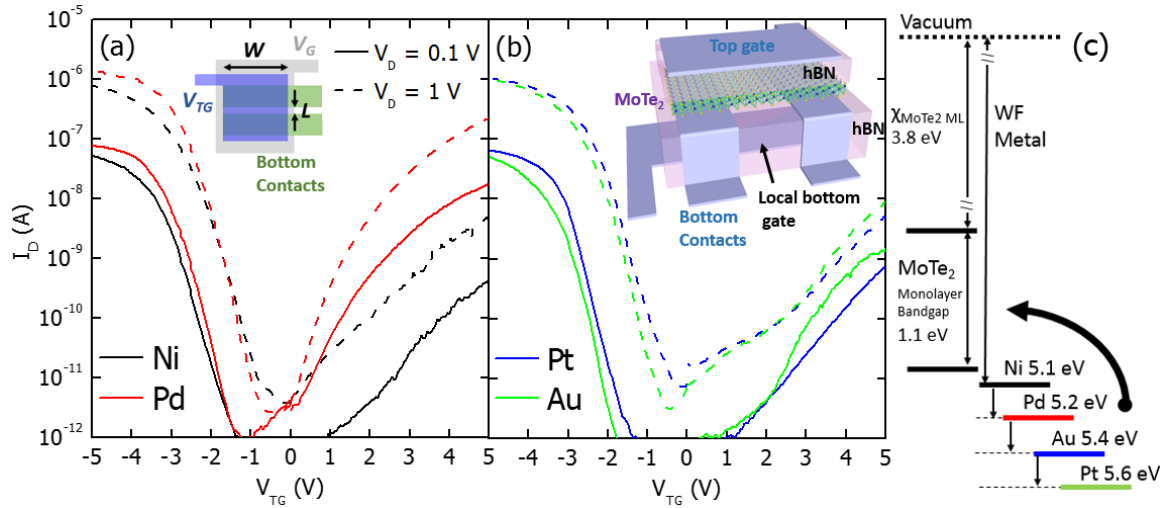
Figure 5.5: (a), (b) I_D vs V_{TG} measured at $V_D = 0.1$ and 1 V, for Ni, Pd metal contacts in panel (a) and for Pt, Au metal contacts in panel (b). I_D vs V_{TG} show ambipolar behavior, injecting holes (electrons) for $V_{TG} < 0$ (> 0). All traces display good hole injection, while electron injection is strongly metal dependent. For all devices $W = 3.5$ μm, $L = 0.75$ μm, $t_{hBN,top} = 11.8$ nm. Panel (a) inset shows the device top-view schematic, while panel (b) inset shows a 3D illustration of the device. (c) Illustration of the expected band alignment between monolayer $MoTe_2$ and the high WF metal contacts [85], [92]. Reprinted with permission from S. Larentis *et al.* ACS Nano 11, 4832, Ref. [1]. © 2017 American Chemical Society.

Figure 5.5(c) shows the expected $MoTe_2$-metal band alignment in the contact region, based on the difference between metal WFs and monolayer $MoTe_2$ electron affinity [85], [92]. Based on this band alignment picture, shown in Figure 5.5(c), we would expect the metals Fermi levels to align towards the monolayer $MoTe_2$ valence band edge, leading to hole injection, for all metals considered. However, our measurements show ambipolar transfer characteristics for each metal contact adopted, particularly in the case of Pd where the peak *p*- and *n*-branch currents at $|V_{TG}| = 5$ V differ by less than an order of magnitude. These experimental results suggest that $MoTe_2$-metal contacts band alignment based on

existing WF and E_{EA} values cannot accurately predict the carrier injection, a finding consistent with experimental observations in MoS$_2$ FETs [148]. The emergence of ambipolar conduction, as opposed to predominant p-type, may result from Fermi level pinning towards mid-gap energies at the MoTe$_2$-metal interface [Figure 5.5(c)]. Tellurium vacancies in MoTe$_2$ are believed to give rise to mid-gap states responsible for the Fermi level pinning [61], which would explain the emergence of ambipolar conduction even when high WF metal contacts are used.
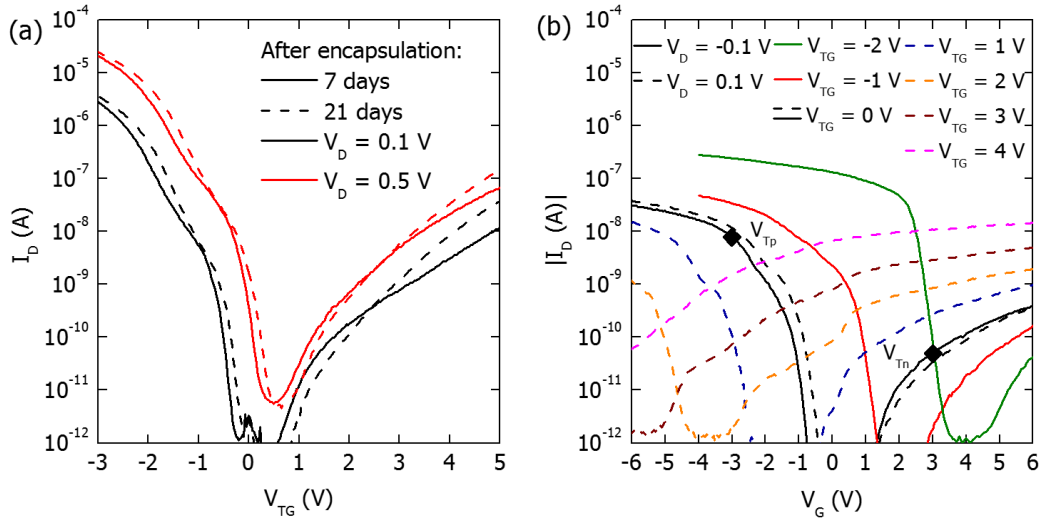
Figure 5.6: (a) I_D vs V_{TG}, measured at $V_D = 0.1$ and 0.5 V. The measurements are taken 7 days and 21 days after the device has been encapsulated in hBN ($W = 13$ μm, $L = 1$ μm, $t_{hBN,top} = 8.2$ nm). (b) $|I_D|$ vs V_G measured at different V_{TG}, for $V_D = \pm 0.1$ V for a device with Pt contacts. While V_{TG} modulates each branch's R_C, depending on the its value and polarity, a variation of both V_{Tp} and V_{Tn} (marked with solid symbols, $V_{TG} = 0$ V trace) depending on the V_{TG} is also observed, not allowing independent adjustment of R_C and V_T ($W = 13$ μm, $L = 1$ μm, $t_{hBN,top} = 8.2$ nm, $t_{hBN,bottom} = 18.5$ nm). Reprinted with permission from S. Larentis *et al.* ACS Nano 11, 4832, Ref. [1]. © 2017 American Chemical Society.

While Raman data confirm that hBN encapsulation prevents monolayer MoTe$_2$ environmental degradation, electrical measurements can provide a more definitive test on the hBN encapsulation effectiveness over longer periods of time. Figure 5.6(a) shows I_D vs V_{TG} at different V_{DS}, for a device using Pt bottom-contacts, measured in vacuum 7, and 21 days after the initial encapsulation. In between the measurements, the sample is stored in a

vacuum desiccator. The transfer characteristics show repeatable current levels and threshold voltage stability, confirming that encapsulated monolayers are electrically stable, over the course of at least to two weeks.

5.4.2 Dual-gate characterization

Figure 5.6(b) shows transfer characteristics ($|I_D|$ vs V_G) measured at different fixed V_{TG}, and at $V_D = \pm 0.1$ V, for a device with Pt contacts, $W = 13$ μm, and $L = 1$ μm, as shown in the device schematic of Figure 5.5(a) inset. The hBN thicknesses for the top and bottom ($t_{hBN\ bottom}$) dielectric are 8.2 nm and 18.5 nm, respectively. The $|I_D|$ vs V_G measurements show ambipolar characteristics displaying a clear insulating state between p- and n-branches. Two threshold voltages, one for each branch, V_{Tp} and V_{Tn} can be defined, and are marked with solid symbols on the $V_{TG} = 0$ V trace, in Figure 5.6(b). Their values are extrapolated from the linear region of each branch. A clear variation of both V_{Tp} and V_{Tn} as a function of the V_{TG} value and polarity is observed. While an applied V_{TG} induces carriers in the channel, and sets both V_{Tp} and V_{Tn} concurrently, it also changes the carrier density in the proximity of the contact metal-MoTe$_2$ interface, thus affecting the R_C value. Increasing the $|V_{TG}|$ value reduces the transfer characteristic typical ambipolar character. For example, negative V_{TG} values result in a decrease of the p-branch and an increase n-branch R_C, and vice versa. While rendering the transport unipolar within the V_G window probed is desirable, the device structure of Figure 5.5(b) does not allow an independent tuning of V_T and R_C. The inherent limitation of this device structure stems from the top-gate geometry, which concurrently controls the contact and channel regions carrier densities. To mitigate the V_{TG} induced V_T shift, and render the device unipolar a different gating scheme is required.

5.5 MULTI-GATE FETS ELECTRICAL CHARACTERIZATION

Figure 5.7(a) illustrates a new gating layout, where a single top-gate [as in Figures 5.5(a) and 5.5(b) insets] is replaced by two separate top contact-gates (CG1, CG2), and by an additional plunger-gate (PG), introduced between the two split contact-gates. The

structure retains the local bottom-gate patterned under the bottom hBN dielectric. The use of two individual contact-gates and a plunger-gate instead of a single top-gate allows us to separately control the carrier density in the contact, and channel regions of the device, thus separately controlling V_T and R_C. An additional contact is introduced [contact 1 in Figure 5.7(a)] to measure the drain current between contacts 1,2 as function of contact-gate 1 bias ($I_{D\,1,2}$ vs V_{CG1}). Figure 5.7(b) shows $I_{D\,1,2}$ vs V_{CG1}, measured at $V_D = 0.1$ V, 1 V and at $V_G = 0$ V, displaying ambipolar behavior, similar to Figure 5.5(b) data. Measuring $I_{D\,1,2}$ vs V_{CG1} allows to evaluate carrier injection as a function of the V_{CG}, i.e. p-type (n-type) injection for $V_{CG} < 0$ (> 0) V and estimate the R_C for each branch.

Figures 5.7(c) and 5.7(d) show the measured bottom-gate transfer characteristic between contacts 2 and 3 a function of V_G ($|I_{D\,2,3}|$ vs V_G), at fixed contact-gates 1,2 ($V_{CG1,2}$) and plunger-gate (V_{PG}) biases. The distance between the two contact-gates (ΔL) is 0.9 μm, the plunger-gate length $L_{PG} = 0.25$ μm, the flake-limited channel width is $W = 4$ μm, and $t_{hBN\,top} = 5.5$ nm and $t_{hBN\,bottom} = 18$ nm. Setting $V_{CG1,2}$ at fixed values, marked with solid symbols in Figure 5.7(b) allows us to measure unipolar p- and n-type $|I_{D\,2,3}|$ vs V_G, where $V_{CG1,2} < 0$ V allows for hole injection and $V_{CG1,2} > 0$ V allows for electron injection [Figure 5.7(c) and 5.7(d)]. The V_{CG} polarity determines electron or hole injection as shown in Figure 5.7(b), while the V_{CG} value determines R_C for either device type. To a higher $|V_{CG}|$ corresponds a lower contact resistance.

As described earlier, Pt contacts are expected to yield lower R_C for hole injection as is reflected by the maximum $|I_{D\,2,3}|$ measured for each characteristic, a behavior consistent with the I_D vs V_{TG} and $I_{D\,1,2}$ vs V_{CG1} data of Figure 5.5(b) and 5.7(b), respectively. Tuning the carrier density in the contact regions electrostatically dopes the contacts, allowing for R_C control, and decoupling the contact-gate dependent R_C from the channel resistance. At the same time, fixed contact-gate biases render the contacts selective for electron or holes, thus enabling reconfigurable unipolar devices. Ideally, reconfigurable devices based on ambipolar, low R_C contacts would allow IC reconfiguration down to the single transistor, which would be either p- or n-type depending on the contact-gates' polarity [199].
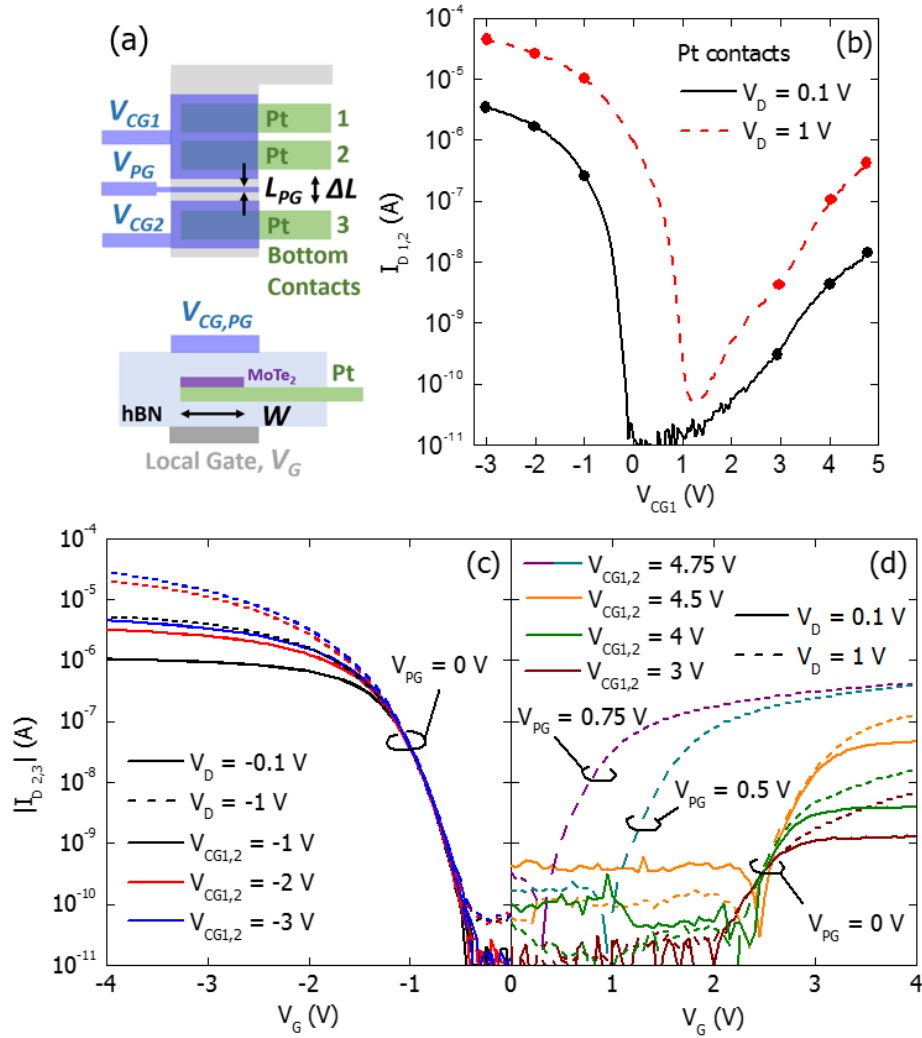
Figure 5.7: (a) Schematic of the gating layout showing top-view and cross-section. The device is characterized by a local bottom-gate, two contact-gates, and a plunger-gate ($W = 4$ μm, $\Delta L = 0.9$ μm, $L_{PG} = 0.25$ μm, $t_{hBN,top} = 5.5$ nm, $t_{hBN,bottom} = 18$ nm). (b) $I_{D\,1,2}$ vs V_{CG1} measured at $V_D = 0.1$ and 1 V (Pt contacts), showing ambipolar behavior. Solid symbols indicate V_{CG}s used in panels (c) and (d). (c, d) $|I_{D\,2,3}|$ vs V_G measured at $|V_D| = 0.1$ and 1 V. Setting different $V_{CG1,2} < 0$ (> 0), determines p-FET (n-FET) reconfigurable operation. The contacts gates induce high carrier densities at the metal-MoTe2 junction, modulating R_C, no longer impacting the V_T. Tuning V_{PG} values allows to adjust the threshold voltage, without affecting the R_C. Reprinted with permission from S. Larentis *et al.* ACS Nano 11, 4832, Ref. [1]. © 2017 American Chemical Society.

Most importantly, Figure 5.7(c) and 5.7(d) data show that the applied $V_{CG1,2}$ no longer impacts the V_T in either p- or n-type configuration, as opposed to Figure 5.6(b) data. We note that devices with split contact-gates, but without a plunger-gate do not allow for R_C and V_T decoupling, because the contact-gates' fringing field will still affect the channel, rendering V_T again V_{CG} dependent. Figure 5.7(d) shows $|I_{D\,2,3}|$ vs V_G measured for $V_{PG} = 0$, 0.5, 0.75 V. Tuning the V_{PG} value compensates for unintentional doping in the region underneath the plunger-gate, allowing for V_{Tn} adjustment without affecting R_C, which is set by the contact-gates. The subthreshold swings for the p- and n-FET are 180 mV/dec ($V_{CG1,2}$ = -3 V, V_{PG} = 0 V) and 240 mV/dec ($V_{CG1,2}$ = 4.75 V, V_{PG} = 0.75 V), respectively, using a 18 nm-thick hBN bottom-gate dielectric. The threshold voltages and subthreshold slopes for either type of FET are largely insensitive to V_D, consistent with a long channel picture, i.e. minimal drain induced barrier lowering. The availability of p- and n-type devices along with the ability to achieve symmetric characteristics, tuning V_{CG} and V_{PG}, allows us to design complementary logic gates.

5.6 COMPLEMENTARY DEVICES: INVERTER GATE

A schematic of the complementary device where two sets of bottom-contacts and top-gates are introduced to integrate two complementary FETs, along with a common local bottom-gate is presented in Figure 5.8(a). Two separate sets of contact and plunger-gates allow to control and decouple each FET's R_C and V_T, in order achieve balanced p- and n-FET performances, required for complementary logic operation. Two separate sets of Pt and Au metal contacts are used to integrate p- and n-FETs, respectively. In this specific implementation, Au contacts are chosen for the n-FET over the Pt contacts because they provide better electron injection, as shown in Figure 5.5(b).
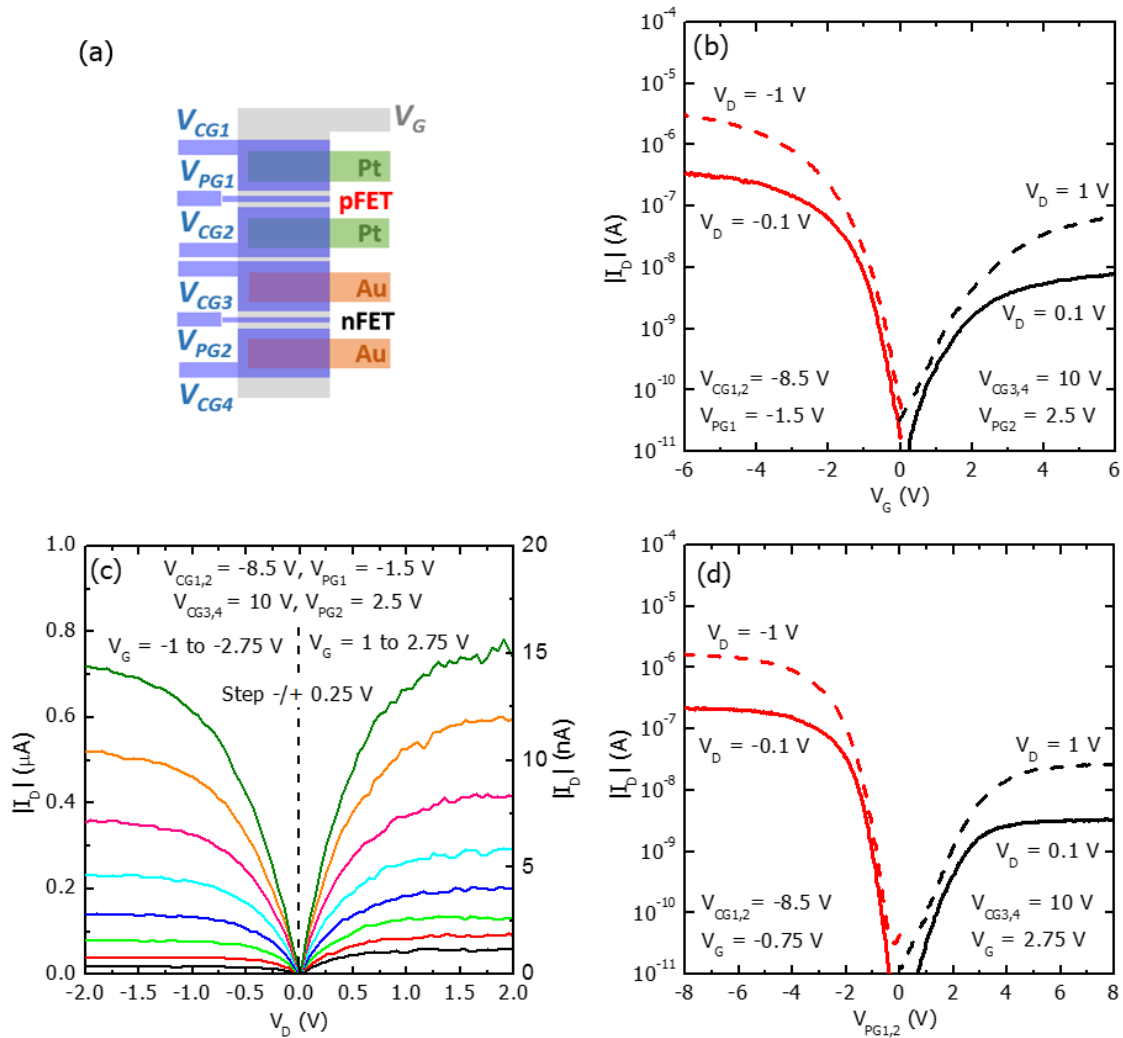
Figure 5.8: (a) Device schematic, with two FETs integrated using separate Pt and Au bottom-contacts ($W = 6.5\ \mu m$, $L' = 0.9\ \mu m$, $L_{PG} = 0.25\ \mu m$, $t_{hBN,top} = t_{hBN,bottom} = 12$ nm). (b) $|I_D|$ vs. V_G measured for p- and n-FET, at $|V_D| = 0.1$ and 1 V. Different $V_{CG}s$' settings allow us to define complementary n- and p-FETs, namely an Au-contacted n-FET ($V_{CG} > 0$ V) and a Pt-contacted p-FET ($V_{CG} < 0$ V). Setting the $V_{PG}s$ values allow us to set matching V_{TS}. (c) $|I_D|$ vs V_D measured for p- (left axis) and n-FET (right axis), at different fixed V_{GS}, showing current saturation. (d) $|I_D|$ vs $V_{PG1,2}$ measured for p- and n-FET, at $|V_D| = 0.1$ and 1 V. Plunger and bottom-gate roles are exchanged, compared to (a), showing good symmetry between V_G and V_{PG} in this device design. Fixed V_G values are used to set either V_T, with $V_{CG}s$ settings same as in (b). Reprinted with permission from S. Larentis *et al.* ACS Nano 11, 4832, Ref. [1]. © 2017 American Chemical Society.

Figure 5.8(b) shows $|I_D|$ vs V_G for both p- (V_G, $V_D < 0$) and n-FET (V_G, $V_D > 0$), measured for a set of fixed V_{CG} and V_{PG} values. The device physical dimensions are: $W = 6.5$ μm, $L' = 0.9$ μm, $L_{PG} = 0.25$ μm, and $t_{hBN,top} = t_{hBN,bottom} = 12$ nm; W is limited by the flake width. The V_{CG} values are set to provide the highest I_D, while the V_{PG} values are set to determine matching threshold voltages for the p- and n-FET, $|V_T| \cong 1.45$ V, extracted from the linear region extrapolation of $|I_D|$ vs V_G traces at $V_D = \pm 0.1$ V. The output characteristics ($|I_D|$ vs V_D) for both p- and n-FET, measured for the same set of V_{CG} and V_{PG} biases in Figure 5.8(b), are shown in Figure 5.8(c). The $|I_D|$ vs V_D characteristic show linearity at low V_D, and current saturation at high V_D.

Figure 5.8(d) shows a set of plunger-gate transfer characteristic ($|I_D|$ vs $V_{PG1,2}$), for both p- (V_{PG1}, $V_D < 0$) and n-FET (V_{PG2}, $V_D > 0$), using the same device considered in Figures 5.8(b) and 5.8(c). In this measurement the roles of bottom-gate and plunger-gates are exchanged compared to Figure 5.8(b), with the plunger-gate modulating the channel and fixed V_G set to achieve matching threshold voltages $V_{Tp} \cong -1.5$ V, $V_{Tn} \cong 1.7$ V, as extracted from the linear region of $|I_D|$ vs $V_{PG1,2}$ traces at $V_D = \pm 0.1$ V. The V_{CG} values used to characterize $|I_D|$ vs $V_{PG1,2}$ are the same as in Figures 5.8(b) and 5.8(c), and are set to minimize R_C (maximize I_D) for both p- and n-FET. Our dual gating scheme using V_G, V_{PG} is largely symmetric, albeit not fully because the PG does not cover the entire channel ($L_{PG} < \Delta L$). Such partial symmetry is displayed by the lower peak $|I_D|$ shown in Figure 5.8(d) as compared to Figure 5.8(c). The peak $|I_D|$ ratios for n- or p-branches measured as function of V_G or V_{PG} is close to 1/2. The channel regions in between contact and plunger-gates behave as contact access regions, when using the plunger-gate as the control gate. These areas are only affected by contact and plunger-gates fringing field. Hence, the contact access regions are lightly doped, limiting the maximum I_D because of their series resistance contribution.

Figure 5.9(a) shows the configuration used to implement a complementary inverter gate, where the p- and n-FET described earlier [Figure 5.8(a) and 5.8(b)] are connected in series. Their drain contacts are shorted, defining the logic gate output voltage (V_{OUT}) node, while the source of the n-FET is grounded, and the source of the p-FET is connected to the

174

supply voltage (V_{DD}). The input voltage of the inverter (V_{IN}) is connected to the local bottom-gate. Figure 5.9(b) shows the voltage transfer characteristic (VTC) of the inverter, for a set of V_{CG} and V_{PG} biases specified in Figure 5.9(c). The inverter operates as follows: for low V_{IN}, the n-FET is off and the p-FET (pull-up) connects V_{OUT} to V_{DD}, while for high V_{IN}, the p-FET is off and the n-FET (pull-down) connects V_{OUT} to ground, inverting the V_{IN} signal, thus performing the NOT logic operation. The VTC displays full logic swing, with wide noise margin and a steep transition between the logic states. The logic state's transition is characterized by the voltage gain = $|dV_{OUT}/dV_{IN}|$, shown in Figure 5.9(c) as function of V_{IN}. In the transition region, near $V_{DD}/2$, the voltage gain is > 1 [Figure 5.9(b)], implying signal regeneration through the logic gate. Noise immunity of the inverter is characterized by the noise margin, which is determined by extracting the maximum low V_{IN} (V_{IL}) and the minimum high V_{IN} (V_{IH}). V_{IL} and V_{IH} are measured at unitary voltage gain and allow to define the high and low noise margins (NM_L, NM_H) respectively, measured as percentage of the V_{DD}: NM_L = 37% and NM_H = 32%, for V_{DD} = 2 V.

While the p- and n-FET performances remains uneven in this demonstration, and further work is needed to improve the n-FET performance, the successful integration of a complementary inverter gate reveals potential for this device scheme, relying on electrostatic doping. To obtain a symmetric VTC transition, $V_{CG1,2}$ values for the p-FET are tuned, as a function of V_{DD}, to balance the pull-up and pull-down transistors. V_{PG} values for the p-FET are left unchanged because, as shown in Figure 5.7(c) and 5.7(d) the V_T is largely independent of V_D and V_{CG}.
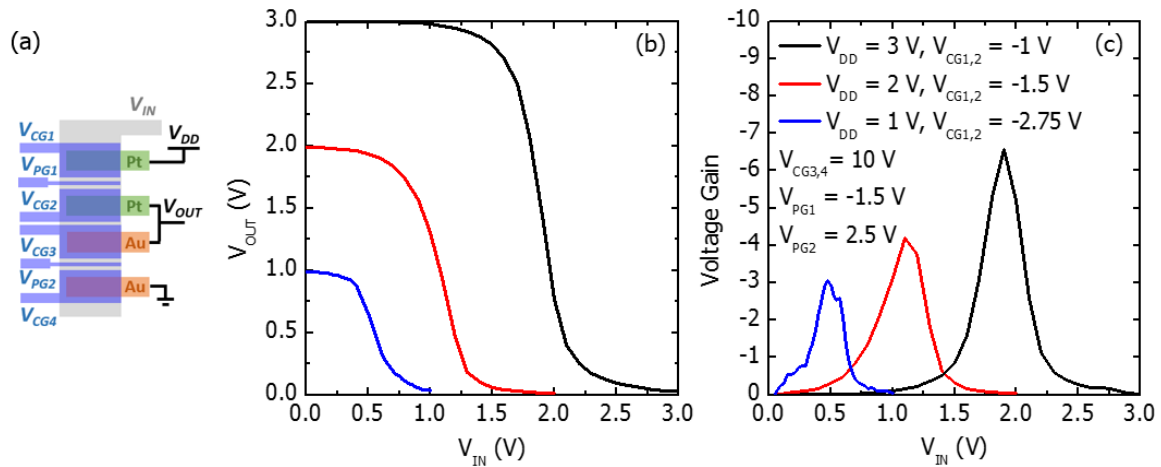
Figure 5.9: (a) Device schematic showing the biasing scheme for the inverter operation, one p-FET (Pt contacts) and one n-FET (Au contacts) are connected in series. (b) Measured VTC of the complementary inverter gate at different V_{DD}, $V_{CG1,2}$, specified in panel (c), and at $V_{CG3,4} = 10$ V, $V_{PG1} = -1.5$ V and $V_{PG2} = 2.5$ V, obtained using the same p- and n-FET characterized in Figure 5.8(b) and 5.8(c). A good VTC symmetry at different V_{DD} is obtained by tuning $V_{CG1,2}$ concurrently, to balance pull-up and pull-down transistors. (c) Voltage gain = $|dV_{OUT}/dV_{IN}|$ vs V_{IN}, for different V_{DD}s. For each V_{DD} in the transition region (near $V_{DD}/2$) the voltage gain is larger than unity, ensuring signal regeneration properties of the logic gate. Reprinted with permission from S. Larentis *et al.* ACS Nano 11, 4832, Ref. [1]. © 2017 American Chemical Society.

5.7 P-I-N DIODE

A useful application for electrostatically doped devices, characterized by split-gate geometries is the fabrication of *p-n* junctions. Figure 5.10(a) shows a schematic of a device structure with split contact-gates, but without a plunger-gate. Applying V_{CG}s with opposite polarity to the adjacent contact-gates, we obtain two contacts selective to hole and electron injection. The contact-gates overlap the channel defining two electrostatically doped regions adjacent to the bottom-contacts, *p* and *n* doped respectively. This scheme resembles a traditional Si *p-i-n* junction, where spatially defined *p* and *n* regions are achieved through substitutional doping. Figure 5.10(b) shows the diode characteristic ($|I_D|$ vs V_D), measured for $V_{CG1} = 8$ V and $V_{CG2} = -6$ V, displays rectifying behavior, coupled with series resistance effects at large V_D biases.

176
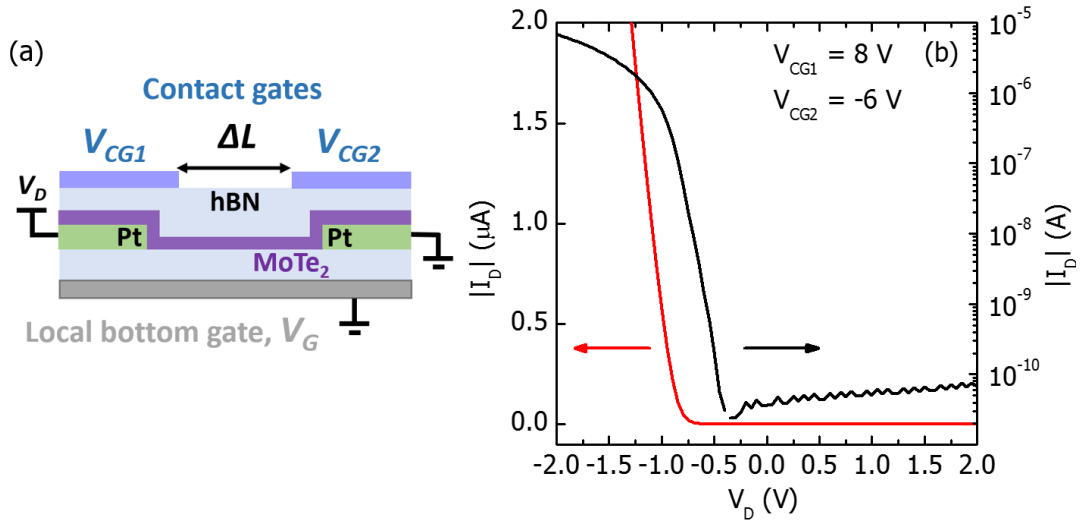
Figure 5.10: (a) Schematic of the device cross-section (W = 5 μm, ΔL = 1.5 μm, $t_{hBN,top}$ = 12.3 nm). (b) $|I_D|$ vs V_D measured for opposite polarity V_{CG1} and V_{CG2}, thus defining a *p-i-n* junction, which shows rectifying behavior. Reprinted with permission from S. Larentis *et al.* ACS Nano 11, 4832, Ref. [1]. © 2017 American Chemical Society.

Electrically tunable monolayer TMD based *p-i-n* diodes are of interest for optoelectronic applications in the red or near infrared spectrum. Device schemes implemented using bottom split-gates and top-contacts, complementary to our architecture [Figure 5.10(a)], have been used to fabricate monolayer WSe_2 electrically tunable *p-i-n* diodes [200]–[203]. These are operated as light emitting diodes (LEDs), showing electroluminescence at 1.65 eV at RT, photodetectors (PDs) and photovoltaic cells. Recently, using the same architecture presented in Figure 5.10(a), with the exception of graphite split gates used instead of metal gates, Bie *el al.* [204] have demonstrated a bilayer $MoTe_2$ near infra-red LED in forward bias, with RT temperature electroluminescence at 1.05 eV, and a PD in reverse bias, both coupled with a silicon waveguide.

5.8 SUMMARY

In summary, we report the fabrication of air-stable, reconfigurable monolayer $MoTe_2$ FETs. The hBN encapsulation of monolayer $MoTe_2$ flakes prevents atmospheric degradation, preserving optical and electrical properties, as confirmed by time-dependent

electrical and Raman spectroscopy measurements. Using a set of pre-patterned high WF contacts and introducing contact specific gates to tune the carrier density at the metal-MoTe$_2$ junction, we obtain a gate-independent low R_C, enabling reconfigurable unipolar operation. Adding a plunger-gate in between individual contact-gates allows us to set V_T independently from R_C. The availability of p- and n-FET with low R_C and adjustable V_T allows for complementary operation. We demonstrate the integration of a complementary inverter gate on a single monolayer MoTe$_2$ flake, highlighting possible integrated circuit applications. Thanks to a similar gating scheme, where the plunger-gate is removed, the MoTe$_2$ electrostatic doping enables p-i-n diode fabrication, of potential interest for optoelectronic applications. The importance of this multi-gate structure goes beyond MoTe$_2$ based devices and can be extended to other TMDs and novel 2D systems allowing to decouple channel gating and Schottky contacts.

References

[1] K. F. Mak, C. Lee, J. Hone, J. Shan, and T. F. Heinz, "Atomically Thin MoS_2: A New Direct-Gap Semiconductor," *Phys. Rev. Lett.*, vol. 105, no. 13, p. 136805, 2010.

[2] R. Fivaz and E. Mooser, "Mobility of charge carriers in semiconducting layer structures," *Phys. Rev.*, vol. 163, no. 3, p. 743, 1967.

[3] A. R. Beal and H. P. Hughes, "Kramers-Kronig analysis of the reflectivity spectra of 2H-MoS_2 , 2H-$MoSe_2$ and 2H-$MoTe_2$," *J. Phys. C Solid State Phys.*, vol. 12, no. 5, p. 881, 1979.

[4] R. Coehoorn, C. Haas, J. Dijkstra, C. J. F. Flipse, R. A. De Groot, and A. Wold, "Electronic structure of $MoSe_2$, MoS_2, and WSe_2. I. Band-structure calculations and photoelectron spectroscopy," *Phys. Rev. B*, vol. 35, no. 12, p. 6195, 1987.

[5] S. Larentis, B. Fallahazad, and E. Tutuc, "Field-effect transistors and intrinsic mobility in ultra-thin $MoSe_2$ layers," *Appl Phys Lett*, vol. 101, no. 22, pp. 223104–223104, 2012.

[6] Q. H. Wang, K. Kalantar-Zadeh, A. Kis, J. N. Coleman, and M. S. Strano, "Electronics and optoelectronics of two-dimensional transition metal dichalcogenides," *Nat Nano*, vol. 7, no. 11, pp. 699–712, 2012.

[7] M. Chhowalla, H. S. Shin, G. Eda, L.-J. Li, K. P. Loh, and H. Zhang, "The chemistry of two-dimensional layered transition metal dichalcogenide nanosheets," *Nat. Chem.*, vol. 5, no. 4, pp. 263–275, 2013.

[8] W. S. Yun, S. W. Han, S. C. Hong, I. G. Kim, and J. D. Lee, "Thickness and strain effects on electronic structures of transition metal dichalcogenides: 2H-MX_2 semiconductors (M = Mo, W; X = S, Se, Te)," *Phys. Rev. B*, vol. 85, no. 3, p. 033305, 2012.

[9] J. A. Wilson and A. D. Yoffe, "The transition metal dichalcogenides discussion and interpretation of the observed optical, electrical and structural properties," *Adv. Phys.*, vol. 18, no. 73, pp. 193–335, May 1969.

[10] K. K. Kam and B. A. Parkinson, "Detailed photocurrent spectroscopy of the semiconducting group VIB transition metal dichalcogenides," *J. Phys. Chem.*, vol. 86, no. 4, pp. 463–467, 1982.

[11] C. Ruppert, O. B. Aslan, and T. F. Heinz, "Optical Properties and Band Gap of Single- and Few-Layer $MoTe_2$ Crystals," *Nano Lett.*, vol. 14, no. 11, pp. 6231–6236, 2014.

[12] A. Kormányos *et al.*, "k · p theory for two-dimensional transition metal dichalcogenide semiconductors," *2D Mater.*, vol. 2, no. 2, p. 022001, 2015.

[13] A. F. Rigosi, H. M. Hill, K. T. Rim, G. W. Flynn, and T. F. Heinz, "Electronic band gaps and exciton binding energies in monolayer $Mo_xW_{1-x}S_2$ transition metal dichalcogenide alloys probed by scanning tunneling and optical spectroscopy," *Phys. Rev. B*, vol. 94, no. 7, p. 075440, 2016.

179

[14] M. M. Ugeda *et al.*, "Giant bandgap renormalization and excitonic effects in a monolayer transition metal dichalcogenide semiconductor," *Nat. Mater.*, vol. 13, no. 12, p. 1091, 2014.

[15] J. Chang, S. Larentis, E. Tutuc, L. F. Register, and S. K. Banerjee, "Atomistic simulation of the electronic states of adatoms in monolayer MoS_2," *Appl. Phys. Lett.*, vol. 104, no. 14, p. 141603, 2014.

[16] D. Xiao, G.-B. Liu, W. Feng, X. Xu, and W. Yao, "Coupled Spin and Valley Physics in Monolayers of MoS2 and Other Group-VI Dichalcogenides," *Phys. Rev. Lett.*, vol. 108, no. 19, p. 196802, May 2012.

[17] F. Rose, M. O. Goerbig, and F. Piéchon, "Spin- and valley-dependent magneto-optical properties of MoS_2," *Phys. Rev. B*, vol. 88, no. 12, p. 125438, 2013.

[18] Y. Zhang *et al.*, "Direct observation of the transition from indirect to direct bandgap in atomically thin epitaxial $MoSe_2$," *Nat. Nanotechnol.*, vol. 9, no. 2, p. nnano.2013.277, 2013.

[19] A. Kuc, N. Zibouche, and T. Heine, "Influence of quantum confinement on the electronic structure of the transition metal sulfide TS_2," *Phys. Rev. B*, vol. 83, no. 24, 2011.

[20] G.-B. Liu, W.-Y. Shan, Y. Yao, W. Yao, and D. Xiao, "Three-band tight-binding model for monolayers of group-VIB transition metal dichalcogenides," *Phys. Rev. B*, vol. 88, no. 8, p. 085433, 2013.

[21] P. Tonndorf *et al.*, "Photoluminescence emission and Raman response of monolayer MoS_2, $MoSe_2$, and WSe_2," *Opt. Express*, vol. 21, no. 4, pp. 4908–4916, 2013.

[22] T. Cheiwchanchamnangij and W. R. L. Lambrecht, "Quasiparticle band structure calculation of monolayer, bilayer, and bulk MoS_2," *Phys. Rev. B*, vol. 85, no. 20, May 2012.

[23] K. S. Novoselov *et al.*, "Electric field effect in atomically thin carbon films.," *Science*, vol. 306, no. 5696, pp. 666–9, 2004.

[24] M. M. Benameur, B. Radisavljevic, J. S. Héron, S. Sahoo, H. Berger, and A. Kis, "Visibility of dichalcogenide nanolayers," *Nanotechnology*, vol. 22, no. 12, p. 125706, 2011.

[25] P. Blake *et al.*, "Making graphene visible," *Appl. Phys. Lett.*, vol. 91, no. 6, p. 063124, 2007.

[26] Y. Hao *et al.*, "The Role of Surface Oxygen in the Growth of Large Single-Crystal Graphene on Copper," *Science*, vol. 342, no. 6159, pp. 720–723, 2013.

[27] D. Chiappe *et al.*, "Controlled Sulfurization Process for the Synthesis of Large Area MoS2 Films and MoS_2/WS2 Heterostructures," *Adv. Mater. Interfaces*, vol. 3, no. 4, p. 1500635, 2016.

[28] A. M. van der Zande *et al.*, "Grains and grain boundaries in highly crystalline monolayer molybdenum disulphide," *Nat. Mater.*, vol. 12, no. 6, pp. 554–561, 2013.

[29] S. Najmaei, Z. Liu, P. M. Ajayan, and J. Lou, "Thermal effects on the characteristic Raman spectrum of molybdenum disulfide (MoS$_2$) of varying thicknesses," *Appl. Phys. Lett.*, vol. 100, no. 1, p. 013106, Jan. 2012.

[30] J. Zhou *et al.*, "A library of atomically thin metal chalcogenides," *Nature*, vol. 556, no. 7701, pp. 355–359, 2018.

[31] X. Zhang, X.-F. Qiao, W. Shi, J.-B. Wu, D.-S. Jiang, and P.-H. Tan, "Phonon and Raman scattering of two-dimensional transition metal dichalcogenides from monolayer, multilayer to bulk material," *Chem. Soc. Rev.*, vol. 44, no. 9, pp. 2757–2785, 2015.

[32] A. Molina-Sánchez and L. Wirtz, "Phonons in single-layer and few-layer MoS$_2$ and WS2," *Phys. Rev. B*, vol. 84, no. 15, p. 155413, 2011.

[33] M. Yamamoto *et al.*, "Strong Enhancement of Raman Scattering from a Bulk-Inactive Vibrational Mode in Few-Layer MoTe$_2$," *ACS Nano*, vol. 8, no. 4, pp. 3895–3903, 2014.

[34] M. S. Dresselhaus, G. Dresselhaus, R. Saito, and A. Jorio, "Raman spectroscopy of carbon nanotubes," *Phys. Rep.*, vol. 409, no. 2, pp. 47–99, 2005.

[35] L. M. Malard, M. A. Pimenta, G. Dresselhaus, and M. S. Dresselhaus, "Raman spectroscopy in graphene," *Phys. Rep.*, vol. 473, no. 5, pp. 51–87, 2009.

[36] N. Wakabayashi, H. G. Smith, and R. M. Nicklow, "Lattice dynamics of hexagonal MoS$_2$ studied by neutron scattering," *Phys. Rev. B*, vol. 12, no. 2, pp. 659–663, 1975.

[37] C. Lee, H. Yan, L. E. Brus, T. F. Heinz, J. Hone, and S. Ryu, "Anomalous Lattice Vibrations of Single- and Few-Layer MoS$_2$," *ACS Nano*, vol. 4, no. 5, pp. 2695–2700, May 2010.

[38] K. Kim, J.-U. Lee, D. Nam, and H. Cheong, "Davydov Splitting and Excitonic Resonance Effects in Raman Spectra of Few-Layer MoSe$_2$," *ACS Nano*, vol. 10, no. 8, pp. 8113–8120, 2016.

[39] T. Sekine, M. Izumi, T. Nakashizu, K. Uchinokura, and E. Matsuura, "Raman Scattering and Infrared Reflectance in 2H-MoSe$_2$," *J. Phys. Soc. Jpn.*, vol. 49, no. 3, pp. 1069–1077, 1980.

[40] P. Soubelet, A. E. Bruchhausen, A. Fainstein, K. Nogajewski, and C. Faugeras, "Resonance effects in the Raman scattering of monolayer and few-layer MoSe$_2$," *Phys. Rev. B*, vol. 93, no. 15, p. 155407, 2016.

[41] X. Luo *et al.*, "Effects of lower symmetry and dimensionality on Raman spectra in two-dimensional WSe$_2$," *Phys. Rev. B*, vol. 88, no. 19, p. 195313, 2013.

[42] R. He *et al.*, "Observation of infrared-active modes in Raman scattering from topological insulator nanoplates," *Nanotechnology*, vol. 23, no. 45, p. 455703, 2012.

[43] A. Alharbi, D. Armstrong, S. Alharbi, and D. Shahrjerdi, "Physically Unclonable Cryptographic Primitives by Chemical Vapor Deposition of Layered MoS$_2$," *ACS Nano*, vol. 11, no. 12, pp. 12772–12779, 2017.

[44] J. Xiao, M. Zhao, Y. Wang, and X. Zhang, "Excitons in atomically thin 2D semiconductors and their applications," *Nanophotonics*, vol. 6, no. 6, pp. 1309–1328, 2017.

[45] N. Scheuschner, O. Ochedowski, A.-M. Kaulitz, R. Gillen, M. Schleberger, and J. Maultzsch, "Photoluminescence of freestanding single- and few-layer MoS_2," *Phys. Rev. B*, vol. 89, no. 12, p. 125406, 2014.

[46] Y. Li *et al.*, "Measurement of the optical dielectric function of monolayer transition-metal dichalcogenides: MoS_2, $MoSe_2$, WS_2, and WSe_2," *Phys. Rev. B*, vol. 90, no. 20, p. 205422, 2014.

[47] J. S. Ross *et al.*, "Electrical control of neutral and charged excitons in a monolayer semiconductor," *Nat. Commun.*, vol. 4, p. 1747, 2013.

[48] G.-B. Liu, D. Xiao, Y. Yao, X. Xu, and W. Yao, "Electronic structures and theoretical modelling of two-dimensional group-VIB transition metal dichalcogenides," *Chem. Soc. Rev.*, vol. 44, no. 9, pp. 2643–2663, 2015.

[49] R. Coehoorn, C. Haas, and R. A. de Groot, "Electronic structure of $MoSe_2$, MoS_2, and WSe_2. II. The nature of the optical band gaps," *Phys. Rev. B*, vol. 35, no. 12, pp. 6203–6206, 1987.

[50] K. von Klitzing, "The quantized Hall effect," *Rev. Mod. Phys.*, vol. 58, no. 3, pp. 519–531, 1986.

[51] "Press Release: The 1998 Nobel Prize in Physics." [Online]. Available: https://www.nobelprize.org/nobel_prizes/physics/laureates/1998/press.html. [Accessed: 03-May-2018].

[52] Y. Zhang, Y.-W. Tan, H. L. Stormer, and P. Kim, "Experimental observation of the quantum Hall effect and Berry's phase in graphene," *Nature*, vol. 438, no. 7065, pp. 201–204, 2005.

[53] K. S. Novoselov *et al.*, "Unconventional quantum Hall effect and Berry's phase of 2π in bilayer graphene," *Nat. Phys.*, vol. 2, no. 3, pp. 177–180, 2006.

[54] B. Radisavljevic, A. Radenovic, J. Brivio, V. Giacometti, and A. Kis, "Single-layer MoS_2 transistors," *Nat. Nanotechnol.*, vol. 6, no. 3, pp. 147–150, 2011.

[55] K. S. Novoselov *et al.*, "Electric Field Effect in Atomically Thin Carbon Films," *Science*, vol. 306, no. 5696, pp. 666–669, 2004.

[56] A. K. Geim and K. S. Novoselov, "The rise of graphene," *Nat. Mater.*, vol. 6, no. 3, pp. 183–191, 2007.

[57] H. Liu and P. D. Ye, "MoS_2 Dual-Gate MOSFET With Atomic-Layer-Deposited Al_2O_3 as Top-Gate Dielectric," *IEEE Electron Device Lett.*, vol. 33, no. 4, pp. 546–548, 2012.

[58] A. Rai *et al.*, "Air Stable Doping and Intrinsic Mobility Enhancement in Monolayer Molybdenum Disulfide by Amorphous Titanium Suboxide Encapsulation," *Nano Lett.*, vol. 15, no. 7, pp. 4329–4336, 2015.

[59] A. Sanne *et al.*, "Radio Frequency Transistors and Circuits Based on CVD MoS_2" *Nano Lett.*, vol. 15, no. 8, pp. 5039–5045, 2015.

[60] C. Liu, Y. Xu, and Y.-Y. Noh, "Contact engineering in organic field-effect transistors," *Mater. Today*, vol. 18, no. 2, pp. 79–96, 2015.

[61] Y. Guo, D. Liu, and J. Robertson, "Chalcogen vacancies in monolayer transition metal dichalcogenides and Fermi level pinning at contacts," *Appl. Phys. Lett.*, vol. 106, no. 17, p. 173106, 2015.

[62] D. Jena, K. Banerjee, and G. H. Xing, "2D crystal semiconductors: Intimate contacts," *Nat. Mater.*, vol. 13, no. 12, pp. 1076–1078, 2014.

[63] M. S. Fuhrer and J. Hone, "Measurement of mobility in dual-gated MoS_2 transistors," *Nat. Nanotechnol.*, vol. 8, no. 3, pp. 146–147, 2013.

[64] B. Radisavljevic and A. Kis, "Reply to 'Measurement of mobility in dual-gated MoS_2 transistors,'" *Nat. Nanotechnol.*, vol. 8, no. 3, pp. 147–148, 2013.

[65] F. Schwierz, J. Pezoldt, and R. Granzner, "Two-dimensional materials and their prospects in transistor electronics," *Nanoscale*, vol. 7, no. 18, pp. 8261–8283, 2015.

[66] J. M. Ukrainskii and A. B. Novoselova, *Dokl. Akad. Nauk SSSR*, vol. 139, p. 1136, 1961.

[67] R. Bissessur and H. Xu, "Nanomaterials based on molybdenum diselenide," *Mater. Chem. Phys.*, vol. 117, no. 2–3, pp. 335–337, 2009.

[68] H. S. S. R. Matte, B. Plowman, R. Datta, and C. N. R. Rao, "Graphene analogues of layered metal selenides," *Dalton Trans.*, vol. 40, no. 40, pp. 10322–10325, 2011.

[69] B. Radisavljevic, a Radenovic, J. Brivio, V. Giacometti, and a Kis, "Single-layer MoS_2 transistors.," *Nat. Nanotechnol.*, vol. 6, no. 3, pp. 147–50, 2011.

[70] H. Fang, S. Chuang, T. C. Chang, K. Takei, T. Takahashi, and A. Javey, "High-Performance Single Layered WSe_2 p-FETs with Chemically Doped Contacts.," *Nano Lett.*, vol. 12, no. 7, pp. 3788–92, 2012.

[71] P. Avouris, J. Appenzeller, R. Martel, S. J. Wind, and S. Member, "Carbon Nanotube Electronics," *Proc. IEEE*, vol. 91, no. 11, pp. 1772–1784, 2003.

[72] E. Liu *et al.*, "Role of Metal – Semiconductor Contact in Nanowire Field-Effect Transistors," *IEEE Trans. Nanotechnol.*, vol. 9, no. 2, pp. 237–242, 2010.

[73] J.-H. Chen, C. Jang, S. Xiao, M. Ishigami, and M. S. Fuhrer, "Intrinsic and extrinsic performance limits of graphene devices on SiO2.," *Nat. Nanotechnol.*, vol. 3, no. 4, pp. 206–9, 2008.

[74] S. Das Sarma, S. Adam, E. H. Hwang, and E. Rossi, "Electronic transport in two-dimensional graphene," *Rev. Mod. Phys.*, vol. 83, no. 2, pp. 407–470, May 2011.

[75] S. D. Sarma and E. H. Hwang, "Screening and transport in 2D semiconductor systems at low temperatures," *Sci. Rep.*, vol. 5, p. 16655, 2015.

[76] K. Kaasbjerg, K. S. Thygesen, and K. W. Jacobsen, "Phonon-limited mobility in n-type single-layer MoS 2 from first principles," *Phys. Rev. B*, vol. 85, no. 11, 2012.

[77] S. Xu *et al.*, "Universal low-temperature Ohmic contacts for quantum transport in transition metal dichalcogenides," *2D Mater.*, vol. 3, no. 2, p. 021007, 2016.

[78] C. R. Dean *et al.*, "Boron nitride substrates for high-quality graphene electronics," *Nat. Nanotechnol.*, vol. 5, no. 10, pp. 722–726, 2010.

[79] L. Wang *et al.*, "One-Dimensional Electrical Contact to a Two-Dimensional Material," *Science*, vol. 342, no. 6158, pp. 614–617, 2013.

[80] K. Watanabe, T. Taniguchi, and H. Kanda, "Direct-bandgap properties and evidence for ultraviolet lasing of hexagonal boron nitride single crystal," *Nat. Mater.*, vol. 3, no. 6, pp. 404–409, 2004.

[81] G.-H. Lee *et al.*, "Electron tunneling through atomically flat and ultrathin hexagonal boron nitride," *Appl. Phys. Lett.*, 2011.

[82] B. Fallahazad *et al.*, "Gate-Tunable Resonant Tunneling in Double Bilayer Graphene Heterostructures," *Nano Lett.*, vol. 15, no. 1, pp. 428–433, 2015.

[83] S. Kim *et al.*, "Direct Measurement of the Fermi Energy in Graphene Using a Double-Layer Heterostructure," *Phys. Rev. Lett.*, vol. 108, no. 11, 2012.

[84] K. Kim *et al.*, "van der Waals Heterostructures with High Accuracy Rotational Alignment," *Nano Lett.*, vol. 16, no. 3, pp. 1989–1995, 2016.

[85] W. M. Haynes, ed., *CRC Handbook of Chemistry and Physics, 97th Edition*. CRC Press/Taylor & Francis, 2017.

[86] G.-H. Lee *et al.*, "Highly Stable, Dual-Gated MoS_2 Transistors Encapsulated by Hexagonal Boron Nitride with Gate-Controllable Contact, Resistance, and Threshold Voltage," *ACS Nano*, vol. 9, no. 7, pp. 7019–7026, 2015.

[87] G.-H. Lee *et al.*, "Flexible and Transparent MoS_2 Field-Effect Transistors on Hexagonal Boron Nitride-Graphene Heterostructures," *ACS Nano*, vol. 7, no. 9, pp. 7931–7936, 2013.

[88] L. Yang *et al.*, "Chloride Molecular Doping Technique on 2D Materials: WS_2 and MoS_2" *Nano Lett.*, vol. 14, no. 11, pp. 6275–6280, 2014.

[89] B. Radisavljevic and A. Kis, "Mobility engineering and a metal–insulator transition in monolayer MoS_2," *Nat. Mater.*, vol. 12, no. 9, pp. 815–820, 2013.

[90] X. Cui *et al.*, "Low-Temperature Ohmic Contact to Monolayer MoS_2 by van der Waals Bonded Co/h-BN Electrodes," *Nano Lett.*, vol. 17, no. 8, pp. 4781–4786, 2017.

[91] H. C. P. Movva *et al.*, "High-Mobility Holes in Dual-Gated WSe_2 Field-Effect Transistors," *ACS Nano*, vol. 9, no. 10, pp. 10402–10410, 2015.

[92] J. Kang, S. Tongay, J. Zhou, J. Li, and J. Wu, "Band offsets and heterostructures of two-dimensional semiconductors," *Appl. Phys. Lett.*, vol. 102, no. 1, p. 012111, 2013.

[93] Z. Jin, X. Li, J. T. Mullen, and K. W. Kim, "Intrinsic transport properties of electrons and holes in monolayer transition-metal dichalcogenides," *Phys. Rev. B*, vol. 90, no. 4, p. 045422, 2014.

[94] X. Cui *et al.*, "Multi-terminal transport measurements of MoS_2 using a van der Waals heterostructure device platform," *Nat. Nanotechnol.*, vol. 10, no. 6, pp. 534–540, 2015.

[95] N. Ma and D. Jena, "Charge Scattering and Mobility in Atomically Thin Semiconductors," *Phys. Rev. X*, vol. 4, no. 1, p. 011043, 2014.

[96] T. Ando, A. B. Fowler, and F. Stern, "Electronic properties of two-dimensional systems," *Rev. Mod. Phys.*, vol. 54, no. 2, pp. 437–672, 1982.

[97] B. W. H. Baugher, H. O. H. Churchill, Y. Yang, and P. Jarillo-Herrero, "Intrinsic Electronic Transport Properties of High-Quality Monolayer and Bilayer MoS$_2$," *Nano Lett.*, vol. 13, no. 9, pp. 4212–4216, 2013.

[98] K. Kim *et al.*, "Band alignment in WSe$_2$–graphene heterostructures," *ACS Nano*, vol. 9, no. 4, pp. 4527–4532, 2015.

[99] S. M. Sze and K. K. Ng, *Physics of semiconductor devices*. Wiley, 2006.

[100] J. Knoch and J. Appenzeller, "Tunneling phenomena in carbon nanotube field-effect transistors," *Phys. Status Solidi A*, vol. 205, no. 4, pp. 679–694, 2008.

[101] J. Knoch, M. Zhang, S. Mantl, and J. Appenzeller, "On the performance of single-gated ultrathin-body SOI Schottky-barrier MOSFETs," *IEEE Trans. Electron Devices*, vol. 53, no. 7, pp. 1669–1674, 2006.

[102] S. Larentis *et al.*, "Large effective mass and interaction-enhanced Zeeman splitting of K-valley electrons in MoSe$_2$," *Phys. Rev. B*, vol. 97, no. 20, p. 201407, May 2018.

[103] D. Xiao, T. F. Heinz, W. Yao, and X. Xu, "Spin and pseudospins in layered transition metal dichalcogenides," *Nat. Phys.*, vol. 10, no. 5, p. 343, May 2014.

[104] X. Li, F. Zhang, and Q. Niu, "Unconventional Quantum Hall Effect and Tunable Spin Hall Effect in Dirac Materials: Application to an Isolated MoS$_2$ Trilayer," *Phys. Rev. Lett.*, vol. 110, no. 6, p. 066803, 2013.

[105] G. Wang *et al.*, "Magneto-optics in transition metal diselenide monolayers," *2D Mater.*, vol. 2, no. 3, p. 034002, 2015.

[106] G. Aivazian *et al.*, "Magnetic control of valley pseudospin in monolayer WSe$_2$," *Nat. Phys.*, vol. 11, no. 2, p. 148, 2015.

[107] Z. Wang, J. Shan, and K. F. Mak, "Valley- and spin-polarized Landau levels in monolayer WSe$_2$," *Nat. Nanotechnol.*, vol. 12, no. 2, p. nnano.2016.213, 2016.

[108] J. M. Riley *et al.*, "Negative electronic compressibility and tunable spin splitting in WSe$_2$," *Nat. Nanotechnol.*, vol. 10, no. 12, pp. 1043–1047, 2015.

[109] C. Zhang *et al.*, "Probing Critical Point Energies of Transition Metal Dichalcogenides: Surprising Indirect Gap of Single Layer WSe$_2$," *Nano Lett.*, vol. 15, no. 10, pp. 6494–6500, 2015.

[110] B. Fallahazad *et al.*, "Shubnikov-de Haas Oscillations of High-Mobility Holes in Monolayer and Bilayer WSe$_2$: Landau Level Degeneracy, Effective Mass, and Negative Compressibility," *Phys. Rev. Lett.*, vol. 116, no. 8, p. 086601, 2016.

[111] H. C. P. Movva *et al.*, "Density-Dependent Quantum Hall States and Zeeman Splitting in Monolayer and Bilayer WSe$_2$," *Phys. Rev. Lett.*, vol. 118, no. 24, p. 247701, 2017.

[112] S. Xu *et al.*, "Odd-Integer Quantum Hall States and Giant Spin Susceptibility in p-Type Few-Layer WSe$_2$," *Phys. Rev. Lett.*, vol. 118, no. 6, p. 067702, 2017.

[113] S. Xu *et al.*, "Probing strong interactions in p-type few-layer WSe$_2$ by density-dependent Landau level crossing," *ArXiv170802909 Cond-Mat*, 2017.

[114] J. Lin *et al.*, "Probing Landau levels of strongly interacting massive Dirac electrons in layer-polarized MoS$_2$," *ArXiv180308007 Cond-Mat*, 2018.

[115] Z. Wu *et al.*, "Even–odd layer-dependent magnetotransport of high-mobility Q-valley electrons in transition metal disulfides," *Nat. Commun.*, vol. 7, p. ncomms12955, 2016.

[116] R. Pisoni *et al.*, "Gate-Defined One-Dimensional Channel and Broken Symmetry States in MoS_2 van der Waals Heterostructures," *Nano Lett.*, 2017.

[117] Q. H. Chen *et al.*, "Inducing and Manipulating Heteroelectronic States in a Single MoS2 Thin Flake," *Phys. Rev. Lett.*, vol. 119, no. 14, p. 147002, 2017.

[118] T. Uwanno, Y. Hattori, T. Taniguchi, K. Watanabe, and K. Nagashio, "Fully dry PMMA transfer of graphene on h -BN using a heating/cooling system," *2D Mater.*, vol. 2, no. 4, p. 041002, 2015.

[119] G. Gouadec and P. Colomban, "Raman Spectroscopy of Nanomaterials: How Spectra Relate to Disorder, Particle Size and Mechanical Properties," *Prog. Cryst. Growth Charact. Mater.*, vol. 53, no. 1, pp. 1–56, 2007.

[120] D. Edelberg *et al.*, "Hundredfold Enhancement of Light Emission via Defect Control in Monolayer Transition-Metal Dichalcogenides," *ArXiv180500127 Cond-Mat*, 2018.

[121] A. V. Suslov, "Stand alone experimental setup for dc transport measurements," *Rev. Sci. Instrum.*, vol. 81, no. 7, p. 075111, 2010.

[122] A. Kormányos, V. Zólyomi, N. D. Drummond, and G. Burkard, "Spin-Orbit Coupling, Quantum Dots, and Qubits in Monolayer Transition Metal Dichalcogenides," *Phys. Rev. X*, vol. 4, no. 1, p. 011034, 2014.

[123] K. Kośmider, J. W. González, and J. Fernández-Rossier, "Large spin splitting in the conduction band of transition metal dichalcogenide monolayers," *Phys. Rev. B*, vol. 88, no. 24, p. 245436, 2013.

[124] H. L. Störmer, A. C. Gossard, and W. Wiegmann, "Observation of intersubband scattering in a 2-dimensional electron system," *Solid State Commun.*, vol. 41, no. 10, pp. 707–709, 1982.

[125] J. H. Davies, "The Physics of Low-dimensional Semiconductors by John H. Davies," *Cambridge Core*, 1997. [Online].

[126] R. B. Dingle, "Some magnetic properties of metals II. The influence of collisions on the magnetic behaviour of large systems," *Proc R Soc Lond A*, vol. 211, no. 1107, pp. 517–525, 1952.

[127] H. C. P. Movva *et al.*, "Tunable Gamma-K Valley Populations in Hole-Doped Trilayer WSe2," *Phys. Rev. Lett.*, vol. 120, no. 10, p. 107703, 2018.

[128] A. Kormányos, P. Rakyta, and G. Burkard, "Landau levels and Shubnikov–de Haas oscillations in monolayer transition metal dichalcogenide semiconductors," *New J. Phys.*, vol. 17, no. 10, p. 103006, 2015.

[129] F. F. Fang and P. J. Stiles, "Effects of a Tilted Magnetic Field on a Two-Dimensional Electron Gas," *Phys. Rev.*, vol. 174, no. 3, pp. 823–828, 1968.

[130] T. Okamoto, K. Hosoya, S. Kawaji, and A. Yagi, "Spin Degree of Freedom in a Two-Dimensional Electron Liquid," *Phys. Rev. Lett.*, vol. 82, no. 19, pp. 3875–3878, May 1999.

[131] J. Zhu, H. L. Stormer, L. N. Pfeiffer, K. W. Baldwin, and K. W. West, "Spin Susceptibility of an Ultra-Low-Density Two-Dimensional Electron System," *Phys. Rev. Lett.*, vol. 90, no. 5, p. 056805, 2003.

[132] K. Vakili, Y. P. Shkolnikov, E. Tutuc, E. P. De Poortere, and M. Shayegan, "Spin Susceptibility of Two-Dimensional Electrons in Narrow AlAs Quantum Wells," *Phys. Rev. Lett.*, vol. 92, no. 22, p. 226401, 2004.

[133] M. V. Gustafsson *et al.*, "Ambipolar Landau levels and strong band-selective carrier interactions in monolayer WSe2," *Nat. Mater.*, vol. 17, no. 5, pp. 411–415, May 2018.

[134] E. Tutuc, E. P. De Poortere, S. J. Papadakis, and M. Shayegan, "In-Plane Magnetic Field-Induced Spin Polarization and Transition to Insulating Behavior in Two-Dimensional Hole Systems," *Phys. Rev. Lett.*, vol. 86, no. 13, pp. 2858–2861, 2001.

[135] G. F. Giuliani and G. Vignale, *Theory of the Electron Liquid*. Cambridge University Press, 2005.

[136] S. De Palo, M. Botti, S. Moroni, and G. Senatore, "Effects of Thickness on the Spin Susceptibility of the Two Dimensional Electron Gas," *Phys. Rev. Lett.*, vol. 94, no. 22, p. 226405, 2005.

[137] R. Geick, C. H. Perry, and G. Rupprecht, "Normal Modes in Hexagonal Boron Nitride," *Phys. Rev.*, vol. 146, no. 2, pp. 543–547, 1966.

[138] A. Kumar and P. K. Ahluwalia, "Tunable dielectric response of transition metals dichalcogenides MX_2 (M=Mo, W; X=S, Se, Te): Effect of quantum confinement," *Phys. B Condens. Matter*, vol. 407, no. 24, pp. 4627–4634, 2012.

[139] C. Attaccalite, S. Moroni, P. Gori-Giorgi, and G. B. Bachelet, "Correlation Energy and Spin Polarization in the 2D Electron Gas," *Phys. Rev. Lett.*, vol. 88, no. 25, p. 256601, 2002.

[140] D. V. Rybkovskiy, I. C. Gerber, and M. V. Durnev, "Atomically inspired k.p approach and valley Zeeman effect in transition metal dichalcogenide monolayers," *Phys. Rev. B*, vol. 95, no. 15, p. 155406, 2017.

[141] E. Tutuc, S. Melinte, E. P. De Poortere, M. Shayegan, and R. Winkler, "Role of finite layer thickness in spin polarization of GaAs two-dimensional electrons in strong parallel magnetic fields," *Phys. Rev. B*, vol. 67, no. 24, p. 241309, 2003.

[142] S. Larentis *et al.*, "Band Offset and Negative Compressibility in Graphene-MoS_2 Heterostructures," *Nano Lett.*, vol. 14, no. 4, pp. 2039–2045, 2014.

[143] J. P. Eisenstein, L. N. Pfeiffer, and K. W. West, "Compressibility of the two-dimensional electron gas: Measurements of the zero-field exchange energy and fractional quantum Hall gap," *Phys. Rev. B*, vol. 50, no. 3, pp. 1760–1778, 1994.

[144] S. Bertolazzi, D. Krasnozhon, and A. Kis, "Nonvolatile Memory Cells Based on MoS_2/Graphene Heterostructures," *ACS Nano*, vol. 7, no. 4, pp. 3246–3252, 2013.

[145] M. S. Choi *et al.*, "Controlled charge trapping by molybdenum disulphide and graphene in ultrathin heterostructured memory devices," *Nat. Commun.*, vol. 4, p. 1624, 2013.

[146] K. Roy *et al.*, "Graphene-MoS2 hybrid structures for multifunctional photoresponsive memory devices," *Nat. Nanotechnol.*, vol. 8, no. 11, pp. 826–830, 2013.

[147] A. Allain, J. Kang, K. Banerjee, and A. Kis, "Electrical contacts to two-dimensional semiconductors," *Nat. Mater.*, vol. 14, no. 12, pp. 1195–1205, 2015.

[148] S. Das, H.-Y. Chen, A. V. Penumatcha, and J. Appenzeller, "High Performance Multilayer MoS2 Transistors with Scandium Contacts," *Nano Lett.*, vol. 13, no. 1, pp. 100–105, 2013.

[149] K.-E. Byun *et al.*, "Graphene for True Ohmic Contact at Metal–Semiconductor Junctions," *Nano Lett.*, vol. 13, no. 9, pp. 4001–4005, 2013.

[150] Y. Liu *et al.*, "Toward Barrier Free Contact to Molybdenum Disulfide Using Graphene Electrodes," *Nano Lett.*, vol. 15, no. 5, pp. 3030–3034, May 2015.

[151] L. Yu *et al.*, "Graphene/MoS2 Hybrid Technology for Large-Scale Two-Dimensional Electronics," *Nano Lett.*, vol. 14, no. 6, pp. 3055–3063, 2014.

[152] J. Yoon *et al.*, "Highly Flexible and Transparent Multilayer MoS2 Transistors with Graphene Electrodes," *Small*, vol. 9, no. 19, pp. 3295–3300, 2013.

[153] J. Y. Kwak *et al.*, "Electrical Characteristics of Multilayer MoS2 FET's with MoS2/Graphene Heterojunction Contacts," *Nano Lett.*, vol. 14, no. 8, pp. 4511–4516, 2014.

[154] Y. Wu *et al.*, "Negative compressibility in graphene-terminated black phosphorus heterostructures," *Phys. Rev. B*, vol. 93, no. 3, p. 035455, 2016.

[155] L. Li, C. Richter, S. Paetel, T. Kopp, J. Mannhart, and R. C. Ashoori, "Very Large Capacitance Enhancement in a Two-Dimensional Electron System," *Science*, vol. 332, no. 6031, pp. 825–828, May 2011.

[156] B. Tanatar and D. M. Ceperley, "Ground state of the two-dimensional electron gas," *Phys. Rev. B*, vol. 39, no. 8, pp. 5005–5016, 1989.

[157] J. P. Eisenstein, L. N. Pfeiffer, and K. W. West, "Negative compressibility of interacting two-dimensional electron and quasiparticle gases," *Phys Rev Lett*, vol. 68, no. 5, pp. 674–677, 1992.

[158] S. C. Dultz and H. W. Jiang, "Thermodynamic Signature of a Two-Dimensional Metal-Insulator Transition," *Phys. Rev. Lett.*, vol. 84, no. 20, pp. 4689–4692, May 2000.

[159] A. C. Ferrari and D. M. Basko, "Raman spectroscopy as a versatile tool for studying the properties of graphene," *Nat. Nanotechnol.*, vol. 8, no. 4, pp. 235–246, 2013.

[160] A. V. Kretinin *et al.*, "Electronic Properties of Graphene Encapsulated with Different Two-Dimensional Atomic Crystals," *Nano Lett.*, vol. 14, no. 6, pp. 3270–3276, 2014.

[161] M. M. Perera *et al.*, "Improved Carrier Mobility in Few-Layer MoS2 Field-Effect Transistors with Ionic-Liquid Gating," *ACS Nano*, vol. 7, no. 5, pp. 4449–4458, May 2013.

[162] Z. Jiang, Y. Zhang, Y.-W. Tan, H. L. Stormer, and P. Kim, "Quantum Hall effect in graphene," *Solid State Commun.*, vol. 143, no. 1–2, pp. 14–19, 2007.

[163] Y.-J. Yu, Y. Zhao, S. Ryu, L. E. Brus, K. S. Kim, and P. Kim, "Tuning the Graphene Work Function by Electric Field Effect," *Nano Lett.*, vol. 9, no. 10, pp. 3430–3434, 2009.

[164] R. Yan *et al.*, "Determination of graphene work function and graphene-insulator-semiconductor band alignment by internal photoemission spectroscopy," *Appl. Phys. Lett.*, vol. 101, no. 2, p. 022105, 2012.

[165] W. Jaegermann, A. Klein, and C. Pettenkofer, "Electronic Properties of Van Der Waals-Epitaxy Films and Interfaces," in *Electron Spectroscopies Applied to Low-Dimensional Materials*, vol. 24, H. P. Hughes and H. I. Starnberg, Eds. Springer Netherlands, 2002, pp. 317–402.

[166] L. F. Mattheiss, "Band Structures of Transition-Metal-Dichalcogenide Layer Compounds," *Phys Rev B*, vol. 8, no. 8, pp. 3719–3740, 1973.

[167] E. J. G. Santos and E. Kaxiras, "Electrically Driven Tuning of the Dielectric Constant in MoS_2 Layers," *ACS Nano*, vol. 7, no. 12, pp. 10741–10746, 2013.

[168] C.-P. Lu, G. Li, J. Mao, L.-M. Wang, and E. Y. Andrei, "Bandgap, Mid-Gap States, and Gating Effects in MoS_2," *Nano Lett.*, vol. 14, no. 8, pp. 4628–4633, 2014.

[169] T. Shimada, F. S. Ohuchi, and B. A. Parkinson, "Work Function and Photothreshold of Layered Metal Dichalcogenides," *Jpn. J. Appl. Phys.*, vol. 33, no. 5R, p. 2696, May 1994.

[170] A. Klein, C. Pettenkofer, W. Jaegermann, M. Lux-Steiner, and E. Bucher, "A photoemission study of barrier and transport properties of the interfaces of Au and Cu with WSe_2(0001) surfaces," *Surf. Sci.*, vol. 321, no. 1, pp. 19–31, Dec. 1994.

[171] H. Jiang, "Electronic Band Structures of Molybdenum and Tungsten Dichalcogenides by the GW Approach," *J. Phys. Chem. C*, vol. 116, no. 14, pp. 7664–7671, 2012.

[172] H. C. P. Movva *et al.*, "Room temperature gate-tunable negative differential resistance in MoS_2/hBN/WSe_2 heterostructures," in *2016 74th Annual Device Research Conference (DRC)*, 2016, pp. 1–2.

[173] G. W. Burg *et al.*, "Coherent Interlayer Tunneling and Negative Differential Resistance with High Current Density in Double Bilayer Graphene–WSe_2 Heterostructures," *Nano Lett.*, vol. 17, no. 6, pp. 3919–3925, 2017.

[174] G. W. Burg *et al.*, "Strongly Enhanced Tunneling at Total Charge Neutrality in Double-Bilayer Graphene-WSe_2 Heterostructures," *Phys. Rev. Lett.*, vol. 120, no. 17, p. 177702, 2018.

[175] A. Kormányos, V. Zólyomi, N. D. Drummond, P. Rakyta, G. Burkard, and V. I. . Fal'ko, "Monolayer MoS_2: Trigonal warping, the valley, and spin-orbit coupling effects," *Phys Rev B*, vol. 88, no. 4, p. 045416, 2013.

[176] R. E. V. Profumo, M. Polini, R. Asgari, R. Fazio, and A. H. MacDonald, "Electron-electron interactions in decoupled graphene layers," *Phys. Rev. B*, vol. 82, no. 8, 2010.

[177] Y. Barlas, T. Pereg-Barnea, M. Polini, R. Asgari, and A. H. MacDonald, "Chirality and Correlations in Graphene," *Phys. Rev. Lett.*, vol. 98, no. 23, 2007.

[178] R. M. Jock *et al.*, "Probing band-tail states in silicon metal-oxide-semiconductor heterostructures with electron spin resonance," *Appl Phys Lett*, vol. 100, no. 2, p. 023503, 2012.

[179] C. Auth *et al.*, "45nm High-k + metal gate strain-enhanced transistors," in *2008 Symposium on VLSI Technology*, 2008, pp. 128–129.

[180] S. Larentis *et al.*, "Reconfigurable Complementary Monolayer MoTe$_2$ Field-Effect Transistors for Integrated Circuits," *ACS Nano*, vol. 11, no. 5, pp. 4832–4839, 2017.

[181] S. B. Desai *et al.*, "MoS$_2$ transistors with 1-nanometer gate lengths," *Science*, vol. 354, no. 6308, pp. 99–102, 2016.

[182] G. Fiori *et al.*, "Electronics based on two-dimensional materials," *Nat. Nanotechnol.*, vol. 9, no. 10, pp. 768–779, 2014.

[183] D. Jariwala, V. K. Sangwan, L. J. Lauhon, T. J. Marks, and M. C. Hersam, "Emerging Device Applications for Semiconducting Two-Dimensional Transition Metal Dichalcogenides," *ACS Nano*, vol. 8, no. 2, pp. 1102–1120, 2014.

[184] N. R. Pradhan *et al.*, "Field-Effect Transistors Based on Few-Layered α-MoTe$_2$," *ACS Nano*, vol. 8, no. 6, pp. 5911–5920, 2014.

[185] H. Fang, S. Chuang, T. C. Chang, K. Takei, T. Takahashi, and A. Javey, "High-Performance Single Layered WSe$_2$ p-FETs with Chemically Doped Contacts," *Nano Lett.*, vol. 12, no. 7, pp. 3788–3792, 2012.

[186] M. Tosun *et al.*, "High-Gain Inverters Based on WSe$_2$ Complementary Field-Effect Transistors," *ACS Nano*, vol. 8, no. 5, pp. 4948–4953, 2014.

[187] L. Yu *et al.*, "High-Performance WSe$_2$ Complementary Metal Oxide Semiconductor Technology and Integrated Circuits," *Nano Lett.*, vol. 15, no. 8, pp. 4928–4934, 2015.

[188] S. Das, M. Dubey, and A. Roelofs, "High gain, low noise, fully complementary logic inverter based on bi-layer WSe$_2$ field effect transistors," *Appl. Phys. Lett.*, vol. 105, no. 8, p. 083511, 2014.

[189] C.-H. Liu, C.-C. Wu, and Z. Zhong, "A Fully Tunable Single-Walled Carbon Nanotube Diode," *Nano Lett.*, vol. 11, no. 4, pp. 1782–1785, 2011.

[190] J. U. Lee, P. P. Gipp, and C. M. Heller, "Carbon nanotube p-n junction diodes," *Appl. Phys. Lett.*, vol. 85, no. 1, pp. 145–147, 2004.

[191] K. Bosnick, N. Gabor, and P. McEuen, "Transport in carbon nanotube p-i-n diodes," *Appl. Phys. Lett.*, vol. 89, no. 16, p. 163121, 2006.

[192] H. Qiu, L. Pan, Z. Yao, J. Li, Y. Shi, and X. Wang, "Electrical characterization of back-gated bi-layer MoS$_2$ field-effect transistors and the effect of ambient on their performances," *Appl. Phys. Lett.*, vol. 100, no. 12, p. 123104, 2012.

[193] J. Gao, B. Li, J. Tan, P. Chow, T.-M. Lu, and N. Koratkar, "Aging of Transition Metal Dichalcogenide Monolayers," *ACS Nano*, vol. 10, no. 2, pp. 2628–2635, 2016.

[194] B. Chen *et al.*, "Environmental Changes in MoTe$_2$ Excitonic Dynamics by Defects-Activated Molecular Interaction," *ACS Nano*, vol. 9, no. 5, pp. 5326–5332, 2015.

[195] C. Kim *et al.*, "Fermi Level Pinning at Electrical Metal Contacts of Monolayer Molybdenum Dichalcogenides," *ACS Nano*, vol. 11, no. 2, pp. 1588–1596, 2017.

[196] Y.-F. Lin *et al.*, "Ambipolar $MoTe_2$ Transistors and Their Applications in Logic Circuits," *Adv. Mater.*, vol. 26, no. 20, pp. 3263–3269, 2014.

[197] S. Cho *et al.*, "Phase patterning for ohmic homojunction contact in $MoTe_2$," *Science*, vol. 349, no. 6248, pp. 625–628, 2015.

[198] J.-S. Kim *et al.*, "Toward air-stable multilayer phosphorene thin-films and transistors," *Sci. Rep.*, vol. 5, p. 8989, 2015.

[199] S. Nakaharai, M. Yamamoto, K. Ueno, and K. Tsukagoshi, "Carrier Polarity Control in α-$MoTe_2$ Schottky Junctions Based on Weak Fermi-Level Pinning," *ACS Appl. Mater. Interfaces*, vol. 8, no. 23, pp. 14732–14739, 2016.

[200] J. S. Ross *et al.*, "Electrically tunable excitonic light-emitting diodes based on monolayer WSe_2 p-n junctions," *Nat. Nanotechnol.*, vol. 9, no. 4, pp. 268–272, 2014.

[201] B. W. H. Baugher, H. O. H. Churchill, Y. Yang, and P. Jarillo-Herrero, "Optoelectronic devices based on electrically tunable p-n diodes in a monolayer dichalcogenide," *Nat. Nanotechnol.*, vol. 9, no. 4, pp. 262–267, 2014.

[202] A. Pospischil, M. M. Furchi, and T. Mueller, "Solar-energy conversion and light emission in an atomic monolayer p-n diode," *Nat. Nanotechnol.*, vol. 9, no. 4, pp. 257–261, 2014.

[203] D. Li *et al.*, "Two-dimensional non-volatile programmable p–n junctions," *Nat. Nanotechnol.*, vol. 12, no. 9, pp. 901–906, 2017.

[204] Y.-Q. Bie *et al.*, "A $MoTe_2$-based light-emitting diode and photodetector for silicon photonic integrated circuits," *Nat. Nanotechnol.*, vol. 12, no. 12, pp. 1124–1129, Dec. 2017.